On the response of brain vasculature to focused ultrasound and microbubbles

by

Dallan William McMahon

A thesis submitted in conformity with the requirements
for the degree of Doctor of Philosophy
Department of Medical Biophysics
University of Toronto

Abstract

On the response of brain vasculature to focused ultrasound and microbubbles

Dallan William McMahon

Doctor of Philosophy

Department of Medical Biophysics

University of Toronto

2019

The treatment of neuropathologies is complicated by many factors; common, however, to most afflictions is the inherent difficulty of delivering therapeutic agents from systemic circulation to brain parenchyma. Specialized cerebrovasculature regulates the passage of molecules, acting to preserve efficient neural function and to protect from infection and toxicity. While essential, the blood-brain barrier (BBB) hinders the development of effective treatment strategies. In combination with circulating microbubbles (MBs), focused ultrasound (FUS) can be used to transiently increase BBB permeability, providing an avenue for localized brain-drug delivery. There are, however, risks associated with perturbing homeostatic conditions by allowing substances to enter the brain that are excluded under physiological conditions. The work described in this thesis focuses on characterizing the impact of FUS+MB-mediated BBB permeability enhancement on brain vasculature and on providing a means to mitigate risk.

To this end, a hypothesis-generating microarray analysis of gene expression changes in hippocampal microvasculature was performed in the acute stages following sonication. The principal finding of this study was differential gene expression indicative of acute inflammation 6 hours following sonication, a response that was present, but diminished, by 24 hours. This observation motivated a study of factors that contribute to sonication-induced inflammation, including MB dose and the degree of BBB permeability enhancement, both of which were found to influence the expression of several key proinflammatory markers. The pattern of gene expression changes detected in microarray analysis 24

hours following FUS+MB exposure also motivated the study of blood vessel growth. A modest increase in blood vessel density and newborn endothelial cell density was observed at 7- and 14-days following sonication, an effect that normalized by 21 days. Finally, to manage the risks associated with transiently increasing BBB permeability, the post-sonication administration of dexamethasone, a synthetic glucocorticoid, was studied. Dexamethasone was found to expedite the return of BBB integrity, as well as limit inflammation, astrocyte activation, and blood vessel growth following FUS+MB exposure. An in-depth description of these studies and their implications are discussed. The findings presented in this thesis have value in informing clinical cost-benefit analyses and may influence the design of novel brain therapies.

Dedication

To Sarah, Betty, Larry, Marissa, Ryan, and Beckett.

Acknowledgements

There are a great number of people I would like to thank, both for their direct contributions to the completion of work detailed in this thesis, as well as to the preservation of my happiness and well-being along the way. First and foremost, I would like to thank Dr. Kullervo Hynynen for providing me with the most important opportunity of my academic career, for allowing me to learn at the highest level, and for inspiring me both personally and professionally. I will forever be grateful for his mentorship and the ways in which he shaped me as a researcher. I would also like to thank the members of my supervisory committee, Dr. Bojana Stefanovic, Dr. Reina Bendayan, and Dr. Dan Dumont, who have all been generous with their time and have forced me to think about my research from unique perspectives. Additionally, I would like to thank Dr. Meghan O'Reilly and Dr. Ryan Jones for their academic mentorship. My transition into therapeutic ultrasound research would certainly have been much more difficult without their sustained and generous transfer of knowledge.

My time in the FUS Lab at Sunnybrook Research Institute (SRI) has afforded me the opportunity to work and learn from many skilled and kind people. I am thankful for the help of veterinary technicians, Shawna Rideout, Viva Chan, and Alexandra Garces, for their efforts in animal preparation and care during many *in vivo* experiments. I would like to thank Rooke Reyes, Anthony Chau, Lucy Deng, Kogee Leung, and Tyler Portelli for their technical assistance and troubleshooting, as well as for ensuring the proper function of experimental setups used in my work. Additionally, I would also like to acknowledge the students that I had the privilege of working with over the years, Alisa Takabe-French, Christopher Povolo, Ethan Mah, Arani Kulamurugan, Joanna Roy, and Yiwen Zhang. I learned a great deal about mentorship and collaboration from these pairings. In addition to the support from those already mentioned, many incredible people have both aided me personally and have been tremendously helpful academically. Marc Santos, Harriet Lea-Banks, Chris Acconcia, Shengkai Wu, Sharshi Bulner, Wendy Oakden, Geneve Awong, and Kristina Mikloska have all been willing to go out of their way to lend a helping hand whenever I have asked.

The friendships I have formed over the years have been one of the major highlights of my degree. Charissa Poon is one of the most selfless and generous people I know, was a terrific conference travel buddy (remember: dog mountain, biking in Herndon, Georgian bread, blueberry, lost ocean shoes), and is a person I can always count on being honest. Skyler Mooney provided an irl echo chamber for voicing my outrage over the constant stream of Trump news and was a terrific co-general manager for the Leafs (Marner will be traded). Conversations about Chef John, Brad Leone, and Matty Matheson really enabled my internet cooking show habit. Kevin Grykuliak was also an outlet for political discussions but did so with a vocabulary that dazzled and confused. He also provided a great deal of generosity and kindness, exemplified with his thunderous distribution of espresso shots. Ryan Jones has been by my side since the first year of undergraduate studies. He was always my model of a successful graduate student and I will forever be thankful for what he did in Gander. And lastly, I want to thank the most important person in my life, Sarah Atwi. She is the definition of a supportive partner, best friend, and is the largest single contributor to my success. Talk show, stairs, snacks, Boat trips, Georgina, walks, Chomp 'n' Stomp, dog parks, and Blythwood make up some of my favorite memories of SRI. In a completely non-cliché way, I would not have completed this degree without her. It is also important to recognize nutritional support from Pizza Pizza and Tim Hortons.

Funding for this work came from the National Institutes of Health, the Canadian Institutes of Health Research, the FUS Foundation, and the Canada Research Chairs program. I am personally grateful for the generous financial support provided by the Ontario Graduate Scholarships program, SRI, and the Department of Medical Biophysics.

Author's Contributions

The primary research presented in this thesis is adapted from original publications. Experimental design for each study was formulated by the thesis author in consultation with the principal supervisor, Dr. Kullervo Hynynen. The thesis author performed all *in vivo* experiments, collected and processed all tissue samples, analysed all data, and was the primary author for all manuscripts. The co-author for work presented in *Chapter 2*, Dr. Reina Bendayan, contributed to the interpretation of microarray results and was involved in manuscript editing. The co-author for work presented in *Chapter 4*, Ethan Mah, participated in the quantification of BrdU positive endothelial cells. The co-author for work presented in *Chapter 5*, Dr. Wendy Oakden, aided in the development of the quantitative magnetic resonance imaging and analysis protocols used in that study, as well as edited the corresponding manuscript. Unless otherwise stated, the author created each figure displayed in this thesis.

Contents

List of Tables

List of Figures

List of Symbols and Abbreviations

AAV	adeno-associated virus
Aβ	amyloid beta
ABC	ATP-binding cassette
ACTB	actin beta
AD	Alzheimer's disease
AIF	arterial input function
ANCOVA	analysis of covariance
ANOVA	analysis of variance
AU	arbitrary units
BBB	blood-brain barrier
BrdU	bromodeoxyuridine
CA1-4	cornus amonis 1-4
CCL	chemokine ligand
CD	cluster of differentiation
CE-T1w	contrast-enhanced T1-weighted
CNS	central nervous system
C_p	concentration of contrast agent in plasma
C_t	concentration of contrast agent in tissue
BRF	burst repetition frequency
DCE	dynamic contrast-enhanced
DEX	dexamethasone
DG	dentate gyrus
EC	endothelial cell
EES	extravascular-extracellular space
ELISA	enzyme-linked immunosorbent assay
f	transmit frequency
FDR	false discovery rate
FFT	fast Fourier transform
FUS	focused ultrasound
GAPDH	glyceraldehyde 3-phosphate dehydrogenase

GFAP	glial fibrillary acidic protein
GLUT1	glucose transporter-1
GO	gene ontology
GSEA	geneset enrichment analysis
H&E	hematoxylin and eosin
IBA1	ionized calcium binding adaptor molecule-1
ICAM1	intercellular adhesion molecule-1
IFNɣ	interferon gamma
IL	interleukin
K^{trans}	transfer constant
LCM	laser capture
MB	microbubble
MCP1	monocyte chemoattractant protein-1
MI	Mechanical index
MRI	magnetic resonance imaging
NES	normalized enrichment score
NFκB	nuclear factor-κB
ORA	over-representation analysis
PB	phosphate buffer
PECAM1	platelet endothelial cell adhesion molecule-1
PNP	peak negative pressure
qRT-PCR	quantitative real-time polymerase chain reaction
r_1	longitudinal relaxivity
RBC	red blood cell
SELL	selectin-L
SLC	solute carrier
t	time
T2*w	T2-star-weighted
T2w	T2-weighted
TBI	traumatic brain injury
TE	echo time
TIMP1	tissue inhibitor of metalloproteinase-1
TJ	tight junction
TNF	tumour necrosis factor
TR	repetition frequency
v_e	fractional EES volume
v_p	fractional plasma volume
VEGF	vascular endothelial growth factor

Chapter 1

Background and Introduction

1.1. Clinical Motivation

In the 25 years spanning 1990 to 2015, the global burden of neurological disorders has increased substantially, this despite reductions in mortality rates for stroke and communicable neuropathologies [1]. Expanding populations and increased life expectancy have contributed to this rise through significant increases in the absolute number and rates of people suffering with age-related neurodegenerative disorders like Alzheimer's disease (AD) and other dementias; this public health challenge is expected to worsen in the coming decades [1]. It is estimated that more than 46 million individuals globally over the age of 60 are living with dementia, a number that is predicted to nearly triple by 2050 [2]. Despite considerable attention and funding, pharmacological treatment options have yielded minimal beneficial effects on disease progression and those focused on the management of dementias (E.g. acetylcholinesterase inhibitors) are yet to strike a balance between efficacy and tolerability [3].

Conversely, many other neurological disorders are of significant global health concern, not solely due to high rates of occurrence, but rather their rapid progression, even in the face of aggressive treatment strategies. For example, glioblastoma multiforme, the most prevalent primary brain cancer, exhibits a five-year survival rate of only 5%. This low rate of treatment success can be attributed, in part, to its high proliferative capacity, diffuse presentation, and a resistance to what is currently considered the best treatment option (I.e. aggressive surgical margins plus concurrent chemoradiotherapy) [4]. While glioblastoma multiforme may only affect 2-3 per 100 000 adults in North America each year [5], it is estimated that brain metastases, which present many of the same treatment challenges, occur in at least 17% of all cancer patients [6].

Parts of this chapter are adapted from: McMahon D, Poon C, Hynynen K. Evaluating the safety profile of focused ultrasound and microbubble-mediated treatments to increase blood-brain barrier permeability. *Expert opinion on drug delivery*. 2019. 16(2):129-42. Used with permission as part of publication agreement.

In addition to the immense impact these diseases have on afflicted individuals and their families, the global economic strains associated with management, patient care, and palliation are also of a considerable magnitude. While prevention likely represents the most fiscally responsible solution, treatments that can offer a significant slowing of disease progression and an increase in quality-adjusted life-years are of tremendous value in the short term. Developing treatment options for neurological disorders is often complicated by unclear or heterogeneous etiologies and a lack of viable treatment targets. Further complicating matters is the limited penetrance of brain vasculature to most exogenous substances, which necessitates either elegant drug design or methods of bypassing the blood-brain barrier (BBB) in order to deliver therapeutic agents to brain parenchyma at sufficient concentrations [7].

Limited success in developing efficacious treatment options for a wide range of neuropathologies motivates the need for new strategies. Given that drug delivery to the brain is pervasively hindered by the BBB for a large number of central nervous system (CNS) disorders, developing flexible solutions to this problem has the potential to aid in the development of new treatment options and to positively impact a large pool of individuals.

1.1.1. Structure and Function of the BBB

Proper cerebral function is highly dependent upon the maintenance of homeostatic conditions in the extracellular milieu surrounding neurons and glia [8]. The BBB plays a major role in regulating this environment by selectively isolating the parenchyma from systemic circulation. Layers of physical and physiological features comprising the BBB function in concert to produce these conditions.

Specialized, non-fenestrated, endothelial cells (ECs) line cerebral vasculature. At the capillary level, this EC layer is surrounded by two basement membranes (endothelial and parenchymal) comprised largely of collagen IV, laminin, nidogen, and perlecan; pericytes reside in between these basement membranes (**Figure 1.1**) [9]. A non-continuous layer of astrocytic endfeet surround a large proportion the parenchymal basement membrane at the capillary level [10], and act to support the maintenance of barrier properties [11]. Neurons innervate smooth muscle cells at the arteriolar level to regulate blood flow [12], but also communicate bidirectionally with other cells of the neurovascular unit, primarily astrocytes, to modulate BBB function [13].

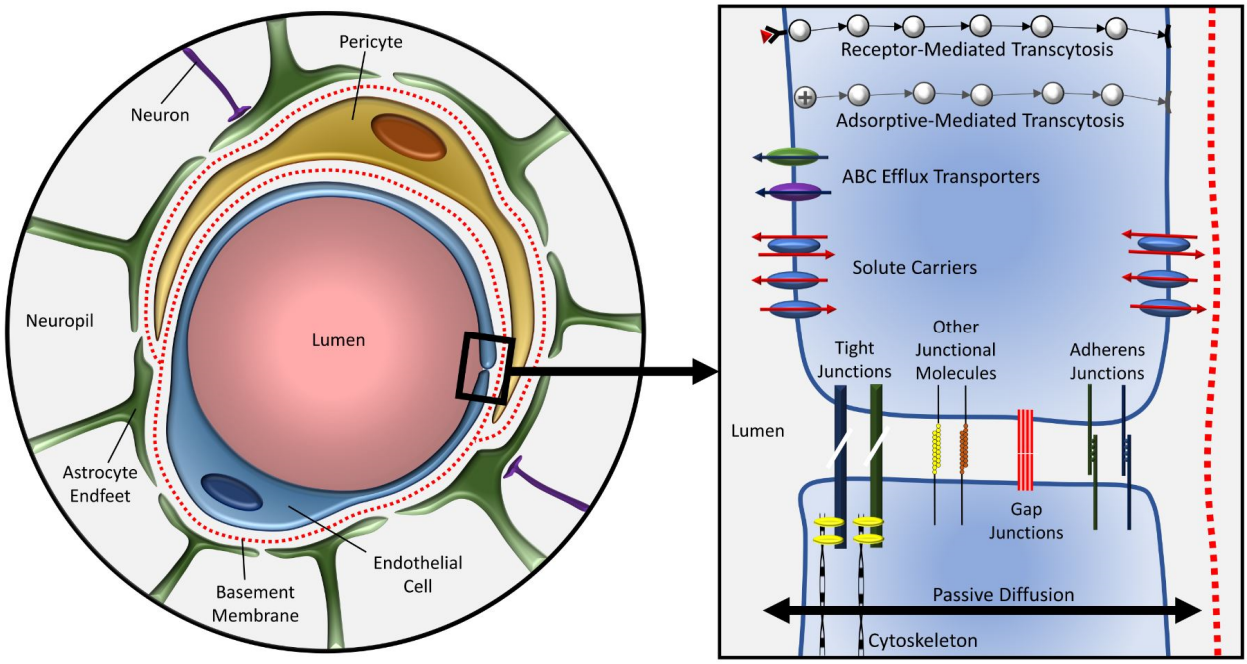

Figure 1.1. Key Components of the Capillary-Level BBB. The BBB is comprised of many features that allow fine control over the substances that transit from systemic circulation to brain parenchyma and *vice versa*. Specialized endothelial cells (ECs) line cerebral vasculature, linked together by tight junction proteins (E.g. claudin-5 and occludin), adherens junction proteins (E.g. vascular endothelial-cadherin and platelet endothelial cell adhesion molecule-1), gap junctions (E.g. connexin-30), and other junctional molecules (E.g. endothelial cell adhesion molecule and junctional adhesion molecule-A). Routes of transcellular transport across ECs includes passive diffusion (E.g. molecular weight < 500 Da and log P_{OCT} = 2-4), receptor-mediated transcytosis (E.g. transferrin and insulin), adsorptive-mediated transcytosis (E.g. histone and tat-derived peptides), solute carriers (E.g. glucose transporter-1 for glucose), ABC-family efflux transports (E.g. multidrug resistance protein). ECs are surrounded by two basement membranes, an endothelial and a parenchymal basement membrane, comprised mainly of collagen IV, laminin, nidogen, and perlecan; pericytes reside in between these layers. Astrocytic endfeet surround the parenchymal basement membrane. Neurons communicate bidirectionally with various cells of the neurovascular unit, primarily astrocytes. Figure created based on information detailed by Sweeney *et al.* [14].

At the points of contact between adjacent ECs are adherens junction, gap junction, and tight junction (TJ) complexes, which consist of transmembrane and anchoring proteins (**Figure 1.1**). Of critical importance to the connection between ECs are various junctional adhesion molecules, claudins (primarily claudin-5 and -3), occludin, and zona occludens (primarily zona occludens-1) [14]. The extracellular domains of proteins like claudin-5 and platelet endothelial cell adhesion molecule-1 form homodimers with proteins on adjacent ECs, while the intracellular domains are anchored directly or indirectly to the cytoskeleton [12]. The tight link between ECs that these bonds create contribute to a *physical barrier* which acts to greatly

limit paracellular diffusion (I.e. between cells); under normal physiological conditions, ions (I.e. Na^+ and K^+) display low levels of paracellular diffusion [15], while small (molecular weight < 500 Da) lipophilic (log P_{OCT} = 2-4) or gaseous molecules can diffuse through cell membranes [16].

Transporter complexes in the luminal and abluminal surfaces of ECs strictly regulate the transcellular movement (I.e. through cells) of larger polar and nonpolar molecules (**Figure 1.1**) [12]. ATP-binding cassette (ABC) family efflux transports (E.g. MDR1 and BCRP) act to pump many of the passively penetrating lipid soluble molecules back into circulation [11]. Conversely, solute carriers (SLCs) generally mediate the influx and efflux of essential polar molecules such as glucose, amino acids, and nucleosides, in addition to displaying an affinity for a wide range of other solutes [11]. Vesicle-based transport also provides a route between the luminal and abluminal surfaces via receptor-mediated or adsorptive-mediated mechanisms; however, cerebrovascular ECs display a much lower degree of endocytosis than peripheral ECs [17]. In combination, these complexes and mechanisms contribute to a *biochemical barrier* (also referred to as a *transport barrier*) which facilitates the maintenance of homeostatic conditions within the brain by tightly controlling the influx and efflux of molecules.

Enzymes associated with the BBB provide an additional layer of control over the substances that reach the brain parenchyma. Extracellular enzymes include proteases and nucleotidases, which act to metabolize peptides and adenosine phosphates, respectively, while intracellular enzymes, including monoamine oxidases and cytochrome P450, can contribute to the breakdown of toxic molecules [12,18]. The expression of these enzymes and others contribute to a *metabolic barrier*.

The BBB also aids in the coordination of immune responses in the brain by providing a niche for the chemoattraction of circulating granulocytes and peripheral blood mononuclear cells [19]. Under normal physiological conditions, however, the CNS exhibits low levels of immune cell infiltration relative to other organs, rendering it an immune privileged site [11,19]. Together, the unique combination of features that make up the BBB act to preserve efficient neural function and protect the brain from infection.

1.1.2. Drug Delivery to the Brain

The highly selective nature of vascular barriers in the CNS, while essential, greatly limit pharmacological options for treating diseases located in these regions. The lack of effective treatments are not always due

to the lack of candidate drugs, but often the difficulty in delivering these agents in therapeutically relevant concentrations to the brain [7]. The physical, transport, and metabolic barrier features of cerebral vasculature, outlined above, limit almost all large molecule, and over 98% of small-molecule, drugs from crossing the BBB [7].

To facilitate the delivery of therapeutic agents to the brain, it is necessary to either bypass the barrier features of cerebral vasculature or to design agents that utilize endogenous transport mechanisms. Several approaches to drug-brain delivery have been investigated. Direct intracranial injection into targeted areas of the CNS is perhaps the simplest and has been shown to produce therapeutically relevant drug concentrations with a high degree of spatial precision [20,21]. For example, Marks *et al.* demonstrated positive results following intraputaminal delivery of a neurturin-producing viral vector in patients with Parkinson's disease [22]; however, due to limited diffusion from the site of injection, as well as the risks of infection and hemorrhage associated with penetrating injury [23], direct intracranial injection approaches are not well suited for the treatment of large tissue volumes (I.e. greater than a cubic centimetre [24,25]) or conducive to repeated administrations.

Intracerebroventricular [26] and intranasal [27] administration have also been shown to increase CNS concentrations of therapeutic agents. Both of these approaches rely on bulk flow and diffusion within cerebrospinal fluid and interstitial fluid, resulting in low concentrations and heterogenous distribution within the brain [28,29]. Intranasal delivery benefits from being noninvasive; however, nasal epithelial cells and the olfactory system as a whole are at risk of damage with repeated administrations [27]. Intracerebroventricular administration, like direct intracranial injection, is associated with risks of infection and tissue damage along the needle tract required to access internal brain structures [23]. Low drug concentrations, non-targeted delivery, and risks of repeated administration limit the clinical flexibility of these approaches.

In contrast to bypassing the BBB physically, several chemical stimuli have been utilized to modify vascular permeability in the brain by acting to increase paracellular diffusion, thus providing an alternative route for systemically administered drugs to enter the brain. The arterial administration of hyperosmotic solutions, such as mannitol [30] or arabinose [31], leads to the osmotic shrinkage of ECs, thereby widening inter-endothelial clefts [32]. A limited degree of spatial specificity can be achieved by infusing the hyperosmotic solution into conduit arteries that feed capillary beds in the targeted tissue, thereby

restricting the effects on BBB permeability to one hemisphere of the brain. Clinical trials have demonstrated enhanced delivery of chemotherapeutic agents in patients with metastatic brain cancers in conjunction with the intracarotid infusions of mannitol [33–36]; however, clinical testing has not progressed to widespread implementation [37]. While this approach may be well-suited for the treatment of diffuse brain cancers, a lack of targeting ability and significant risks, including vascular damage [38], neuropathologic changes [33], and seizures [33,34], limit its flexibility as a general brain-drug delivery strategy.

Conversely, novel drug development and modifications to existing therapeutics have been employed to avoid bypassing or modifying the BBB, while achieving efficacious drug delivery to the brain. The development of small (<400 Da), lipid soluble therapeutic agents with a low affinity for efflux transports and low systemic toxicity, are ideal for BBB penetration [17]. However, balancing these physical features while maintaining pharmacological action is not always feasible and is associated with large research and development costs [17]. To enhance BBB permeability of existing therapeutics, several modification strategies can be utilized. For example, the number of hydrogen bonds within a molecule can be reduced, thereby increasing its lipid solubility and BBB permeability [17]. While this approach has proven beneficial in a limited number of cases, drug activity is often altered and the hydrolysis of modified hydrogen bonds can occur rapidly *in vivo*, rendering the drug unable to transit cerebral vascular walls [17].

Alternatively, drug design strategies that make use of endogenous transporters or receptor-mediated transport systems have resulted in a number of promising approaches. For instance, the covalent linkage of small molecule drugs to L-cysteine may enable significant improvement in brain delivery. By taking advantage of the innate affinity of L-cysteine for *large neutral amino acid transporter*, which is found in high abundance in cerebral vasculature, candidate drugs that permeate the BBB in higher concentrations can be produced [39]. Similarly, therapeutic agents can also be conjugated to molecules that bind luminal membrane receptors in brain vasculature and mediate transcytosis. This *molecular Trojan horse* technique is more conducive to large compound delivery than endogenous transporter-based methods, as the conjugated drugs are endocytosed in vesicles rather than being transported through narrow channels [17]. While these approaches may prove beneficial for specific applications, the maintenance of therapeutic action after drug modifications can be challenging [17]. Additionally, these drug delivery strategies are spatially non-specific within the brain, unless additional biological or physical targeting techniques are employed, which increases the risk of off-target effects.

Other strategies for increasing therapeutic agent delivery to the brain include BBB-penetrating viruses [40], immune cell-based approaches [41], nanoparticle delivery [42], amongst others [43]. All of the aforementioned methods have advantages and limitations. Ultimately, the development of flexible strategies to non-invasively achieve therapeutically relevant concentrations of drugs in the brain, while maintaining a low risk of inducing damage, remains a challenge. Added to this is the difficulty of engineering an approach that can aid in the treatment of both highly localized pathologies, by producing localized drug delivery, and to those with more diffuse distributions, by producing more widespread delivery. Given the scope of neuropathologies for which the BBB presents an impediment to treatment, as well as the number of individuals impacted by this challenge, there is a great need for the development of versatile techniques for brain-drug delivery. The work presented in this thesis explores the use of focused ultrasound and microbubble-mediated BBB permeability enhancement, a promising approach that may aid in addressing this problem.

1.2. Therapeutic Ultrasound

Ultrasound is one of the most widely used imaging technologies in medicine today. As a non-invasive and non-ionizing modality, diagnostic ultrasound exhibits a high safety profile and can be used to infer detailed anatomical and physiological information. This approach involves transforming electrical energy into mechanical energy via an ultrasound transducer, which acts to transmit waves of compression and rarefaction into the body (**Figure 1.2B**). As these pressure waves travel through tissue, energy is scattered and absorbed. Detection of the reflected waves can be used to generate images and glean certain biological characteristics of the tissue, while the absorbed energy is a byproduct. Conversely, therapeutic ultrasound uses these same principles, but focuses instead on the biological effects of depositing acoustic energy within tissue.

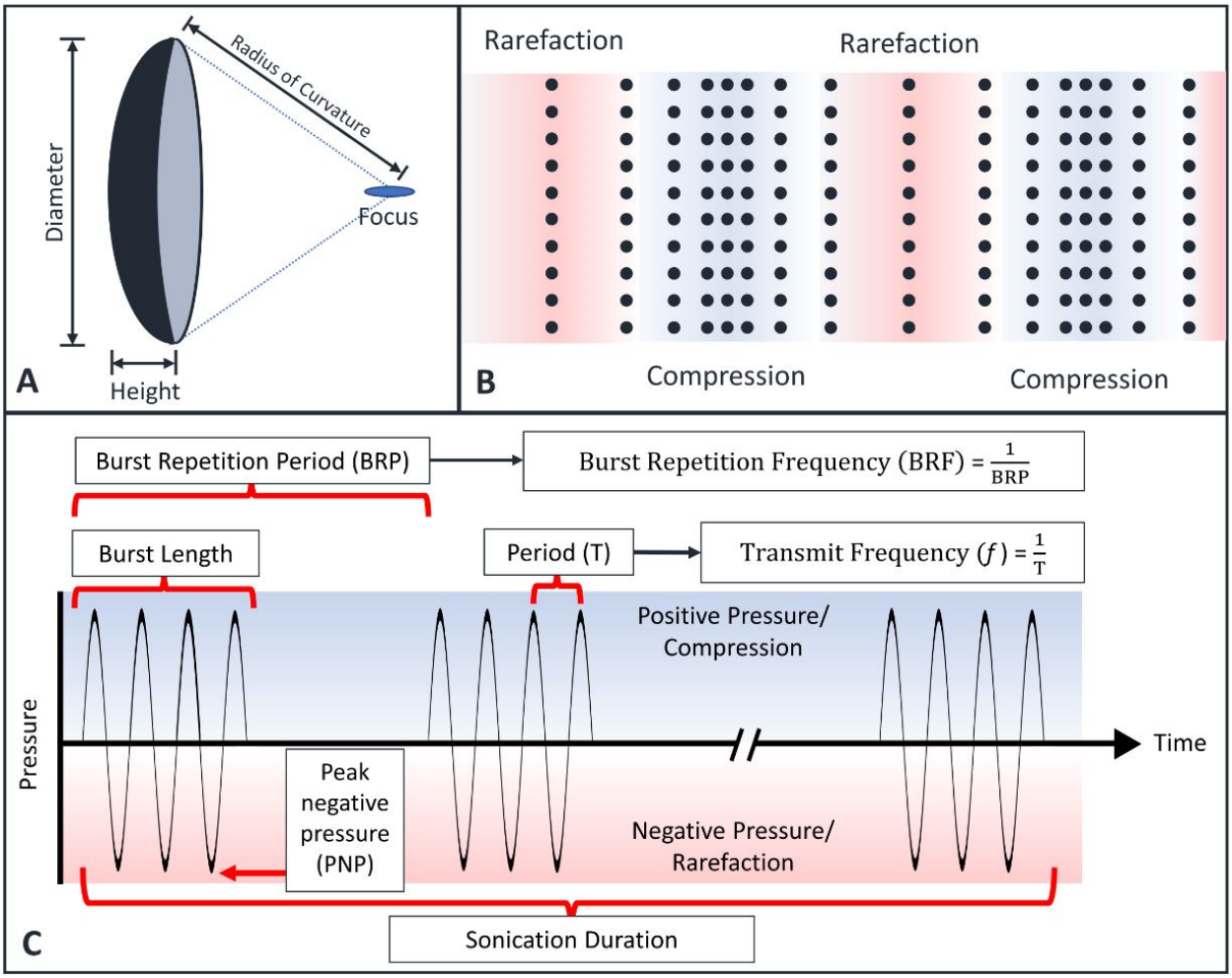

Figure 1.2. Ultrasound Nomenclature. (A) A spherically curved, single element focused ultrasound transducer is depicted. The size and shape of the focal volume generated by a given transducer is influenced by its diameter, height, radius of curvature, and transmit frequency. (B) Ultrasound propagates through media as a pressure wave. As regions of compression (higher relative pressure) and rarefaction (lower relative pressure) travel through tissue, mechanical stresses and thermal deposition can lead to a variety of transient and long-lasting biological changes. (C) The entirety of primary research described in this thesis utilizes burst-mode ultrasound (as opposed to continuous wave ultrasound) for which periods of ultrasound transmission alternate with periods of no transmission (off-time).

Depending on exposure parameters, ultrasound can be used to induce a range of biological responses, from enhanced vascular permeability [44,45] to tissue necrosis [46,47]. The amount of energy deposition required to elicit these effects is typically much greater than is achieved with diagnostic imaging, generally necessitating the use of longer bursts (I.e. milliseconds to minutes vs. microseconds) and greater peak intensities (I.e. approximately 10^2 to 10^4 W/cm^2 vs. 10^0 to 10^1 W/cm^2). For a visual depiction of ultrasound

terms, see **Figure 1.2C**. Broadly speaking, the bioeffects of therapeutic ultrasound can be categorized as thermal and non-thermal, although therapies often use a combination of effects.

1.2.1. Thermal Effects

Thermal effects result from the conversion of mechanical energy to heat as waves propagate through a medium. The magnitude of temperature increase is influenced by the absorption coefficient of tissue and the local time-averaged acoustic intensity (proportional to mean pressure squared), along with local blood flow, which can act to carry heat away from the target tissue [48]. While thermal bioeffects are influenced by the absolute temperature achieved, exposure duration is also of importance. The combination of these metrics can be used to calculate thermal dose, expressed as *equivalent minutes at 43°C*, which can be predictive of the biological impact of thermal exposures [48].

Mild elevations in temperature (I.e. 40°C - 45°C) applied over minutes to hours can result in increased blood flow, enhanced vascular permeability [49], altered immune cell behaviour [50], and a sensitization of cells to chemotherapeutics [51] and radiation therapy [52]. For example, Song *et al.* demonstrated that heating rat skeletal muscle for one hour at 43°C lead to an approximately two-fold increase in vascular permeability and three-fold increase in blood flow, effects that normalized to baseline levels within an hour of normothermia [53]. While a complete return to physiological conditions may follow mild, sustained temperature elevations, measurable increases in mammalian cell death are observed *in vitro* when heated above 41°C and sustained for more than a few hours [54]; this effect is likely influenced by a reduction in enzyme activity at these temperature [55]. Ultrasound-mediated mild hyperthermia is capable of non-invasively inducing these changes to cellular and physiological function at depth within tissue and with spatial specificity, an approach that has been clinically tested for various applications [56–58]

With larger temperature elevations (I.e. 55°C - 60°C) applied over seconds to minutes, rapid protein denaturation occurs, inducing irreversible cellular damage and necrosis [59]. As with mild hyperthermia, these temperatures can be achieved non-invasively with ultrasound and have been employed extensively for spatially localized thermal ablations [46,60,61].

1.2.2. Non-Thermal Effects

In addition to the generation of heat, there are a number of non-thermal effects induced by ultrasound exposure. One such effect, acoustic radiation force, results from the transfer of momentum from the ultrasound wave to the medium in the direction of propagation [62]. This force can result in tissue displacement, generate acoustic streaming in fluid [63], and has been exploited in several biomedical applications, including harmonic motion imaging [64] and elastography [65].

A second non-thermal effect of considerable utility for therapeutic applications is *acoustic cavitation*, which refers to the interaction of ultrasound waves with gas-filled cavities [66]. There are two primary sources of such ultrasound-responsive cavities, the first being bubbles that are created *de novo* when dissolved gases coalesce under high rarefactional pressure. These bubbles are short-lived, dissolving within tens of milliseconds after an ultrasound burst [67], but can generate dramatic biological effects, including mechanical tissue ablation (E.g. histotripsy) [68].

The second source of cavitation nuclei is exogenous; intravenously administered, encapsulated microbubbles (MBs) were first developed as ultrasound contrast agents for the enhanced visualization of perfused tissue [69]. Commercially available formulations, such as Definity and Optison, consist of a protein, polymer, or phospholipid shell surrounding an air or perfluorocarbon gas core. Encapsulation enhances the stability of MBs, allowing circulation half-lives to be on the order of minutes [70]. The mean diameter of commercially available MBs are typically below 5 µm (Definity: 1.1-3.3 µm; Optison: 2.5-4.5 µm), but display wide size distributions [71]. While MBs were first developed for diagnostic imaging purposes, their utility in therapeutic applications are now well-established [72].

Ultrasound-stimulated MBs can expand and contract in response to cycles of rarefaction and compression (**Figure 1.3**); these volumetric oscillations and surface vibrations can be complex. Cavitation activity within an ultrasound field will vary substantially depending on the acoustic parameters of the insonating wave, the surrounding environment, and the physical characteristics of the MBs, leading to a wide range of biological effects, from enhanced vascular permeability (nonthermal) [73,74] to hemorrhage [75] and necrosis [76]. From a therapeutic perspective, these effects have great relevance for drug delivery [73,77] and tissue ablation [76].

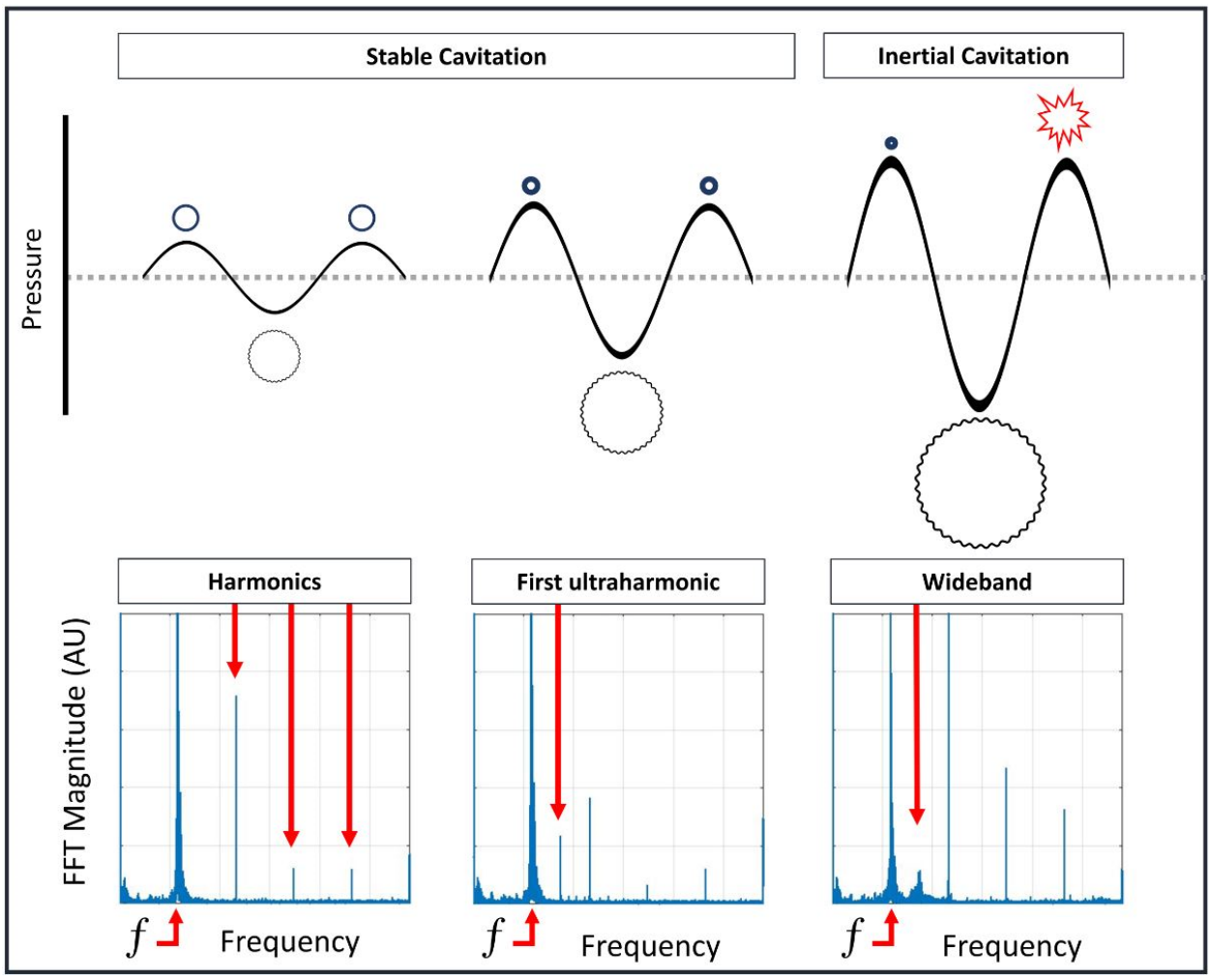

Figure 1.3. Regimes of MB Activity and Spectral Frequency Content of Acoustic Emissions. Ultrasound-stimulated MBs can expand and contract in response to cycles of rarefaction and compression, themselves generating pressure waves referred to as *acoustic emissions*. Assessing the spectral frequency content of acoustic emissions from insonated MBs can give insight into their behaviour. As the PNP of sonication is increased, MBs will begin to oscillate in a fashion that generates acoustic emissions at harmonics (integer multiples) of the transmit frequency (*f*). If the pressure amplitude is further increased above a threshold value, nonlinear volumetric oscillations will generate sub- and ultraharmonic emissions (subharmonic = 0.5*f*, ultraharmonics = 1.5*f*, 2.5*f*, etc.). Generally speaking, MB behaviours in this regime are referred to as *stable cavitation*. As the PNP is further increased, MBs will begin to collapse in the compressional phase, referred to as *inertial cavitation*. This behaviour is characterized by a sharp increase in the production of wideband emissions and is often associated with tissue damage. AU = arbitrary units, FFT = fast Fourier transform. Figure created based on information detailed by Leighton [66].

1.2.3. Focused Ultrasound

To confine ultrasound-induced bioeffects to predictable volumes and to achieve high acoustic pressures deep within tissue requires the ability to focus ultrasound energy. One of the simplest approaches to achieve focused ultrasound (FUS) is to employ a spherically-curved, single-element transducer (**Figure 1.2A**). The focal spot volume for a given transducer is determined largely by its geometry (I.e. radius of curvature and diameter) and transmit frequency. As the transducer diameter or transmit frequency increases, or the radius of curvature decreases, the focal spot volume will be reduced [78]; however, the shape of focus will remain ellipsoidal, with the long axis parallel to the direction of ultrasound propagation [79]. For example, a transducer with a radius of curvature of 8 cm, diameter of 10 cm, and transmit frequency of 500 kHz, the lateral and axial dimensions of the focus (I.e. full-width at half-maximum pressure in water) will be approximately 3.4 mm and 43.1 mm, respectively.

The use of FUS as a noninvasive alternative to neurosurgery has been explored for decades. In 1942, Lynn *et al.* first demonstrated the ability to transcranially ablate focal volumes in the cortex of canine and feline specimens [47]; however, subsequent work from Lynn and Putnam described extensive tissue damage extending from the inner skull surface to the focal target, as well as severe skin necrosis associated with these sonications [80]. The challenge of producing a spatially confined ultrasound focus at depth within the brain and through the human skull was tackled by the Fry brothers in the 1970's and 1980's. They demonstrated the ability to produce focal thermal ablations in feline brains with a human cadaver skull section placed within the path of ultrasound propagation [81,82]. While this work showed that transcranial FUS-mediated brain tissue ablation was possible with single-element transducers driven at low frequencies (I.e. below 1 MHz), a lack of predictability in ablated volume, focal distortions, and target shifts caused by the skull, restricted the advancement of this technique for human neurosurgical applications for decades.

The development of techniques to correct for the aberrating effects of the skull were paramount to the advancement of transcranial ultrasound therapies. Using a linear imaging array (I.e. multiple transducers arranged in a line), Thomas and Fink first showed that a time-reversal acoustics approach (I.e. adjusting the phase and amplitude of each transducer element to produce constructive interference at the intended target) could be used to improve focusing through the skull [83]; however, it was not until this method of aberration correction was used in combination with a large-element (64 elements), high-powered 2D array that the feasibly of transcranial ablation was demonstrated [84]. Since these studies, more advanced

systems have been developed that employ hundreds or thousands of transducer elements arranged in planar or spherically curved arrays. The ability to control the phase and amplitude of each individual element allows for: (1) electronic steering of the focus [85] and (2) the ability to produce a spatially confined focal volume through a heterogenous aberrator (I.e. focusing through the skull) [84]. Using this technology, current clinical systems have been able to achieve ablated volumes of approximately 2 mm in diameter with transcranial propagation in humans (650 kHz system, ExAblate Neuro from InSightec) [86]. While smaller focal volumes may be achievable with the use of higher transmit frequencies, skull heating becomes progressively prohibitive as transmit frequency is increased due to the corresponding increase in skull aberrations.

This early work on transcranial, FUS-mediated brain tissue ablation established the foundation for clinical trials that aimed to alleviate the symptoms of essential tremor through ablation of the ventral intermediate nucleus of the thalamus [60,86]. In 2016, InSightec's high frequency, hemispherical array system (ExAblate Neuro) received Health Canada approval for the treatment of essential tremor. While tissue ablation was the chief focus of much of the early brain-FUS research, careful observation revealed that the margins of these thermal lesions contained vasculature with increased permeability [87–89]. These observations, combined with the long-realized challenge of delivering therapeutic agents to the brain, motivated further study into how this effect could be achieved without the creation of thermal lesions.

1.3. Focused Ultrasound, Microbubbles, and the BBB

Research in the mid-1990's demonstrated that acoustic cavitation from bubbles created *de novo* could be used to increase BBB permeability without the formation of a thermal lesion; however, ultrasound exposure conditions which could consistently modulate vascular leakage without generating overt tissue damage could not be established and raised concerns with respect to safety and repeatability [44]. In 2001, a major advancement in the field saw the introduction of encapsulated MBs into systemic circulation prior to sonication [90]. MB administration allowed for FUS-induced enhancement of vascular permeability (termed *FUS+MB exposure* in this thesis for brevity) to be achieved at substantially lower time-averaged intensities relative to FUS alone, allowing for transcranial exposures without concern of skull heating-induced damage and largely removing cavitation from bubbles created *de novo* and thermal effects as mechanisms driving these changes. Instead, the physical forces exerted on vasculature by ultrasound-stimulated MBs are thought to be the dominant contributor to observed bioeffects [90]. MB behaviour can

vary widely depending on the characteristics on the insonating wave, local environment, and MB type, resulting in a range of forces exerted on vascular walls.

When stimulated by ultrasound at low pressure, MBs oscillate volumetrically in size around their equilibrium state, a regime of activity referred to as *stable cavitation* (**Figure 1.3**) [66]. This behaviour can generate microstreaming in surrounding fluid, which in turn produces shear stresses in the endothelial lining of blood vessels [91,92]. Depending on ultrasound exposure conditions, this force may result in the activation of physiologically relevant shear stress mechanisms, including Ca^{2+} influx and subsequent nitrous oxide production, or may produce reversible membrane perforation, cell detachment, and/or lysis [93]. Stably cavitating MBs can also generate circumferential stress within vascular walls, which creates tension in the proteins that link ECs together [94]. Additionally, acoustic waves exert radiation force on circulating MBs, propelling them in the direction of ultrasound propagation [95]. The force of displaced MBs on vascular walls may be sufficient to contribute to subsequent bioeffects [95].

As acoustic pressure is further increased, MBs can collapse in the compressional phase of an ultrasound wave under the inertia of the surrounding fluid (**Figure 1.3**). This behaviour, referred to as *inertial cavitation*, can generate shockwaves, jets streams, free radicals, and extreme heat [66,96]. The violent collapse of MBs within vasculature can result in ischemia, apoptosis, necrosis, edema, and hemorrhage [97].

1.3.1. Parameters Affecting FUS+MB Exposure

Given the range of MB oscillation behaviours observed in response to ultrasound and the dependency of this behaviour on characteristics of the insonating wave, it is important to consider the relationship between sonication parameters and the resulting bioeffects. For a visual depiction of ultrasound parameter terms, see **Figure 1.2C**.

1.3.1.1. Frequency

Transmit frequency, along with the physical characteristics of MBs (E.g. shell composition, size, gas core, etc.), strongly influence their behaviour within an ultrasound field [66]. These physical MB characteristics [98], as well as the composition of the surrounding medium [99] and acoustic pressure [100], influence the transmit frequency at which MBs exhibit maximal radial expansion at a given pressure, termed the *resonance*

frequency of a MB. All else equal, MBs insonated by transmit frequencies above or below their resonance frequency will display radial expansion amplitudes below peak levels, thus impacting the magnitude of stress exerted on blood vessel walls.

While transmit frequencies ranging between 28 kHz [101] and 8 MHz [102] have been employed to enhance BBB permeability with FUS+MB exposures, it is important to consider that as frequency increases, so too does the degree of tissue aberration. This can lead to heating and distortion of the ultrasound focus [103–105], factors that are especially relevant for large animal and human applications where skull thickness can pose substantial challenges at high frequencies. Conversely, the use of lower frequencies is accompanied by larger focal volumes, which also may be undesirable for small targets that require precise targeting. For transcranial applications in humans, the upper limit of effective transmit frequencies has been proposed to be below 1.5 MHz (corresponding to a focal volume of less than 1 mm^3 for a fully populated hemispherical array of 30 cm in diameter) [106]. While a focal volume of this size may have relevance for transcranial ablations (I.e. focal volume smaller than structures to be ablated; E.g. ventral intermediate nucleus has dimensions of $4 \times 4 \times 6$ mm [107]), the lower limit of clinically relevant focal volumes for FUS+MB-mediated BBB permeability enhancement has yet to be thoroughly explored. Further consideration of specific clinical applications is required in this regard, as is the study of therapeutic agent diffusion outside of the focal volume.

1.3.1.2. Pressure

Acoustic pressure amplitude refers to the difference between peak positive and peak negative pressure (PNP), divided by two. Given that MB expansion occurs in the rarefactional phase of an acoustic wave, PNP is often of primary interest. For a range of PNPs, the magnitude of radial expansion, as well as the associated stresses exerted on vascular walls and BBB permeability enhancement, are positively correlated with PNP [108,109]. As PNP is further increased, the probability of inertial cavitation within a population of MBs also increases, generating more extensive vascular leakage and tissue damage [110,111]. Whether due to stable or inertial cavitation, the magnitude and types of stresses produced within blood vessel walls will influence both the degree of BBB permeability enhancement and extent of tissue damage induced by FUS+MB exposure.

Additionally, as the transmit frequency is increased, the PNP required to generate enhanced vascular permeability also increases (provided all other parameters remain constant). This relationship is captured in the equation for mechanical index (MI = PNP/√*f*, where *f* is the center frequency of the ultrasound wave). McDannold *et al.* demonstrated that the MI threshold to produce a detectable increase in BBB permeability was approximately constant (MI = 0.42-0.50) for frequencies between 0.26 and 1.63 MHz [112]. It is important to note that the range of MIs reported in this study should not be considered universally applicable; factors such as bursting scheme (discussed below), MB type, MB dose, and species will have a substantial impact on the biological outcomes of sonications at any MI. The complexity of comparing FUS+MB exposure parameters and outcome measures between studies is further discussed in *Section 6.2.2.*.

1.3.1.3. Bursting Scheme

The magnitude of stresses exerted on vasculature by oscillating MBs have a large impact on the resulting biological responses, as do factors that influence the temporal distribution of these stresses. Burst length, burst repetition frequency (BRF), and sonication duration all have been shown to have relevance in this regard.

McDannold *et al.* demonstrated that as burst length is increased from 0.1 to 10 ms, the magnitude of BBB permeability enhancement also increases [113]; earlier work found no further increase between 10 and 100 ms [74]. Burst lengths beyond 10 ms may not result in additional vascular permeability enhancement if the complete destruction of MBs occurs before the end of each burst [113]. Conversely, short burst lengths, down to a single cycle pulses, have been shown to produce increased BBB permeability [114]. This study also found burst length to be positively correlated to signal intensity changes in contrast-enhanced T1-weighted magnetic resonance imaging (CE-T1w MRI), a measure of vascular permeability [114].

Work from Choi *et al.* has shown that when BRF is increased from 0.1 Hz to 1 Hz there is a significant increase in BBB permeability enhancement [115]. This result may be related to the rapid decay of MBs in circulation; the half-life of Definity, a commercially available MB formulation, in circulation is approximately 1.3 min [70]. As BRF is increased from 0.1 Hz to 1 Hz, the duration of sonication is necessarily reduced by 10-fold to deliver the same number of bursts. The reduced duration - and thus reduced MB decay - results in the average number of cavitation nuclei available to exert stresses on vasculature during

each burst being higher [115]. This same study found that beyond 1 Hz, BRF did not contribute to a larger magnitude of BBB permeability enhancement [115], a finding that may be attributed to an incomplete reperfusion of MBs into vasculature in the focal region between bursts [116]. Similarly, Chopra *et al.* observed that when BRF and burst length are kept constant, sonication duration is positively correlated to BBB permeability enhancement and tissue damage [117].

1.3.1.4. Microbubbles

Given that ultrasound-stimulated MBs drive changes in vascular permeability, it is unsurprising that factors governing their behaviour have been shown to influence biological responses. MB size distribution [118,119], composition [120,121], administration method (E.g. bolus vs slow infusion) [114], and dose [122,123] have all been shown to influence FUS+MB-mediated vascular permeability enhancement. Additionally, factors that influence the persistence of MBs in circulation, such as blood-oxygen level [124], also impact the bioeffects induced by FUS+MB exposure [125].

1.3.2. Acoustic Feedback Control

Local differences in vascularity and inhomogeneities in MB dispersion can lead to inconsistent effects of FUS+MB exposure on BBB permeability throughout the brain [126–128]. As an example, Wu *et al.* found that the probability of detecting contrast enhancement following sonication at fixed PNP was approximately three times greater in gray matter than white matter. Authors hypothesize that differences in vascular density account for much of this effect [127]. In addition, defocusing of the ultrasound beam(s) by the skull (E.g. due to skull thickness, non-normal ultrasound propagation, standing waves, etc.) can lead to inaccuracies in predicting *in situ* ultrasound pressures [104,105]. Given the relatively narrow safety window between a clinically relevant increase in BBB permeability and widespread distribution of microhemorrhages [128], methods of monitoring and controlling FUS+MB exposures in real-time are essential for minimizing the chance of causing substantial tissue damage, though fixed PNP approaches are commonly used.

The volumetric oscillations and surface vibrations of ultrasound-stimulated MBs generate pressure waves that are emitted in all directions. Assessing the spectral frequency content of acoustic emissions (collected during sonication with one or many hydrophones) from insonated MBs can give insight into their *in vivo*

behaviour (**Figure 1.3**) [129,130]. At PNPs that elicit stable cavitation, an increase in the magnitude of acoustic emissions at harmonics of the transmit frequency (f) can be observed (E.g. $2f$, $3f$, etc.) [66]. If the pressure amplitude is increased above a threshold value, nonlinear volumetric oscillations will lead to the generation of sub- and ultraharmonic emissions (subharmonic = $0.5f$, first ultraharmonic = $1.5f$, second ultraharmonic = $2.5f$, etc.) [131]. As the applied PNP is further increased, inertial cavitation will occur. This behaviour is characterized by a sharp increase in the production of wideband emissions [66].

The violent collapse of MBs at high PNPs can result in ischemia, apoptosis, necrosis, edema, and hemorrhage if sustained over a sufficient number of bursts or at a high enough magnitude [97]. McDannold *et al.* demonstrated that as the magnitude of wideband emissions (averaged over all bursts) increases, the probability of observing RBC extravasation also increases [111]; thus, efforts to reduce inertial cavitation are essential in the context of FUS+MB-mediated BBB permeability enhancement. Studies have also demonstrated that increased BBB permeability can be achieved without wideband emissions indicative of inertial cavitation [110,111]. While stable cavitation can produce increased BBB permeability without overt tissue damage [110,128], it would be overly simplistic to describe stable cavitation as *safe*. If the magnitude of stress generated by stably oscillating MBs is sufficient, blood vessel rupture can occur [132]. Thus, avoiding wideband emissions while achieving precise *in situ* PNP - with well-characterized effects on tissue health - is essential for minimizing overt tissue damage induced by FUS+MB exposures.

A number of strategies have been developed to control PNP in real-time based on acoustic emissions. In one method, PNP is adjusted to produce an empirically determined magnitude of harmonic emissions [133]. Recently, Sun *et al.* demonstrated that a closed-loop algorithm based on modulating the magnitude of emissions at multiple harmonic frequencies (and suppressing wideband emissions) can be used to consistently increase BBB permeability and may be effective in controlling the degree of permeability enhancement [134]. One potential drawback of this approach is the necessity to determine the target setpoint for harmonic emissions based on a host of factors (E.g. the animal model, MB type, acoustic field, transmit frequency, and hydrophone sensitivity). Furthermore, this method relies on the magnitude of the signal emitted by a population of MBs at the focus, thus rendering the signal dependent on the spatial distribution of MBs within the vascular network; nevertheless, the ability to control the degree of BBB permeability enhancement represents a substantial advancement in this field.

Another approach for controlling FUS+MB exposures is to incrementally increase PNP until detecting a threshold event, such as ultraharmonic [135] or subharmonic emissions [136], then reducing the applied pressure to a fraction (aka. scaling factor) of the threshold-triggering PNP (**Figure 1.4**). O'Reilly and Hynynen first demonstrated the effectiveness of this approach in consistently producing vascular permeability enhancement. They also showed a linear relationship between the scaling factor after a threshold event and mean intensity in CE-T1w MRI. A variation of this approach has been used in clinical trials that employ transcranial ultrasound propagation [137]. Technological advancements have seen spatial information incorporated into this method of acoustic feedback control through the use of three-dimensional beamforming of subharmonic emissions [75]. Potential drawbacks of this general strategy include the necessity to adjust the scaling factor for MB type and hydrophone sensitivity.

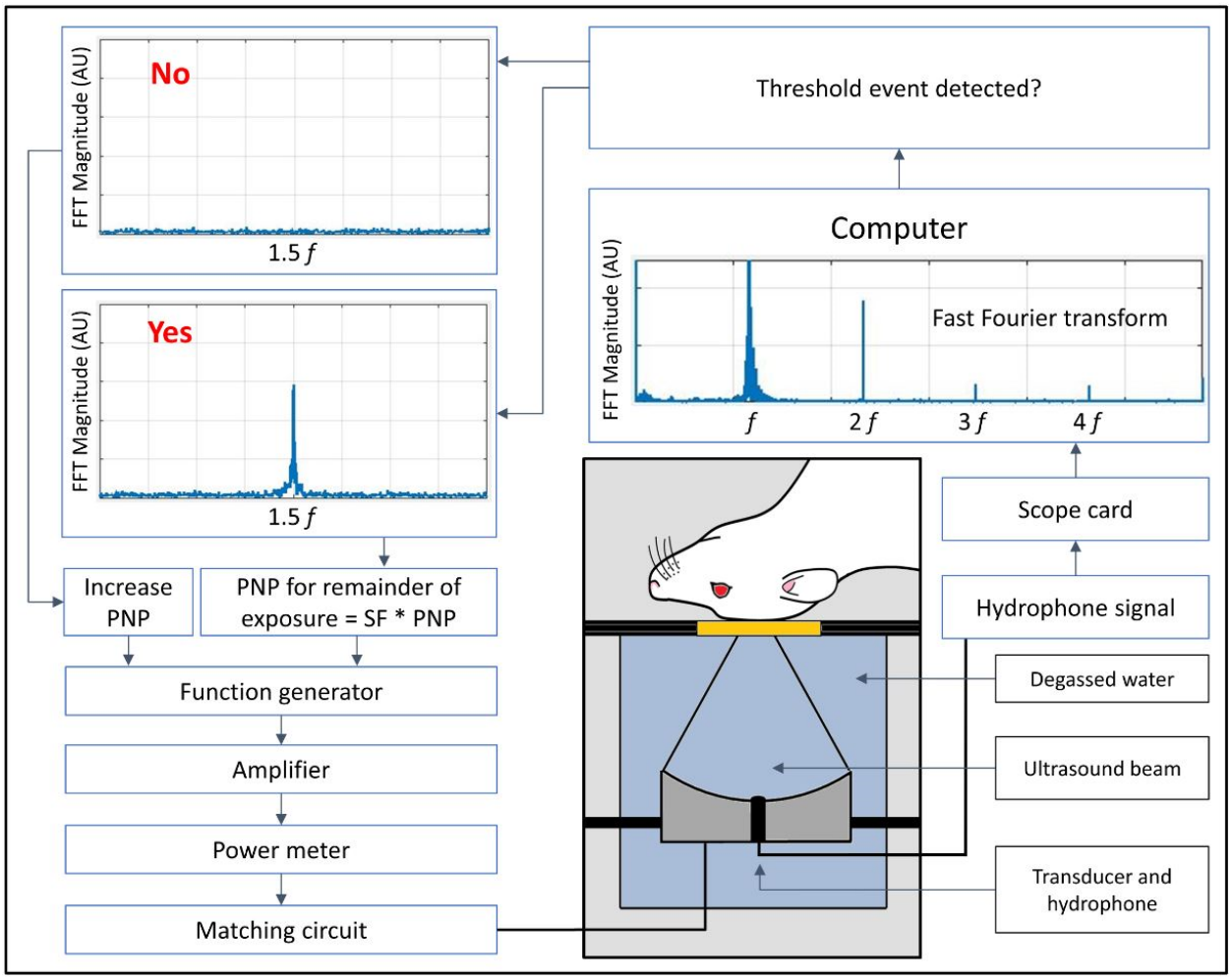

Figure 1.4. Acoustic Feedback Control. There are several strategies to control PNP based on acoustic emissions. The algorithm depicted here describes that employed for all primary research in this thesis. The computer initiates a signal that is sent to the transducer through the function generator, amplifier, power meter, and matching circuit. The ultrasound burst generated propagates through the water to the brain. The hydrophone receives acoustic emissions, which are processed (fast Fourier transformed) to evaluate their spectral frequency content. If emissions at the first ultraharmonic frequency are elevated above baseline noise, then the pressure is reduced by a scaling factor (E.g. PNP is reduced by 50%). If ultraharmonic emissions are not detected, then the pressure is increased by a predetermined step size. This loop continues until ultraharmonic emissions are detected or the specified duration of sonication is reached. SF = scaling factor, PNP = peak negative pressure, *f* = transmit frequency, AU = arbitrary units, FFT = fast Fourier transform. Figure adapted from McMahon *et al.* [138] with permission from the authors.

Whether calibrating PNP based on the magnitude of harmonic emissions or a threshold event, it is important to consider that MB size in most commercially available formulations is polydispersed. Given that the resonance frequency of a single MB is largely influenced by its size, this can result in a growing

fraction of the MB population cavitating as PNP is increased. The point at which a sufficient number of MBs are generating signals that are detectable above baseline noise will influence the efficacy of any acoustic feedback control algorithm. Thus, when assessing or modifying the parameters of such algorithms, the sensitivity of the detector(s) implemented, which is influenced by size, shape, and material, should be taken into account.

There continues to be efforts directed at improving the accuracy in predicting biological outcomes based on acoustic emissions. However, acoustic feedback control strategies have been essential in improving the consistency and reducing the risks associated FUS+MB exposures, thereby facilitating progression to clinical testing as a drug delivery strategy.

1.3.3. Delivery of Therapeutics

Given the scarcity of drugs which permeate the BBB in therapeutically relevant concentrations and the considerable efforts required to engineer biochemical or physical solutions to this problem [7], the flexibility of FUS+MB exposure as a drug delivery strategy is advantageous. A large variety of therapeutic agents have been successfully delivered to targeted regions in the brains of disease models with efficacious results. This section will briefly outline the most significant findings in this area.

Chemotherapeutics continue to be one of the most widely utilized class of drugs in medical oncology; however, their efficacy in the treatment of brain tumors remains low due to poor penetrance [139]. In addition, the toxicity of these drugs to healthy brain tissue, if able to cross the BBB, amplifies the need for targeted delivery. The ability to increase the concentration of doxorubicin in the brain using FUS+MB exposure and systemic drug delivery was first demonstrated in healthy rats without tumors [122]. Further work demonstrated efficacy in preclinical studies, reporting reduced tumor volumes and increased survival times following FUS+MB-mediated delivery of doxorubicin in a glioma rat model [140], two syngeneic glioblastoma mouse models [141], and others [134,142–147]. Enhanced delivery of other chemotherapeutic agents, such as methotrexate [148], carmustine [149,150], and temozolomide [151,152], have also been demonstrated following FUS+MB exposures.

While substantial obstacles remain (E.g. immune responses [153,154] and scaling production [155]), viral vector-based gene therapy may present a powerful avenue for controlling gene expression, providing a flexible

tool in the treatment or prevention of a large number of pathologies. However, delivery of viral vectors to specific regions within the brain has thus far been primarily achieved by invasive intracranial injections. Proof-of-concept for FUS+MB-mediated viral vector-based gene therapy was first demonstrated in mice with the delivery of adeno-associated virus (AAV) 9- green fluorescent protein to the striatum and hippocampus. Green fluorescent protein was found to be primarily expressed in neurons and astrocytes 12 days following sonication, with minimal expression in non-targeted brain areas [156]. Others have demonstrated FUS+MB-mediated delivery and green fluorescent protein-gene transfection using AAV2 [157,158] and AAV1 and 2 under a synapsin promoter [159]. Xhima *et al.* demonstrated the delivery of an AAV9 vector bearing a short hairpin RNA sequence targeting the α-synuclein gene. Authors reported at least a 50% reduction in α-synuclein protein expression in the targeted hippocampus, substantia nigra, and olfactory bulb one month following sonication and virus delivery, a result that may have relevance for the treatment of Parkinson's disease [160]. Non-viral gene therapy approaches have also been combined with FUS+MB exposures, leading to the enhanced delivery of small interfering RNA for huntingtin protein knockdown [161], liposome-encapsulated plasmid DNA for the expression of trophic factors [162–164], and DNA-bearing nanoparticles [165].

In addition to chemotherapeutics and viral vectors, many other therapeutic agents have been shown to permeate the BBB following sonication, including neural stem cells [166], natural killer cells [167], anti-amyloid beta (Aβ) antibodies [168], anti-dopamine receptor D4 antibodies [169], herceptin [170], and brain-derived neurotrophic factor [171].

1.3.4. Non-Drug Delivery Applications

Interestingly, FUS+MB exposures without therapeutic agent delivery have been shown to generate biological changes that may be beneficial in specific contexts. In a study designed to explore the impact of FUS+MB exposure in a mouse model (TgCRND8) of AD, Jordao *et al.* first described positive sonication-mediated effects on pathology, free of drug delivery. Authors reported a significant reduction in mean Aβ plaque size and total Aβ plaque surface area in the sonicated, relative to the non-sonicated, hemisphere. Additionally, they found increased microglial activation surrounding Aβ plaques, as well as greater levels of Aβ within microglia and astrocytes, suggesting that FUS+MBs promotes phagocytosis of Aβ [172]. Given the progressive nature of AD, research on this effect has largely focused on repeated exposures. Burgess *et al.* demonstrated that weekly sonications (across three weeks) targeted bilaterally to the hippocampus

produced a significant reduction in plaque load, increased proliferation of neural progenitor cells in the dentate gyrus, and improved performance on hippocampal-dependent tasks in TgCRND8 mice [136]. Using longitudinal *in vivo* two-photon microscopy, Poon *et al.* found that the maximal effect on plaque size occurs approximately four to seven days following FUS+MB exposure and that plaques returned to baseline size within three weeks [173]. This would suggest that frequent sonications without therapeutic agent delivery would be required for this treatment strategy [173]. Since the initial study by Jordao *et al.*, others have found beneficial effects of FUS+MB exposure in APP23 [174,175] and pR5 [176] mouse models of AD (Aβ and tau pathology models, respectively).

FUS has also been shown to influence neural activity, both in the presence and absence of MBs, potentially providing a more targeted, less invasive alternative to techniques like deep brain stimulation and implanted electrocortical stimulation [177]. As early as the 1950s, there was evidence to suggest that ultrasound may alter neural activity in the CNS of mammals [178]. More recently, various groups have demonstrated that the application of FUS (without MBs) to *ex vivo* brain slices results in the activation of sodium and voltage-gated calcium channels, triggers SNARE-mediated exocytosis [179], and induces an increase in synaptic transmission [179,180]. *In vivo* studies have demonstrated that ultrasound can induce motor function when targeted to the motor cortex [181], increase dopamine and serotonin concentrations in the thalamic areas of rats [182], and modulate visuomotor behaviour in awake macaques [183]. Due to the wide range of ultrasound parameters shown to modulate neural activity [181–184], there may be several mechanisms at play, including the activation of mechanosensitive ion channels [179,185], temperature-induced changes in excitation thresholds [186,187], and changes in membrane capacitance [188]. Recent work also suggests that some of the neural activation previously reported may be the result of cochlear fluid vibration generated by ultrasound propagating from the skull to the inner ear, evoking a startle response [189,190].

FUS+MB exposures may also transiently alter neural function. Chu *et al.* observed the suppression somatosensory evoked potential amplitudes and blood-oxygen level dependent responses in rat cortex for one week following sonication with exposure conditions that produced extensive RBC extravasation. Conversely, with parameters that produced BBB permeability enhancement without significant RBC extravasation, reductions in blood-oxygen level dependent responses were observed at one hour, but not one week, following sonication [191]. Author suggest these effects may be used as an alternative to other

clinical neuromodulation techniques; however, further work is required to assess the efficacy of this approach.

1.3.5. Clinical Trials

The first use of FUS+MB exposure in humans for the purpose of increasing BBB permeability came as part of a clinical trial in July of 2014. This trial involved the implantation of a single element ultrasound device system into the skulls of 17 patients with recurrent glioblastoma, avoiding the complications of transcranial ultrasound propagation, but necessitating an invasive surgical procedure. Patients were sonicated at fixed PNPs to induce increased BBB permeability, after which carboplatin, a chemotherapeutic agent, was administered. Treatments were repeated two to four times, monthly. Authors reported that patients tolerated the procedure well, with no evidence of acute hemorrhage, ischemia, or edema in images acquired with susceptibility-weighted angiography, diffusion, or FLAIR sequences. Clinical symptoms relating to the FUS+MB procedure were not present in any patients in the subsequent hours or days, including the 11 epileptic patients that participated. Two adverse events occurred during the trial but were deemed unrelated to the procedure [192].

Phase one clinical trials conducted at *Sunnybrook Research Institute* in Toronto, Canada were the first to utilize transcranial ultrasound exposures, employing a multi-element hemispherical phased array system [193]. The first detailed results published from these trials came from a study in which a presumed non-eloquent region, the superior frontal gyrus white matter of the dorsolateral prefrontal cortex, was targeted in five patients with mild to moderate AD. Two stages of sonications, separated by one month, were performed, with the volume of targeted tissue doubling in the second stage. No participant presented with clinical symptoms believed to be related to FUS+MB exposure during this study, nor displayed persistent BBB permeability enhancement in CE-T1w imaging 24 hrs following the procedure. Two participants displayed hypointensities on T2*w images, indicative of microhemorrhages [194], immediately following sonication that resolved within 24 hrs. Tests interrogating cognition and daily functioning revealed no clinically significant changes between pre- and three months post-treatment [137].

As of March 2019, there are eight clinical trials recruiting participants around the world (ClinicalTrials.gov Identifiers: NCT03321487, NCT03119961, NCT02343991, NCT03608553, NCT03626896, NCT03616860, NCT03671889, NCT03712293). Thus far, studies have demonstrated the ability to increase BBB

permeability with minimal short-term, and no evidence of long-term side-effects (assessed two months following sonication by psychometric tests and MRI [137]) in human participants. Ongoing trials are focused on determining the safety of using FUS+MB exposures in a variety of pathological contexts, including glioblastoma, AD, Parkinson's disease, and amyotrophic lateral sclerosis. Demonstrating a high safety profile in these studies will enable future work to explore the use of FUS+MBs to deliver therapeutic agents and the sonication of larger volumes.

1.4. Biological Responses to FUS+MB Exposure

Both clinical and preclinical work have demonstrated the feasibility of using FUS+MB exposure to increase BBB permeability for the primary purpose of targeted therapeutic agent delivery. Also of importance for the widespread clinical implementation of this technique is a full characterization of the range of biological effects that may be expected to arise. This section will discuss the biological responses that have been observed following FUS+MB exposure, as assessed by MRI, behavioral testing, and biochemical and histological assays.

1.4.1. Magnetic Resonance Imaging

Non-invasive imaging is currently essential for precise targeting of FUS within the brain. MRI is not only effective in this regard, but also allows for flexibility in how targets are located (E.g. anatomically identified brain structures, regions of abnormal blood-oxygen level dependent responses, etc.). Additionally, MRI can also be utilized for detailed post-sonication assessment of tissue effects.

CE-T1w imaging is commonly used to confirm BBB permeability enhancement following FUS+MB exposure, however, more quantitative MRI approaches have provided valuable insights into the duration and kinetics of this effect. Using T1-mapping and MR contrast agents of varying hydrodynamic diameters, Marty *et al.* demonstrated that the time required for vascular permeability enhancement to reduce by half following sonication (I.e. half closure time) is dependent on the size of particle extravasating from systemic circulation into the brain. Half closure times were found to be approximately one and five hours, for contrast agents with diameters of 7 nm and 1 nm, respectively [195]. Similarly, dynamic contrast enhanced-MRI (DCE-MRI), which can provide information regarding the kinetics of vascular permeability, has been used to show that the initial magnitude of BBB permeability enhancement influences the

duration for which elevated permeability can be detected [196]. These studies emphasize the notion that the effects of FUS+MB exposure on BBB permeability are not binary (I.e. open vs closed BBB, commonly used terms in the field), and that the extent of initial permeability enhancement is dependent on a wide range of factors relating to both sonication parameters, as well as the compounds crossing the BBB.

MRI is also commonly used to qualitatively assess tissue damage following sonication. Hypointensities in images collected with T2*w or susceptibility-weighted sequences are indicative of microhemorrhages or hemosiderin deposits [194]. These effects have been reported in studies that employ high PNP [128,197] or high MB doses [197,198], and have been shown to correlate with inertial cavitation [128]. Studies employing optimized acoustic feedback control strategies have demonstrated that BBB permeability enhancement can be achieved without the detection of T2* effects [75,198,199]; however, small regions of red blood cell (RBC) extravasation (I.e. less than 50 µm in diameter) have been noted in hematoxylin and eosin (H&E) stained sections from animals that did not display T2* effects following FUS+MB exposure [75,128], highlighting the sensitivity limits of this detection method. While field strength and imaging parameters have significant impact on sensitivity, the detection of microhemorrhages smaller than 1 mm in diameter poses a challenge in most clinical settings [200].

Imaging with T2w sequences, which can aid in the detection of vasogenic edema [201], has also provided insight into the impact of FUS+MB exposure. Abnormal hyperintensities were noted by Downs *et al.* in approximately 6% of targets at 30 minutes to 30 hours following FUS+MB exposure, all of which resolved within one week. These effects were only seen after multiple sonications, spaced over a maximum of 20 months [202]. Vasogenic edema after multiple FUS+MB exposures may be indicative of a gradual deterioration of BBB integrity caused by inappropriate exposure parameters, as other have demonstrated that vascular permeability can be repeatedly enhanced without evidence of T2 effects [199]. Similarly, hyperintensities have been reported following single sonications in studies that employ high PNP [197] or high MB doses [197,198].

1.4.2. Behavioural Testing

As a course-level assessment of treatment risk, a variety of behavioural tests have been performed following FUS+MB exposures in small and large animal models. The most thorough and clinically relevant studies have employed longitudinal designs with repeated sonications.

Using a clinical-prototype, multi-element, MRI-guided FUS system (ExAblate 400, Insightec), McDannold *et al.* studied the impact of repeated FUS+MB exposures at fixed PNPs on behaviour in rhesus macaques. Five sessions over the course of five to nine weeks were performed in three macaques, with FUS targeted bilaterally to the lateral geniculate nucleus (a relay system for the visual pathway) and primary visual cortex (focal volume = ~1 cm^3). BBB permeability enhancement and hemorrhage were assessed with CE-T1w and T2*w sequences, respectively. Animals, trained to select and match symbols of varying sizes on touchscreens, were tested prior to and following sonications as a test of visual acuity, memory, and motor skills. Results suggested that repeated FUS+MB exposures did not induce significant changes in any measure over the course of the study; however, 3 of 75 targets displayed evidence of hemorrhage in T2*w images, without behavioural changes detected, suggesting low test sensitivity [128].

In a similar study, Downs *et al.* investigated the effects of repeated FUS+MB exposures, using a single-element transducer at fixed PNP, on decision-making and motor control. FUS was targeted unilaterally to the putamen and caudate nucleus of the basal ganglia over 4 to 20 months in three macaques. Evidence of edema was present in 4 of 61 targets over the course of this study. Assessed using the reward magnitude bias and random dot motion tasks, none of the macaques displayed aberrant visual perception, decision making, or motor function; however, the authors did note that responses differed between high and low rewards on non-sonication days. This suggests that FUS+MB exposures targeted to the dorsal striatum may negatively impact motivation. Additionally, no changes in heart rate, blood pressure, or motor evoked potentials were detected during sonications [203].

Moreover, O'Reilly *et al.* evaluated the impact of repeated, large volume (I.e. targets covering the majority of one hemisphere) FUS+MB exposures on motor function, cranial nerve function, postural reactions, and alertness in a natural canine model of aging. An acoustic feedback control algorithm, similar to that depicted in **Figure 1.4**, was used for this study. Four weekly sonications resulted in no detectable behavioural deficits nor evidence of edema or hemorrhage on follow-up imaging [199].

These studies, and others, suggest that FUS+MB exposures can be used to repeatedly enhance BBB permeability with little or no detectable changes in behaviour. However, the lack of detectable changes in cases for which transient indications of damage were evident on MRI, suggest that these studies are not ideal for the assessment of less overt biological effects.

1.4.3. Histological and Biochemical Assays

Much of the current understanding of how the brain responds to FUS+MB exposure has come from histological and biochemical analysis. While a complete characterization of the physical and biological processes that drive changes in BBB permeability is lacking, studies have provided detailed information on the routes of leakage and content of extravasated material, as well as changes in protein expression and cell morphology. However, the knowledge required to tightly control the duration of BBB permeability enhancement or fully evaluate the safety profile of this drug delivery technique has yet to be established. This section will review FUS+MB studies that have explored vascular and extravascular changes at the cellular and biochemical levels.

1.4.3.1. Vascular Effects

Early electron microscopy studies by Sheikov *et al.* described an increase in the number of vesicles, vacuoles, fenestrations, and transcellular channels in ECs at one to two hours following FUS+MB exposure [204]. Further work demonstrated transcellular vesicular trafficking [205] and paracellular leakage past TJ complexes [206] of systemically administered horseradish peroxidase and lanthanum chloride (tracers that do not traverse the BBB under physiological conditions), respectively. These changes in TJ integrity were mirrored at the protein level, with a significant reduction in the immunoreactivity of occludin, claudin-5, and zonula occludens-1 in the inter-endothelial clefts at 1 and 2 hours, but not 4 to 24 hours, following FUS+MB exposure [206]. While it is unclear whether this effect is due to a downregulation of TJ proteins or is the product of TJ protein trafficking away from the inter-endothelial cleft, it is apparent that FUS+MB exposure disrupts the integrity of the link between vascular ECs. Similarly, the increased density of EC vesicles may be driven by changes in protein expression, with upregulation of caveolin-1 observed one hour following sonication [207].

These changes in transcellular and paracellular permeability seem to be non-specific, as a variety of large molecules from systemic circulation have been observed in the brain following sonication. Significant increases in the levels of endogenous molecules, like albumin [208,209], IgG [172,204,210], and IgM [172], as well as exogenous substances, like therapeutic agents (discussed in *Section 1.3.3*) and tracer dyes [123,170,204,205] (**Figure 1.5**), have been observed in brain parenchyma after FUS+MB exposure. It should be emphasized that the quantity of extravasated material following sonication appears to be related to the initial magnitude of BBB permeability enhancement (E.g. $r^2 = 0.43$ for linear correlation of signal intensity

increase in CE-T1w images collected ~6 min post-FUS+MBs vs extravasated IgM in mouse cortex 4 days post-FUS+MBs [172]). Additionally, macrophage infiltration, as assessed by H&E staining [128,211–213], CD68 immunodetection [174,197,208], and MRI of superparamagnetic iron oxide nanoparticle-labeled cells [214], has been reported hours [214] to weeks [128,197] following sonication. Conversely, some reports have found no or few macrophages in the brain following sonications at low PNP [211,214].

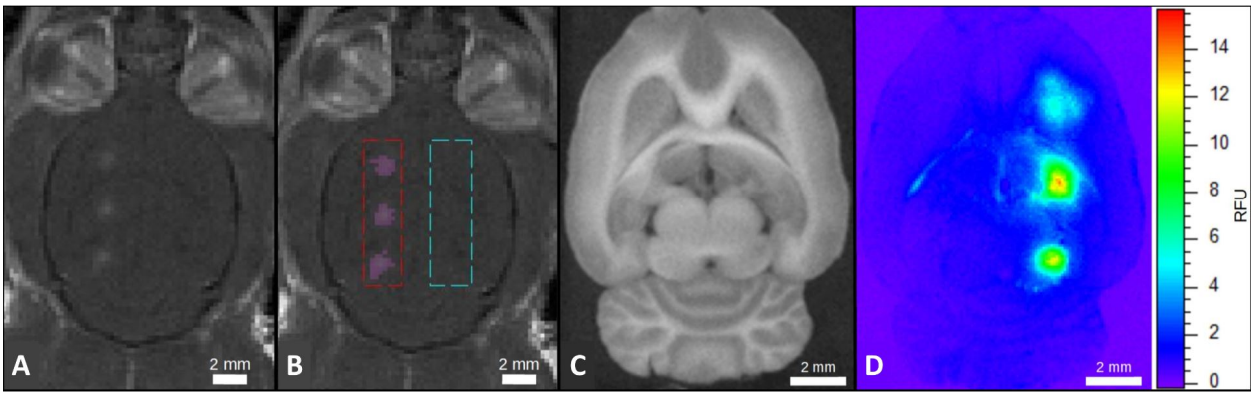

Figure 1.5. Methods of Evaluating BBB Permeability Enhancement. The impact of FUS+MB exposure on BBB permeability enhancement can be assessed with a variety of methods. CE-T1w MRI is commonly used in both preclinical and clinical settings. Typically, a gadolinium-based contrast agent is administered intravenously during or shortly after sonication. (A) T1w images are then acquired to assess the magnitude and spatial distribution of vascular permeability enhancement to the contrast agent. (B) Signal intensity in the targets locations can be compared to non-sonicated regions to quantify, for example, the volume of tissue affected (I.e. the number of voxels with signal intensity values the are 3 standard deviation above the mean of signal intensity in an equivalent region that has not been sonicated). Alternatively, BBB permeability enhancement can be assessed in *ex vivo* tissue. Evans blue dye, which under normal physiological conditions does not cross the BBB in significant quantities, can be administered intravenously following sonication and extravasate in regions of enhanced BBB permeability. To quantitatively assess this, brain sections can first be imaged under (C) brightfield to gain anatomical data, then (D) fluorescently imaged to identify regions with elevated Evans blue concentrations (RFU = relative fluorescence units). Figure adapted from McMahon *et al.* [215] with permission from the authors.

In vivo two-photon microscopy has been valuable in providing observations of the morphological changes and kinetics of vascular permeability that occur during and after FUS+MB exposure. In the very acute stages following sonication in mice (I.e. seconds after or while sonicating), Raymond *et al.* consistently noted vasomotor responses that typically consisted of heterogeneous vasoconstriction (described as "lumpy" or "beaded") along the entire arterial network (mean reduction of ~60% in diameter of arteries), followed by a relaxation phase lasting several minutes, where vessels returned to baseline size. Blood flow

during the constriction phase was described qualitatively as "reduced"; authors also describe instances of transiently halted blood flow [216]. This change in vascular tone may be driven by the mechanical stimulation of smooth muscle cells by oscillating MBs, as similar responses are observed following physical contact to arterial walls by guide wires or catheters during interventional radiology procedures [217]. Vasoconstriction, during or shortly after FUS+MB exposure, has also been observed in rats; however, the frequency of this effect was found to be lower, occurring in only 25% of vessels analysed (versus 87.5% in mice) [218]. While it is unclear if these discordant reports are the result of species differences, FUS+MB parameters, or other experimental differences, the occurrence of vasoconstriction in a substantial proportion of arteries would be expected to transiently reduce local blood flow and may initiate ischemic response mechanisms. Conversely, vasodilation has also been noted in the minutes following sonication [219], an effect that may be related to enhanced nitric oxide production induced by shear stress from oscillating MBs [220], though this is has not been shown experimentally.

Quantitative and qualitative evaluation of BBB permeability enhancement using *in vivo* two-photon microscopy also suggests that there are at least three distinct types of leakage generated by FUS+MB exposure: hemorrhagic, focal disruption (aka. microdisruption or fast leakage), and slow leakage (aka. transcytosis) [216,218,219,221]. Hemorrhagic leakage seems to be largely avoidable with the use of appropriate exposure conditions, as few regions of RBC extravasation are observed when PNP is adjusted to limit inertial cavitation [169]. Focal disruptions are characterized by a rapid diffusion of dyes (I.e. K^{trans} of 0.005 to 0.04 min^{-1} for 10-70 kDa dextrans [221]) into brain parenchyma at distinct points along blood vessels, evident during or shortly after sonication [216,218,219,221]. This type of leakage occurs more frequently in vasculature with diameters less than 30 µm and is speculated to result from a widening of inter-endothelial clefts [216,219,221]. The onset of slow leakage is delayed, starting at least 10 minutes after sonication, and is characterized by a gradual (I.e. K^{trans} of less than 0.005 min^{-1} for 10-70 kDa dextrans [221]), diffuse accumulation of dye in the regions surrounding vessels of varying diameters [216,218,219,221]. It has been widely speculated that vesicle-mediated transcytosis contributes to this type of leakage [216,218,219,221], a hypothesis supported by the electron microscopy studies previously discussed [204,205]; however, there is no direct experimental evidence to link slow leakage to enhanced endocytosis. Additionally, the relative contribution of confounding factors, like laser-induced heating, cranial window-induced inflammation, and prolonged exposure to anesthetics, have not been thoroughly explored in the context of FUS+MB exposures.

An alternative explanation for the different types of leakage observed following sonication may be that sonoporation of ECs contributes largely to focal disruptions and slow leakage is chiefly the product of paracellular diffusion; the delayed presentation of slow leakage may be due to the time required for substances to diffuse through the inter-endothelial clefts and basement membranes surrounding cerebral vasculature, and accumulate in quantities sufficient for detection. Indeed, ultrasound and MB-mediated sonoporation of cell membranes has been demonstrated *in vitro* extensively [222–225]. For example, Park *et al.* observed the influx of propidium iodide (excluded when cell membranes are intact) and calcium into murine brain microvascular ECs immediately following a single 8 µs burst with a transmit frequency of 1.25 MHz, spatial negative pressure of 0.24 MPa, and Definity MBs in close proximity to ECs [224]. This suggests that of sonoporation of ECs can occur *in vitro* at MIs and burst lengths below what is typically employed to produce BBB permeability enhancement *in vivo*. The diameters of pores created by ultrasound-stimulated MBs have been measured to range from 100 nm to several micrometres [226–229]. Further evidence for the occurrence of sonoporation during FUS+MB exposures comes from Sheikov *et al.* who observed EC fenestrations and channel formation in targeted rabbit cerebrovascular one to two hours following sonication (1.5 or 1.63 MHz transmit frequency, 100 ms burst length, 1 Hz brf, estimated *in situ* PNP of 1 MPa, Optison MBs) [204].

1.4.3.2. Extravascular Effects

Beyond direct effects on vasculature, FUS+MB exposure has also been shown to produce cellular and biochemical changes in brain parenchyma. Perhaps the two best characterized effects, glial cell activation and neurogenesis, have been observed in several animal models and under a variety of exposure conditions.

Changes in the expression level of glial fibrillary acidic protein (GFAP) and ionized calcium-binding adapter molecule-1 (IBA1), markers for astrocytes and microglia, respectively, have been investigated as indicators of glial cell activation following FUS+MB exposure. In non-transgenic mice, IBA1 expression has been shown to increase in the sonicated cortex, relative to the non-sonicated contralateral cortex, at four hours and four days following sonication, with no significant differences present at 15 days. GFAP expression in these mice displayed no significant differences at four hours or 15 day post-FUS+MBs (~2.5-fold increase in mean expression at 15 days was not statistically significant), but was found to be significantly elevated at four days [172]. Others have also reported ~65% reduction in microglial process length (IBA1 stained

sections) across the targeted area 24 hrs following sonication, indicative of microglial activation, without clear morphological indications of astrocyte activation at this early time point [174]. Conversely, with higher exposure levels, significantly elevated GFAP and IBA1 immunoreactivity have been reported seven weeks after a single sonication and seven days after six weekly sonications, with morphological changes indicative of glial scar formation [197]. Together, these studies indicate that some degree of glial cell activation follows FUS+MB exposure, with microglial activation observed prior to astrocytic changes. It is also apparent that these changes can be transient, normalizing within one month [160], or can persist for at least seven weeks, depending on exposure conditions.

While the induction of glial cell activation likely acts to clear debris and restore homeostasis, the function of FUS+MB-mediated neurogenesis is less clear. Adult hippocampal neurogenesis occurs in the subgranular layer of the dentate gyrus (hippocampal subfield) and is often quantified by staining for bromodeoxyuridine (BrdU), an exogenous molecule that is incorporated into the DNA of dividing cells, and neuronal markers that indicate cell maturity. Scarcelli *et al.* first demonstrated that unilateral sonication of the hippocampus results in a significant increase in the number of cells in the dentate gyrus that are double-positive for BrdU and NeuN (I.e. mature neurons), compared to the contralateral hemisphere [230]. Mooney *et al.* showed that proliferation and survival of newborn hippocampal neurons is dependent on producing BBB permeability enhancement, as sonications at low PNP or at high PNP without MB administration (I.e. conditions with no detectable effect on BBB permeability) did not generate increases in neurogenesis [231]. Others have also shown that repeated FUS+MB exposures lead to a significant increase in dendritic branching and total dendritic length in granule neurons in the dentate gyrus [136].

There is a large body of literature examining changes in tissue health following FUS+MB exposures as assessed by basic histological stains, such as H&E [75,144,232,233], Prussian blue [128], and vanadium acid fuchsin [109,234]. Reports vary considerably between studies. Some note very low levels of RBC extravasations with rare occurrences of darkly stained, potentially ischemic neurons at 1-24 hours following sonication [134]; others have observed dilated blood vessels, astroglial scars, and metallophagocytic cells (I.e. microglia or macrophages that have phagocytosed RBCs) 13 weeks following FUS+MB exposure [197]. Each of these studies employed exposure conditions that were designed to be relevant to clinical use (I.e. trying to achieve BBB permeability enhancement with minimal effects on tissue health) but report disparate effects on tissue health. This emphasizes the necessity of considering both the FUS+MB parameters employed

and the amount of time that has passed between sonication and euthanasia. The former affects the magnitude of impact on tissue health and the latter influences the opportunity for lesion formation or tissue repair.

1.5. Impact of Acute BBB Dysfunction

The movement of FUS+MB-mediated BBB permeability enhancement into clinical trials has been motivated by promising preclinical results, combined with a great need for flexible brain-drug delivery strategies. Safety assessments in rodents and non-human primates have focused largely on detecting overt tissue damage or severe behavioural impairments, with less attention to the study of more subtle biochemical changes. While the results of these these studies were sufficient to gain approval for phase one testing in severely diseased brain tissue (E.g. glioblastoma and moderate/severe AD), a clear picture of how unimpaired or more functionally intact brain tissue responds to FUS+MB exposure has not been fully developed.

BBB dysfunction is increasingly recognized as a prominent feature of many CNS disorders (reviewed by Sweeney *et al.* [14]). While the causal relationship between normal vascular function and etiology are not always clear for slowly progressing diseases, the study of acute disorders and medical interventions designed to modulate BBB permeability may be informative as to the events that commonly follow a sudden loss of BBB integrity. This section will explore such scenarios in order to inform hypotheses of the events which may follow FUS+MB exposure.

1.5.1. Traumatic Brain Injury

Traumatic brain injury (TBI) is caused by an external force that produces mechanical stress in the neuropil, resulting in sheer forces that are particularly damaging to axons and microvasculature. Depending on the severity, shortly after impact, reduced cerebral blood flow can lead to increased lactate metabolism, reduced ATP production, oxidative stress, intracellular Ca^{2+} accumulation, and excitotoxicity [235]. In the hours following primary injury, tight junction complexes can lose integrity, leading to a widening of inter-endothelial clefts [236]; enhanced caveolin-1-mediated EC transcytosis has also been observed during this time [236]. This disruption in BBB integrity allows plasma proteins to extravasate, which stimulates the release of pro-inflammatory cytokines, such as interleukin-1β (IL1β), IL6, and tumor necrosis factor alpha

(TNFα), from glia [237]. The release of cytokines can also be triggered by axonal damage, cellular debris, ionic imbalances, and reactive oxygen and nitrogen species that result from the primary injury [237]. These chemical signals, along with elevated expression of adhesion molecules in damaged ECs, attract peripheral immune cells to brain parenchyma. Infiltrating macrophages, for example, can have a positive impact on injury progression by aiding in the clearance of cellular debris but may also create a less desirable cellular environment through the production of additional inflammatory mediators [238].

Apart from attracting immune cells, pro-inflammatory cytokines promote a number of other processes. As an example, IL1β can stimulate the release of matrix metalloproteinase-9 from astrocytes, which degrades the basement membrane surrounding vasculature and further promotes a loss of BBB integrity [239]. Moreover, TNFα signalling is positively linked to the expression aquaporin-4, a water channel that contributes both to the exacerbation and resolution of edema following TBI [240].

Pro-inflammatory cytokines may also act to promote neovascularization and neurogenesis following TBI. Monocyte chemoattractant protein-1 (MCP1), Il6, TNFα, and others, influence the expression of growth factors, such as vascular endothelial growth factor (VEGF) [241–243] and brain-derived neurotrophic factor [244–246], priming the neurovascular niche for repair. An upregulation of VEGF isoforms and VEGF receptors have been noted following TBI, along with increased vascular density [247–251]. Similarly, enhanced neurogenesis in the subgranular layer of the dentate gyrus and subventricular zone of the lateral ventricles have been reported weeks after diffuse [252] or focal [253] TBI. This growth and remodeling (I.e. angiogenesis and neurogenesis) is thought to promote tissue repair [236,238]; however, increased vascular density is not necessarily associated with increased cerebral blood flow or improved functional outcomes [254].

Acute inflammation in the brain is a protective response that is initiated to return physiological functions to naive levels when homeostatic control pathways are insufficient [255]. Microglia, astrocytes, and peripheral immune cells play vital roles following TBI in clearing debris, isolating the area of damage, and producing trophic factors and anti-inflammatory cytokines that allow for the resolution of inflammation and the restoration of BBB integrity. However, if conditions are pushed too far from the setpoint (E.g. the production of cytokines like IL10 and TGFβ are insufficient to initiate the resolution of inflammatory processes [256]), inflammation can become chronic and result in severe tissue damage, persistent BBB dysfunction, amyloid pathology, and recurrent seizures [257–260]. The loss of BBB integrity that can

accompany TBI both drives the inflammatory response and is exacerbated by it. The extent and duration of this interplay can largely influence subsequent tissue damage.

While the nature of the forces exerted on brain tissue during TBI and those that occur during FUS+MB exposure differ substantially, both scenarios present a situation in which physical forces are translated into a transient loss of BBB integrity. In the hours following TBI and FUS+MB exposure, increased paracellular and transcellular transport have been reported, along with the extravasation of plasma proteins and immune cells. Depending on the severity of primary injury, sustained BBB permeability enhancement can last for days following TBI, a result mirrored with high PNP FUS+MB exposures [119]. Additionally, neurogenesis and glial cell activation are generally associated with both TBI and FUS+MBs. A preponderance of evidence from the TBI field would suggest that the characterization of a potential acute inflammatory response following sonication is warranted. Reducing the magnitude and duration of such a response would be essential to ensure the safety of repeated FUS+MB exposures, especially in scenarios for which the goal of treatment is to restore or preserve neural function.

1.5.2. Hyperosmotic Solutions

As briefly discussed in *Section 1.1.2*, intra-arterial delivery of hyperosmotic solutions, such as mannitol and arabinose, have been used to transiently increase BBB permeability for hemisphere-specific drug delivery. While the effects of hyperosmotic solutions on BBB integrity have been known since at least 1945 [261], surprisingly little work has focused on investigating the biochemical changes that result from this intervention; however, histopathological changes and clinical symptoms are well documented, providing insight that may be relevant to FUS+MB-mediated BBB permeability enhancement.

Hyperosmotic solutions act to rapidly dehydrate and shrink ECs, which widens inter-endothelial clefts and allows paracellular diffusion across the BBB [32]. Increased vesicle-mediated transcytosis has also been observed following hypertonic arabinose administration [262]. Depending on the type of hyperosmotic solution, the concentration, and the perfusion rate, as well as on the method used to assess BBB integrity, effects on vascular permeability have been reported in the range of minutes [263] to several hours [38,264]. Albumin immunoreactivity has been found throughout the targeted hemisphere 24-48 hrs following intra-carotid mannitol delivery, along with a widening of perivascular spaces, microinfarctions, ischemic neurons, and focal edema [38]. Regions of focal ischemia largely coincide with increased GFAP and mistletoe

lectin-1 immunoreactivity 2-6 days post-mannitol, which are indicative of astrocyte and microglial activation, respectively [38]. H&E staining has demonstrated evidence of axonal dystrophy and immune cell infiltration at 3 days following hyperosmotic solution administration, as well as the presence of foamy cells (indicative of phagocytosing macrophages) at 7 days post-administration [265].

One of the most common clinical complications arising from this method of BBB modulation is the occurrence of seizures, with one study reporting an incidence rate of 15% in glioblastoma patients within 24 hrs of the delivery of mannitol and chemotherapeutics [33]. In a separate clinical trial, Marchi *et al.* reported seizures in 25% of glioblastoma patients following treatment, most commonly originating in the hemisphere contralateral to intra-arterial infusion. Importantly, this subset of individuals exhibited higher serum S100β levels, an indication of compromised BBB integrity and astrocyte damage [266], after BBB modulation [34]. The same study found a similar incidence of mannitol-induced seizures in healthy pigs, suggesting that the magnitude of BBB permeability enhancement, not chemotherapeutic agent administration or the presence of primary brain lymphoma, was driving the occurrence of seizures [34]. It may be hypothesized that this aberrant neuronal activity is generated by dramatic changes in brain-ion concentrations and/or the extravasation of glutamate, an excitatory neurotransmitter found at high concentrations in systemic circulation. To increase safety, some clinical trials employing hyperosmotic/BBB modulation have implemented anticonvulsant pretreatment to reduce the incidence of seizures [35]. Other physiological observations following intra-carotid mannitol administration have included stroke-like symptoms in glioblastoma patients [33] and a high incidence of respiratory arrest in rats [267].

Preclinical and clinical work in the hyperosmotic-BBB modulation field may be informative of potential risks and biological effects of FUS+MB exposure. Both interventions induce increases in vascular permeability that peak shortly after or during treatment and resolve hours later. Similarly, plasma protein and immune cell extravasation, along with glial cell activation, accompany these increases in BBB permeability. While there have been no explicit reports of seizures accompanying FUS+MB exposure, this may be due to the smaller volumes of tissue affected (E.g. maximum of 850 mm^3 in rabbits [75], 2430 mm^3 in humans [268]), compared to the hemisphere-wide changes associated with intra-carotid mannitol delivery. Indeed, seizure activity is commonly associated with pathologies in which BBB integrity is compromised (E.g. stroke, TBI, and CNS infections) [34]. Alternatively, the dynamics of BBB leakage following these interventions may differ in ways that alter the risk of aberrant neuronal activity. Review of

hyperosmotic-BBB modulation literature would suggest that there is a need to investigate potential changes in neuronal firing, ionic homeostasis, and neurotransmitter extravasation following sonication, along with a need to assess any additional risks associated with large volume exposures.

1.5.3. Other Pathologies

There are several other pathologies in which acute BBB dysfunction is commonly noted. Following ischemic stroke, the time course of increased vascular permeability can be biphasic. The first phase is influenced by alterations to the cytoskeletons of ECs (30-60 min following reperfusion) and by the enzymatic cleavage of TJ proteins after immune cell infiltration (3-6 hrs following reperfusion) [269]. The second phase, if present, is seen 2-3 days following ischemic stroke and coincides with major TJ structural abnormalities [270]; however, there is some evidence that BBB permeability does not completely return to baseline between these temporal windows [271]. Increased caveolin-1-mediated transcytosis begins in the hours following reperfusion and can persist for days [270]. These changes in BBB permeability contribute to oxidative stress, plasma protein extravasation, immune cell infiltration, glial cell activation, and inflammation, all of which are hallmarks of ischemic stroke [236]. Additionally, in the penumbra - the region surrounding the necrotic core - the production of angiogenic mediators can spur blood vessel growth in the days and weeks following injury, aiding in functional recovery [236].

Another example of BBB dysfunction in pathology can be seen with epilepsy. The loss of TJ integrity and IgG leakage are observed in the surgically removed hippocampi of humans with temporal lobe epilepsy, along with increased VEGF expression and greatly elevated vascular density [272]. In the lithium-pilocarpine model of epilepsy, rats display these same features, as well as astrocyte activation [272]. While the aberrant neuronal activity at the core of epilepsy displays a bidirectional relationship with BBB dysfunction, being both driven by and exacerbating barrier breakdown [14], excitotoxicity alone has been shown to increase BBB permeability [273]. Neuroinflammation and immune cell infiltration also play an integral role in the vascular permeability associated with seizures [274]; several anti-inflammatory treatment strategies, including the administration of dexamethasone [275], have been shown to positively impact BBB integrity and seizure frequency in epilepsy [274].

There are several common observations from the various scenarios discussed above: (1) Inflammation, glial cell activation, and immune cell infiltration seem ubiquitous in all situations in which BBB integrity is

compromised; (2) Increased trans- and paracellular leakage are rarely seen independently; (3) Rapid restoration of BBB integrity is essential for limiting both the duration of inflammation and extent of tissue damage; (4) Inflammation is bidirectionally linked to BBB dysfunction; (5) Trophic factors are often produced following the loss the BBB integrity and this is tied to the induction of neurogenesis and angiogenesis. Given the frequency of these observations, there is a need for research in the FUS+MB field to thoroughly investigate the well-established effects of transient BBB dysfunction, with a focus on inflammation and its downstream effects. This is essential for the complete evaluation of clinical risk and is the focus of the work described in this thesis.

1.6. Thesis Structure, Rationale, and Hypotheses

FUS+MB exposure is a promising approach to achieve targeted drug delivery to the brain, a challenge that has undoubtedly hindered the development of treatment strategies for many neuropathologies. While preclinical work has spawned the initiation of clinical testing, there exist large gaps in our understanding of the biological events that follow sonication. Without a more detailed characterization of the range of effects on cerebrovascular health induced by FUS+MB exposures, thorough risk assessments are not possible. This knowledge is especially relevant to scenarios in which the goal of treatment is to restore or preserve neural function. Observations common to other scenarios in which BBB integrity is acutely compromised highlight areas of assessment that require focus.

The work presented in this thesis investigates the response of brain vasculature to FUS+MB exposures designed to increase BBB permeability, with the overarching goal of presenting clinically relevant information to aid in risk-benefit analyses. The general approach was first, to conduct a hypothesis generating assessment of microvascular gene expression changes following sonication (*Chapter 2*), from which subsequent studies were based. Microarray analysis of laser capture microdissected microvasculature was performed at 6 and 24 hrs following FUS+MB exposure. The remaining chapters explore the following hypotheses:

1. Acute inflammation following FUS+MB exposure is influenced both by the degree to which BBB permeability has been increased and MB dose (*Chapter 3*). Differential expression of genes implicated in the progression of acute inflammation were assessed at 6 hrs and 4 days following FUS+MB exposure in whole brain tissue. Three sonication schemes were evaluated: (1) a clinical imaging dose of MBs + PNP controlled with acoustic feedback, (2) 10x clinical imaging dose of MBs +

high fixed PNP, and (3) 10x clinical imaging dose of MBs + PNP controlled with acoustic feedback. CE-T1w, T2w, and T2*w imaging were performed to assess BBB permeability enhancement, edema, and hemorrhage, respectively.

2. Angiogenic processes are initiated following FUS+MB exposure, leading to blood vessel growth (*Chapter 4*). Blood vessel growth was assessed by the immunoreactive density of blood vessels, the density of newborn ECs, and the size distribution of blood vessel diameters. Immunoreactivity of VEGFA was qualitatively assessed as a potential driver of blood vessel growth. Three time points were evaluated, 7, 14, and 21 days following FUS+MB exposure.
3. The post-sonication administration of dexamethasone, a synthetic glucocorticoid, will expedite the restoration of BBB integrity and significantly limit inflammation and blood vessel growth (*Chapter 5*). Quantitative MRI methods were used to explore changes in BBB permeability enhancement following sonication. The expression of inflammatory markers was assessed at 2 days and astrocyte activation and blood vessel growth were assessed at 10 days following FUS+MB exposure.

Chapter 6 briefly summarizes the principal findings presented in this thesis and discusses some of the future directions that stem from this work. The need for flexible strategies that aid in the delivery of therapeutic agents to the brain in great. It is important, however, that the risks of such strategies are fully understood in order for appropriate clinical implementation, as well as to allow for the development of risk mitigating, counteractive measures.

Chapter 2

Acute Effects of Focused Ultrasound and Microbubble Exposure on the Hippocampal Microvascular Transcriptome

2.1. Introduction

While preclinical research has demonstrated the utility of FUS+MB exposures for therapeutic agent delivery, detailed knowledge regarding the impact of this intervention on vascular health is largely limited to observations from electron microscopy and *in vivo* two-photon microscopy studies. Given the active role of cerebrovascular in maintaining homeostasis, influencing metabolism, and supporting neurogenesis [276], characterizing the impact of FUS+MB-mediated BBB permeability enhancement on vascular health is of importance for assessing risk.

The cerebral vascular response to a sudden loss of BBB integrity has been studied in various contexts outside of therapeutic ultrasound (reviewed in Section 1.5). Common observations from this body of literature include increased production of pro-inflammatory/ anti-inflammatory cytokines, cell adhesion molecules, and trophic factors, which can directly or indirectly act to restore homeostatic conditions and limit neuronal damage; however, if the magnitude of this response is severe, neuroinflammation can become chronic, amplified by positive feedback loops, and secondary injury may occur [277].

In the context of FUS+MB exposure, the response of cerebral vasculature (opposed to brain tissue in general) is of particular interest, as this location experiences the largest magnitude of stresses during

Parts of this chapter are adapted from: McMahon D, Bendayan R, Hynynen K. Acute effects of focused ultrasound-induced increases in blood-brain barrier permeability on rat microvascular transcriptome. *Scientific reports*. 2017. 7:45657. Used with permission as part of publication agreement.

sonication [108]. Given the relatively small proportion of total brain volume occupied by blood vessels (E.g. blood volume accounts for ~2.5-5.0% of total brain volume in Sprague Dawley rats [278]), it may be important to limit analyses to this specific tissue type in order for biologically significant changes to be detected. Indeed, previous work has shown that the response of brain tissue to FUS+MB exposure is not homogeneous across cell types [172]. Additionally, previous observations of FUS+MB-induced hippocampal neurogenesis, as well as the intimate relationship between neurogenesis and the vascular niche, motivates the study of this brain region. For these reasons, the work described in *Chapter 2* focuses on the transcriptional response of hippocampal microvasculature at acute timepoints following sonication.

More specifically, this chapter describes the results of microarray analysis performed on laser capture microdissected microvascular samples collected from the dorsal hippocampi of rats sacrificed at 6 and 24 hrs following FUS+MB exposure. Changes in the expression of individual genes and bioinformatic pathway analyses were used to glean a more detailed picture of the acute impact of sonication on microvascular health, as well as to generate hypotheses to inform subsequent work.

2.2. Materials and Methods

2.2.1. Animals and Preparation

Male Sprague Dawley rats (n = 12), weighing 200-300 g on the day of sonication, were used in this study (Taconic Biosciences, Germantown, NY, USA). Animals were housed in the *Sunnybrook Research Institute* animal facility (Toronto, ON, Canada) and had access to food and water *ad libitum*. All animal procedures were approved by the *Animal Care Committee* at *Sunnybrook Research Institute* and are in accordance with the guidelines established by the *Canadian Council on Animal Care*.

To prepare animals for sonication, anesthesia was induced with 5% isoflurane (carrier gas: 100% oxygen at 1 L/min), hair on the dorsal surface of the head was removed with depilatory cream, and a 22-gauge angiocath was placed in the tail vein. Anesthesia was maintained with a mixture of 80 mg/kg ketamine (Vétoquinol, Magny-Vernois, France) and 10 mg/kg xylazine (Bayer Inc., Toronto, ON, Canada) administered intramuscularly. During imaging and sonication, animals were secured in a supine position on an MRI-compatible sled, allowing transport between the bore of the MRI and the FUS system (**Figure 2.1D**). The dorsal surface of the head was coupled to a degassed, deionized water-filled polyimide window with ultrasound gel. Body temperature was maintained with heated saline bags.

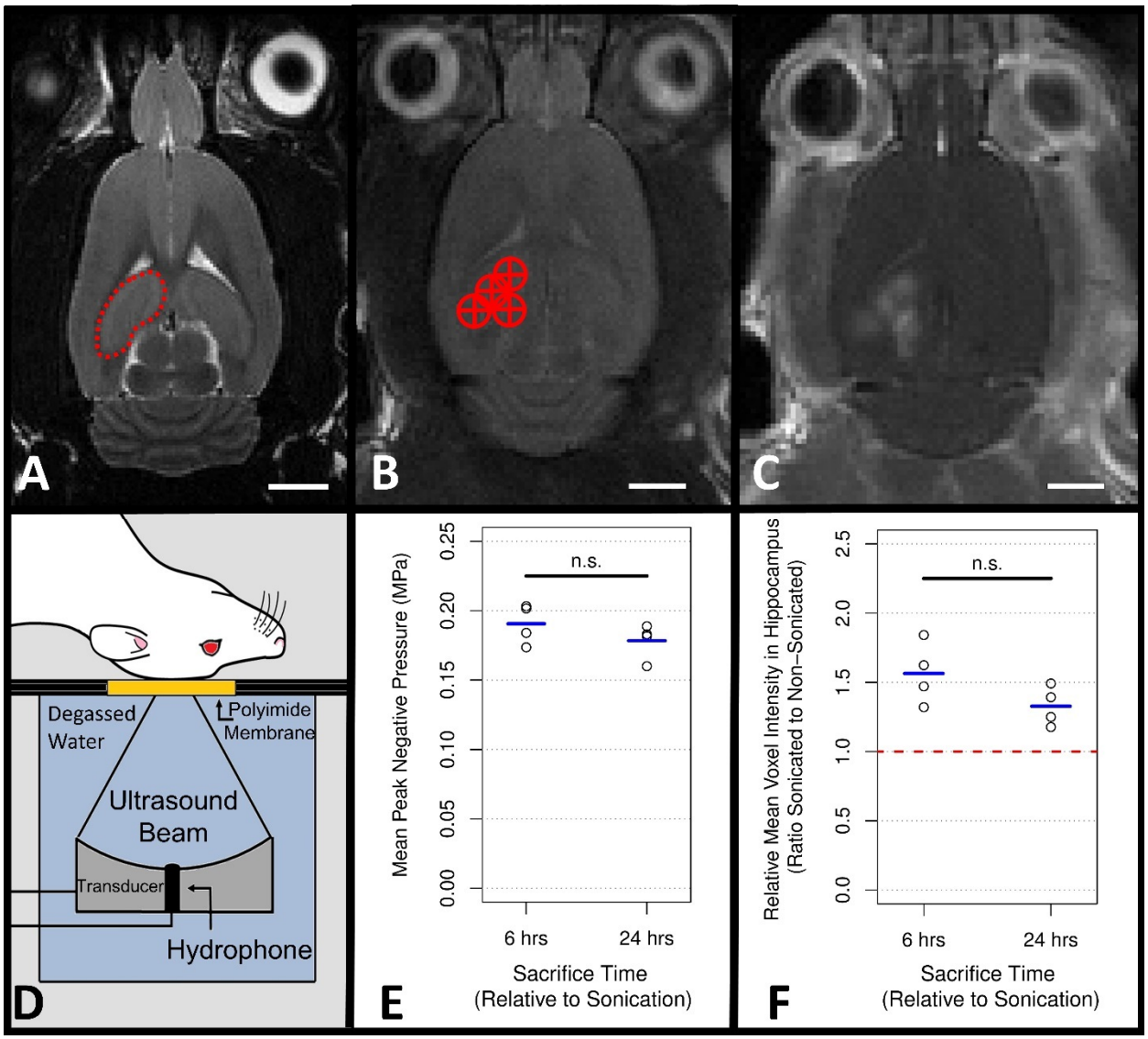

Figure 2.1. MRI-Guided FUS+MB Exposure. The dorsal hippocampus (A) (indicated by red dotted line) was targeted from T2w MR images (B) acquired prior to FUS+MB exposure (targets indicated by red circle with cross). (D) During sonication and imaging, rats were positioned supine on an MRI compatible sled with the dorsal surface of the head coupled to a polyimide membrane. The bottom of the membrane was coupled to a tank filled with degassed, deionized water, housing the transducer/hydrophone assembly. (E) Mean PNP for dorsal hippocampal targets following a software-triggered pressure drop were 190 kPa ± 20 kPa and 184 kPa ± 19 kPa ($p = 0.24$) for groups of animals sacrificed at 6 and 24 hrs post-FUS+MB exposure, respectively. (C) Following sonication, CE-T1w MR images were acquired to confirm BBB permeability enhancement. (F) Relative contrast enhancement was assessed by calculating the ratio of mean voxel intensity in the sonicated dorsal hippocampi to the non-sonicated hemispheres in each animal. The ratios of mean voxel intensity in the sonicated hippocampi to non-sonicated hippocampi were 1.56 ± 0.22 and 1.33 ± 0.14 for groups of animals sacrificed at 6 and 24 hrs post-FUS+MB exposure, respectively ($p = 0.12$). $n = 4$ animals per time point. Scale bars = 4 mm.

2.2.2. MRI-Guided FUS+MB Exposure

MRI-guided FUS+MB exposure was performed using a commercially available system (RK100, FUS Instruments Inc., Toronto, ON, Canada). A spherically focused transducer driven at 551.5 kHz (f = transmit frequency, focal number = 0.8, external diameter = 75 mm, internal diameter = 20 mm), calibrated using a planar fiber optic hydrophone with an active tip diameter of 10 µm (Precision Acoustics Ltd., Dorset, UK), was used for all sonications. The transducer was situated in a tank of degassed, deionized water and its movement was controlled with a motorized positioning system. To allow ultrasound propagation from the transducer to the brain, the bottom of the polyimide membrane (part of the MRI-compatible sled) was coupled to the water tank below (**Figure 2.1D**). The spatial coordinates of the FUS positioning system were co-registered to that of a 7T horizontal bore Avance BioSpec 70/30 scanner (Bruker BioSpin, Ettlingen, Germany) with a 20 cm inner diameter gradient insert coil (Bruker BioSpin, Ettlingen, Germany). Co-registration enabled FUS targets to be chosen in software from T2w images (TR = 2000 ms, TE = 60 ms) acquired prior to sonication using an 8 cm inner diameter volume coil for transmit and receive. Four locations were targeted per MB dose (**Figure 2.1B**). Eight locations were unilaterally targeted in a single hemisphere of each animal (4 targets in the dorsal hippocampus and 4 targets in the striatum).

Ultrasound was delivered in 10 ms bursts with a BRF of 1Hz for 120 sec. Acoustic emissions were monitored with an in-house manufactured polyvinylidene difluoride hydrophone located in a 25 mm opening in the centre of the transducer. To calibrate PNP, an acoustic feedback control algorithm, similar to that described by O'Reilly and Hynynen [232], was employed. Briefly, starting PNP was set at 128 kPa (measured in water without skull attenuation) and increased by an increment of 8 kPa each second. A slow bolus of MBs (20 µl/kg; Definity, Lantheus Medical Imaging, North Billerica, MA, USA), diluted in saline (1:9), was administered via tail vein catheter following the start of sonication. This delay allowed baseline hydrophone measurements to be obtained prior to MBs entering cerebral vasculature in the targeted locations. Once the ratio of signal to baseline at $1.5f$ or $2.5f$ passed 3.5, PNP was dropped by 50% and maintained at this level for the remainder of sonication. This algorithm is designed to calibrate pressure based on *in vivo* MB response [232].

To confirm BBB permeability enhancement, a gadolinium-based contrast agent (Gadovi, Schering AG, Berlin, Germany) was administered via tail vein catheter during sonication. CE-T1w images (repetition time (TR) = 500 ms, echo time (TE) = 10 ms) were acquired approximately 2 min following the end of sonication (**Figure 2.1C**). Targets which did not demonstrate gadolinium contrast enhancement were

sonicated a second time. All animals that received FUS+MB exposure displayed contrast enhancement throughout either the left or right dorsal hippocampus, without changes apparent in the contralateral hemisphere. Animals were sacrificed at 6 or 24 hrs post-sonication by transcardial perfusion with ice-cold saline, followed by 4% Evans blue (Sigma-Aldrich Corporation, St. Louis, MO, USA) in saline to highlight vasculature for subsequent sample collection. Brains were snap frozen in liquid nitrogen and stored at -80^{o}C until processing.

2.2.3. Tissue Processing

Brains were horizontally cryosectioned (10 µm thick) and mounted onto nuclease and nucleic acid free slides (MembraneSlide NF 1.0 PEN, Zeiss, Göttingen, Germany). Eight sections throughout the dorsal hippocampus were collected from each brain. Mounted sections were stored up to three days at -80^{o}C before laser capture microdissection (LCM). Immediately prior to LCM, sections were briefly dehydrated in ethanol (ice-cold 95% for 30 sec, ice-cold 100% for 30 sec, and room temperature 100% for 30 sec) and cleared in xylenes (twice at room temperature for 30 sec). Sections were dried for 5 min prior to the start of LCM.

2.2.4. Laser Capture Microdissection

Dorsal hippocampal microvascular samples were collected using a PALM Microbeam system (Zeiss, Göttingen, Germany). The non-contact nature of this technology minimizes risks of contamination. A semi-automated image processing algorithm was developed (AxioVision 4.8.3 software, Zeiss, Göttingen, Germany) to select Evans blue-perfused microvessels (< 50 µm in diameter) for collection in an unbiased manner based on RGB and size thresholds (**Figure 2.2A-D**). Imaging and collection of microvascular samples were performed using a 40x objective. Approximately 10 000 000 µm^3 of tissue was collected into microcentrifuge tubes (AdhesiveCap 500, Zeiss, Göttingen, Germany) per sample, comprising approximately 3000 microvessel segments and yielding 3-5 ng of total RNA. Collection times were limited to four hours to minimize the degree of RNA degradation. RNA isolation was performed using the PicoPure kit (Life Technologies Inc., Waltham, MA, USA) in accordance with manufacturer's instructions. Samples were treated with DNase (Qiagen, Hilden, Germany). RNA concentration and quality was assessed using the 2100 Bioanalyzer system with RNA 6000 Pico chip (Agilent, Santa Clara, CA, USA). All samples had an RNA integrity number of 6.8 or higher (7.3 ± 0.3).

2.2.5. Composition of Microvascular Samples

In a separate cohort of male Sprague Dawley rats not receiving FUS+MB exposure (n = 3), the composition of LCM collected microvascular samples were assessed by semi-quantitative polymerase chain reaction (PCR). The tissue processing and LCM collection protocols for these samples were as described above. Microvascular samples were collected from three brains (~1 000 000 μm^2 of tissue/sample); from the same tissue sections and region of the brain, an equal amount of whole tissue was also collected by LCM to compare sample composition. RNA was isolated, treated with DNase, and assessed as described above.

Semi-quantitative PCR was used to assess the level of platelet and endothelial cell adhesion molecule-1 (*Pecam1*; endothelial cell marker), microtubule associated protein-2 (*Map2*; mature neuronal marker), *Gfap* (astrocyte marker), and beta-actin (*Actb*; housekeeping gene). The forward and reverse primers used were as follows: *Pecam1*, forward, 5'-CCGTGATAGTGAACAGCAAGGA-3', and reverse, 5'-AGGATGCTACTGGCCTTGGAGA-3'; *Map2*, forward, 5'-CATACCACCAGCGGTTTGAGT-3', and reverse, 5'-GCTGAGGAACTAAGGCAGCA-3'; *Gfap*, forward, 5'-CGCGGCACGAACGAGTCC-3', and reverse, 5'-GTGTCCAGGCTGGTTTCTCG-3'; *Actb*, forward, 5'-AGGGAAATCGTGCGTGACAT-3', and reverse, 5'-GCAGCTCAGTAACAGTCCGC-3'.

SuperScript III one-step RT-PCR system with platinum taq (Life Technologies Inc., Waltham, MA, USA) was used with an annealing temperature of 58^o C for all PCR reactions except with Gfap primers (56^o C). A total of 35, 32, 35, and 30 PCR cycles were completed for *Pecam1*, *Map2*, *Gfap*, and *Actb*, respectively. PCR products were separated by electrophoresis on 2% agarose gels with TAE and ethidium bromide. All samples were run in triplicate. Gels were photographed under ultraviolet light using the MiniBIS Pro gel image analysis instrument (DNR Bio-Imaging Systems Ltd., Jerusalem, Israel). To assess the expression of *Pecam1*, *Map2*, and *Gfap*, the integrated density values of PCR product bands were normalized to *Actb* density. Paired, two-tailed, Student's t-tests were used to assess statistical significance. A p-value of 0.05 was used as a threshold for statistical significance.

2.2.6. Microarray Processing and Analysis

Relative gene expression was assessed using Affymetrix Rat 2.0 ST arrays (Santa Clara, CA, USA). Sample preparation was performed using GeneChip WT Pico Kit (Affymetrix, Inc., Santa Clara, CA, USA) with 500 pg of starting total RNA. Sample preparation and microarray processing was performed at *The Centre for*

Applied Genomics (Toronto, ON, Canada). A total of 20 microvascular samples were analysed from 5 groups (n=4/group); groups included: (1) 6 hrs post-FUS+MBs, ipsilateral hippocampus, (2) 6 hrs post-FUS+MBs, contralateral hippocampus, (3) 24 hrs post-FUS+MBs, ipsilateral hippocampus, (4) 24 hrs post-FUS+MBs, contralateral hippocampus, and (5) rats receiving no FUS+MB exposure.

All microarray data analysis was performed using R 3.2.1. Robust multi-array averaging (*oligo* package, Bioconductor) was used for pre-processing, empirical bayes analysis (*limma* package, Bioconductor) to assess differential expression, and the Benjamini-Hochberg method to adjust for multiple comparisons. Microarray quality control included performing outlier detection on MA plots by computing Hoeffding's statistic D on the joint distribution of A and M for each microarray ($D < 0.02$ for all microarrays). A gene was considered differentially expressed between groups if the log2 fold change was greater or less than 1.0 or -1.0, respectively, and had an adjusted p-value of less than 0.05.

2.2.7. Gene Ontology Overrepresentation and Geneset Enrichment Analysis

ToPASeq (Bioconductor) was used to identify gene ontology (GO) terms that were altered in microvasculature samples following FUS+MB exposure. For both over-representation analysis (ORA) and geneset enrichment analysis (GSEA), the GO sub-ontologies, *Biological Process* and *Molecular Function*, were assessed and the Benjamini-Hochberg method was used to adjust for multiple comparisons. ORA can be used to assess whether a subset of genes with related functions (GO terms) are enriched in a list of differentially expressed genes using a hypergeometric test. For this analysis, genes displaying significant changes between groups in relative expression were divided into up- and downregulated genes. An adjusted p-value of 0.001 was used as a threshold for significance.

Similarly, GSEA can be used to analyse whether a significant proportion of genes that are part of a GO term fall in the extremes of a ranked list of genes. For this analysis, all of the genes assessed by microarray were ranked by log2 fold change of differential expression between groups and a normalized enrichment score (NES) was calculated for each GO term. The advantage of this technique is that it utilizes information from the entire microarray dataset to determine which GO terms are enriched and to what degree. An adjusted p-value of 0.05 and NES of less than -1.5 or greater than 1.5 were used as thresholds for significance.

2.2.8. Quantitative Real Time Polymerase Chain Reaction

To validate changes in gene expression observed with microarray analysis, relative expression of nine genes were also assessed by quantitative real time-PCR (qRT-PCR). The gene-specific primers used are listed in **Table 2.1**. Amplified cDNA from the GeneChip WT pico kit was used as template. qRT-PCR was performed in triplicate on a CFX-96 real-time PCR detection system (BioRad Laboratories, Inc., Hercules, CA, USA), using SYBR green master mix (Thermo Fisher Scientific, Waltham, MA, USA). Relative gene expression of each transcript was determined by normalizing against glyceraldehyde 3-phosphate dehydrogenase (*Gapdh*), using the ΔΔCt method. Following qRT-PCR, specificity of each gene amplicon was confirmed by melting curve analysis and gel electrophoresis.

Table 2.1: Primers used for microarray validation

Target Gene	Fwd Sequence	Rev Sequence	Annealing Temperature (°C)
Gapdh	CAGGGCTGCCTTCTCTTGTG	GATGGTGATGGGTTTCCCGT	62.7
Cd74	AGCGCCCGTGAAGAATGTTA	CTGTGGGTAGTTCACGGGTC	61.1
Lcn2	GATTCGTCAGCTTTGCCAAGT	CATTGGTCGGTGGGAACAG	61.1
Slc22a6	CATTGCAATCAACTGCATGACACTA	AGGAACTGGCCCAGGCTGTA	62.7
Gfap	TGGCCACCAGTAACATGCAA	CAGTTGGCGGCGATAGTCAT	61.1
Abcb1a	TACATCTTGGCGGACCTTAC	CGCTGGTTTCTTTTCTTTCTTC	61.1
Itgb2	CAGCTGGCCCACAAACTTTC	TGGAATCGTCAGACAGCTCG	61.1
Ccl2	CCAGAAACCAGCCAACTCTC	GCTACAGGCAGCAACTGTGA	61.1
Serpine1	GAGGATGAAAGAAACAGCCAGCT	CCCGCTATGAAATTAGATTCACGT	61.4
Mmp9	TGCTCCTGGCTCTAGGCTAC	GCTTCTCTCCCATCATCTGG	61.4

2.3. Results

2.3.1. Characterization of Laser Capture Microdissection-Collected Microvascular Samples

The composition of LCM collected microvasculature samples was assessed by semiquantitative PCR in a separate cohort of rats not receiving FUS+MB exposure. The expression of *Pecam1*, *Map2*, and *Gfap* were compared between LCM collected microvascular and LCM collected whole tissue samples as a measure of EC, mature neuron, and astrocyte content, respectively (**Figure 2.2E-G**). Relative to whole tissue, microvascular samples contained averages of 248% ($p = 0.002$) and 142% ($p = 0.04$) higher levels of *Pecam1* and *Gfap*, respectively, and 62% ($p = 0.02$) lower levels of *Map2*. Given the structural organization of the BBB, with vasculature tightly ensheathed by astrocytic endfeet and innervated by excitatory neurons, an enrichment of *Gfap* and reduction, but not absence, of *Map2* in LCM collected microvasculature samples compared to whole brain tissue is expected. Elevated *Gfap* expression in

isolated microvessels compared to whole tissue has been previously reported with other collection techniques [279,280].

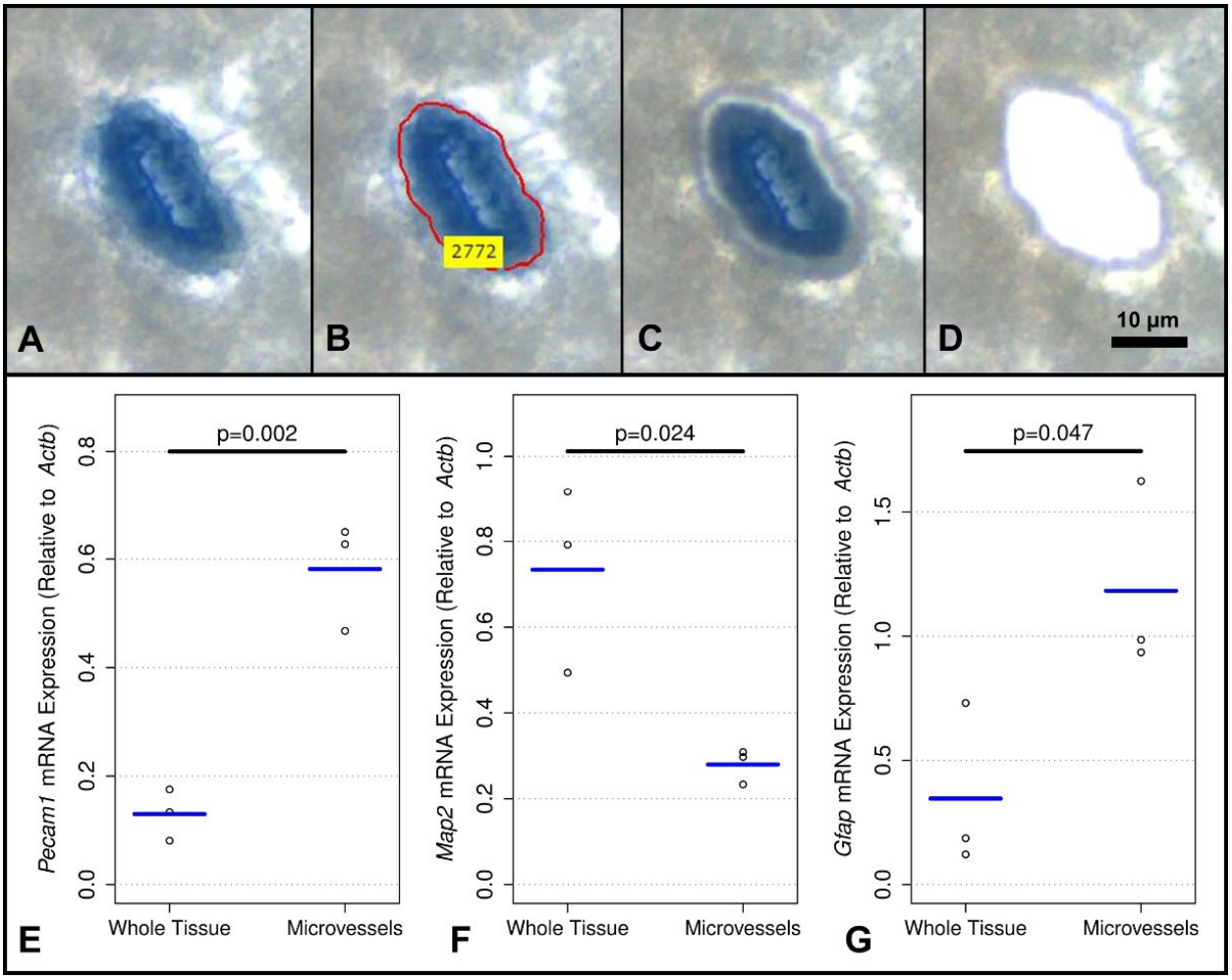

Figure 2.2. Laser Capture Microdissection and Characterization of Microvascular Samples. Animals were transcardially perfused with ice-cold saline, followed by Evans blue dye. Samples were collected from cryosection using LCM microscopy. The dye perfused blood vessels (A) were identified with an image analysis algorithm based on RGB colour thresholds (B). These regions of interest were cut with a focused laser (C) and catapulted into a collection vessel (D) for subsequent RNA extraction. Relative to LCM collected whole tissue, LCM collected microvascular samples contained averages of 248% (p = 0.002) and 142% (p = 0.04) higher levels of *Pecam1* (E) and *Gfap* (G), respectively, and 62% (p = 0.02) lower levels of *Map2* (F). n = 3 animals.

2.3.2. Peak Negative Pressure and Contrast Enhancement Following FUS+MB Exposure

BBB permeability enhancement was assessed following FUS+MB exposure by CE-T1w MRI. Relative contrast enhancement was assessed by calculating the ratio of mean voxel intensity in the sonicated

dorsal hippocampus to the non-sonicated hemisphere in each animal. The ratios of mean voxel intensity in the sonicated hippocampi to non-sonicated hippocampi were 1.56 ± 0.22 and 1.33 ± 0.14 for groups of animals sacrificed at 6 and 24 hrs post-FUS+MB exposure, respectively ($p = 0.12$; **Figure 2.1F**). Similarly, for animals sacrificed at 6 and 24 hrs post-FUS+MB exposure, respectively, mean PNPs in the dorsal hippocampus following a software-triggered pressure drop were 192 MPa ± 20 kPa and 184 MPa ± 19 kPa ($p = 0.25$; **Figure 2.1E**). These data suggest that FUS+MB exposures were similar between groups (animals sacrificed at 6 and 24 hrs post-sonication) and resulted in similar BBB permeability enhancement.

2.3.3. Differential Gene Expression Assessed by Microarray Analysis

Differential gene expression in dorsal hippocampal microvasculature was assessed between samples collected in the sonicated and contralateral hemispheres at 6 and 24 hrs following FUS+MB exposure (**Figure 2.3**). Just over 17000 genes were included in analysis; 60 genes were upregulated in the sonicated hemisphere after 6 hrs (**Appendix Table 2.1**), while 109 were downregulated (**Appendix Table 2.2**). At the 24 hr time point, 101 and 8 genes were up- and downregulated, respectively (**Appendix Tables 2.1 and 2.2**). When comparing samples collected from the hemisphere contralateral to sonication at 6 or 24 hrs post-FUS+MBs and samples from animals not receiving sonication, no transcripts displayed significant changes in expression at either time point investigated, suggesting that non-local effects of FUS+MB exposure on transcription were minimal.

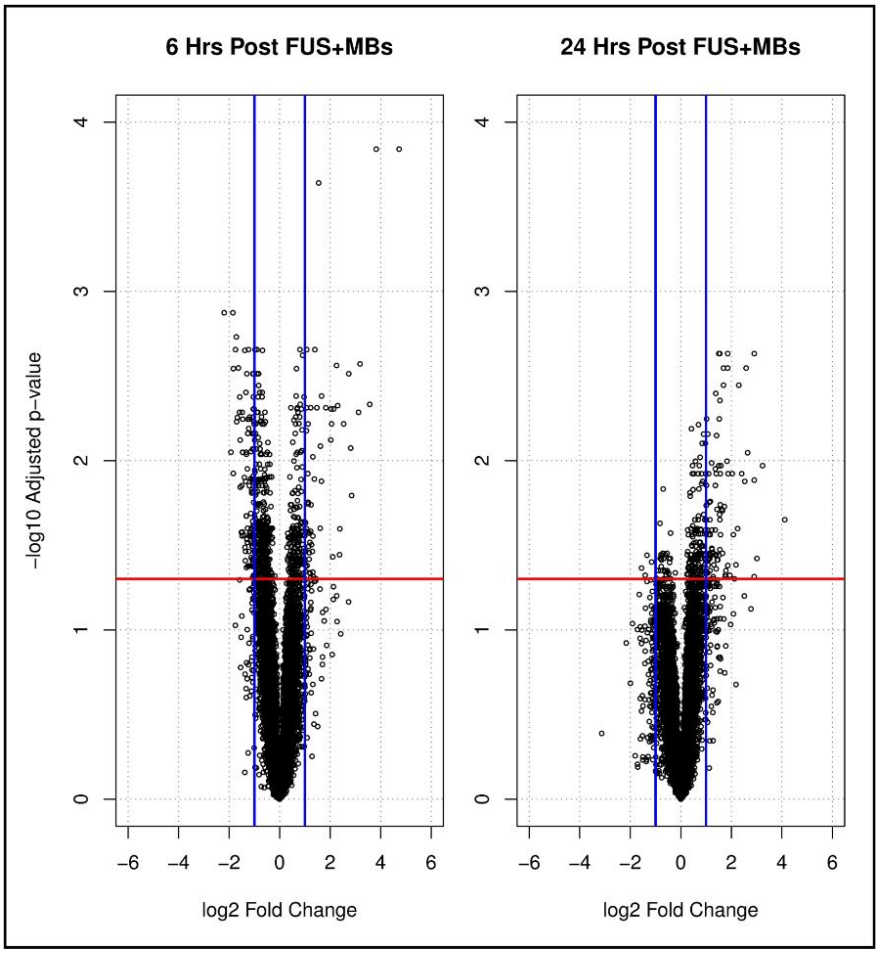

Figure 2.3. Volcano Plots of Differential Gene Expression. Relative gene expression in hippocampal microvascular samples was compared between the sonicated and non-sonicated hemispheres at 6 and 24 hrs post-FUS+MB exposure. A positive log2 fold change indicates increased relative expression in sonicated microvessels compared to the contralateral hemisphere. Blue vertical lines indicate a log2 fold change of 1.0 or −1.0. The red horizontal lines indicate a -log10 adjusted p-value of 1.30, corresponding to an adjusted p-value of 0.05. n = 4 animals per time point.

2.3.4. Inflammation-Related Genes

A consistent upregulation in many genes related to an acute inflammatory response were detected in dorsal hippocampal microvascular samples at 6 hrs post-FUS+MBs. Genes of note include, *Sele*, *Cxcl1*, *Ccl3*, and *Ccl2*, displaying log2 fold changes of 3.82 ($p < 0.001$), 2.74 ($p = 0.003$), 1.83 ($p = 0.005$), and 4.73 ($p < 0.001$), respectively, compared to the contralateral hemisphere (**Figure 2.4**). There was a reduction in the differential expression of many of these genes by 24 hrs following sonication. For the same genes listed above, there was a non-significant log2 fold change of 0.40 ($p = 0.650$), 0.47 ($p = 0.621$), 0.44 ($p = 0.495$), and 1.70 ($p = 0.082$), respectively, at 24 hrs post-FUS+MB exposure, compared to the contralateral hemisphere (**Figure 2.4**). It appears that FUS+MB exposure induces an acute inflammatory response that partially returns to baseline or is dampened at 24 hrs post-sonication; however, several inflammatory markers remained significantly upregulated at 24 hrs including, *C3*, *Ccl6*, *Gfap*, and *Itgb2*. These genes

displayed log2 fold changes of 1.55 (p = 0.023), 1.94 (p = 0.045), 1.54 (p = 0.003), and 1.38 (p = 0.034), respectively, compared to the contralateral hemisphere (**Table 2.2**).

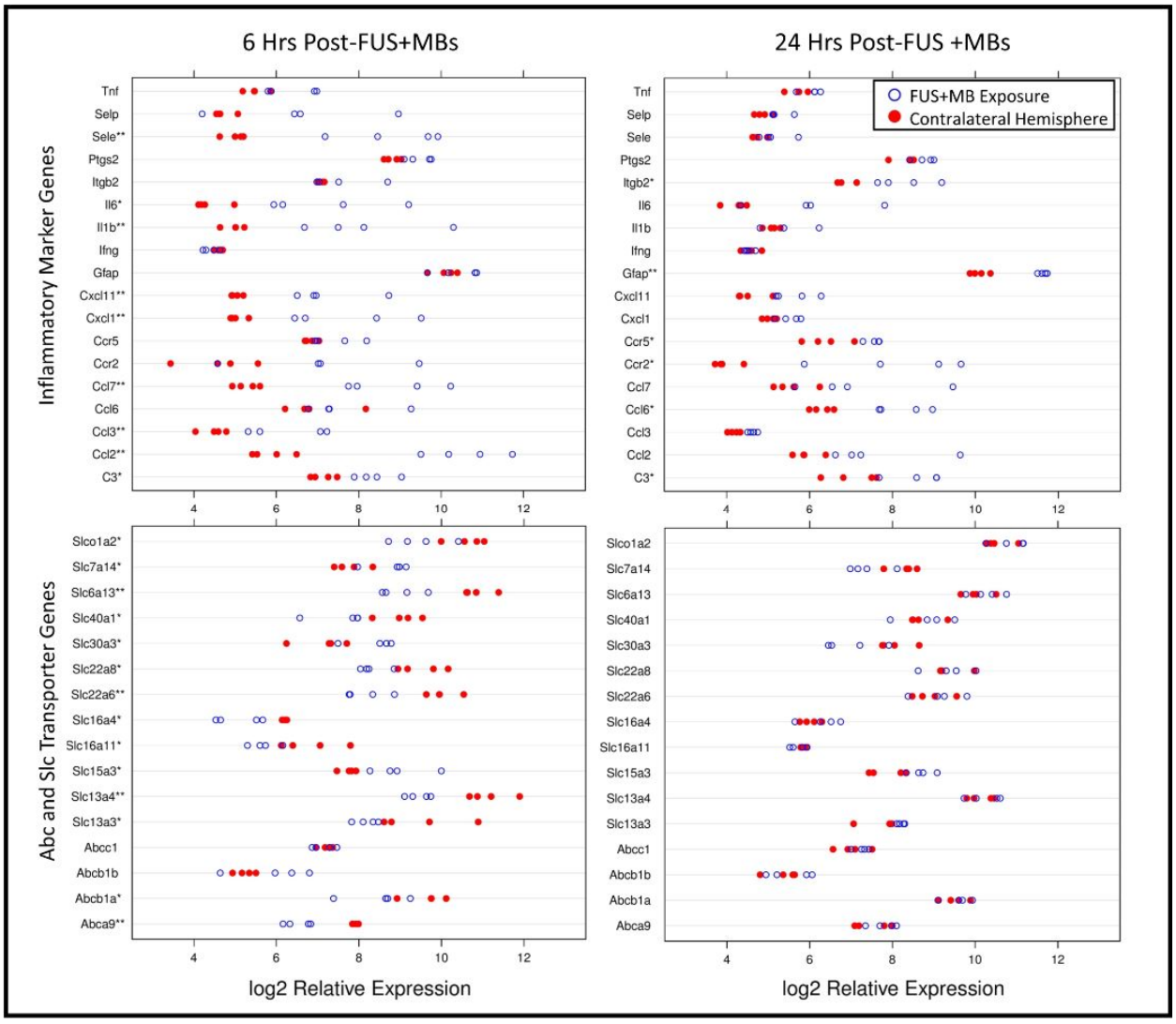

Figure 2.4. Dotplots of Differential Gene Expression for Inflammatory Markers and Abc and Slc Genes. Relative gene expression in hippocampal microvascular samples were compared between the sonicated (open circle) and non-sonicated (close red circle) hemispheres at 6 and 24 hrs post-FUS+MB exposure. Relative expression of all genes are displayed for each animal. * Indicates adjusted $p < 0.05$. ** Indicates adjusted $p < 0.01$. n = 4 animals per time point.

Table 2.2: Differential expression of selected genes in hippocampal microvessels at 6 and 24 hrs post-FUS+MB exposure relative to contralateral hemisphere

			6 hrs Post-FUS+MBs		24 hrs Post-FUS+MBs	
Related Functions	**Entrez ID**	**Gene Symbol**	**Log2 FC**	**Adjusted P-Value**	**Log2 FC**	**Adjusted P-Value**
Inflammation	24232	*C3*	**1.26**	**0.031**	**1.55**	**0.023**
	24770	*Ccl2*	**4.73**	**<0.001**	1.70	0.083
	25542	*Ccl3*	**1.83**	**0.005**	0.44	0.495
	287910	*Ccl6*	0.68	0.454	**1.94**	**0.045**
	287561	*Ccl7*	**3.57**	**0.005**	1.56	0.170
	60463	*Ccr2*	2.42	0.106	**4.11**	**0.023**
	117029	*Ccr5*	0.62	0.191	**1.15**	**0.036**
	81503	*Cxcl1*	**2.74**	**0.003**	0.47	0.622
	305236	*Cxcl11*	**2.25**	**0.003**	1.07	0.097
	24387	*Gfap*	0.29	0.468	**1.54**	**0.003**
	25712	*Ifng*	-0.20	0.374	-0.05	0.875
	24494	*Il1b*	**3.18**	**0.003**	0.35	0.762
	24498	*Il6*	**2.85**	**0.016**	1.78	0.119
	309684	*Itgb2*	0.47	0.427	**1.38**	**0.034**
	29527	*Ptgs2*	**0.65**	**0.049**	0.43	0.210
	25544	*Sele*	**3.82**	**<0.001**	0.40	0.650
	25651	*Selp*	1.83	0.076	0.38	0.788
	24835	*Tnf*	0.90	0.037	0.34	0.478
Oxidative Stress	24404	*Gpx1*	-0.27	0.399	0.59	0.077
	297029	*Gstk1*	-0.36	0.197	0.03	0.942
	24426	*Gstp1*	-0.25	0.415	0.00	0.993
	29253	*Maoa*	-0.28	0.462	0.19	0.663
	24598	*Nos1*	-0.40	0.515	0.10	0.914
	24599	*Nos2*	0.83	0.064	-0.07	0.925
	24600	*Nos3*	-0.17	0.803	0.42	0.484
	24786	*Sod1*	-0.02	0.831	-0.01	0.936
	24787	*Sod2*	**1.31**	**0.010**	0.28	0.623
	25352	*Sod3*	-0.44	0.066	0.43	0.087
Resolution of Inflammation	287454	*Alox12*	-0.12	0.760	0.00	0.997
	81639	*Alox15*	0.32	0.287	0.02	0.973
	25290	*Alox5*	-0.12	0.764	0.22	0.566
	29624	*Alox5ap*	-0.21	0.705	**1.13**	**0.033**
	79242	*Hpgd*	-0.41	0.569	0.81	0.235
	299732	*Lta4h*	-0.11	0.751	0.55	0.068
	59264	*Ltb4r*	-0.01	0.988	-0.05	0.887
	25211	*Lyz2*	0.79	0.321	**1.77**	**0.044**
	25526	*Ptgds*	-0.59	0.028	0.03	0.935
	81752	*Ptger2*	0.14	0.790	0.22	0.671
	59103	*Ptges*	**2.03**	**0.005**	0.82	0.216
	192227	*Ptgr1*	-1.07	0.065	0.15	0.865
	29527	*Ptgs2*	0.65	0.049	0.43	0.210
	364049	*Slamf7*	-0.20	0.708	**1.08**	**0.036**
	116510	*Timp1*	1.27	0.059	**2.59**	**0.003**
ABC and SLC	287788	*Abca9*	**-1.38**	**0.002**	0.26	0.548

Transporters	170913	*Abcb1a*	**-1.14**	**0.042**	0.08	0.927
	24646	*Abcb1b*	0.71	0.352	0.19	0.868
	24565	*Abcc1*	-0.05	0.903	0.23	0.522
	25303	*Abcc2*	0.00	0.995	-0.16	0.613
	170924	*Abcc4*	-0.69	0.180	0.10	0.901
	312382	*Abcg2*	-1.23	0.161	0.14	0.922
	64846	*Slc13a3*	**-1.31**	**0.043**	0.48	0.518
	503568	*Slc13a4*	**-1.72**	**0.002**	0.07	0.914
	246239	*Slc15a3*	**1.24**	**0.018**	0.82	0.107
	287450	*Slc16a11*	**-1.14**	**0.021**	-0.13	0.847
	295356	*Slc16a4*	**-1.11**	**0.015**	0.27	0.602
	29509	*Slc22a6*	**-1.83**	**0.003**	0.18	0.794
	83500	*Slc22a8*	**-1.19**	**0.028**	0.00	0.997
	366568	*Slc30a3*	**1.23**	**0.049**	-1.03	0.106
	170840	*Slc40a1*	**-1.42**	**0.028**	0.10	0.913
	171163	*Slc6a13*	**-1.85**	**0.001**	0.24	0.671
	499587	*Slc7a14*	**1.19**	**0.046**	-1.05	0.088
	170698	*Slco1a2*	**-1.13**	**0.037**	0.29	0.659
Angiogenesis	89807	*Angpt1*	-0.62	0.135	0.37	0.435
	89805	*Angpt2*	-0.23	0.648	0.76	0.091
	25148	*Egr3*	**1.23**	**0.005**	-0.42	0.294
	79114	*Fgfr1*	-0.14	0.576	0.23	0.351
	309684	*Itgb2*	0.47	0.427	**1.38**	**0.034**
	83781	*Lgals3*	0.42	0.527	**2.29**	**0.004**
	81687	*Mmp9*	**2.53**	**0.006**	1.55	0.083
	24628	*Pdgfb*	-0.07	0.893	0.18	0.699
	59086	*Tgfb1*	0.03	0.945	0.69	0.052
	83785	*Vegfa*	0.17	0.568	-0.1	0.798
Tight Junction Integrity	310655	*Cgn*	0.06	0.850	0.01	0.976
	65131	*Cldn5*	-0.75	0.069	0.09	0.885
	307505	*Ctnna1*	-0.39	0.168	0.31	0.310
	84353	*Ctnnb1*	-0.32	0.135	0.11	0.703
	619374	*Jam2*	-0.65	0.027	0.26	0.395
	83497	*Ocln*	-0.99	0.035	0.09	0.901
	292994	*Tjp1*	-0.42	0.073	0.12	0.696
	115769	*Tjp2*	-0.09	0.811	0.47	0.107
	314640	*Tjp3*	0.17	0.538	-0.07	0.853
Endocytosis	64310	*Arf1*	0.15	0.375	0.12	0.516
	79121	*Arf6*	-0.02	0.944	0.22	0.284
	25404	*Cav1*	-0.62	0.136	0.24	0.639
	64465	*Cdc42*	-0.16	0.101	0.07	0.493
	140694	*Dnm1*	0.56	0.111	-0.79	0.048
	313474	*Eps15*	-0.18	0.451	0.09	0.783
	64665	*Flot1*	-0.04	0.887	0.21	0.280
	83764	*Flot2*	0.07	0.818	0.16	0.554
	25150	*Fyn*	0.39	0.075	0.22	0.352
	287710	*Ptrf*	-0.61	0.104	0.19	0.688

The differential expression of individual transcripts related to an acute inflammatory response were reiterated by GSEA. GO terms related to inflammation, such as *chronic inflammatory response* (GO:0002544) and *inflammatory response to antigenic stimulus* (GO:0002437), showed significant enrichment at 6 hrs post-FUS+MB exposure with NESs of 2.27 (p = 0.015) and 2.18 (p = 0.015), respectively (**Table 2.3**). At 24 hrs following sonication, the NESs for these same GO terms were 1.99 (p = 0.009) and 2.13 (p = 0.009), respectively, suggesting a plateau in these inflammatory responses. GSEA and ORA of genes displaying increased expression in dorsal hippocampal microvascular samples following FUS+MB exposure show considerable overlap in GO terms related to a transient inflammatory response. There is, however, a consistent reduction in ORA significance levels at the later time point, relative to the 6 hr time point, for these GO terms.

Table 2.3: Geneset Enrichment Analysis of selected Gene Ontology terms in hippocampal microvessels at 6 and 24 hrs post-FUS+MB exposure relative to contralateral hemisphere

		6 hrs Post-FUS+MBs		24 hrs Post-FUS+MBs	
GO ID	**GO Description**	**NES**	**Adjusted P-Value**	**NES**	**Adjusted P-Value**
GO:0002544	chronic inflammatory response	**2.27**	**0.015**	**1.99**	**0.009**
GO:0002437	inflammatory response to antigenic stimulus	**2.18**	**0.015**	**2.13**	**0.009**
GO:0048514	blood vessel morphogenesis	**-1.57**	**0.015**	**2.34**	**0.009**
GO:0045766	positive regulation of angiogenesis	1.43	0.080	**2.48**	**0.009**
GO:0043536	positive regulation of blood vessel endothelial cell migration	-0.94	0.710	**1.95**	**0.009**
GO:1904018	positive regulation of vasculature development	1.39	0.101	**2.48**	**0.009**
GO:0010573	vascular endothelial growth factor production	**2.29**	**0.015**	**2.23**	**0.009**
GO:0022804	active transmembrane transporter activity	**-1.63**	**0.025**	-1.33	0.041
GO:0015171	amino acid transmembrane transporter activity	**-1.59**	**0.037**	-1.48	0.080
GO:0090484	drug transporter activity	**-1.85**	**0.037**	0.93	0.754
GO:0008028	monocarboxylic acid transmembrane transporter activity	**-1.97**	**0.025**	1.06	0.592
GO:0015291	secondary active transmembrane transporter activity	**-1.65**	**0.025**	-1.34	0.065
GO:0015085	calcium ion transmembrane transporter activity	**1.68**	**0.025**	**-2.37**	**0.020**
GO:0015108	chloride transmembrane transporter activity	1.04	0.630	**-1.93**	**0.020**
GO:0015075	ion transmembrane transporter activity	1.37	0.025	**-2.14**	**0.022**
GO:0015079	potassium ion transmembrane transporter activity	**1.91**	**0.025**	**-2.44**	**0.020**
GO:0015081	sodium ion transmembrane transporter activity	1.20	0.330	**-1.93**	**0.020**

2.3.5. BBB Transporter Genes

Downregulation in the expression of BBB transporter genes in the targeted hippocampus was observed at 6 hrs following sonication for several members of the ABC and SLC families of transporters including, *Abcb1a*, *Abca9*, *Slc22a6*, *Slc22a8*, and *Slc6a13* with log2 fold changes of -1.14 (p = 0.042), -1.38 (p =

Table0.002), -1.83 (p = 0.003), -1.19 (p = 0.028), and -1.85 (p = 0.001), respectively, compared to the contralateral hemisphere (**Figure 2.4**; **Table 2.2**). Differential expression of these transcripts largely returned to baseline by 24 hrs, displaying non-significant log2 fold changes of 0.08 (p = 0.927), 0.26 (p = 0.548), 0.18 (p = 0.794), -0.01 (p = 0.997), and 0.24 (p = 0.671), respectively (**Figure 2.4**).

Differential expression of genes related to transport across the BBB are reiterated in GSEA. NES at 6 hrs following FUS+MB exposure for the GO term *drug transporter activity* (GO:0090484) was -1.85 (p = 0.033), indicating significant suppression (**Figure 2.5**). At 24 hrs post-FUS+MBs, NES for this GO term partially normalized to 0.93 (p = 0.754). In addition to *drug transporter activity*, various other GO terms related to BBB transporter activity displayed significantly negative NESs at 6 hrs post-FUS+MBs. These include, *amino acid transmembrane transporter activity* (GO:0015171), *monocarboxylic acid transmembrane transporter activity* (GO:0008028), *active transmembrane transporter activity* (GO:0022804), and *secondary active transmembrane transporter activity* (GO:0015291), with NESs of -1.59 (p = 0.037), -1.97 (p = 0.025), -1.63 (p = 0.025), and -1.65 (p = 0.025), respectively. NESs for these same GO terms at 24 hrs post-FUS+MB exposure were -1.48 (p = 0.080), 1.06 (p = 0.592), -1.33 (p = 0.041), and -1.34 (p = 0.065), respectively, indicating a move towards baseline (**Table 2.3**).

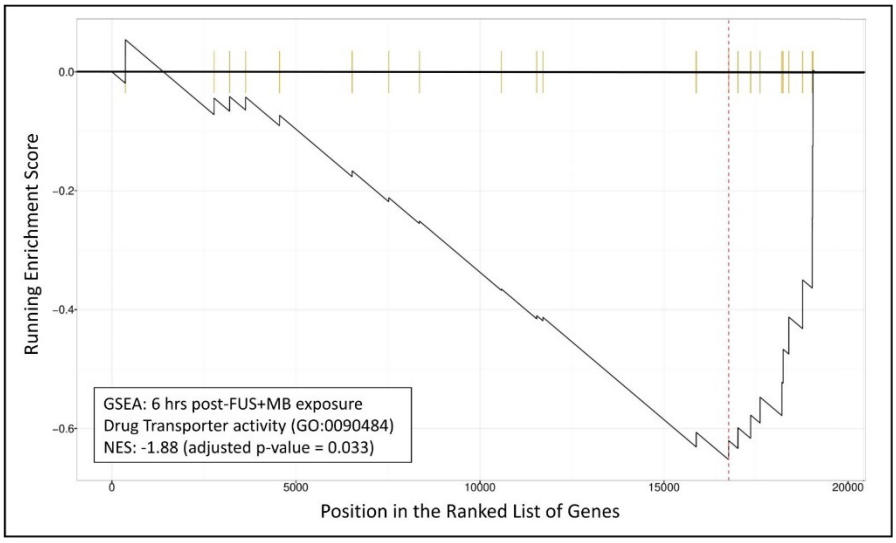

Figure 2.5. Geneset Enrichment Analysis for *Drug Transporter Activity* 6 hrs Post-FUS+MB Exposure. Running enrichment score for the GO term *drug transporter activity* (GO:0090484) is depicted in relation to a list of genes ranked by log2 fold change at 6 hrs post-FUS+MB exposure. Each vertical yellow line indicates the location of a gene in the ranked list that is associated with this GO term. NES = −1.85 (adjusted p = 0.033). GO terms are comprised of a list of genes whose functions are related. The non-random distribution of these genes within the ranked list can be interpreted as a suppression of drug transporter activity.

An examination of individual transcript expression and GSEA would suggest that actions of several BBB transporters in the dorsal hippocampus may be reduced 6 hrs following sonication, with a return to, or move towards, baseline by 24 hrs; however, GSEA indicates that BBB ion transporter activity at 24 hrs post-FUS+MBs may become suppressed. GO terms related to ion transporter activity which displayed significant suppression include, *potassium ion transmembrane transporter activity* (GO:0015079), *calcium ion transmembrane transporter activity* (GO:0015085), *sodium ion transmembrane transporter activity* (GO:0015081), *chloride transmembrane transporter activity* (GO:0015108), and *ion transmembrane transporter activity* (GO:0015075), with NESs of -2.44 (p = 0.020), -2.37 (p = 0.020), -1.93 (p = 0.020), -1.93 (p = 0.020), and -2.14 (p = 0.022), respectively (**Table 2.3**).

2.3.6. Angiogenesis-Related Genes

At 6 hrs post-FUS+MB exposure, there was a significant increase in the differential expression of several genes related to angiogenesis, including *Serpine1*, *Ccl2*, *Egr3*, and *Mmp9*, with log2 fold changes of 2.37 (p = 0.036), 4.73 (p < 0.001), 1.23 (p = 0.005), and 2.53 (p = 0.006), respectively, compared to the contralateral hemisphere. At the later time point, *Itgb2*, *Ccr5*, *Lcn2*, *Lgals3*, and *Ccr2* displayed significant increases in differential expression, with log2 fold changes of 1.38 (p = 0.034), 1.15 (p = 0.036), 2.91 (p = 0.003), 2.29 (p = 0.004), and 4.12 (p = 0.023), respectively, compared to the contralateral hemisphere (**Table 2.2**).

GSEA of differential microvascular gene expression between sonicated and contralateral dorsal hippocampi indicated that angiogenesis-related pathways may be activated by FUS+MB exposure. GO terms, such as *positive regulation of angiogenesis* (GO:0045766; **Figure 2.6**), *positive regulation of vasculature development* (GO:1904018), *blood vessel morphogenesis* (GO:0048514), and *positive regulation of blood vessel endothelial cell migration* (GO:0043536), display NESs of 2.48 (p = 0.009), 2.48 (p = 0.009), 2.34 (p = 0.009), and 1.95 (p = 0.009), respectively at 24 hrs post-FUS+MBs. At 6 hrs following FUS+MB exposure, NES for *vascular endothelial growth factor production* (GO:0010573) was 2.29 (p = 0.015; **Table 2.3**).

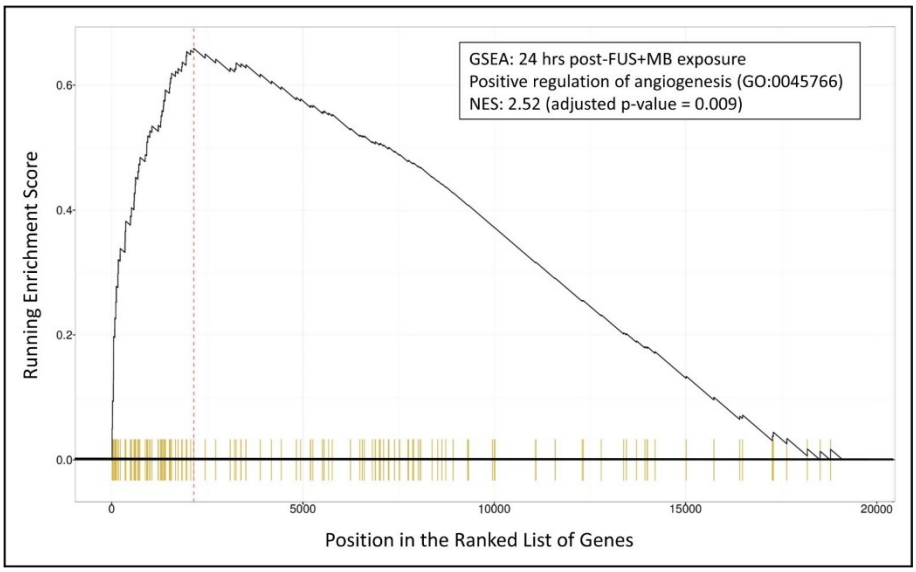

Figure 2.6. Geneset Enrichment Analysis for *Positive regulation of Angiogenesis* 24 hrs Post-FUS+MB Exposure. Running enrichment score for the GO term *positive regulation of angiogenesis* (GO:0045766) is depicted in relation to a list of genes ranked by log2 fold change at 24 hrs post-FUS+MB exposure. Each vertical yellow line indicates the location of a gene in the ranked list that is associated with this GO term. NES = 2.48 (adjusted p = 0.009). GO terms are comprised of a list of genes whose functions are related. The non-random distribution of these genes within this ranked list can be interpreted as an activation of angiogenic processes.

ORA also gives some indication that angiogenic processes are upregulated following FUS+MB exposure. At 6 hrs post-sonication, there was a significant over-representation of differentially expressed genes that are part of the following GO terms, *regulation of angiogenesis* (GO:0045765; $p < 0.001$), *positive regulation of vasculature development* (GO:1904018; $p < 0.001$), *regulation of vascular endothelial growth factor production* (GO:0010574; $p < 0.001$), *blood vessel morphogenesis* (GO:0048514; $p < 0.001$), and *vascular endothelial growth factor production* (GO:0010573; $p < 0.001$). At 24 hrs following sonication, there was a significant over-representation of differentially expressed genes that are part of the *positive regulation of vasculature development* (GO:1904018; $p < 0.001$) and *positive regulation of angiogenesis* (GO:0045766; $p < 0.001$) GO terms.

2.3.7. Correlation Between Microarray Analysis and qRT-PCR Results

Differential expression of nine transcripts, shown to be up- or downregulated at one or both of the post-FUS+MB time points by microarray analysis were assessed using qRT-PCR. Genes of interest included, *Abcb1a*, *Ccl2*, *Cd74*, *Gfap*, *Itgb2*, *Lcn2*, *Serpine1*, and *Slc22a6*. A strong linear correlation ($r^2 = 0.96$) was found for log2 fold changes between analysis methods (**Appendix Table 2.3**), adding confidence to the conclusions drawn from the microarray data. Regression analysis of differential expression measured

using microarray and qRT-PCR suggest that the microarray analysis may be a conservative estimate of differential gene expression, with a slope of 0.66 (log2 fold change measured by qRT-PCR vs log2 fold change measured by microarray).

2.4. Discussion

The work described in *Chapter 2* represents the first in-depth exploration of how brain microvasculature responds at a transcriptional level in the acute stages following FUS+MB exposure. An assessment of gene expression changes and bioinformatic analysis of microarray data suggests that an acute inflammatory response in hippocampal microvasculature follows sonication. This response may be related to both the stresses exerted on vascular ECs by oscillating MBs and the subsequent extravasation of circulating proteins, triggering an increase in the transcription of proinflammatory cytokines. At 6 hrs post-sonication there were significant differences detected in the transcription of *Ccl2*, *Ccl3*, *Ccl7*, *Cxcl1*, *Cxcl11*, *Il1b*, and *Il6* compared to microvasculature in the contralateral hemisphere. Additionally, the expression of several other indicators of inflammation were elevated at this early time point. If the observed changes in gene expression are in fact indicative of increased vascular EC activation and release of proinflammatory cytokines and chemokines, this would likely act to promote the infiltration of leukocytes, as indicated by GSEA. Importantly, this inflammatory response seems to be dampened by 24 hrs post-FUS+MBs, with non-significant changes in the differential expression of *Ccl2*, *Ccl3*, *Ccl7*, *Cxcl1*, *Cxcl11*, *Il1b*, and *Il6*. Additionally, increased expression of *Sele*, indicative of EC activation, returned to baseline by 24 hrs; expression of *Vcam1* and *Icam1* are not significantly elevated at either time point.

In line with previous literature showing increased immunodetection at four days following sonication [172], differential expression of *Gfap* was detected at 24 hrs post-FUS+MB exposure, indicative of astrocyte activation. While chronic gliosis, a hallmark of many CNS pathologies, can lead to inhibitory effects on neuroplasticity and regeneration, acute astrocyte activation can play a critical role in neuroprotection and the regulation of homeostasis in acute ischemia and various types of stress [258]. The astrocyte activation in endfeet surrounding microvasculature suggested by this work may play an important role in restoring the extracellular environment following sonication. Activation of astrocytes following FUS+MB exposure may be related to increased gene expression of cytokines by ECs, as well as from astrocytes and other cells of the parenchyma [281].

While chronic inflammation in the brain has detrimental effects, inducing necrosis, apoptosis, and pyroptosis [282], acute inflammation can induce a wide spectrum of changes, some of which are essential for tissue repair. The release of chemokine ligand-2 (CCL2) and CCL3, as well as signalling through chemokine receptor-2 and -5 can promote the migration, proliferation, differentiation, and survival of neural progenitor cells [283]. A transient and controlled level of neuroinflammation can also promote myelin debris clearance, myelin repair [284], angiogenesis [285], and Aβ plaque clearance [286]. When inflammation becomes chronic, however, the production of TNFα, IL6, and reactive oxygen species within the CNS can act to suppress neurogenesis and leads to apoptosis and neurodegenerative processes [283].

Increased gene expression of *Alox5ap* 24 hrs following FUS+MB exposure may contribute to the resolution of inflammation by affecting the activity of arachidonate 5-lipoxygenase and subsequently the production of lipoxins and resolvins [287]. Additionally, increased expression of tissue inhibitor matrix metalloproteinase-1 (TIMP1) has been found to attenuate inflammation in endothelium [288]; LYZ2 has been implicated in reduction of IL1β, IL6, TNFα, and CCL2 production in human ECs [289]; SLAMF7 has been shown to inhibit the production of proinflammatory cytokines [290]. The upregulation of *Timp1*, *Lyz2*, *Slamf7*, and *Alox5ap* 24 hrs following FUS+MB exposure (**Table 2.2**) may contribute to a reduction in cytokine/chemokine gene expression, reduce EC activation, and mediate a resolution of inflammation.

Evidence of acute inflammation observed following FUS+MB exposure may be the driving force for many of the bioeffects previously reported, as well as some suggested from the results presented here. Hippocampal neurogenesis has previously been observed following sonication [230,231], an effect that requires an increase in BBB permeability [231]. While neurogenesis can be induced by a wide variety of stimuli, the production of specific factors related to acute inflammation, such as CCL2, CCL3, and TNFα, have been demonstrated to promote migration, proliferation, differentiation and survival of neural progenitor cells [283]. There is, however, a point at which inflammation has deleterious effects on neurogenesis. Chronic production and release of proinflammatory cytokines, like IL6, IL1β, TNFα, and IFNɣ, suppress proliferation and survival of neural progenitor cells [283].

Apart from inflammation-related changes, the reduction in ABC and SLC transporter gene expression 6 hrs following sonication, as well as the negative enrichment scores for several BBB transport-related GO terms, suggest that FUS+MB exposure may induce a reduction in BBB efflux. Previous work by Cho *et al.* has shown that FUS+MB exposure induces a downregulation in immunodetection of MDR1 24 hrs post-

sonication [291]. Results presented here are consistent with this finding, as there was a significant reduction in *Abcb1a* gene expression (I.e. the gene for MDR1) 6 hrs following FUS+MB exposure. Due to the well characterized role of MDR1 in drug efflux and its contributions to drug resistance [292], a reduction in its expression could act to increase the efficiency of FUS+MB-mediated drug delivery. Additionally, decreased gene expression of several members of the SLC family, including *Slc22a6* and *Slc22a8*, were detected at 6 hrs following FUS+MB exposure. These genes code for organic anion transport-1 and -3, which have been implicated in the transport of a variety of therapeutic agents, including antiretroviral drugs [293] and chemotherapeutics [294–296], amongst others [297,298]. While organic anion transport-1 and -3 have primarily been characterized as *uptake transporters*, several reports describe their roles in drug efflux [299–301]. If FUS+MB exposure induces a transient downregulation in the expression of drug efflux transporters in the BBB, this could act to increase the effectiveness of FUS+MB-mediated therapeutic agent delivery. This would also be an important consideration when developing dosing strategies that avoid toxicity following sonication.

Inflammation has previously been reported to induce a rapid reduction in *Abcb1a* gene expression in the rat brain, peaking at 6 hrs following the delivery of an inflammatory stimulus [301,302]. At the protein level, human immunodeficiency virus-1-associated brain inflammation has been shown to induce a downregulation in MDR1 expression both *in vitro*, in primary cultures of rat astrocytes [303], and *in vivo*, in rats [304]. Pro-inflammatory cytokines have also been shown to reduce protein expression and functionality of MDR1 in the BBB [305]. Likewise, lipopolysaccharide-induced inflammation has been shown to reduce the expression of *Slc22a6* and *Slc22a8* in rat liver starting at 6 hrs following administration [306]. Given the concurrent increase and decrease in pro-inflammatory cytokine and transporter gene expression, respectively, at 6 hrs following sonication reported here, it is plausible that there may be a causal link between the two observations [303,307]. While these transporters are largely expressed in brain microvascular ECs, changes in their expression have been reported in astrocytes and other parenchymal cells following the induction of seizures [308,309] or in human immunodeficiency virus-1 infection of the brain [303,304]. Thus, it is possible the changes detected in the current study are influenced by gene expression changes in cells beyond ECs.

The changes in microvascular gene expression observed following sonication may also indicate an increase in early angiogenic processes, as evidenced by increased expression of several angiogenesis-related genes, including *Timp1*, *Egr3*, *Lgals3*, *Mmp9*, and *Itgb2*, as well as positive enrichment scores for several

angiogenesis-related GO terms. FUS+MB exposure has previously been shown to enhance angiogenesis in skeletal muscle, with an approximately 65% increase in arterioles per muscle fiber reported at 7 and 14 days following sonication [310]. Similarly, microarray analysis of differential gene expression in ECs subjected to shear stress suggests that angiogenic pathways are upregulated after 24 hrs [311]. Given the well-established link between angiogenesis and inflammatory mediators [312], as well as the results presented here, further investigation into the effects of FUS+MB exposure on blood vessel density and cerebral blood flow are warranted. If FUS+MB-mediated angiogenesis occurs in the brain, this could have major implications for patients recovering from stroke or traumatic brain injury [313] by providing a means to encourage the repair and regeneration of injured brain tissue and promote functional recovery.

In addition to increasing the permeability of the BBB, FUS+MB exposure has been reported to generate a variety of other bioeffects in the CNS. The transcriptome data presented here may provide insight into the factors which drive these effects. Besides the potential influence on neurogenesis, angiogenesis, and transporter expression discussed above, FUS+MB-induced inflammation could plausibly contribute to the increased endocytosis [205], reduced immunoreactivity of tight junction proteins [206], and diminished Aβ plaque load [172,136,174] previously observed.

Electron microscopy evidence from Sheikov *et al.* demonstrated increases in the number of endocytotic vesicles in vascular ECs following FUS+MB exposure in rabbits [205]. This observation was supported at the protein expression level with increases in the immunodetection of caveolin-1 post-sonication [207]. The rate of transcytosis across cerebrovascular ECs has previously been shown to be influenced by proinflammatory cytokines [314], thus, it is possible that the changes in proinflammatory cytokine gene expression reported here may be a contributing factor to the increased EC endocytosis previously observed following FUS+MB exposure. Likewise, Sheikov *et al.* have also shown that immunodetection of tight junction proteins in inter-endothelial clefts are reduced up to 4 hrs following FUS+MB exposure [206]. This effect may also be influenced by increased proinflammatory cytokine gene expression, as CCL2 has been shown to mediate internalization of occludin and claudin-5 in brain ECs [315].

Notably, FUS+MB exposure has been shown to reduce Aβ plaque load and improve performance in a variety of behavioural tasks in two mouse models of AD [172,136,174]. While there is ample evidence implicating neuroinflammation in the pathogenesis of AD [316], it is possible that induction of a transient inflammatory response in brain microvasculature following sonication could paradoxically contribute to

an increase in plaque clearance. This could be achieved by the infiltration and activation of immune cells, such as chemokine receptor-2-positive mononuclear phagocytes [317] and LY6Clo monocytes [318], that act to clear Aβ deposits. While much focus has been on reducing neuroinflammation to attenuate AD progression, Guillot-Sestier *et al.* have proposed that a rebalancing of innate immunity in the brain through the inhibition of key anti-inflammatory cytokines may encourage a reduction in AD pathology [319]. FUS+MB exposure may act to shift innate immunity in a similar way, contributing to the observed improvements in AD-like pathology in mouse models.

2.4.1. Limitations

As with any assessment of differential gene expression, there must be a level of caution taken when inferring conclusions regarding the functional outcomes of these changes since protein expression may not follow the same trend. However, the inclusion of GSEA may lessen this risk, as examining expression changes in groups of related genes acts to distribute the burden of conclusions across the entire genome rather than changes in single genes [320]. Moreover, while the cellular composition of samples used for microarray analysis can be characterized as *enriched* microvascular samples, they contain transcriptional markers of other cell types. Thus, some of the reported changes in gene expression may be influenced by cell types beyond ECs, especially astrocytes. Due to the unbiased method of collection, however, the cellular composition of samples should be consistent across groups. Lastly, this study focused on the characterization of gene expression changes in microvasculature, as this is the site of increased permeability following sonication and experiences the largest magnitude of stresses from oscillating MBs. Thus, the results presented here can not necessarily be extended to other tissue types within the brain or outside the CNS.

An assessment of gene expression changes can provide insight into cellular responses; however, the exploratory nature of this work necessitates further investigation. Among the most pertinent areas requiring research is determining the time course of the inflammatory response. The gene expression profile in microvasculature 24 hrs following sonication suggests that the inflammatory response is dampened at this time point; however, given the acute nature of this investigation, a biphasic response cannot be ruled out. In addition to investigating the long-term impact of FUS+MB exposure, it will be important to look at how repeated sonications impact gene expression and functional changes in brain microvasculature. While previous long-term survival and behavioural studies would suggest that there are

no overt long-term effects of FUS+MB exposure [321], a full characterization of changes induced by any medical intervention is important to assess risk. Future work should also focus on determining if FUS+MB exposure induces angiogenesis in the CNS, alters BBB transporter function, and whether the bioeffects reported to follow sonication are driven by the production of pro-inflammatory cytokines and chemokines.

2.4.2. Conclusion

The challenge of drug delivery across the BBB represents a substantial obstacle to the treatment of many neurological diseases. FUS+MB exposure has demonstrated great promise as a method to transiently enhance BBB permeability in a targeted manner. While the safety profile of this technique appears sufficient to aid in the treatment of severe neuropathologies, like glioblastoma, further work is needed to fully characterize the long-term effects of repeated sonications in brain tissue with less overt dysfunction. Additionally, the opportunity to explore novel applications related to FUS+MB exposure remains, as the spectrum of its utility may yet to be fully identified.

Chapter 3

Inflammatory Response Following Focused Ultrasound and Microbubble Exposure is Influenced by Microbubble Dose

3.1. Introduction

A large body of literature supports the notion that FUS+MB-mediated BBB permeability enhancement *can be achieved* without evidence of overt tissue damage; however, the safety profile of this drug delivery technique is strongly influenced by exposure conditions. The wide range of transmit frequencies, PNPs, MB doses, MB compositions, acoustic feedback control methods, etc., employed in preclinical FUS+MB research has contributed to conflicting conclusions regarding risk.

Kovacs *et al.* reported the rapid development of a damage-associated molecular pattern following FUS+MB exposure, leading to a severe inflammatory response in brain parenchyma [208]. It is noteworthy, however, that the MB dose administered in this study was approximately ten times the dose used for clinical imaging [120] (0.1 ml Optison/rat; ~0.5 ml/kg, based on the reported age and sex of rats). This dose of Optison MBs has previously been shown to induce significant RBC extravasation at a fixed PNP for which no overt tissue damage was observed at lower MB doses [122]. Thus, it is hypothesized that the FUS+MB parameters used by Kovacs *et al.* contributed to an exaggerated inflammatory response, inconsistent with that seen when optimized parameters are employed.

Parts of this chapter are adapted from: McMahon D, Hynynen K. Acute inflammatory response following increased blood-brain barrier permeability induced by focused ultrasound is dependent on microbubble dose. *Theranostics*. 2017. 7(16):3989-4000. Used with permission as part of publication agreement.

Chapter 3 explores the impact of FUS+MB exposure on the expression of genes related to the nuclear factor-κB (NFκB) signalling pathway, as well as whether MB dose can influence this response. Additionally, this work investigates how MB dose influences the function of an acoustic feedback control algorithm that calibrates PNP based on ultraharmonic emissions. More specifically, *Chapter 3* describes a study in which differential expression of NFκB signalling pathway-related genes were assessed in rats at 6 hrs and 4 days following FUS+MB-mediated BBB permeability enhancement. Three sonication schemes were tested: (1) a clinical imaging dose of MBs + PNP controlled with acoustic feedback, (2) 10x clinical imaging dose of MBs + fixed PNP of 290 kPa (designed to approximate parameters used in Kovacs *et al.* [208]), and (3) 10x clinical imaging dose of MBs + PNP controlled with acoustic feedback. CE-T1w, T2w, and T2*w imaging were performed to assess BBB permeability, edema, and hemorrhage, respectively.

3.2. Materials and Methods

3.2.1. Animals

Male Sprague Dawley rats (n = 8), weighing 270-340 g on the day of sonication, were used in this study (Taconic Biosciences, Germantown, NY, USA). Animals were housed in the *Sunnybrook Research Institute* animal facility (Toronto, ON, Canada) and had access to food and water *ad libitum*. Prior to sonication, animals were randomly assigned to one of two groups, sacrificed at 6 hrs or 4 days post-FUS+MB exposure. All animal procedures were approved by the *Animal Care Committee* at *Sunnybrook Research Institute* and are in accordance with the guidelines established by the *Canadian Council on Animal Care*.

3.2.2. MRI-Guided FUS+MB Exposure

Animal preparation and FUS+MB exposures were conducted as described in *Chapter 2*, with the following exceptions. Anesthesia was maintained for the duration of sonication and imaging with 1.5-2% isoflurane and medical air (1 L/min) due to the impact of 100% oxygen as a carrier gas on MB circulation half-life [125,322].

Three locations were sonicated per animal, each with a different sonication scheme (plus a non-sonicated control region). The three sonications were separated in time by approximately 15 min to allow MBs to clear from circulation [120,323]. FUS+MB parameters used for each sonication scheme are listed in **Table 3.1**. To mitigate the effects of regional variance within the brain, sonication schemes were rotated around the

4 target regions (**Figure 3.1A**) within each group. At the commencement of sonication, MBs (Definity, Lantheus Medical Imaging, North Billerica, MA, USA), were administered via tail vein catheter using an infusion pump (0.12 mL/min).

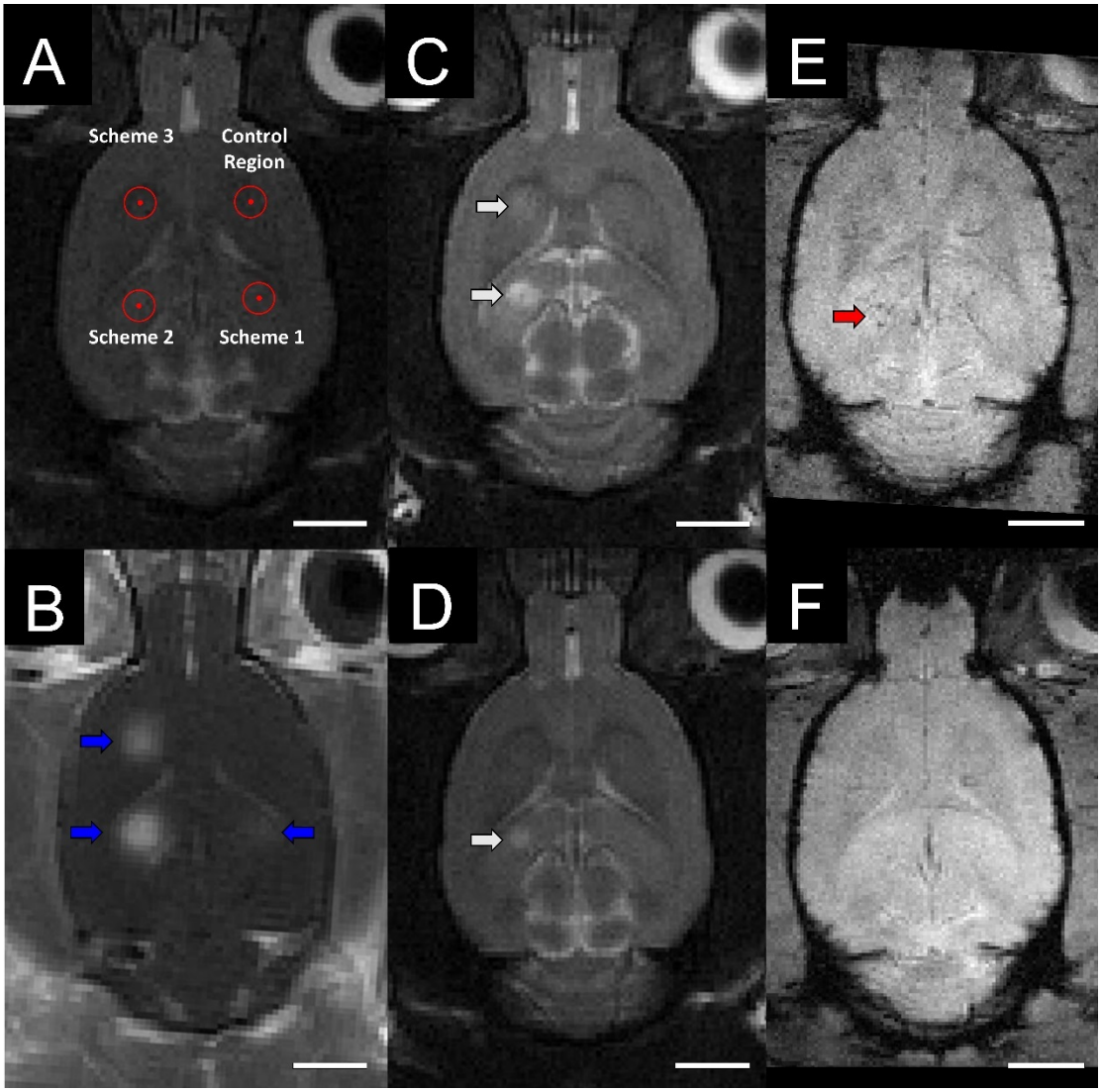

Figure 3.1. MRI Targeting and Post-FUS+MB Assessment. (A) Targets for sonication were chosen from T2w images. To reduce the impact of regional variance, sonication schemes were rotated around the 4 target regions within each group. (B) Contrast-enhanced T1w images illustrate regions of BBB permeability enhancement (blue arrows) in the sonicated locations. Four hours (C) and four days (D) following sonication, edema (white arrows) was evident in T2w images at several locations sonicated with schemes 2 and 3. T2*w imaging was also performed at 4 h (E) and 4 days (F) post-FUS+MB exposure. Evidence of hemorrhage (red arrow) was observed in one animal at a target sonicated with scheme 2. Scale bars = 4 mm.

Table 3.1. FUS+MB parameters used for each sonication scheme

Scheme	MB Dose (µl Definity/kg)	PNP (kPa)	Burst Repetition Frequency (Hz)	Burst Length (ms)	Sonication Duration (s)
1	10	acoustic controller used	1	10	120
2	100	290	1	10	120
3	100	acoustic controller used	1	10	120

For sonication schemes 1 and 3, the acoustic feedback control algorithm described in *Chapter 2* was used. Sonication scheme 2 employed a fixed PNP of 290 kPa, designed to replicate parameters used by Kovacs *et al.* [208]. Animals in groups 1 (n = 4) and 2 (n = 4) were sacrificed at 6 hrs and 4 days post-sonication, respectively, by transcardial perfusion with ice-cold saline. Brains were snap frozen in liquid nitrogen and stored at -80 °C until processing.

3.2.3. MRI Evaluation

All MR experiments were conducted on a 7T horizontal bore Avance BioSpec 70/30 scanner (Bruker BioSpin, Ettlingen, Germany) with a 20 cm inner diameter gradient insert coil with maximum gradient amplitude of 668 mT/m (Bruker BioSpin, Ettlingen, Germany). Images were acquired using an 8 cm inner diameter volume coil for transmit and receive. Immediately prior to each sonication, a gadolinium-based contrast agent (Gadovist, Schering AG, Berlin, Germany) was injected into venous circulation via tail vein catheter. By delivering the contrast agent prior to FUS+MB exposure, changes in BBB permeability which occur during sonication are also assessed. For the duration between each sonication, approximately 15 min, 3-4 CE-T1w scans were performed. BBB permeability enhancement was assessed for each sonication scheme by calculating the ratio of mean voxel intensity at the focus to the non-sonicated control region. To assess edema and hemorrhage, T2w and T2*w scans, respectively, were performed at 4 hrs post-FUS for group 1 and at both 4 hrs and 4 days post-FUS for group 2. MRI parameters can be found in **Table 3.2**.

Table 3.2. MRI parameters

Parameters	T1w	T2w	T2*w
Sequence type	RARE	RARE	GEFC
Echo time (ms)	10	70	19
Repetition time (ms)	500	4000	1043.9
RARE factor	2	10	NA
Averages	3	4	4
Field of view (mm)	50 x 50	50 x 50	30 x 30
Matrix	150 x 150	200 x 200	150 x 150
Slice thickness (mm)	1.5	1.5	1.0

3.2.4. Sample Collection and Preparation

Brains were horizontally cryosectioned (10 µm thick) and freeze-mounted onto nuclease and nucleic acid free slides (MembraneSlide NF 1.0 PEN, Zeiss, Göttingen, Germany). Sections were collected every 250 µm throughout the thickens of the brain. Mounted sections were stored up to 3 days at -80°C before LCM. Immediately prior to LCM, sections were briefly dehydrated in ethanol (ice-cold 95% for 30 s, ice-cold 100% for 30 s, and room temperature 100% for 30 s) and cleared in xylenes (twice at room temperature for 30 s). Sections were allowed to dry for 5 min prior to LCM.

Tissue was collected by LCM from sections at the focal plane of FUS targeting using a PALM Microbeam system (Zeiss, Göttingen, Germany). CE-T1w images were used as a guide for tissue selection. Approximately 30 000 000 μm^3 of tissue was collected from each targeted location (plus a non-sonicated control region) into microcentrifuge tubes (AdhesiveCap 500, Zeiss, Göttingen, Germany), yielding 9-15 ng of total RNA per sample. Collection times were limited to 1 hr to minimize the degree of RNA degradation.

RNA was isolated using the PicoPure kit (Life Technologies Inc., Waltham, MA, USA) in accordance with manufacturer's instructions. Samples were treated with DNase (Qiagen, Hilden, Germany). RNA concentration and quality was assessed using the 2100 Bioanalyzer system with RNA 6000 Pico Kit (Agilent, Santa Clara, CA, USA).

3.2.5. Quantitative Real Time Polymerase Chain Reaction Array Analysis

Synthesis and amplification of cDNA was performed using the RT^2 PreAMP cDNA Synthesis Kit (Qiagen, Hilden, Germany). RT^2 SYBR Green qPCR Master Mix (Qiagen, Hilden, Germany) was used in conjunction with CFX96 Touch Real-Time PCR Detection System (Bio-Rad Laboratories, Inc., Hercules, CA, USA) for quantitative real-time polymerase chain reaction (qRT-PCR). The expression of 84 genes related to inflammatory response and apoptosis were screened with RT2 Profiler PCR Array Rat NFκB signalling Pathway (Qiagen, Hilden, Germany). Relative gene expression of each transcript was determined by normalizing against the mean Ct value of 5 housekeeping genes (Actb, B2m, Hprt1, Ldha, and Rplp1), using the ΔΔCt method. Within each animal, log2 fold change for each sonication scheme was calculated relative to the non-sonicated control region.

3.2.6. Histology

Sections adjacent to those collected for LCM were freeze-mounted onto charges glass slides (Xtra, Leica Microsystems GmbH, Wetzlar, Germany) and stored at -80°C until processing. H&E staining was used to broadly assess tissue health in each brain from groups 1 and 2. Tissue sections from the focal plane of FUS were imaged with a 20x objective (Axios Imager 2, Zeiss, Göttingen, Germany); post-FUS+MB CE-T1w images were used to locate targeted areas.

3.2.7. Statistics

The difference in mean PNP between schemes 1 and 3 was assessed by paired, two-tailed, Student's t-test. Relative contrast enhancement between sonication schemes was assessed for statistical significance with paired, two-tailed, Student's t-tests with FDR correction for multiple comparisons. Relative gene expression at each sonication target was compared to the non-sonicated control region within each animal with one-way, repeated measures ANOVA and post-hoc, paired, two-tailed, Student's t-tests with FDR correction for multiple comparisons. All log2 fold changes are relative to the control region in each animal. Least-squares linear regression was used to assess the relationship between log2 fold changes in gene expression and mean relative voxel intensity at each target (relative to control region) in the final T1w MR image for each animal. For all analyses, a p-value of 0.05 was used as the threshold for statistical significance. Unless otherwise specified, variance is expressed as standard deviation of the mean.

3.3. Results

3.3.1. Peak Negative Pressure

For sonication schemes 1 and 3, PNP was calibrated based on acoustic emissions at $1.5f$ or $2.5f$. Once the ratio of signal to baseline at either of these frequencies passed 3.5, the PNP was dropped by 50% and maintained at this level for the remainder of sonication. While the MB dose for schemes 1 and 3 differed by an order of magnitude (10 µl/kg vs 100 µl/kg), the PNP following a software-triggered drop in pressure was not significantly different between these schemes (scheme 1: 192 kPa ± 20 kPa; scheme 3: 201 kPa ± 15 kPa; p = 0.46; **Figure 3.2A**). PNP for scheme 2 was set at 290 kPa to approximate parameters used by Kovacs *et al.* [208].

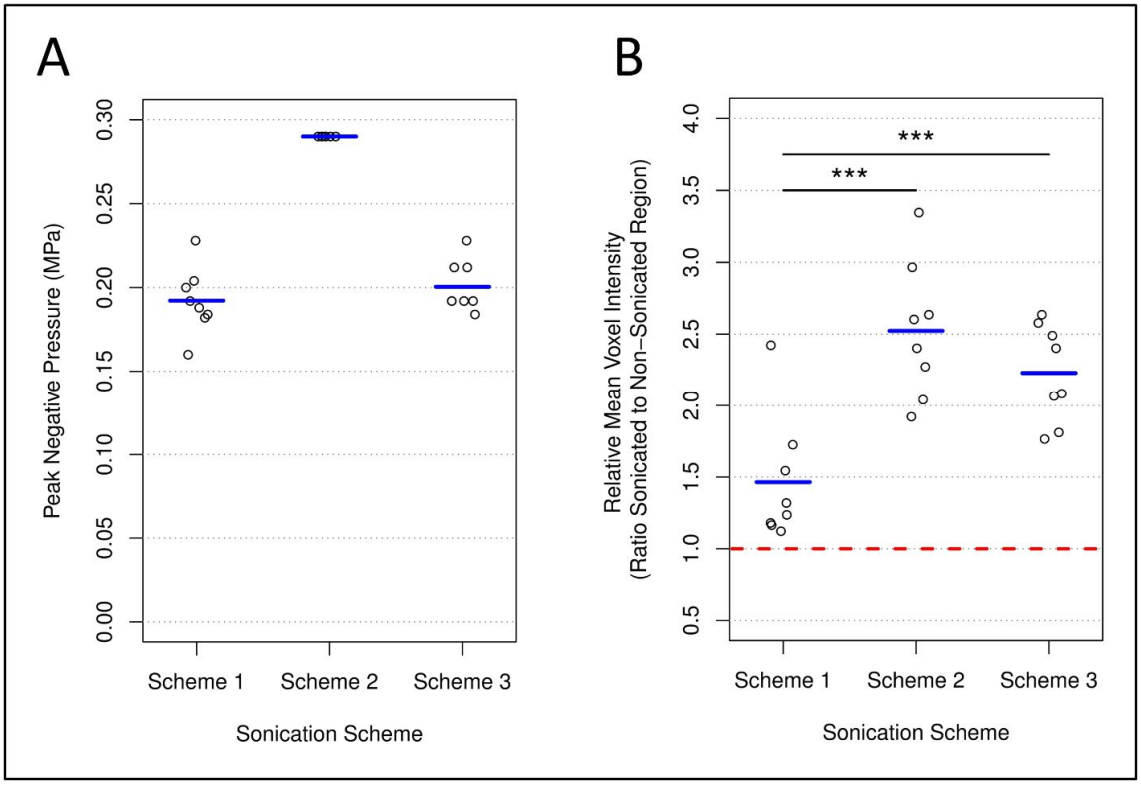

Figure 3.2. Peak Negative Pressure and Post-FUS+MB Contrast Enhancement for Each Sonication Scheme. PNP for schemes 1 and 3 were calibrated based on acoustic emissions, as described in *Section 2.2.2*. (A) Mean PNP following a software-triggered pressure drop were 192 kPa ± 20 kPa and 201 kPa ± 15 kPa (p = 0.46) for groups of animals sonicated with schemes 1 and 3, respectively. (B) Relative contrast enhancement was assessed by calculating the ratio of mean voxel intensity at each sonicated target to the non-sonicated control areas in each animal. Targets sonicated with schemes 2 and 3 both resulted in a significantly greater degree of relative enhancement than scheme 1 (ratios of 1.46 ± 0.44, 2.52 ± 0.47, and 2.23 ± 0.34 relative to the control region for schemes 1, 2, and 3, respectively). *** indicates $p < 0.01$; n = 8 targets for each sonication scheme in 8 animals.

3.3.2. Post-FUS+MB Contrast Enhancement

CE-T1w images were used to assess BBB permeability enhancement for each sonication scheme by calculating the ratio of mean voxel intensity at each sonicated target to the non-sonicated control area in each animal (**Figure 3.2B**). Targets sonicated with scheme 2 displayed the greatest mean relative contrast enhancement (mean ratio of 2.52 ± 0.47 relative to non-sonicated control region), significantly greater than targets sonicated with scheme 1 (mean ratio of 1.46 ± 0.44 relative to non-sonicated control region; $p = 0.002$). While schemes 1 and 3 both utilized acoustic emissions to control PNP, targets sonicated with scheme 3 displayed significantly greater mean relative enhancement (mean ratios of 2.23 ± 0.34 and 1.46 ± 0.44 relative to non-sonicated control region for schemes 1 and 3, respectively; $p = 0.003$). Given the similarities in mean PNP for schemes 1 and 3, these results suggest that for a transmit frequency of 551 kHz, MB dose has a significant effect on the degree of BBB permeability enhancement.

3.3.3. MRI Indications of Edema and Hemorrhage

T2w and T2*w images were acquired for all animals at 4 hrs post-FUS+MB exposure and for group 2 animals at 4 days post-FUS+MB exposure (**Figure 3.1**). Hyperintensities in T2w images, indicative of edema, were evident in 0/8, 6/8, and 4/8 animals for schemes 1, 2, and 3, respectively, at 4 hrs following sonication. One animal displayed evidence of edema at 4 days post-FUS+MB exposure, at a location sonicated with scheme 2 (**Figure 3.1D**). Microhemorrhage, as indicated by hypointense regions in T2*w images, was observed in one animal at 4 hrs and no animals at 4 days following sonication. The one region of microhemorrhage was observed at a target sonicated with scheme 2 and was the same region that displayed edema 4 days post-FUS+MB exposure (**Figure 3.1E**).

3.3.4. Inflammation-Related Gene Expression

Overall shifts in gene expression, relative to non-sonicated control regions in each animal, are depicted for each sonication scheme and group in **Figure 3.3**. At 6 hrs following FUS+MB exposure, schemes 2 and 3 resulted in a marked skew towards increased expression of NFκB signalling pathway-related genes, with the relative levels of several transcripts significantly upregulated. This pattern was also seen at 4 days in locations sonicated with these schemes, albeit to a less dramatic extent. Conversely, for scheme 1, at both 6 hrs and 4 days post-FUS+MB exposure, differences in gene expression relative to the control regions were less evident; differential expression is evenly distributed around 0 in the x direction (log2 fold

change) and below the threshold for significance ($p < 0.05$ and log2 fold change greater or less than 1.0 or −1.0, respectively). It should be noted, however, that the low number of animals used in this study and the whole tissue assessment of gene expression are conducive only to the detection of large (I.e. log2FC of at least ± 2.12), non-specific changes. When effect size alone is considered, *Bcl10*, *Birc3*, *Ccl2*, *Egr1*, *Icam1*, *Ilb1 and Tnf*, all displayed a log2 fold change of at least 0.58 (corresponding to a 50% increase in relative expression) at targets sonicated with scheme 1, relative to the non-sonicated control region (**Table 3.3**).

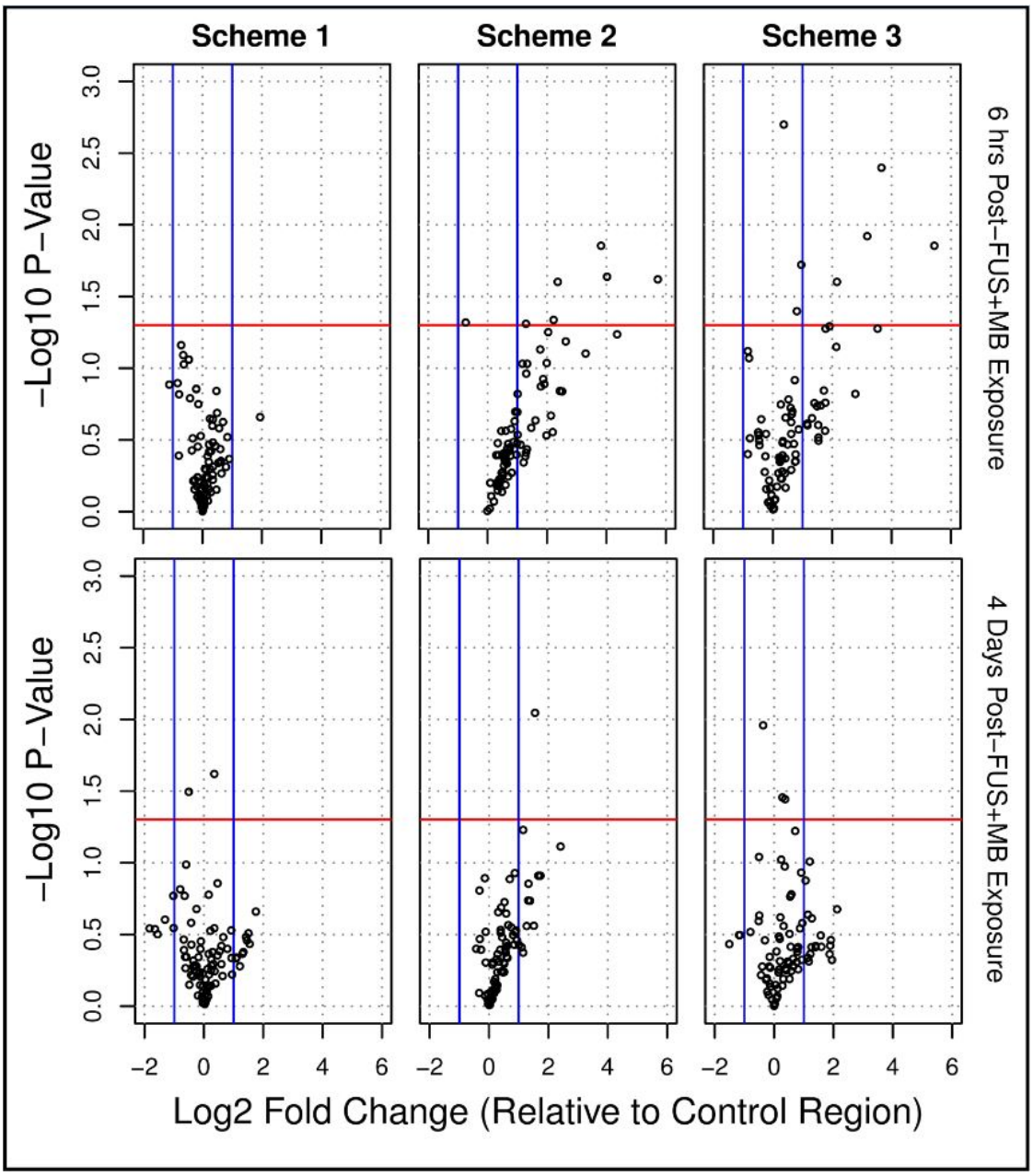

Figure 3.3. Volcano Plots of Differential Gene Expression. Relative gene expression at targeted locations was compared to the non-sonicated control region at 6 hrs and 4 days post-FUS+MB exposure. A positive log2 fold change indicates increased relative expression in the sonicated location compared to control region. Blue vertical lines indicate a log2 fold change of 1.0 or −1.0. Red horizontal lines indicate a -log10 p-value of 1.30, corresponding to a p-value of 0.05. Schemes 2 and 3 resulted in a marked skew towards increased expression of NFκB signaling pathway genes at 6 h post-FUS+MB exposure. n = 4 animals for each time point.

Genes whose relative expression at 6 hrs post-FUS+MB exposure for any sonication scheme was at least 50% greater than the non-sonicated control regions are listed in **Table 3.3**. Amongst the genes exhibiting significant differences in expression for both schemes 2 and 3 include *Birc3*, *Ccl2*, and *Tnf*; all have established roles in inflammatory signalling and apoptosis.

Table 3.3: Genes displaying mean increases of greater than 50% in expression relative to control regions 6 hrs post-FUS+MB exposure for at least one sonication scheme

Gene Names	Log2FC: Scheme 1	P-Value: Scheme 1	Log2FC: Scheme 2	P-Value: Scheme 2	Log2FC: Scheme 3	P-Value: Scheme 3
Ccl2	1.94	0.219	**5.73**	**0.024**	**5.44**	**0.014**
Il1b	0.6	0.366	4.36	0.058	3.53	0.053
Tnf	0.84	0.302	**4.02**	**0.023**	**3.18**	**0.012**
Birc3	0.6	0.45	**3.82**	**0.014**	**3.66**	**0.004**
Timp1	0.21	0.695	3.3	0.079	2.78	0.151
Icam1	0.69	0.237	2.63	0.065	2.14	0.071
Hmox1	-0.12	0.752	2.51	0.145	1.54	0.304
Bcl2a1	0.35	0.599	2.43	0.144	1.4	0.175
Fos	0.53	0.457	**2.36**	**0.025**	**2.16**	**0.025**
Tlr1	0.28	0.732	**2.22**	**0.046**	1.91	0.051
Tnfrsf1a	-0.19	0.665	2.19	0.279	1.54	0.32
Map2k3	0.29	0.378	2.13	0.214	1.76	0.273
Nfkb2	0.11	0.575	2.04	0.056	1.49	0.184
Ccl5	-0.27	0.699	1.99	0.092	1.77	0.174
Il1a	-0.42	0.162	1.98	0.294	0.77	0.399
Nfkbia	0.02	0.95	1.91	0.129	1.17	0.25
Cd40	-0.04	0.881	1.87	0.119	1.72	0.143
Irf1	0.06	0.822	1.79	0.134	1.61	0.182
Bcl3	0.25	0.503	1.77	0.074	1.78	0.053
Tlr2	0.07	0.877	1.61	0.231	1.32	0.223
Tnfrsf1b	0.47	0.703	1.47	0.26	0.43	0.68
Egr1	0.9	0.429	1.33	0.093	0.81	0.04
Atf2	0.49	0.205	1.32	0.367	1.15	0.244
Csf1	-0.04	0.791	1.3	0.109	0.77	0.445
Csf3	-0.46	0.087	1.29	0.388	-0.49	0.28
Rel	0.44	0.349	**1.29**	**0.049**	0.96	0.019
Tollip	-0.1	0.826	1.27	0.411	1.53	0.249
Casp1	-0.31	0.611	1.21	0.454	0.75	0.448
Irak2	0.19	0.58	1.17	0.093	0.66	0.2
Ltbr	-0.09	0.767	1.11	0.341	0.87	0.267
Atf1	0.08	0.503	1.01	0.291	0.62	0.287
Nfkb1	0.35	0.227	1.01	0.151	0.74	0.121
Rela	0.21	0.45	1	0.202	0.62	0.238
Map3k1	0.64	0.541	0.99	0.335	0.5	0.34

Tlr6	-0.26	0.601	0.97	0.401	0.62	0.511
Ripk2	0.22	0.34	0.93	0.201	-0.25	0.411
Cflar	0.47	0.144	0.91	0.234	0.64	0.209
Bcl10	0.62	0.443	0.87	0.327	0.6	0.189
Casp8	0.34	0.554	0.81	0.535	0.42	0.425
Myd88	-0.13	0.619	0.79	0.265	0.41	0.541
Kat2b	0.17	0.579	0.76	0.408	0.32	0.524
Faslg	0.18	0.841	0.75	0.356	0.37	0.002
Jun	0.16	0.77	0.74	0.375	0.71	0.337
Tbk1	0.33	0.252	0.74	0.371	0.53	0.165
Il1r1	-0.72	0.069	0.69	0.568	0.04	0.948
Tnfrsf10b	-0.84	0.127	0.69	0.337	-0.07	0.914
Chuk	0.12	0.509	0.66	0.362	0.34	0.322
Traf2	0.05	0.644	0.65	0.462	0.27	0.585
Fadd	0.17	0.41	0.64	0.39	0.27	0.179
Bcl2l1	0.56	0.262	0.63	0.449	0.3	0.433
Ikbkb	-0.17	0.576	0.62	0.394	0.21	0.419
F2r	0.28	0.377	0.61	0.273	0.08	0.82
Ikbkg	0.01	0.976	0.6	0.411	0.19	0.539
Tlr3	-0.17	0.79	0.6	0.651	0.01	0.965

Log2FC = log2 fold change; p-values from post-hoc Student's t-tests with FDR correction

While there appears to be a trend towards increased expression of NFκB signalling pathway-related genes in locations sonicated with schemes 2 and 3 at 4 days post-FUS+MBs (evidenced by a skew towards positive log2 fold changes, **Figure 3.3**), no significant differences were detected in the expression of any single gene. A complete list of log2 fold change values relative to control and p-values for all genes assessed at 6 hrs and 4 days post-FUS+MB exposure are listed in **Appendix Tables 3.1 and 3.2**, respectively.

3.3.5. Correlation of Contrast Enhancement and Differential Gene Expression

Least-squares linear regression was used to assess the relationship between log2 fold changes in gene expression at 6 hrs post-FUS+MBs and mean relative voxel intensity at each target, both expressed as a ratio to the non-sonicated control region (**Figure 3.4**). For several genes with established roles in acute inflammation and apoptosis, such as *Ccl5*, *Faslg*, *Tnf*, and *Il1b*, there were significant positive correlations between changes in expression and relative contrast enhancement. The same analysis for animals sacrificed 4 days post-FUS+MBs suggests that relative contrast enhancement has little predictive value for changes in the expression of NFκB signalling pathway-related genes at this later time point (data not shown).

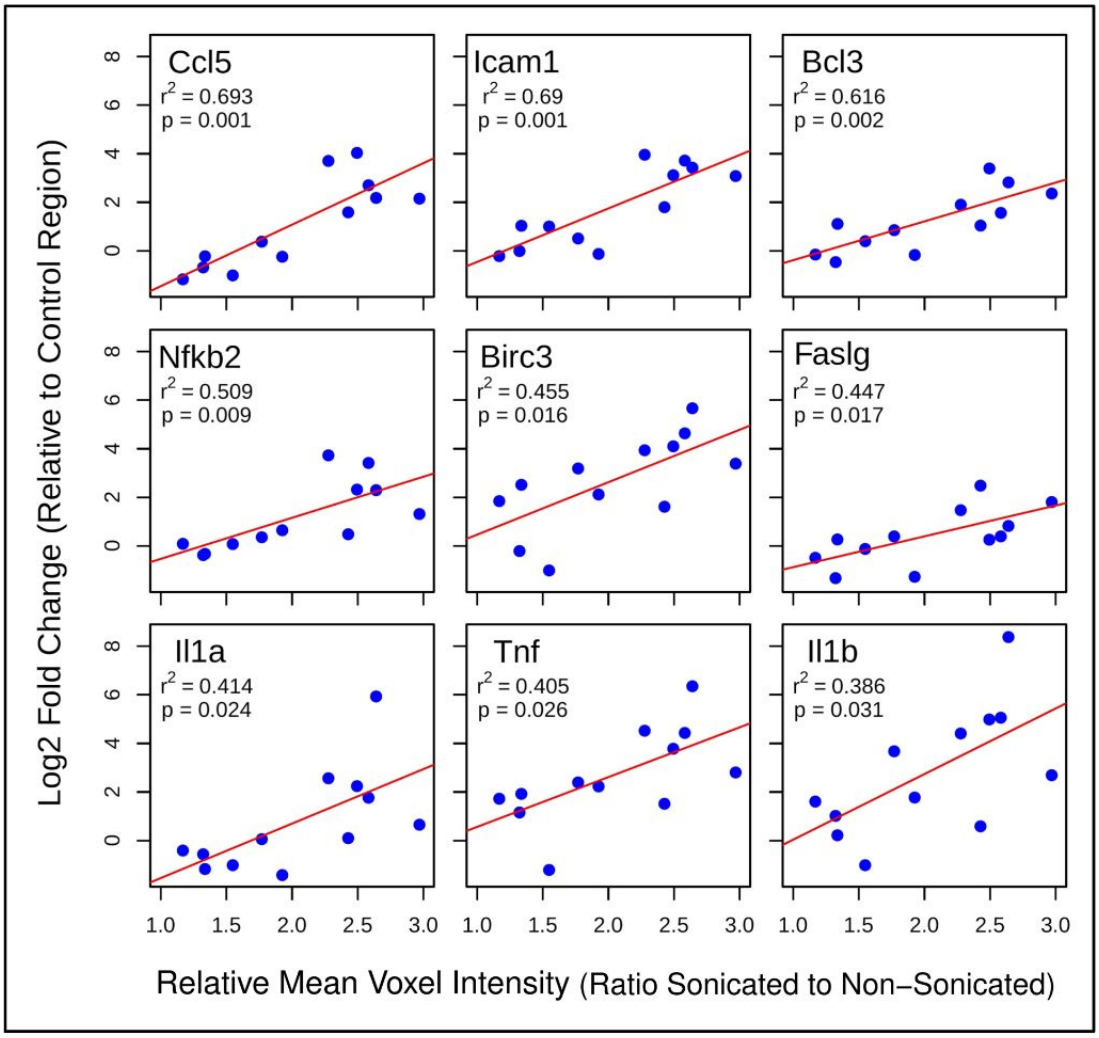

Figure 3.4. Correlation Between Post-FUS+MB Contrast Enhancement and Differential Gene Expression. Least-squares linear regression was used to assess the relationship between log2 fold changes in gene expression relative to the control region at 6 hrs post-FUS+MB exposure and mean voxel intensity at each sonicated target (normalized to control region) in CE-T1w MR images for each animal. Significant positive correlations were detected for 9 genes with well-established roles in acute inflammation and immune activation. n = 12 sonicated targets.

3.3.6. Histological Observations

H&E staining was used to broadly assess tissue health in each brain from groups 1 and 2. At targets sonicated with scheme 1 (**Figure 3.5D**), no evidence of RBC or leukocyte extravasation were observed at 6 hrs or 4 days following FUS+MB exposure, nor signs of overt neuronal degeneration (eosinophilic neurons). Targets sonicated with schemes 2 and 3 resulted in regions of RBC extravasation and granular leukocyte infiltration at 6 hrs and evidence of widespread neuronal degeneration and gliosis at 4 days

post-FUS+MB exposure. There were also microglial nodules present 4 days after FUS+MB exposure (**Figure 3.5B**) in several locations sonicated with scheme 2, indicative of small foci (I.e. less than 250 µm in diameter) of necrotic brain tissue. A summary of histological observations, including localized RBC extravasations, granular leukocyte infiltration, and microglial nodules, for each sonication scheme at 6 hrs and 4 days following FUS+MB exposure is presented in **Table 3.4**.

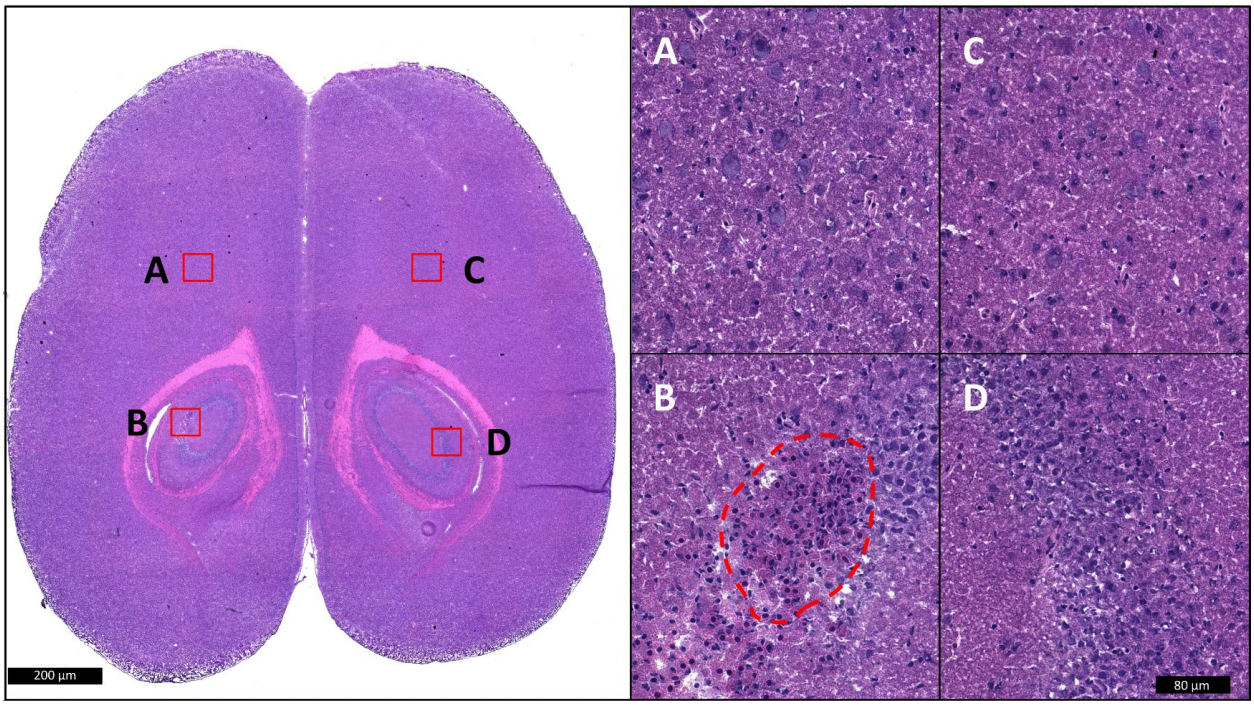

Figure 3.5. Histological Assessment of Tissue Health. H&E stained sections were imaged to broadly assess tissue health in each brain from animals sacrificed 6 hrs and 4 days post-FUS+MB exposure. Images acquired with a 20x objective lens at locations sonicated with schemes 1 (D), 2 (B), and 3 (A), are displayed for a single animal at 4 days post-FUS+MBs. A microglial nodule (red dotted line), indicative of degenerated neuron clearance, was apparent in the left hippocampus following sonication with scheme 2. No signs of RBC extravasation, neuronal degeneration, or neutrophil infiltration were seen at any of the other sonicated locations or the control region (C) in this animal.

Table 3.4: Histological events at the focal plane summated across animals

	6 hrs Post-FUS+MBs			4 days Post-FUS+MBs		
	Scheme 1	**Scheme 2**	**Scheme 3**	**Scheme 1**	**Scheme 2**	**Scheme 3**
Regions of RBC Extravasations	0	12	3	0	26	6
Granular Leukocytes	0	6	1	0	0	2
Microglial Nodules	0	0	0	0	7	1

n = 4 animals for each time point/scheme combination

3.4. Discussion

The aim of this study was to explore how FUS+MB-mediated BBB permeability enhancement changes the expression of genes related to the NFκB signalling pathway and to assess how MB dose can influence this response. Significant upregulation of genes associated with acute inflammation, immune response, and apoptotic processes, such as *Tnf*, *Ccl2*, and *Birc3*, was observed when the MB dose administered during sonication was 10x that recommended for clinical imaging. This response was accompanied by MRI evidence of edema and histological indications of neuronal degeneration, leukocyte infiltration, and microhemorrhage. Conversely, when a lower dose of MBs was administered, minimal changes in the expression of inflammatory markers were observed to accompany BBB permeability enhancement.

The NFκB signalling pathway affects a wide range of biological processes including innate and adaptive immunity, inflammation, and stress responses [324]. Broadly speaking, nuclear translocation of NFκB rapidly alters the expression of a number of cytokines, chemokines, adhesion molecules, etc., and leads to the recruitment of immune cells. As an example, global ischemia has been shown to result in a ten-fold increase in the DNA binding activity of NFκB at 6 to 12 h following ischemia, which gradually declines in the following 24 to 72 h, suggesting that ischemia-induced NFκB translocation is time-dependent [325]. The current study explored changes in the expression of genes related to the NFκB signalling pathway at 6 hrs and 4 days following sonication. The early time point was chosen to capture a peak in NFκB pathway-related transcription, as well as to allow more direct comparisons to previous work on the acute inflammatory response following FUS+MB exposure [208,326]; the late time point was chosen to capture a point when NFκB pathway-related transcription should return to baseline following an acute inflammatory response [325,327,328].

Previous work examining changes in the NFκB signalling pathway following FUS+MB exposure have reported the induction of a sterile inflammatory response compatible with ischemia or mild traumatic brain injury [208]. In order to test the conclusions of this study, the sonication parameters were replicated and compared to schemes in which the MB dose was lowered and the PNP was calibrated based on acoustic emissions. The changes in gene expression 6 hrs post-FUS+MB exposure previously reported [208] strongly correlate to those measured in the present study at targets sonicated with scheme 2 (**Table 3.5**), suggesting that these parameters may be unsuitable for clinical translation. It should be noted that these parameters may be beneficial in situations where minimizing tissue damage is not paramount, such as in the delivery of chemotherapeutic agents to brain tumours. Importantly, at targets sonicated with scheme

1, an increase in BBB permeability was demonstrated without significant changes in the expression of NFκB signalling pathway-related genes, histological damage, or MRI indications of edema and hemorrhage. However, as iterated above, the low number of animals used in this study is conducive only to the detection of large changes in gene expression (I.e. log2FC of at least ± 2.12). When effect size alone is considered, several genes related to inflammation and apoptosis displayed increases in relative expression of at least 50% compared to non-sonicated control regions (*Bcl10*, *Birc3*, *Ccl2*, *Egr1*, *Icam1*, *Ilb1 and Tnf*) at targets sonicated with scheme 1.

Table 3.5: Comparing differential gene expression 6 hrs post-FUS+MB exposure for each scheme to previously published research

Gene	Fold Change in Gene Expression (relative to control region)			
	Kovacs *et al.* 2017	**Scheme 1**	**Scheme 2**	**Scheme 3**
Tnf	10.87	1.87	16.22	9.00
Il1b	31.2	1.55	20.53	11.55
Ccl5	6.86	0.93	4.00	3.41
Birc3	18.96	1.77	14.52	12.55
Icam1	6.35	1.58	6.19	4.44
Il1a	5.31	0.75	3.95	1.71
Nfkb2	2.57	1.23	4.11	2.81
Bcl2a1	3.84	1.45	5.35	2.64
Cd40	2.62	1.22	3.66	3.29
Csf3	4.43	0.73	2.46	0.73
Irf1	3.12	1.25	3.43	3.07
Nfkbia	2.25	1.12	3.73	2.25
Tnfrsf1b	1.70	0.62	2.77	1.34

Linear regression between Kovacs *et al.* 2017 and scheme 2: $r^2 = 0.84$, slope = 0.64, p = 0.00001

The lack of overt tissue damage at targets sonicated with scheme 1 is consistent with a large body of research examining the safety profile of this technique; FUS+MB exposure has been shown to increase BBB permeability without inducing detrimental changes in behaviour [128,329,330] or significant cellular damage [128,212,233,234]. While it is important to recognize that the BBB plays a crucial role in ensuring proper brain homeostasis and preventing infection, it also severely limits the delivery of therapeutics to the brain. Thus, as with any medical intervention, a proper cost-benefit analysis will be required on an application-specific basis to ensure FUS+MB exposure is used in a manner that maximizes positive outcomes.

The positive correlation between CE-T1w relative voxel intensity and changes in the expression of several NFκB signalling pathway-related genes highlights the idea that treatment risk is not binary, safe or unsafe; there exists a spectrum, along which the effects of FUS+MB exposure moves beyond a transient change in BBB permeability, towards the induction of overt damage to brain tissue. Genes whose expression display a significant correlation to CE-T1w voxel intensity include *Ccl5*, *Icam1*, *Birc3*, *Faslg*, *Tnf*, and *Il1b*. Given the relationship between the expression of these genes and acute inflammation, immune response, and apoptotic processes [331–336], quantitative measures of BBB permeability enhancement may have value in estimating the magnitude of damage induced by sonication.

It is important to note, however, that the exact relationships between changes in gene expression and relative contrast enhancement described here are not universal. A large number of factors will affect this relationship, including the concentration/type of contrast agent administered, imaging parameters (E.g. imaging sequence, field strength, receive-coil sensitivity), species of animal, brain region, etc. It may be possible, however, to establish correlations, specific to a particular experimental or clinical setup, that will help guide safety standards based on CE-T1w MRI or other more quantitative measures of BBB permeability enhancement.

Analysis of post-FUS+MB exposure contrast enhancement and PNP also highlights the influence of MB dose on BBB permeability. When comparing the PNP required for the detection of $1.5f$ emissions above baseline noise levels at two different MB doses (10 µl/kg vs 100 µl/kg), there was no significant influence of MB dose observed; PNP required to elicit a software triggered drop in pressure for schemes 1 and 3 were not statistically different. However, the higher MB dose produced significantly greater relative contrast enhancement and transcription of genes involved in inflammatory processes. This indicates that while calibrating PNP based on $1.5f$ emissions may produce more consistent changes in BBB permeability [232], there remains a need for methods that are more flexible to variations in experimental conditions.

3.4.1. Limitations

While the FUS+MB parameters employed for scheme 2 were designed to replicate those used by Kovacs *et al.* [208], there are some differences to note. The first is in MB type, Optison versus Definity. Differences in the acoustic properties of these MB types complicate choosing a MB dose that will produce an equivalent effect; using MB number or gas volume as a means of matching doses may be over simplistic

due to key differences in shell composition (Optison: human serum albumin; Definity: lipid) and mean diameter (Optison: 2.0-4.5 µm; Definity: 1.1-3.3 µm), both of which affect their response to ultrasound. The larger proportion of Optison MBs that are near resonant size at the sonicating frequency used by Kovacs *et al.* (compared to the proportion of Definity MBs near resonant size in the present study) increases the probability of inertial cavitation and subsequent vascular damage. Conversely, the higher concentration of MB number/µl in Definity may influence the biological response to sonication by affecting the magnitude of stress on vascular walls and the amount/type of bubble-bubble interactions.

The approach employed in the present study was to use the clinically recommended imaging dose of each MB type as a guide. Since the dose of ~500 µl of Optison/kg used by Kovacs *et al.* is approximately 10x greater than the recommended clinical dose for imaging [120], we administered 100 µl of Definity/kg (10x greater than the recommended clinical dose for imaging). While we believe the high degree of correlation between gene expression changes in scheme 2 and that reported in Kovacs *et al.* (**Table 3.5**) suggest similar *in vivo* effects, we recognize that the discordance in MB type between studies may contribute to more subtle differences that were not detected. Additionally, in order to account for differences in transmit frequencies between studies, PNP was adjusted to match mechanical indexes (current study: 290 kPa at 551 kHz; Kovacs et *al.*: 300 kPa at 589 kHz). Given the minor differences in PNP and frequencies, this should not preclude a comparison of results.

Another limitation to note is in the quantification of relative contrast enhancement. Mean voxel intensity at each target was normalized to the non-sonicated control region in each animal. This measurement was performed on the last CE-T1w images acquired for each animal. Thus, sonications performed first had more time for gadolinium to accumulate, skewing the relative enhancement between schemes towards: scheme 1 > scheme 2 > scheme 3. However, since gadolinium was administered immediately prior to each sonication, which was necessitated by the time interval between sonications for MB clearance, the concentration of gadolinium in circulation would be higher for the last sonications. This skews the relative enhancement between schemes towards: scheme 3 > scheme 2 > scheme 1. While relative contrast enhancement in the final CE-T1w images acquired should approximate differences in BBB permeability enhancement between schemes, this experimental design precludes more accurate quantification. Further work should be directed at establishing relationships between contrast enhancement and inflammation using a more robust experimental design.

3.4.2. Conclusion

This study sought to explore how FUS+MB-mediated BBB permeability enhancement affects the expression of genes related to the NFκB signalling pathway and to assess how MB dose can influence this response. While a significant and damaging inflammatory response was observed at the high MB dose, results suggest that BBB permeability enhancement can be achieved without a drastic upregulation of NFκB signalling pathway-related gene expression in whole brain tissue at 6 hrs post-sonication. This emphasizes the importance of employing optimized FUS+MB parameters in order to mitigate the chance of causing overt injury to brain tissue at the targeted locations. This work also suggests that the magnitude of BBB permeability enhancement following FUS+MB exposure has an influence on the expression of genes related to acute inflammation, immune response, and apoptotic processes following sonication.

Chapter 4

Angiogenic Response of Hippocampal Vasculature to Focused Ultrasound and Microbubble Exposure

4.1. Introduction

As discussed in *Chapter 2*, transcriptional changes in hippocampal microvasculature following sonication are indicative of the initiation of angiogenic processes. Gene expression changes observed in that study also indicated the presence of a FUS+MB-induced acute inflammatory response, a potential driver of blood vessel growth [285]. This acute response to sonication was also found to be present in whole tissue brain samples, with changes in proinflammatory cytokine transcription correlating to signal intensity changes in CE-T1w MR images (described in *Chapter 3*). Given that downstream effects of inflammation have been observed following FUS+MB exposure, such as increased hippocampal neurogenesis [230,231,337], immune cell infiltration [128,174,197,208,211–214], glial cell activation [172,174,175,208], and Aβ plaque clearance [136,172,174,175], further study of blood vessel growth in this context is warranted. Additionally, previous work has demonstrated significant and enduring blood vessel growth in skeletal muscle following exposure to FUS+MBs [310,338,339].

Despite brain vasculature being the biological target of FUS+MB exposure in the context of BBB applications and ECs experiencing the largest magnitude of physical stresses from insonated MBs, blood vessel growth had yet to be studied in this context. The work presented in *Chapter 4* explores the impact of FUS+MB-mediated BBB permeability enhancement on vascular density, newborn EC density, VEGFA

Parts of this chapter are adapted from: McMahon D, Mah E, Hynynen K. Angiogenic response of rat hippocampal vasculature to focused ultrasound-mediated increases in blood-brain barrier permeability. *Scientific reports*. 2018. 8(1):12178. Used with permission as part of publication agreement.

immunoreactivity, and blood vessel diameter at 7, 14, and 21 days following sonication. While preclinical research has demonstrated the ability to mediate BBB permeability enhancement without lasting indications of overt tissue damage [75,134,232,340] and limited and/or temporary impact on behaviour in healthy animals [128,136,321], knowledge regarding the long-term response of brain vasculature is sparse, but has relevance for both further characterization and risk assessment.

4.2. Materials and Methods

4.2.1. Animals

Male Sprague Dawley rats (n = 24), weighing 200-300 g on the day of sonication, were used in this study (Taconic Biosciences, Germantown, NY, USA). Animals were housed in the *Sunnybrook Research Institute* animal facility (Toronto, ON, Canada) and had access to food and water *ad libitum*. All animal procedures were approved by the *Animal Care Committee* at *Sunnybrook Research Institute* and are in accordance with the *Canadian Council on Animal Care* guidelines.

4.2.2. MRI-Guided FUS+MB Exposure

Animal preparation and FUS+MB exposures were conducted as described in *Chapter 3*, with the following exceptions. Three locations in either the right or left dorsal hippocampus were targeted in each animal based on T2w MR images (TR = 2000 ms, TE = 60 ms; **Figure 4.1B**). T1w images (TR = 500 ms, TE = 10 ms) were acquired approximately 10 min following sonication to assess BBB permeability enhancement (**Figure 4.1C**). All MR experiments were conducted on a 7T horizontal bore Avance BioSpec 70/30 scanner (Bruker BioSpin, Ettlingen, Germany) with a 20 cm inner diameter gradient insert coil with maximum gradient amplitude of 668 mT/m (Bruker BioSpin, Ettlingen, Germany). Images were acquired using an 8 cm inner diameter volume coil for transmit and receive. To label proliferating cells, BrdU was administered daily (50 mg/kg; 10 mg/ml diluted in saline; i.p.), starting 24 hrs post-FUS+MBs, until the day before sacrifice.

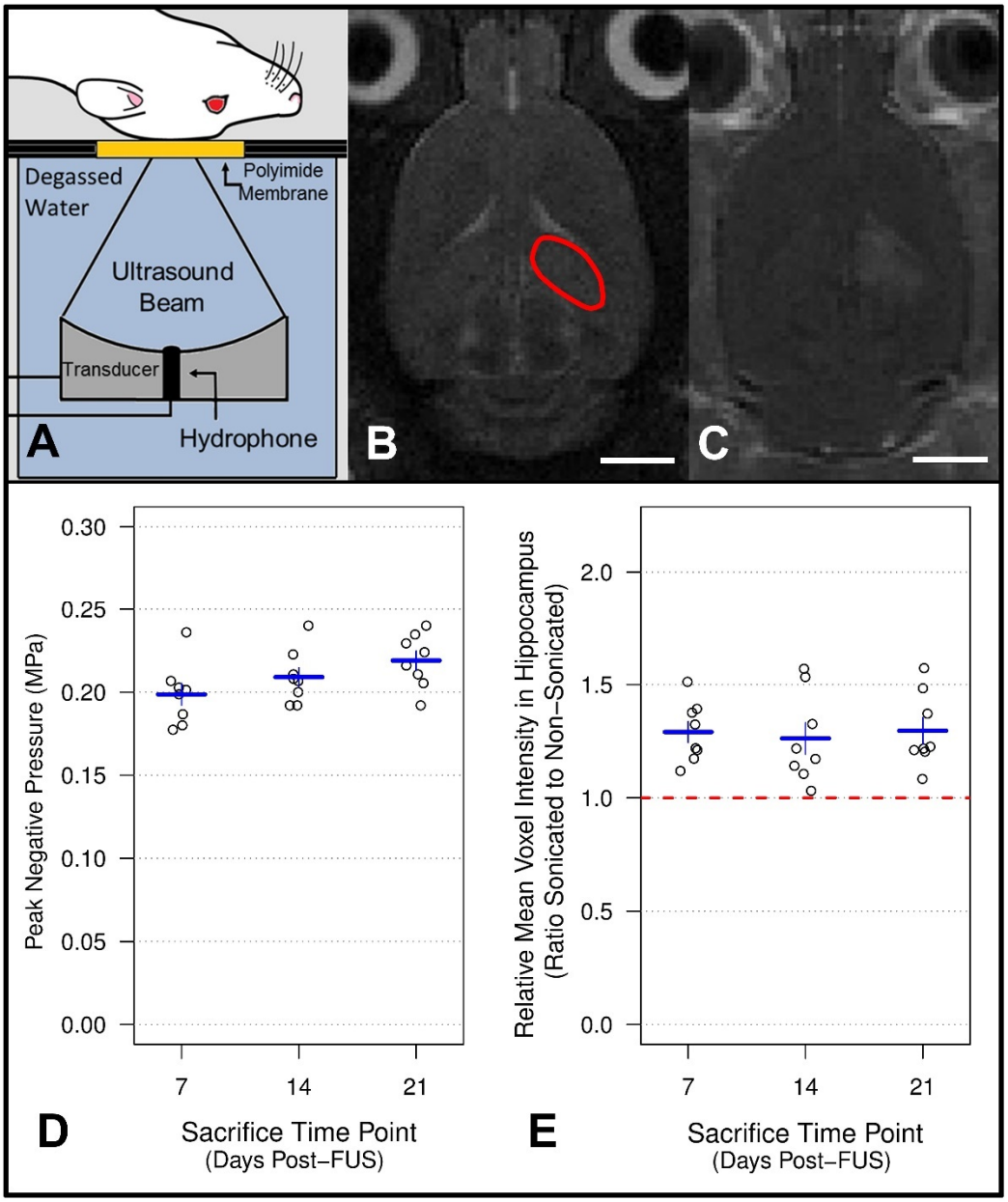

Figure 4.1. MRI-Guided FUS+MB Exposure. (A) During sonication and imaging, rats were positioned supine on an MRI compatible sled with the dorsal surface of the head coupled to a polyimide membrane. The bottom of the membrane was coupled to a tank filled with degassed, deionized water, housing the transducer/hydrophone assembly. (B) The dorsal hippocampus (indicated by red outline) was targeted from T2w images. (C) Following sonication, CE-T1w MR images were acquired to confirm BBB permeability enhancement. (D) For rats sacrificed at 7, 14, and 21 days post-FUS+MB exposure, mean PNPs following an algorithm-triggered pressure drop at targets in the dorsal hippocampus were 199 ± 20 kPa, 209 ± 17 kPa, and 219 ± 17 kPa, respectively. No significant differences in mean PNPs were detected between time points (p=0.08). (E) The ratio of mean voxel intensity in the sonicated dorsal hippocampus to non-sonicated dorsal hippocampus for rats sacrificed at 7, 14, and 21 days post-FUS+MB exposure were 1.29 ± 0.14, 1.26 ± 0.20, and 1.29 ± 0.20, respectively. No significant differences were detected between time points (p = 0.91). Error bars indicate standard error of the mean. n = 8 animals for each sacrifice time point. Scale bars = 4 mm.

4.2.3. Immunohistochemistry

At 7, 14, and 21 days following sonication, rats were transcardially perfused with ice-cold phosphate buffer (PB; 0.1 M, pH 7.4), followed by 4% paraformaldehyde in PB. Brains were extracted, post-fixed for 24 hrs at 4° C, then transferred to 30% sucrose in PB and stored at 4° C until fully saturated (~3 days). Brains were embedded in optimum cutting temperature compound (Tissue-Tek, Torrance, CA, USA) and stored at -80° C. Coronal cryostat sections (40 µm thick) were stored in cryoprotectant (glycerin, ethylene glycol, and 0.2 M PB in a ratio of 2:3:5, respectively) at -10° C until immunohistological processing.

Co-staining for BrdU and glucose transporter-1 (GLUT1) was performed on free-floating sections with sequential primary antibody incubations. Three 10-min washes in PBST were performed between each step of this protocol except after blocking. Antigen retrieval proceeded with 90 min in 2 M HCl at room temperature followed by 10 min in 0.1 M borate buffer (pH 8.5). Sections were blocked for 1 hr at room temperature (0.1% Triton X-100, 1% bovine serum albumin, 2% goat serum, 1x PBS), then incubated in rat anti-BrdU primary antibody (1:400; OBT0030, Bio-Rad, Hercules, CA, USA), diluted in blocking buffer, overnight at 4° C. Sections were incubated in goat anti-rat IgG Alexa Fluor 488 secondary antibody (1:400; ab150165, Abcam Inc, Cambridge, MA, USA) for 2 hrs at 4° C, then incubated in rabbit anti-GLUT1 primary antibody (1:400; ab15309, Abcam Inc, Cambridge, MA, USA), diluted in blocking buffer, overnight at 4° C. Sections were then incubated in goat anti-rabbit IgG Alexa Fluor 647 secondary antibody (1:400; ab150079, Abcam Inc, Cambridge, MA, USA) for 2 hrs at 4° C and mounted onto charged glass slides (X-tra, Leica Microsystems, Wetzlar, Germany) with aqueous mounting media (Fluoroshield™ with DAPI, Sigma-Aldrich Corporation, St. Louis, MO, USA). Slides were stored in the dark at 4° C until imaging.

In another series of sections, immunohistochemical staining proceeded as indicated above; however, mouse anti-VEGFA primary antibody (1:400; ab1316, Abcam Inc, Cambridge, MA, USA) was used in place of the BrdU primary antibody and rabbit anti-mouse Alexa Fluor 555 (1:400; ab150126, Abcam Inc, Cambridge, MA, USA) was used as secondary antibody. More detailed justifications for methods described in *Sections 4.2.3-4.2.5* can be found in **Appendix Table 4.1**.

4.2.4. Confocal Imaging

For quantification of blood vessel density, blood vessel diameter, and newborn EC density, image stacks (2 µm spacing, 1.24 µm/pixel, 512 x 512-pixel field of view) were collected through the entire section

thickness, bilaterally, in each of the 3 major subfields of the hippocampus, cornus amonis 1 (CA1), CA3, and dentate gyrus (DG). Sections (7-9 per animal) were imaged with a 20x objective (NA 0.75) using a scanning laser confocal microscope system (A1+, Nikon, Tokyo, Japan) at excitation wavelengths of 639.1 nm, 488.0 nm, and 403.1 nm for GLUT1, BrdU, and DAPI, respectively. Emissions were received at 663-738 nm, 500-550 nm, and 425-475 nm, respectively. To ensure subsequent image analysis was performed on equivalent regions of the hippocampus, image stacks were rotated and cropped to include only regions of CA1 and CA3 between stratum radiatum and stratum oriens, inclusive, as well as only regions of DG between the granular cell layer and the outer molecular layer. Image stacks were also cropped in the z-direction, keeping 5 images starting at the first complete optical section.

4.2.5. Blood Vessel Density and Diameter Analysis

GLUT1 positive blood vessels were segmented using an in-house designed *ImageJ* pipeline (**Figure 4.2**). First, background signal intensity in the GLUT1 channel was reduced by subtraction of the BrdU channel with high intensity pixels (BrdU positive cells) removed with global thresholding (**Figure 4.2B**). Next, blood vessels were highlighted in maximum intensity projections with the *Tubeness* plugin (ImageJ), which identifies tube-like structure (**Figure 4.2C**). These highlighted structures were extracted by auto-thresholding and binary masking (**Figure 4.2D**). GLUT1 positive area (from binary masks) was normalized to imaging volume for each image stack and averaged within animals for each subfield. Density ratios (sonicated to control hemisphere) for each subfield were log2 transformed and averaged within animals to obtain hippocampal means.

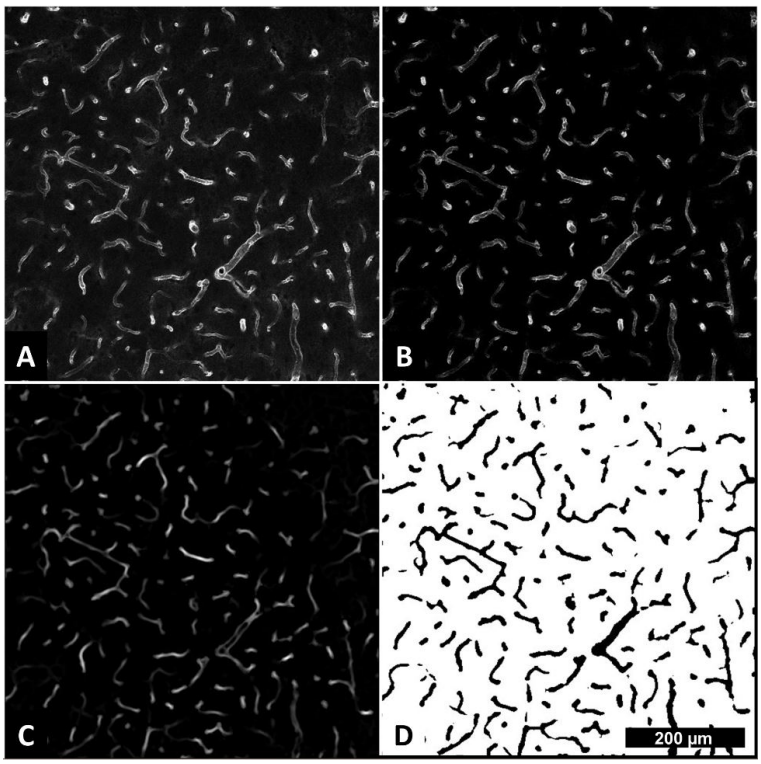

Figure 4.2. Blood Vessel Segmentation Pipeline. Image stacks were collected for the full thickness of sections stained for GLUT1 (2µm spacing, 1.24µm/pixel, 512×512-pixel field of view). (A) Maximum intensity projections of 5 images after the first complete optical slice were used to assess blood vessel density. (B) Subtraction of the BrdU channel, with high intensity regions (BrdU positive cells) thresholded out, was used to reduce background intensity. (C) *Tubeness* macro (ImageJ), was used to identify *tube-like* structures. (D) The outputs of *Tubeness* processing were thresholded and masked. Binary mask images were normalized to imaging volume to determine blood vessel density. All image segmentation steps were performed in ImageJ. n = 8 animals for each sacrifice time point.

Maximum intensity projections of cropped GLUT1 channel image stacks were used to measure the diameter of blood vessel segments. Using the *ObjectJ* plugin (ImageJ), the diameter of each blood vessel segment was manually measured by an author (DM) blinded to treatment. Diameter histograms, binned to <5 µm, 5-7.5 µm, 7.5-10 µm, and >10 µm (integer multiples of the spatial resolution of images), were normalized to image stack volumes and averaged within the hippocampi of each animal. Relative differences between hemispheres are expressed as a frequency of blood vessel segments per 1 000 000 μm^3 of brain tissue.

4.2.6. Newborn Endothelial Cell Density Analysis

Cropped image stacks (GLUT1, BrdU, and DAPI channels) were used to quantify the density of newborn ECs. An author (EM) blinded to treatment manually quantified the number of BrdU positive ECs, defined as the colocalization of BrdU, GLUT1, and DAPI, with a nuclei shape characteristic of ECs (oblong/elliptical in shape with its major axes aligned to the long axes of blood vessels; **Figure 4.3**). Newborn EC density was normalized to imaging volume for each image stack and averaged within animals for each subfield.

Density ratios (sonicated to control hemisphere) for each subfield were log2 transformed and averaged within animals to obtain hippocampal means. In some regions of brain tissue, traces of BrdU+ blood cells were evident in blood vessels due to poor perfusion; these subfields/sections/animals were not included in this analysis.

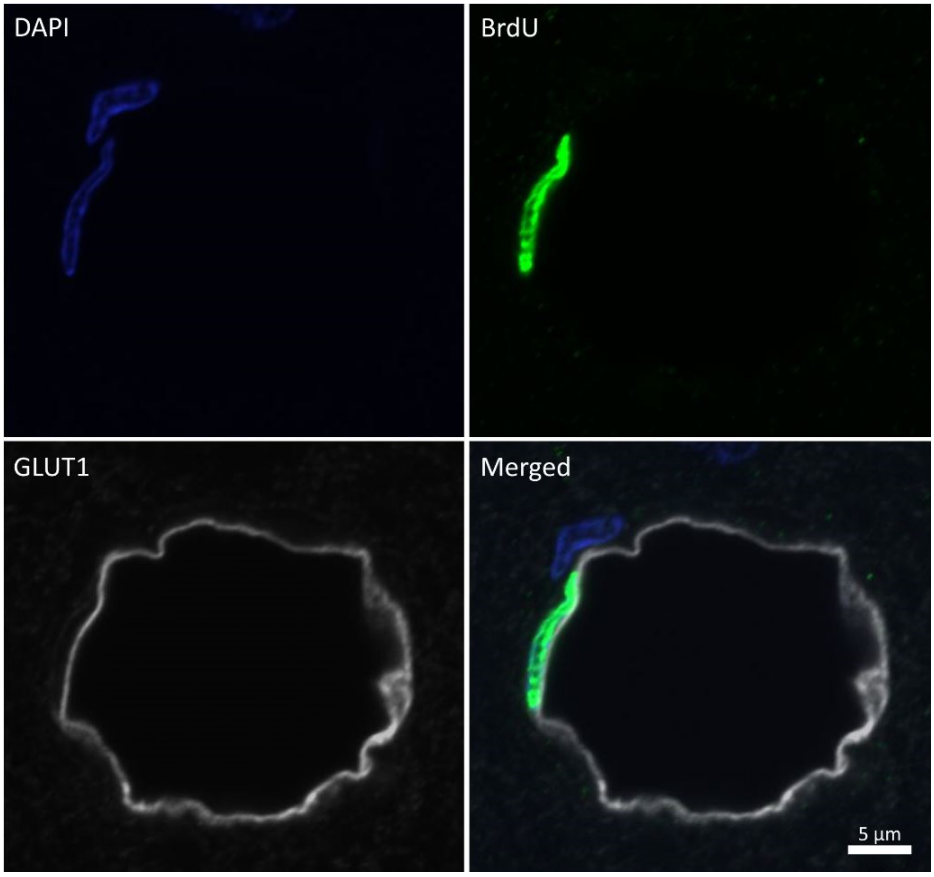

Figure 4.3. BrdU Positive Endothelial Cell Example. Newborn ECs were defined as the colocalization of BrdU, GLUT1, and DAPI, with a nuclei shape characteristic of ECs (elliptical in shape with major axes aligned to the long axes of blood vessels). Newborn ECs were found lining the full spectrum of blood vessel sizes in the hippocampus.

4.2.7. Statistics

All statistical analyses were performed in R 3.4.3. Repeated measures, two-way, ANOVA was performed at each time point for blood vessel density, blood vessel diameter, and newborn EC density with subfield specific post-hoc Student's t-tests (two-sample, two-tailed, paired). FDR correction for multiple comparisons was used to account for the analysis of 3 time points and 3 subfields. Contrast-enhancement and PNP were compared between animals at different time points with one-way ANOVA. For all analyses,

a p-value of 0.05 was used as the threshold for statistical significance. Unless otherwise specified, variance is expressed as standard deviation of the mean.

4.3. Results

4.3.1. PNP and Contrast Enhancement Across Time Points

During sonication, acoustic emissions were monitored. Once the ratio of signal to baseline at the first or second ultraharmonic frequency passed 3.5 (threshold event), the PNP was dropped by 50% and maintained at this level for the remainder of sonication. PNP after detecting a threshold event was not significantly different between groups (**Figure 4.1D**). For rats sacrificed at 7, 14, and 21 days post-FUS+MB exposure, mean PNPs were 199 ± 20 kPa, 209 ± 17 kPa, and 219 ± 17 kPa, respectively ($p = 0.08$; one-way ANOVA).

Ten min following sonication, CE-T1w images were collected to confirm FUS+MB-mediated BBB permeability enhancement and to quantify relative contrast-enhanced signal intensity. No significant differences were observed between groups (**Figure 4.1E**). The ratios of mean voxel intensity in the sonicated dorsal hippocampi to non-sonicated dorsal hippocampi for rats sacrificed at 7, 14, and 21 days post-FUS+MB exposure were 1.29 ± 0.14, 1.26 ± 0.20, and 1.29 ± 0.20, respectively ($p = 0.91$; one-way ANOVA). Together, PNP and relative contrast-enhanced signal intensity measurements suggest that there were no significant group-wise differences in FUS+MB exposures.

4.3.2. Density of Newborn Endothelial Cells

Newborn EC density in sonicated hippocampi were found to be significantly increased at all time points relative to the contralateral hemisphere (**Figure 4.4**). Mean log2 density ratios (sonicated to non-sonicated dorsal hippocampi), averaged across the hippocampus, were measured to be 0.79 ± 0.63 ($p < 0.01$), 1.00 ± 0.85 ($p < 0.01$), and 1.01 ± 0.85 ($p < 0.01$) at 7, 14, and 21 days post-FUS+MB exposure, respectively. These mean log2 ratios correspond to relative increases in newborn EC density in the sonicated hippocampi of 72.4% ± 54.8%, 100.4% ± 76.5%, and 100.9% ± 76.5%, respectively, compared to the non-sonicated hemisphere. Post-hoc analysis at each time point revealed significantly increased relative newborn EC density at 21 days post-FUS+MB exposure in the sonicated DG (log2 ratio of 1.17 ± 1.10, sonicated to non-sonicated DG, $p = 0.02$); however, post-hoc analyses may be underpowered for the

detection significant differences when accounting for multiple comparisons. No significant differences were detected between time points. Qualitative evaluation of newborn ECs following FUS+MB exposure revealed no obvious pattern with regards to the size of the blood vessels affected; BrdU positive ECs were found in the full spectrum of blood vessel sizes in the hippocampus.

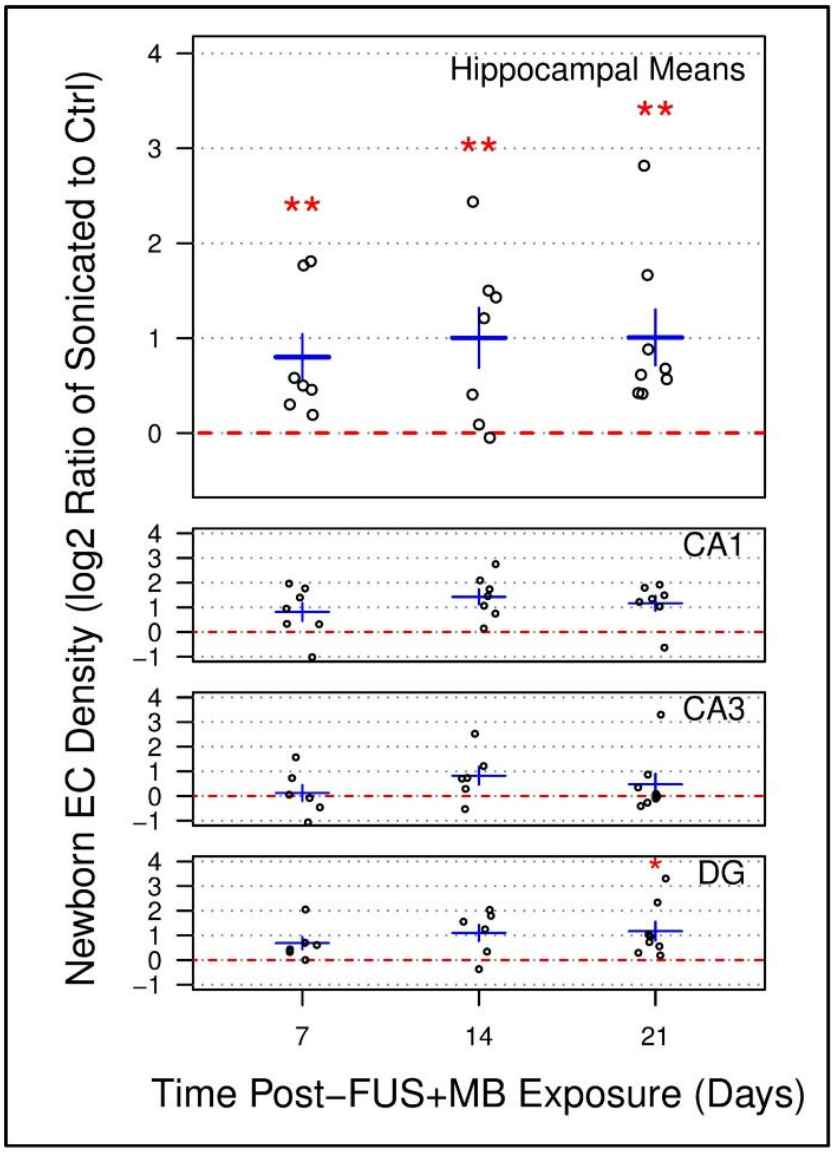

Figure 4.4. Newborn Endothelial Cell Density Following FUS+MB Exposure. Newborn ECs density in sonicated hippocampi were significantly increased at all time points relative to the contralateral hemisphere. Mean log2 density ratios (sonicated to non-sonicated dorsal hippocampi), averaged across the hippocampus, were measured to be 0.79 ± 0.63, 1.00 ± 0.85, and 1.01 ± 0.85 at 7, 14, and 21 days post-FUS+MB exposure, respectively. Post-hoc analysis at each time point revealed significantly increased relative newborn EC density at 21 days post-FUS+MB exposure in the sonicated DG (log2 ratio of 1.17 ± 1.10, sonicated to non-sonicated DG, $p = 0.02$). Red dotted lines at $y = 0$ indicate no difference between sonicated and control dorsal hippocampi. * indicates $p < 0.05$. ** indicates $p < 0.01$. Error bars represent standard error of the mean. $n = 7$, 7, and 8 for sacrifice time points of 7, 14, and 21 days post-FUS+MB exposure, respectively.

4.3.3. Blood Vessel Density

Relative blood vessel density was assessed by calculating the log2 ratio of GLUT1 immunoreactive area (normalized to imaging volume) in the sonicated, relative to the non-sonicated, hippocampus (**Figure 4.5**). At 7 and 14 days post-FUS+MB exposure, mean log2 density ratios across the hippocampus were measured to be of 0.15 ± 0.22 ($p = 0.02$) and 0.16 ± 0.12 ($p < 0.01$), respectively. These mean log2 ratios correspond to increases in blood vessel density in the sonicated hippocampi of 10.9% ± 16.5% and 12.1% ± 8.7%, respectively. No significant differences were observed across the hippocampus 21 days following sonication (mean log2 ratio of 0.08 ± 0.10, $p = 0.12$). Post-hoc analysis at each time point revealed significantly increased mean log2 density ratios in DG at 7 days post-FUS+MB exposure (0.23 ± 0.12, $p < 0.01$), as well as in CA1 and CA3 at 14 days post-FUS+MB exposure (CA1: 0.18 ± 0.12, $p < 0.01$; CA3: 0.21 ± 0.24, $p = 0.04$). No significant differences were detected between time points. Representative images of increased relative blood vessel density 14 days post-FUS+MB exposure in CA1 are displayed in **Figure 4.6**.

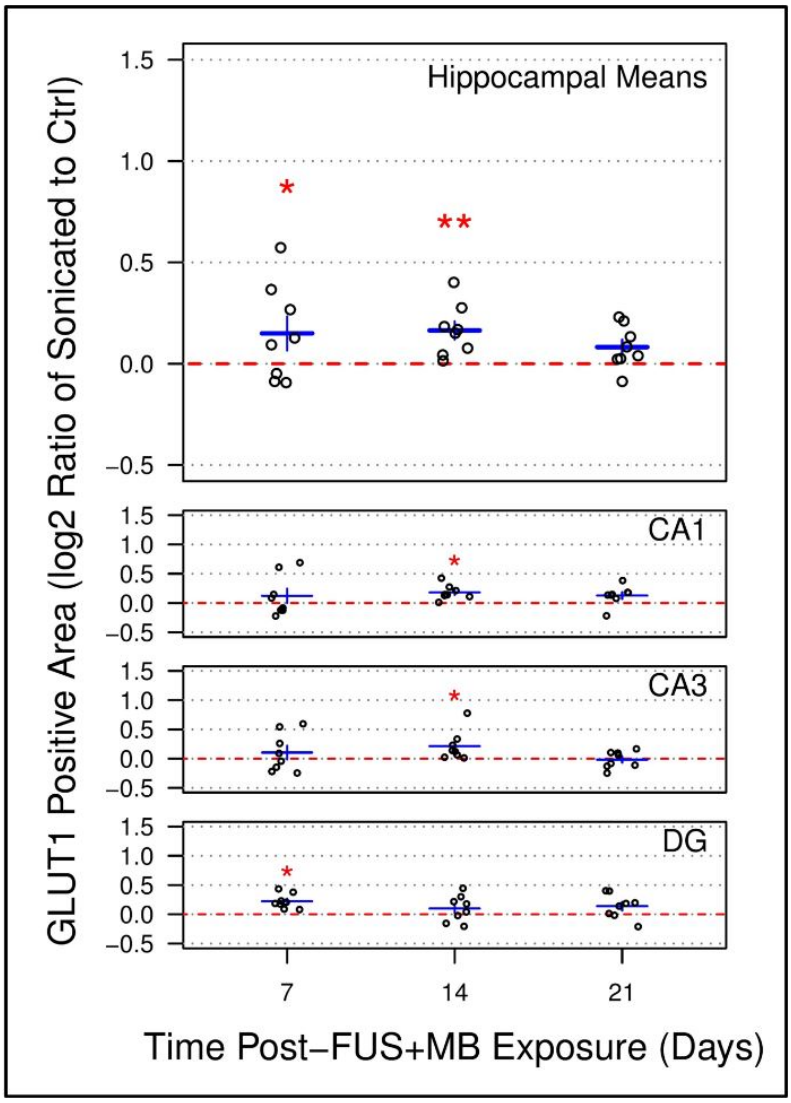

Figure 4.5. Hippocampal Blood Vessel Density Following FUS+MB Exposure. Relative blood vessel density was assessed by calculating the log2 ratio of GLUT1 immunoreactive area (normalized to imaging volume) in the sonicated, relative to the non-sonicated, hippocampus. At 7 and 14 days post-FUS+MB exposure, mean log2 density ratios across the hippocampus were measured to be 0.15 ± 0.22 and 0.16 ± 0.12, respectively. No significant differences were observed across the hippocampus 21 days following sonication (log2 ratio of 0.08 ± 0.10, $p = 0.12$). Post-hoc analysis at each time point revealed significantly increased mean log2 density ratios in DG at 7 days post-FUS+MB exposure (0.23 ± 0.12), as well as in CA1 and CA3 at 14 days post-FUS+MB exposure (CA1: 0.18 ± 0.12; CA3: 0.21 ± 0.24). Red dotted lines at $y = 0$ indicate no difference between sonicated and control hippocampi. * indicates $p < 0.05$. ** indicates $p < 0.01$. Error bars represent standard error of the mean. $n = 8$ animals for each sacrifice time point.

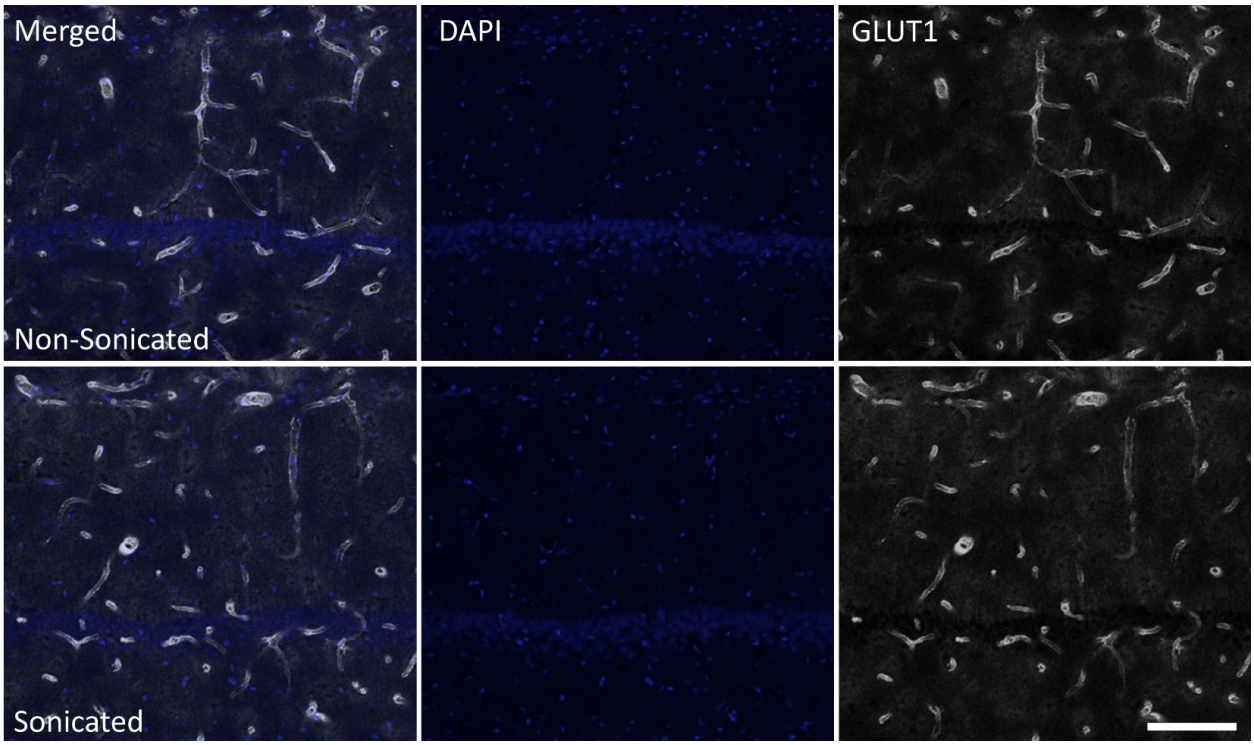

Figure 4.6. Increased Relative Blood Vessel Density Following FUS+MB Exposure. Images collected in CA1 of the sonicated (bottom row) and non-sonicated (top row) hippocampi at 14 days post-FUS+MB exposure demonstrate a small relative increase (12.1% ± 8.7%) in GLUT1 immunoreactive area in the sonicated hemisphere. DAPI, GLUT1 immunoreactivity, and merged channels are displayed. Scale bar = 100 µm.

4.3.4. Blood Vessel Diameter

Histograms of blood vessel segment diameters across each hippocampus were compared between sonicated and non-sonicated hemispheres (**Figure 4.7**). At 14 days post-FUS+MB exposure, the mean frequency of small blood vessel segments (< 5 µm) was significantly greater in the sonicated hippocampi (1.73 ± 2.04 more small blood vessels per 1 000 000 μm^3 of brain tissue than control hemisphere; $p = 0.049$). No significant differences were observed at any other time point or for any other size of blood vessels. At 21 days following sonication, the effect size and variance in both the < 5 µm and 5 - 7.5 µm bins was smaller than at 7 or 14 days.

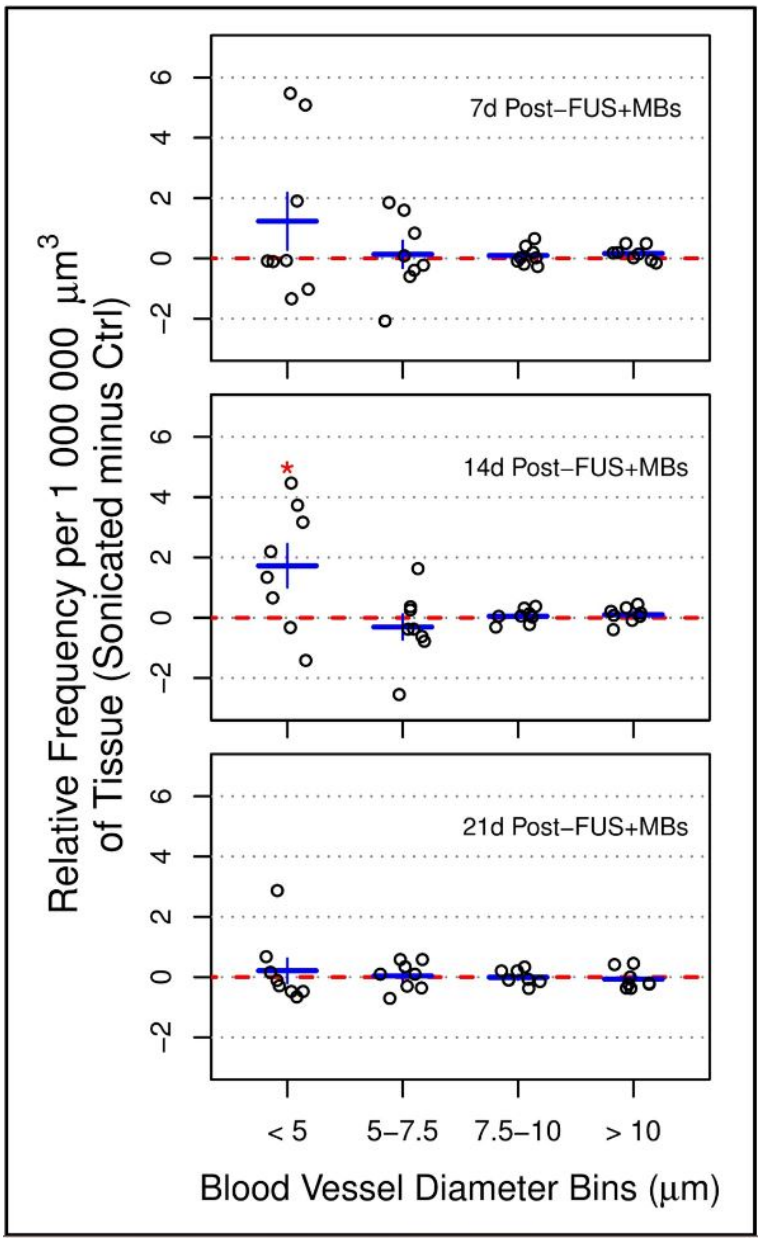

Figure 4.7. Relative Density of Blood Vessel Segments Following FUS+MB Exposure. At 14 days post-FUS+MB exposure, the mean frequency of small blood vessel segments (< 5 µm) was significantly greater in the sonicated hippocampi (1.73 ± 2.04 more small blood vessels per 1 000 000 μm^3 of brain tissue than in the non-sonicated hippocampus, p = 0.049). No significant differences were observed at any other time point or for any other size of blood vessels. At 21 days following sonication, the effect size and variance in both the < 5 µm and 5–7.5 µm bins was smaller than at 7 or 14 days. Red dotted lines at y = 0 indicate no difference between sonicated and control hemispheres. * indicates p < 0.05. Error bars represent standard error of the mean. n = 8 animals for each sacrifice time point.

4.3.5. VEGFA Immunoreactivity

VEGFA immunoreactivity was qualitatively evaluated in sections stained for VEGFA, GLUT1, and DAPI. At 7 days post-FUS+MB exposure, sparse vascular and perivascular VEGFA immunodetection was evident in the sonicated hemisphere (**Figure 4.8**) for 4 of 8 animals; minimal levels of VEGFA staining were seen in the contralateral hemisphere. Qualitatively, no differences in VEGFA immunoreactivity were apparent between the sonicated and control hemispheres at 14 or 21 days post-FUS+MB exposure in any animal.

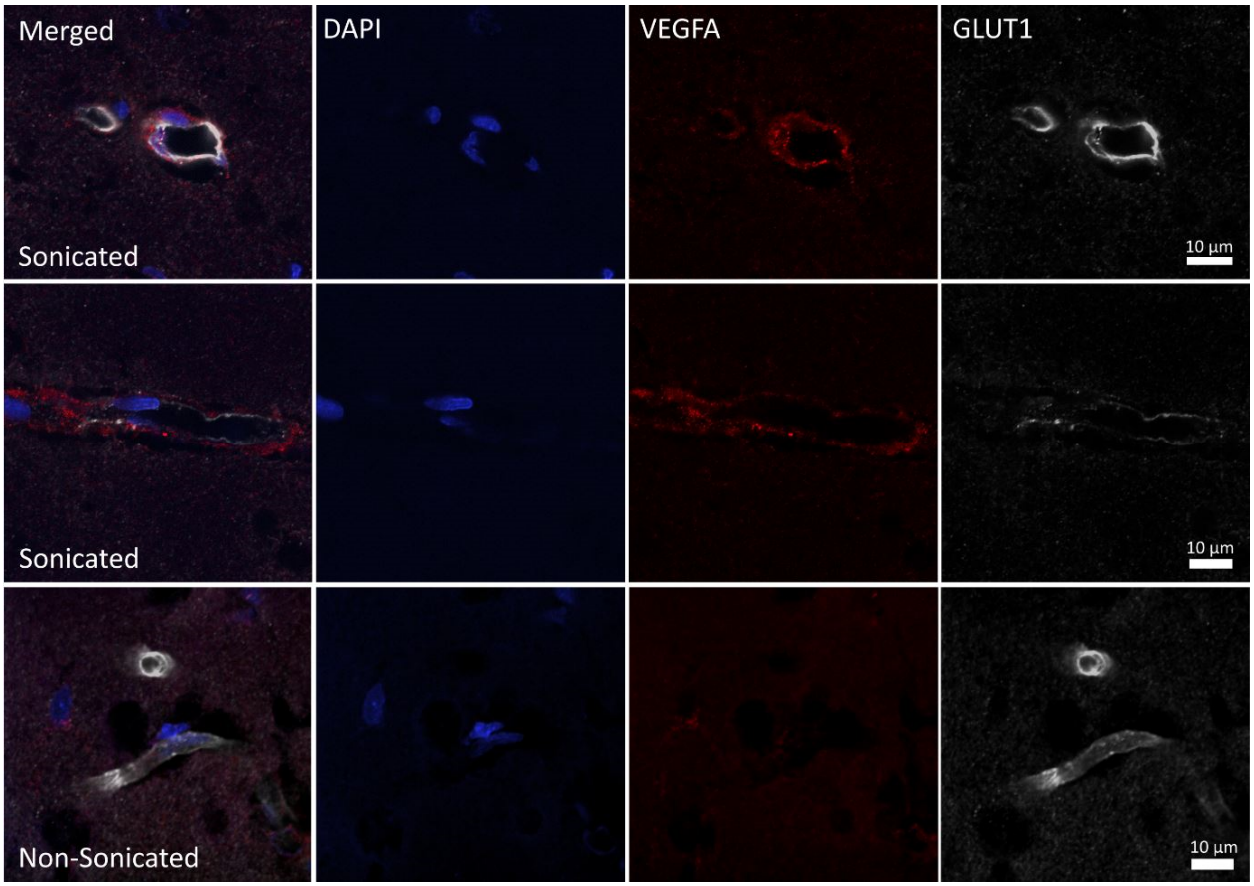

Figure 4.8. VEGFA immunoreactivity 7 days post-FUS+MB Exposure. VEGFA immunoreactivity was qualitatively evaluated in sections stained for VEGFA, GLUT1, and DAPI. At 7 days post-FUS+MB exposure, sparse vascular (upper panels) and perivascular (middle panels) VEGFA immunodetection was evident in the sonicated hemisphere for a subset of animals. In the contralateral hemisphere of the same rat (bottom panels), immunodetection of VEGFA was greatly reduced.

4.4. Discussion

Results presented here indicate that FUS+MB-mediated BBB permeability enhancement induces a transient, mild increase in hippocampal blood vessel density, accompanied by increases in newborn EC density, the frequency of small blood vessel segments, and VEGFA immunoreactivity. The differences detected 7 and 14 days following sonication appear to largely normalize to levels found in the contralateral hemisphere by 21 days. To the best of our knowledge, this is the first report of vascular growth following FUS+MB exposure in brain tissue. Although the mechanisms driving these changes were not thoroughly investigated here, previous work demonstrating acute inflammatory responses following FUS+MB-mediated BBB permeability enhancement [172,174,198,208,326] may implicate this as a contributing factor.

While increases in the relative area of GLUT1 immunodetection and the density of BrdU positive ECs indicate blood vessel growth in general, an increase in the frequency of blood vessel segments smaller than 5 µm in diameter may suggest that sprouting angiogenesis is responsible for these morphological changes. In general, angiogenesis proceeds with the breakdown of vascular basement membranes and sprouting of new blood vessels from existing vasculature, followed by a maturation of size and function. Previous work has shown that gene expression for proteins involved in basement membrane breakdown, such as matrix metalloproteinase-9 [341] and cathepsin-B [342], as well as other proteins implicated in EC proliferation, including galectin-3 [343] and early growth response-3 [344], are upregulated following FUS+MB exposure (described in *Chapter 2*) [326]. Thus, an increase in the relative frequency of small blood vessel segments 14 days following sonication, combined with previously characterized gene expression changes, may suggest that new blood vessels are being formed following sonication through angiogenic processes.

In addition, the observation that BrdU positive ECs were present in both small capillaries and larger vessels in the hippocampus may suggest that circulating endothelial progenitor cells are incorporated into vasculature following sonication. These cells are produced in bone marrow and respond to many of the same chemokines and growth factors that drive angiogenesis [345,346]. The incorporation of circulating endothelial progenitor cells into vasculature may be involved in blood vessel growth and repair following FUS+MB exposure and may contribute to increases in the relative area of GLUT1 immunodetection.

Qualitative analysis of VEGFA immunoreactivity may implicate this signalling pathway in the observed morphological changes. In a subset of rats, sparse vascular and perivascular VEGFA immunodetection was observed in the sonicated hippocampus 7 days after FUS+MB exposure (**Figure 4.8**). Given its well-established role in vascular growth [347], it is reasonable to hypothesize that increased VEGFA expression following sonication could contribute to the changes in vascular density observed here. Previous work has demonstrated an approximately 200% increase in VEGF expression 5 days after ultrasound exposure (with Definity MBs) in skeletal muscle, which was accompanied by vascular growth [339]. While the mechanical index (MI = PNP/√frequency) used in this work (MI = 0.7) was substantially higher than that employed in the present study (MI = 0.24 - 0.32; differences in duty cycle and sonication duration were also present), it is possible that FUS+MB exposures at lower MIs may induce VEGF expression at lower levels. Future work, utilizing more quantitative assays, is needed to investigate this effect in the brain. Additionally, evaluation of more acute time points may be necessary to observe the protein expression changes that drive these morphological changes.

Increased expression of several growth factors, including fibroblast growth factor, brain-derived neurotrophic factor, and VEGF, have previously been demonstrated by Kovacs *et al.* in the acute stages following FUS+MB exposure in the brain [208]. While these changes may be important drivers in the growth of blood vessels following sonication, it is important to note that there are several key differences in the sonication parameters used by Kovacs *et al.* and those used in the current study [348,349], making direct comparisons difficult; however, elevated levels of phosphorylated AKT, a downstream signalling molecule of VEGFA, has been reported at 1.5 and 24 hrs following sonication [350] with parameters closer to those employed in the current study. This supports the idea that VEGF levels may be elevated in the acute stages following FUS+MB exposure.

Changes in the expression of other well-established drivers of angiogenesis have previously been observed to follow FUS+MB exposure [326]. Of key importance may be CCL2, a cytokine involved in recruiting monocytes, memory T cells, and dendritic cells to sites of inflammation. Gene expression of *Ccl2* has been found to be increased at 6 hrs, and its receptor *Ccr2*, at 24 hrs, post-FUS+MB exposure [326]. Importantly, CCL2 has previously been shown to induce angiogenesis directly [351] and indirectly through recruitment of macrophages [241,352,353] and subsequent VEGFA production [353]. Other chemokines and cytokines produced in response to FUS+MB exposure, such as *Il1β*, *Ccl3*, and *Cxcl1* [326], have also been shown to promote angiogenesis in other contexts [354–357].

Previous work has demonstrated that an acute inflammatory response, as measured by NfκB pathway activation [198,208] and the expression of genes related to inflammation [326], follows FUS+MB exposure in the brain. Downstream indicators of inflammation and those potentially related to FUS+MB-induced inflammation have also been observed, including glial cell activation [172,174,175,208], neurogenesis [230,231,358,359], Aβ plaque clearance [136,172,174,360], immune cell infiltration [128,174,197,208,211–214], downregulation of transporters [291,326,361], and now angiogenesis. The magnitude and implications of these responses have been the topic of debate [198,208,348,349,362,363]. A large body of evidence suggests that single exposures to FUS+MB-mediated BBB permeability enhancement result in minimal short term and no evidence of long-term behavioral deficits [203,330,364,365]. Repeated FUS+MB exposures have similarly been shown to have limited detrimental effects on behavior [128,136,321,330], and even improvements in mouse models of AD [136,174]; however, determining the impact of different treatment repetition frequencies has not been an area of thorough investigation. Results presented here would suggest that 21 days between sonications may serve as a conservative guideline to ensure brain tissue is allowed to recover from intervention, reducing the

potential for detrimental impacts to accumulate. When considering treatment strategies and disorders for which the risks of minor tissue damage or acute inflammation are of less concern (E.g. brain tumors), a less conservative treatment repetition frequency may be warranted.

4.4.1. Limitations

In the present study, no significant correlations were found between BBB permeability enhancement and blood vessel density or newborn EC density. CE-T1w MR images were acquired following sonication and while this approach is valuable for confirming BBB permeability enhancement, MR methods exist that can provide a more quantitative assessment of vascular leakage. The information provided by dynamic contrast enhanced-MRI, for example, would enable a more accurate assessment of the effects of FUS+MB exposure on BBB permeability and potentially reveal correlations to the bioeffects observed. Alternatively, the angiogenic response following sonication may not follow a linear progression; sampling at course time intervals following FUS+MB exposure may capture blood vessel growth/angiolysis at different phases depending on the magnitude of initial BBB permeability enhancement.

Another limitation of this work is that it does not differentiate between BrdU positive ECs incorporated into vessels or formed by division and those in which DNA damage was significant. It is important to note that BrdU is incorporated into any cell in which DNA synthesis is occurring, thus it is possible that a portion of the BrdU positive ECs quantified in this work were in the process of DNA damage repair while BrdU was present. Administration of BrdU was delayed until 24 hrs after sonication to reduce the potential for this to significantly impact results.

Lastly, assessment of VEGFA expression following FUS+MB exposure was qualitative. While differences in immunoreactivity between sonicated and control hemispheres were visually apparent in a subset of rats at 7 days post-FUS+MBs, the magnitude of this difference was not quantified. Investigation into the time course of VEGFA expression with more quantitative assays is warranted and would provide valuable information as to the magnitude and duration of this response. In addition, this would allow direct comparisons to other conditions in which VEGFA expression is acutely elevated and blood vessel growth results.

4.4.2. Conclusion

Work presented here indicates that FUS+MB-mediated BBB permeability enhancement is followed by a mild, temporary increase in hippocampal blood vessel density, accompanied by increases in newborn EC density, frequency of small blood vessel segments, and sparse VEGFA immunoreactivity. Importantly, the differences detected 7 and 14 days following sonication appear to normalize to levels found in the contralateral hemisphere by 21 days. It is possible that an acute inflammatory response following sonication drives the transient morphological changes observed here. These findings may have less significance for the safety of single FUS+MB exposures, given the magnitude of effect and results of previous behavioural studies, but may have relevance to the optimal frequency of repeated exposures. While FUS+MB exposure as a method to increase BBB permeability remains a promising strategy for drug delivery to the brain, this work emphasizes the importance of continued effort to characterize the biological changes that follow in order to tailor treatment strategies to specific disorders and to fully understand the risks of this technique.

Chapter 5

Dexamethasone Reduces Vascular Permeability and Inflammatory Response Following Focused Ultrasound and Microbubble Exposure

5.1. Introduction

The safety of modulating BBB permeability for drug delivery using FUS+MB exposure continues to spark debate [197,198,208,348,349,362,363], specifically in the context of diseases for which the aim of treatment is to preserve or improve long-term neural function. The development [133,232] and continued refinement [75,134,340] of acoustic feedback control strategies have largely removed the risk of overt tissue damage (I.e. microhemorrhage, necrosis, substantial apoptosis); however, the transient induction of inflammation [198,326], changes in gene and protein expression [198,326,366], and altered cell morphology [337] have all been noted following FUS+MB exposures that employ some form of acoustic feedback control. While there is debate regarding the degree, duration, and impact of these responses, it would be advantageous to develop strategies to mitigate the remaining risks.

Dexamethasone (DEX) is a synthetic glucocorticoid, used in a wide range of clinical applications, including the management of severe allergies, rheumatic diseases, and shock [367]. Acting via glucocorticoid receptor binding, DEX can activate or suppress the transcription of specific genes controlled by glucocorticoid response elements. DEX can also act through non-transcriptional pathways, leading to the rapid activation of protein kinases. This can result in the activation of endothelial nitric oxide synthase, leading to altered blood flow and decreased vascular inflammation [368]. In preclinical models, DEX has been shown to reduce inflammation and edema following intracerebral hemorrhage [369,370] and rapidly decrease vascular permeability in glioma [371,372]. The effects of DEX on inflammation,

cerebral edema, and BBB integrity, have been utilized in the context of mannitol-induced BBB permeability enhancement [373] in response to adverse events in clinical trials [374].

The goals of the work presented in *Chapter 5* were to explore the impact of post-sonication DEX administration on vascular permeability, inflammation, blood vessel growth, and astrocyte activation. Dynamic contrast-enhanced magnetic resonance imaging (DCE-MRI) was used to quantitatively assess vascular permeability. The overarching goal of this work was to assess the suitability post-FUS+MB DEX administration as a means to control the duration of BBB permeability enhancement and to minimize the risks of inflammation-induced tissue damage.

5.2. Materials and Methods

5.2.1. Animals

Male Sprague Dawley rats (n = 40), weighing 230–330 g on the day of sonication, were used in this study (Taconic Biosciences, Germantown, NY, USA). Animals were housed in the *Sunnybrook Research Institute* animal facility (Toronto, ON, Canada) with access to food and water *ad libitum*. All animal procedures were approved by the *Animal Care Committee* at *Sunnybrook Research Institute* and are in accordance with the *Canadian Council on Animal Care* guidelines.

5.2.2. Study Design

FUS+MB exposure was unilaterally targeted to the dorsal hippocampus, followed by quantitative MRI at 15 min post-sonication, consisting of T1-mapping and DCE-MRI, to assess BBB permeability. Saline or DEX (5 mg/kg; ip) was administered following imaging and animals were allowed to recover from anesthesia. At 2 hrs following sonication, quantitative MRI was repeated to determine the change in BBB permeability relative to 15 min post-FUS+MBs. A second dose of saline or DEX (5 mg/kg; ip) was administered 24 hrs following sonication.

Prior to FUS+MB exposure, animals were randomized to receive either saline or DEX following sonication. Within these treatment groups, animals were further randomized to be sacrificed at either 2 days or 10 days post-FUS+MBs, for protein expression and immunohistological analysis, respectively. These time

points were designed to capture changes in inflammatory protein expression, astrocyte activation, and vascular growth, based on previous work [172,208,326,366].

5.2.3. Animal Preparation and FUS+MB Exposure

Animal preparation and anesthesia were as described in *Chapter 3*. For the structural imaging and sonication, animals were secured in a supine position on an MRI-compatible sled (**Figure 5.1A**), allowing transport between the bore of the MRI and the FUS system. For quantitative MRI, animals were positioned prone to allow the receive coil to be placed in closer proximity to the brain. A bite bar and nose cone were used to secure the position of the head.

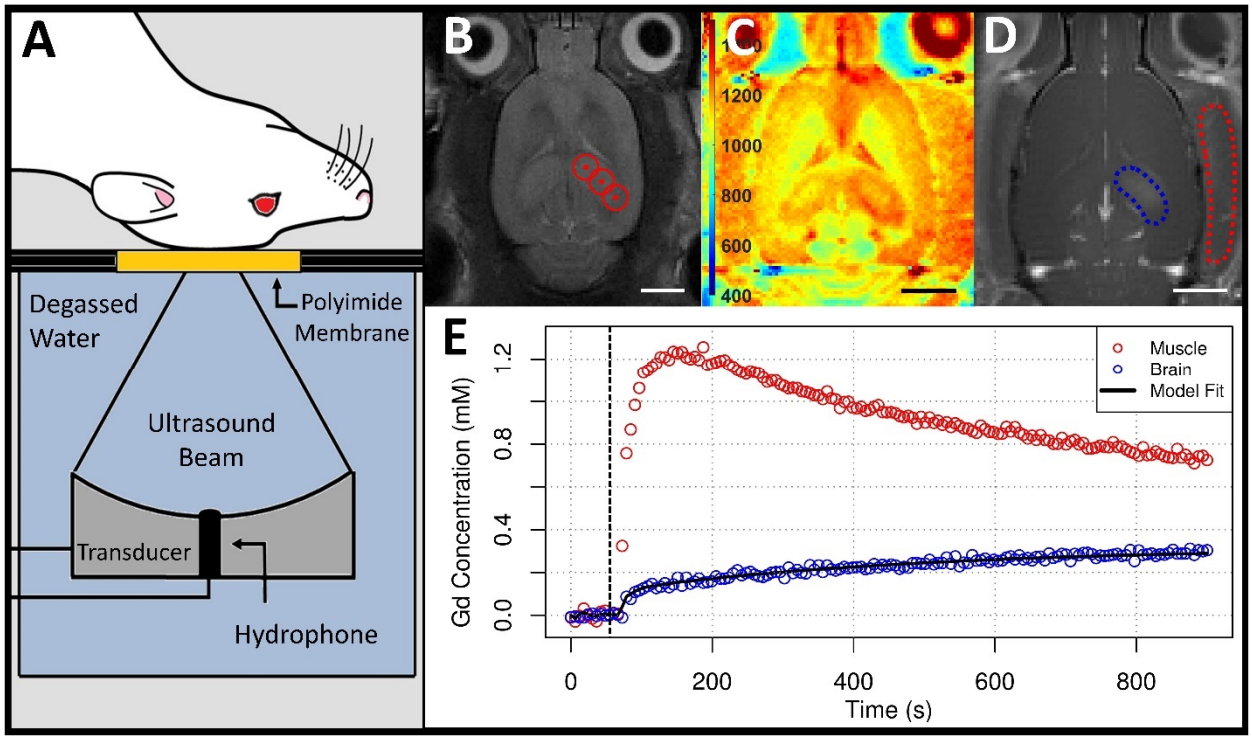

Figure 5.1. MRI-Guided FUS+MB Exposure and Quantitative MRI. (A) During structural imaging and sonication, rats were positioned supine on an MRI compatible sled with the dorsal surface of the head coupled to a polyimide membrane. The bottom of the membrane was coupled to a tank below filled with degassed, deionized water, housing the transducer/hydrophone assembly. (B) FUS was unilaterally targeted to the dorsal hippocampus based on T2w images. Quantitative MRI protocol consisted of (C) pre-contrast T1 mapping (scale bar indicates longitudinal relaxation time in ms) and (D) DCE-MRI (depicts an average of the final 20 images captured). ROIs were drawn in the sonicated dorsal hippocampus and left temporal muscle based on pre-contrast inversion prepared RARE images (TI = 500 ms). (E) Contrast agent concentration was fit to a modified Tofts-Kermode model to estimate K^{trans} in the dorsal hippocampus. A reference-tissue (temporal muscle) method was used to estimate an arterial input function for this model. Scale bars = 4 mm.

Sonications were performed as described in *Chapter 4*, with the following changes. The FUS system was equipped with a spherically focused transducer driven at 580 kHz (f = transmit frequency, focal number = 0.8, external diameter = 75 mm). Acoustic emissions were monitored with an in-house manufactured PZT hydrophone located in a 25 mm opening in the centre of the transducer. For acoustic feedback control, once the magnitude of acoustic emissions at $1.5f$ or $2.5f$ passed the mean of baseline (MBs not in circulation) plus 10 standard deviations of the mean, the sonicating pressure was dropped by 50% and maintained at this level for the remainder of sonication. Three targets were placed in the left dorsal hippocampus of each animal (**Figure 5.1B**).

5.2.4. Retrospective Acoustic Emissions Analysis

Hydrophone signals captured during each burst (capture length = 11 ms, sampling rate = 20 MS/s) using a 14-bit scope card (ATS460; AlazarTech, Pointe-Claire, Quebec, Canada) were analysed retrospectively to explore potential relationships between BBB permeability enhancement (prior to DEX or saline administration) and spectral characteristics of the acquired acoustic emissions. At each target, the first 10 bursts were used as baseline measurements (MBs not in circulation). Fast Fourier transforms (FFT) were calculated for each burst to obtain signal spectra, from which specific frequencies of interest were analysed (integration bandwidth = ± 0.2 kHz). The exposure-average magnitude of $0.5f$, f, $1.5f$, $2f$, and wideband emissions were calculated for each target by subtracting the corresponding baseline signal values from each burst and then averaging across all bursts and targets within an animal. Wideband emissions were monitored at 890 kHz ± 5 kHz, corresponding to the peak sensitivity of the hydrophone. The peak magnitude of $0.5f$, f, $1.5f$, $2f$, and wideband emissions were defined as the maximum signal value (after subtracting corresponding baseline signal values) at a single burst over the duration of sonication.

5.2.5. MRI Data Acquisition

All MR experiments were conducted on a 7T horizontal bore Avance BioSpec 70/30 scanner (Bruker BioSpin, Ettlingen, Germany) with a 20 cm inner diameter gradient insert coil with maximum gradient amplitude of 668 mT/m (Bruker BioSpin, Ettlingen, Germany). Images were acquired using an 8 cm inner diameter volume coil for transmit and a quadrature rat brain coil to receive (Bruker BioSpin, Ettlingen, Germany). MRI examinations were conducted under 1.5-2% isoflurane anesthesia with medical air.

Structural T2w images used for FUS targeting were acquired using a RARE sequence with TE 46.2 ms, TR 4000 ms, and 1.0 mm slice thickness, prior to sonication. Targets were chosen in the sonication system software based on these images.

Quantitative MRI consisted of DCE-MRI with pre-contrast T1 mapping. A single slice with an axial orientation at the level of the dorsal hippocampus was selected for imaging. Identical slice location and geometry were used for all quantitative MRI.

For the DCE-MRI, a FLASH sequence with TE 2.175 ms, TR 20 ms, 20° flip angle, 3 averages, matrix size 100 x 100, field of view 24 mm x 24 mm, and slice thickness 1.0 mm, was acquired at a temporal resolution of 6.0 sec for 15 min. A bolus of gadobutrol (0.4 mmol/kg; Gadovist, Bayer AG, Leverkusen, Germany) was administered intravenously after 1 min (10 pre-contrast images), followed by an additional 14 min of imaging.

T1 mapping was performed immediately prior to DCE-MRI using an inversion recovery RARE sequence with TE 7 ms, TR 5000ms, rare factor of 16, 1 average, matrix size 100 x 100, field of view 24 x 24 mm^2, slice thickness 1.0 mm, and 5 inversion times: 125, 250, 500, 1500, and 4500 ms.

5.2.6. DCE-MRI Analysis

To quantitatively assess BBB permeability, the transfer constant (K^{trans}) of gadobutrol from plasma to extravascular-extracellular space (EES) was calculated from T1-mapping and DCE-MRI. K^{trans} measurements were obtained at 15 min and 2 hrs post-FUS+MBs, denoted as $K^{trans,\ 15\ min}$ and $K^{trans,\ 2\ hrs}$, respectively. The relationship between the concentration of contrast agent and change in relaxation rate can be expressed as:

$$CA(t) = \frac{1/T_1(t) - 1/T_{10}}{r_1} \qquad (1)$$

where CA(t) is contrast agent concentration as a function of time, r_1 is the longitudinal relaxivity of gadobutrol (4.2 s^{-1} mM^{-1} in human whole blood at 37°C in a 7T field [367]), $T_1(t)$ is the T1 of tissue as a function of time, and T_{10} is the T1 of tissue in the absence of contrast agent.

T_{10} was calculated from the T1 maps acquired immediately prior to DCE-MRI (**Figure 5.1C**). T1 maps were calculated by fitting the inversion recovery data to the following equation using Matlab (Mathworks Inc., Natick, MA, USA):

$$S(TI) = M_0\left(1-(1+cos(\alpha))e^{\frac{-TI}{T1}}+cos(\alpha)e^{\frac{-TR}{T1}}\right) \quad (2)$$

where the initial magnetization (M_0), the error in flip angle (α), and T1 are the free parameters. Contrast agent concentration was fit to a modified Tofts-Kermode model [368] that accounts for the presence of separate intravascular and extravascular extracellular compartments (**Figure 5.1E**). Least squares regression was used for fitting. The tissue concentration of gadobutrol, was modeled with the following equation:

$$C_t(t) = v_p\,C_p(t) + K^{trans}\int_0^t C_p(t')\,e^{\frac{-K^{trans}(t-t')}{v_e}}\cdot dt' \quad (3)$$

where $C_t(t)$ is the concentration of contrast agent in tissue (calculated using Equation 1) as a function of time, K^{trans} is the transfer rate constant from the intravascular space to the EES, v_p and v_e are the plasma volume and distribution volume of contrast agent in the EES (per unit volume of tissue), respectively. $C_p(t)$, the plasma concentration of gadobutrol as a function of time (arterial input function, AIF), was estimated using a reference-tissue method [369,370].

The time-dependent concentration of gadobutrol in temporal muscle (C_{muscle}; calculated using Equation 1) was used to derive the AIF using literature values of $K^{trans,\,muscle}$ (0.11 min^{-1}) and $v_{e,\,muscle}$ (0.20) in rat muscle [369] as follows:

$$C_p(t) = \frac{1}{K^{trans,muscle}}\cdot dC_{muscle}(t)/dt + C_{muscle}(t)/v_{e,muscle} \quad (4)$$

This data-driven AIF approach has previously been shown to produce accurate estimates of K^{trans} when compared to direct measurement [371,372] and population-derived AIF approaches [370]. For estimates of K^{trans} in the dorsal hippocampus, a region of interest was drawn based on pre-contrast inversion prepared RARE images (TI = 500 ms).

5.2.7. Protein Analysis

Two days following sonication, animals randomized to protein analysis were transcardially perfused with ice-cold PB (0.1M, pH 7.4). Dorsal hippocampi were rapidly dissected on ice, frozen with dry ice, and stored at -80 °C until further processing. For protein extraction, tissue was placed in 1x RIPA buffer with protease inhibitors (ab65621, Abcam Inc, Cambridge, MA, USA) on ice at a concentration of 10 µl/mg of tissue. Samples were homogenized via sonication (Sonifier 250, Branson Ultrasonics, Danbury, CT, USA) then centrifuged at 15000 g for 20 min at 4 °C. Supernatant was aliquoted and stored at -80 °C until analysis. BCA assay (Thermo Scientific, Waltham, MA, USA) was used to determine total protein concentration for each sample.

Rat Cytokine Array Q2 (Raybiotech, Norcross, GA, USA) was used to assess concentrations of MCP1, intercellular adhesion molecule-1 (ICAM1), interferon gamma (IFNɣ), IL10, IL1β, IL6, leptin (LEP), L-selectin (SELL), TIMP1, and TNFα. The assay was performed in accordance with manufacturer's instructions using a total protein concentration of 1000 µg/ml.

To assess the concentrations of GFAP and VEGF, enzyme-linked immunosorbent assays (ELISAs) were performed in accordance with manufacturer's instructions (GFAP: ab233621, Abcam Inc, Cambridge, MA, USA; VEGF: ab100787, Abcam Inc, Cambridge, MA, USA). Total protein concentrations of 1 µg/ml and 100 µg/ml were used for GFAP and VEGF ELISAs, respectively. All protein concentrations are expressed as a ratio of sonicated to non-sonicated hippocampi within each animal.

5.2.8. Immunohistochemistry

Ten days following sonication, animals randomized to immunohistochemical analysis were transcardially perfused with ice-cold PB (0.1M, pH 7.4), followed by 4% paraformaldehyde in PB. Brains were extracted, post-fixed for 24 hrs at 4 °C, then transferred to 30% sucrose in PB and stored at 4 °C until fully saturated (~3 days). Brains were embedded in optimum cutting temperature compound (Tissue-Tek, Torrance, CA, USA) and stored at -80 °C until cryostat sectioning. Coronal sections (35 µm thick) were stored in cryoprotectant (glycerin, ethylene glycol, and 0.2M PB in a ratio of 2:3:5, respectively) at -10°C until immunohistological processing.

Free-floating sections were blocked for 1 hr at room temperature (0.1% Triton X-100, 1% bovine serum albumin, 2% goat serum, 1x PBS), then incubated in rabbit anti-GFAP primary antibodies (1:800; ab7260, Abcam Inc, Cambridge, MA, USA) for 48 hrs at 4 °C. Sections were incubated in goat anti-rabbit IgG Alexa Fluor 647 secondary antibody (1:800; ab150079, Abcam Inc, Cambridge, MA, USA) for 24 hrs at 4 °C, then mounted onto charged glass slides (X-tra, Leica Microsystems, Wetzlar, Germany) and coverslipped with aqueous mounting media (Fluoroshield™ with DAPI, Sigma-Aldrich Corporation, St. Louis, MO, USA). Three 10-min washes were performed following each step, except blocking. Slides were stored in the dark at 4 °C until imaging.

Staining for blood vessels followed the same protocol as above with the addition of an antigen retrieval step. Prior to primary antibody incubation, sections were placed in 2 M HCl for 90 min, followed by 10 min in 0.1 M borate buffer (pH 8.5). A combination of rabbit anti-cluster of differentiation 31 (CD31; 1:800; ab28364, Abcam Inc, Cambridge, MA, USA) and rabbit anti-GLUT1 (1:800; ab15309, Abcam Inc, Cambridge, MA, USA) primary antibodies were used to produce more complete blood vessel labeling.

5.2.9. Confocal Imaging

For quantification of GFAP immunoreactive density and blood vessel density by size, image stacks (3 µm spacing, 0.60 µm/pixel, 1024×1024-pixel field of view) were collected through the entire thickness of each section, bilaterally, in each of 3 hippocampal subfields, CA1, CA4, and the DG. Sections (7-9 per animal) were imaged with a 20x objective (NA 0.75) using a confocal laser scanning microscope system (A1+, Nikon, Tokyo, Japan) at excitation wavelengths of 639.1 nm and 403.1 nm for GFAP/GLUT1/CD31 and DAPI, respectively. Emissions were received at 663-738 nm and 425-475 nm, respectively. To ensure subsequent image analysis was performed on consistent regions of the dorsal hippocampus, image stacks were rotated and cropped to include only stratum radiatum of CA1, between the blades of the DG for CA4, and the molecular layer of the DG. Image stacks were also trimmed in the z-direction, keeping 5 images starting at the first complete optical section.

5.2.10. Confocal Image Analysis

GFAP positive astrocytes were segmented using an in-house designed *ImageJ* pipeline. The *Tubeness* plugin (ImageJ), with sigma values of 0.2, 0.4, and 0.75, was used to detect *tube-like* structures within

each image. This plugin uses eigenvalues of the Hessian matrix to calculate a measure of *tubeness* for each pixel within an image [381]. Using larger values of sigma, thicker tubes are detected. The sigma values used in this study were empirically chosen to highlight the full range of sizes of astrocytic processes. Once detected, structures were segmented by auto-thresholding and binary masking. GFAP immunoreactive density for each image stack was calculated as a sum of densities for all images, then averaged across all image stacks in each hemisphere. Density measurements are expressed as a ratio of sonicated to non-sonicated dorsal hippocampus for each animal.

Maximum intensity projections of GLUT1/CD31 stained sections were used to quantify the density of blood vessel segments by size. Using *ObjectJ* (ImageJ), the diameter of each blood vessel segment was manually measured in each image by an author (DM) blinded to treatment. For each animal, a histogram of blood vessel segment frequency, binned to diameters of <5 µm, 5–7.5 µm, 7.5–10 µm, and >10 µm, was normalized to imaging volume to calculate density. Mean densities of blood vessel segments for each bin are expressed as a relative difference between sonicated and non-sonicated dorsal hippocampus for each animal.

5.2.11. Statistics

All statistical analyses were performed using R 3.4.3. For the comparison of dorsal hippocampal $K^{trans,\ 15\ min}$ to $K^{trans,\ 2\ hrs}$, between saline and DEX-treated animals, analysis of covariance (ANCOVA) was used to assess statistical significance. Differences in the density of blood vessel segments, protein expression, and GFAP immunoreactive density between sonicated and non-sonicated hemispheres within experimental groups were assessed by paired Student's t-tests (two-tailed). False discovery rate (FDR) correction for multiple comparisons was used to account for the simultaneous measurement of 5 proteins by rat cytokine array and for the assessment of 4 bins of blood vessel diameters. Linear least-squares regression was used to assess the relationship between dorsal hippocampal $K^{trans,\ 15\ min}$ and both the peak and exposure-average magnitude of acoustic emissions at specific frequencies. For all analyses, a p-value of 0.05 was used as the threshold for statistical significance. Unless otherwise specified, variance is expressed as standard deviation of the mean.

5.3. Results

5.3.1. Peak Negative Pressure and BBB Permeability Enhancement

BBB permeability was assessed at 15 min and 2 hrs post-FUS+MB exposure by quantitative MRI. $K^{trans,\ 15\ min}$ in the sonicated dorsal hippocampus, prior to the administration of DEX or saline, ranged from 0.0023 min^{-1} to 0.0231 min^{-1}. The $K^{trans,\ 15\ min}$ values reported here are consistent with previous observations following FUS+MB exposure [121,142,196,382].

For inclusion in all analyses focused on the effects of DEX, a minimum $K^{trans,\ 15\ min}$ threshold was set at 0.005 min^{-1}, based on pilot work. This threshold was set to ensure that changes in BBB permeability were detectable 2 hrs following sonication, enabling an accurate assessment of the changes in vascular permeability relative to 15 min post-FUS+MBs. Of the 40 animals that underwent unilateral dorsal hippocampal FUS+MB exposure and DCE-MRI, 29 satisfied this criterion and 11 were excluded. Of these 29 animals, 14 were treated with saline and 15 were treated with DEX following sonication.

Prior to saline or DEX administration, no significant difference was detected in dorsal hippocampal $K^{trans,\ 15\ min}$ between groups (saline = 0.0132 min^{-1} ± 0.0059 min^{-1}; DEX = 0.0128 min^{-1} ± 0.0047 min^{-1}; p = 0.85). Similarly, no significant differences were detected in dorsal hippocampal $K^{trans,\ 15\ min}$ between groups sacrificed at 2 days (saline = 0.0136 min^{-1} ± 0.0050 min^{-1}; DEX = 0.0138 min^{-1} ± 0.0045 min^{-1}; p = 0.95) or 10 days (saline = 0.0128 min^{-1} ± 0.0070 min^{-1}; DEX = 0.0121 min^{-1} ± 0.0050 min^{-1}; p = 0.80) following sonication.

5.3.2. Correlations Between Acoustic Emissions and BBB Permeability

During sonication, PNP was increased until acoustic emissions at $1.5f$ or $2.5f$ were detected above baseline. Maximum PNP values (triggering PNP) were 362 kPa ± 74 kPa and 388 kPa ± 72 kPa, in DEX and saline-treated animals, respectively (p = 0.27). PNP was maintained at 50% of the triggering pressure for the remainder of sonication.

Due to software errors, complete scope card data were captured for only 32 of 40 animals. The 8 animals with truncated data were excluded from retrospective acoustic emissions analysis; however, no minimum $K^{trans,\ 15\ min}$ threshold was set for inclusion.

Retrospective analysis of the exposure-average magnitude of $2f$ emissions showed a strong linear correlation to dorsal hippocampal $K^{trans,\ 15\ min}$ (r^2 = 0.689; **Figure 5.2**). The exposure-average magnitude of $0.5f$, f, $1.5f$, or wideband emissions showed no strong correlations to dorsal hippocampal $K^{trans,\ 15\ min}$, with r^2 values of 0.012, 0.156, 0.107, and 0.004, respectively (**Appendix Figure 5.1**). Similarly, linear regression analysis of the peak magnitude of $0.5f$, f, $1.5f$, $2f$, or wideband emissions during sonication versus $K^{trans,\ 15\ min}$ displayed r^2 values of 0.033, 0.046, 0.0264 0.597, and 0.005, respectively (**Appendix Figure 5.1**).

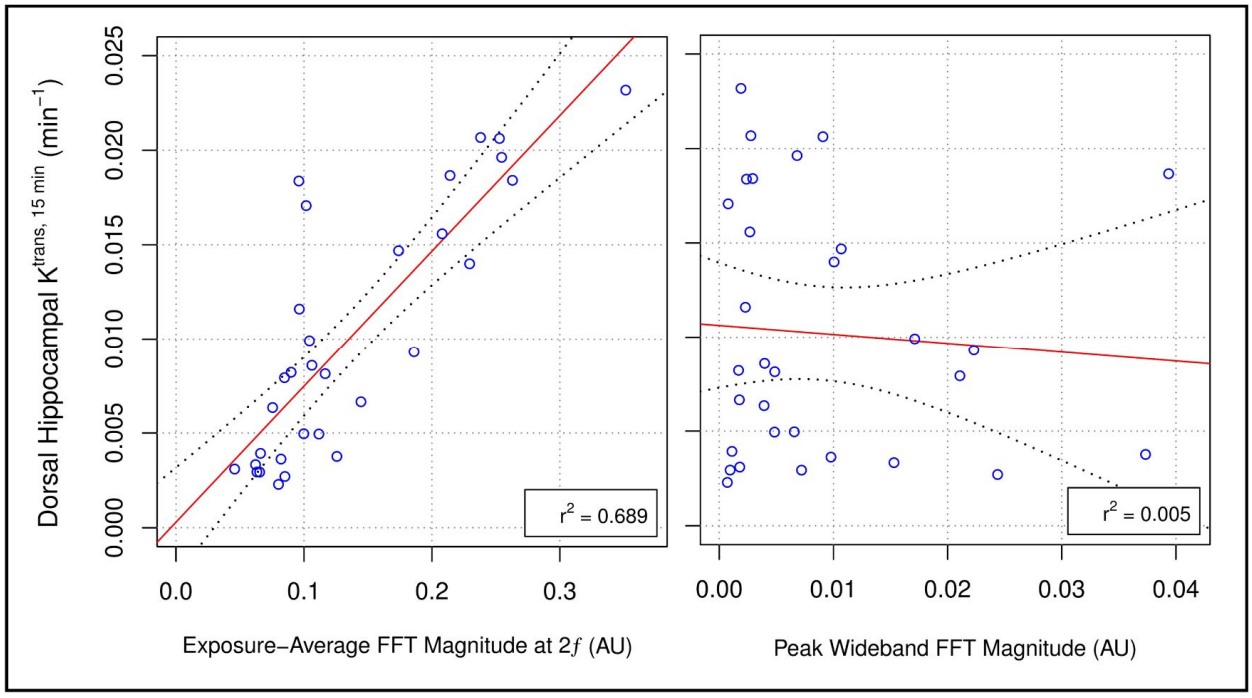

Figure 5.2. Correlations Between Acoustic Emissions and Dorsal Hippocampal $K^{trans,\ 15\ min}$. Hydrophone signals captured during FUS+MB exposures were analysed retrospectively to explore potential relationships between $K^{trans,\ 15\ min}$ measurements and spectral characteristics of the acquired acoustic emissions. The exposure-average magnitude of $2f$ emissions displayed a strong linear correlation to $K^{trans,\ 15\ min}$ in the sonicated dorsal hippocampus (r^2 = 0.689). Peak wideband emissions did not explain a significant portion of the variance in $K^{trans,\ 15\ min}$ measurements. These results suggest that the changes in BBB permeability observed in this study were not driven inertial cavitation. Black dotted lines indicate 95% confidence intervals. AU = arbitrary units.

5.3.3. Effects of DEX on BBB Permeability

To determine its impact on BBB permeability following FUS+MBs, DEX was administered following $K^{trans,\ 15\ min}$ measurements. ANCOVA was used to assess the effect of treatment (saline vs DEX) on the change in

dorsal hippocampal K^{trans} between 15 min and 2 hrs following sonication. Compared to saline-control (n = 14), DEX (n = 15) was found to significantly reduce $K^{trans,\ 2\ hrs}$ after administration (p = 0.003). At 2 hrs following sonication, K^{trans} had dropped by 60.8% ± 9.7% and 74.2% ± 10.4% in animals that received saline and DEX, respectively (**Figure 5.3B**). This result suggests that DEX significantly alters BBB permeability following FUS+MBs, acting to expedite the restoration of BBB integrity.

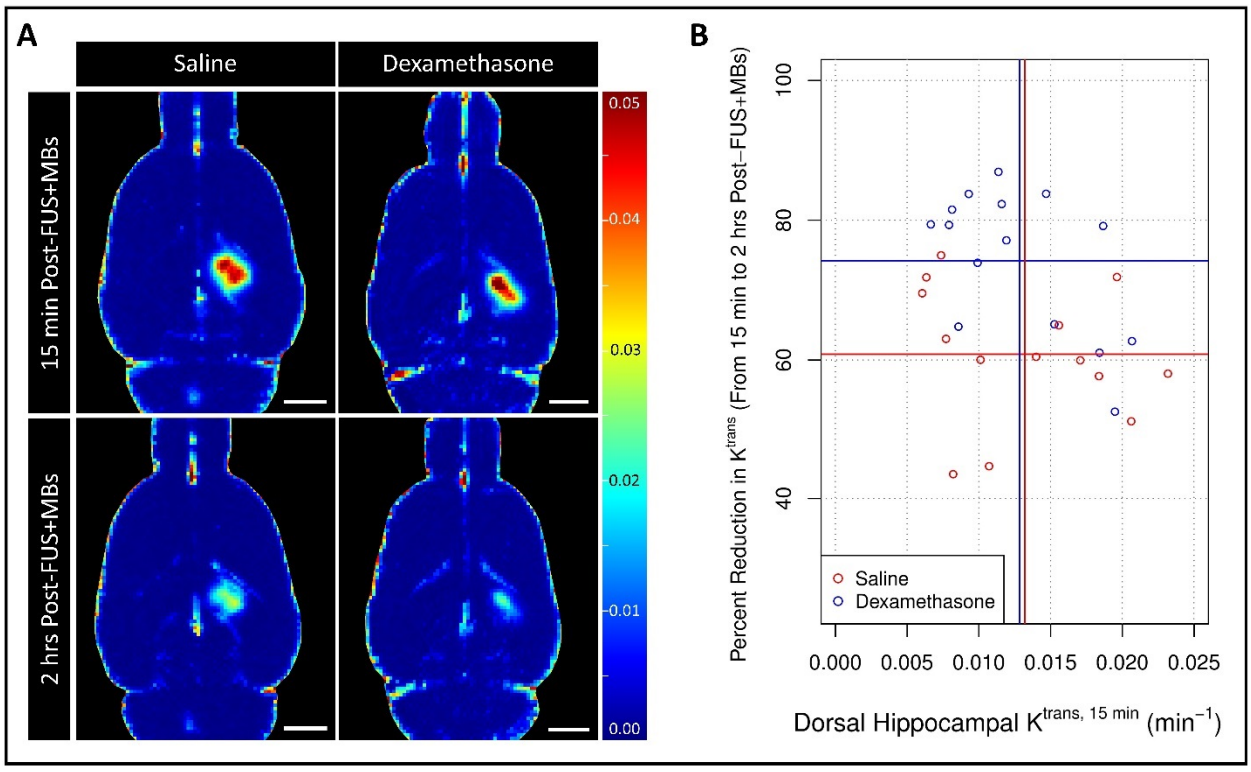

Figure 5.3. Impact of DEX on BBB Permeability Enhancement Following FUS+MB Exposure. (A) Representative K^{trans} maps acquired at 15 min and 2 hrs post-FUS+MB exposure, demonstrate a more rapid restoration of BBB integrity in DEX-treated animals. (B) DEX administration resulted in a significantly greater reduction in mean dorsal hippocampal K^{trans} from 15 min to 2 hrs post-FUS+MBs (74.2% ± 10.4%), compared to saline administration (60.8% ± 9.7%). p = 0.003 (ANCOVA). No significant differences were detected in mean dorsal hippocampal $K^{trans,\ 15\ min}$ between saline and DEX-treated animals. Vertical and horizontal lines represent group means relative to their respective axes. n = 14 saline-treated and 15 DEX-treated animals. Scale bars = 3 mm.

5.3.4. Expression of Inflammatory Markers

The expression of select inflammatory markers were assessed bilaterally in the dorsal hippocampi 2 days following sonication by rat cytokine array (**Figure 5.4**). The mean ratios of ICAM1 and MCP1 expression in

the sonicated to non-sonicated dorsal hippocampi for saline-treated animals (n = 7) was 1.83 ± 0.81 (p = 0.049) and 2.05 ± 0.72 (p = 0.049), respectively. No significant differences in the expression of TIMP1, LEP, and IFNg were detected between hemispheres. For proteins of interest with more than 25% of samples below the dynamic range of measurement (IL10, IL1β, IL6, SELL, and TNFα), analysis of differential expression between hemispheres was not performed. No significant differences between sonicated and non-sonicated dorsal hippocampi in the expression of any of proteins assessed were observed in DEX-treated animals (n = 7).

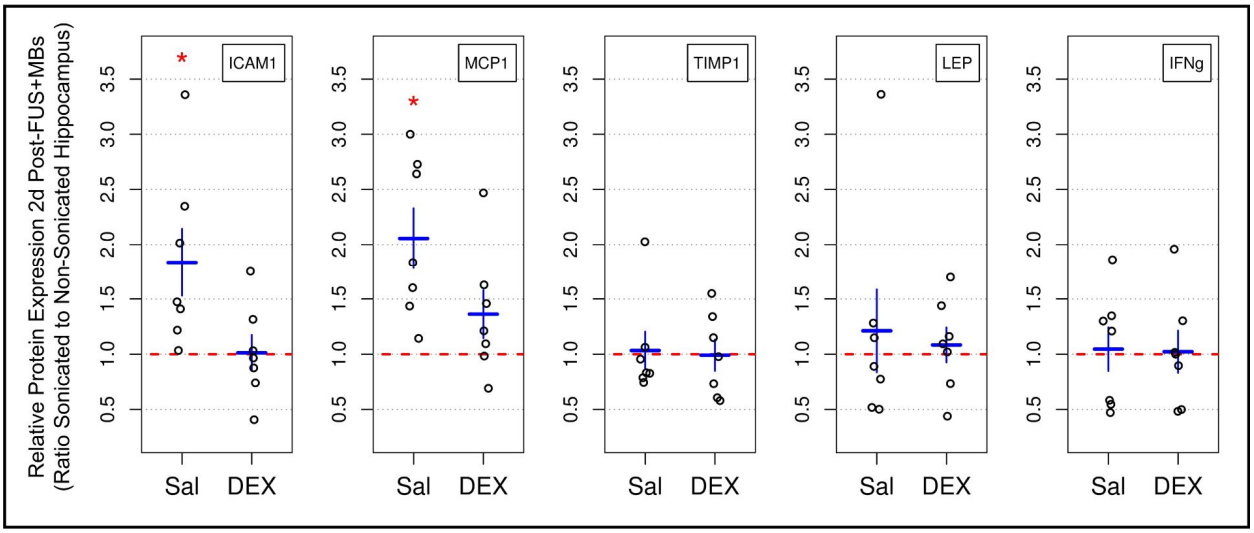

Figure 5.4. Relative Protein Expression 2 Days Post-FUS+MB Exposure. The expression of select inflammatory markers were assessed bilaterally in dorsal hippocampi 2 days following sonication by rat cytokine array. The mean ratios of ICAM1 and MCP1 expression in the sonicated to non-sonicated dorsal hippocampi for saline-treated animals was 1.83 ± 0.81 (p = 0.049) and 2.05 ± 0.72 (p = 0.049), respectively. No significant differences in the expression of TIMP1, LEP, and IFNg were detected between hemispheres. Animals receiving DEX following FUS+MBs (n = 7) did not display significant differences between sonicated and non-sonicated dorsal hippocampi in the expression of any of the proteins assessed. * indicates p < 0.05, paired Student's t-test, corrected for multiple comparisons. Red, horizontal, dashed line indicates no difference between sonicated and non-sonicated dorsal hippocampi. Error bars represent standard error of the mean. n = 7 saline-treated and 7 DEX-treated animals.

5.3.5. GFAP Expression and Immunoreactivity

Elevations in GFAP protein expression [172] and immunoreactivity [172,197,208] have previously been observed following FUS+MB-mediated BBB permeability enhancement. In the current study, dorsal hippocampi were bilaterally dissected 2 days following sonication and GFAP expression was measured by ELISA (**Figure**

5.5A). The mean ratio of GFAP expression in the sonicated to non-sonicated dorsal hippocampi for saline-treated animals (n = 7) was 1.36 ± 0.26 (p = 0.005). Conversely, animals receiving DEX (n = 7) displayed no significant differences between hemispheres; the mean ratio of GFAP expression in the sonicated to non-sonicated dorsal hippocampi for DEX-treated animals was 1.07 ± 0.24 (p = 0.56).

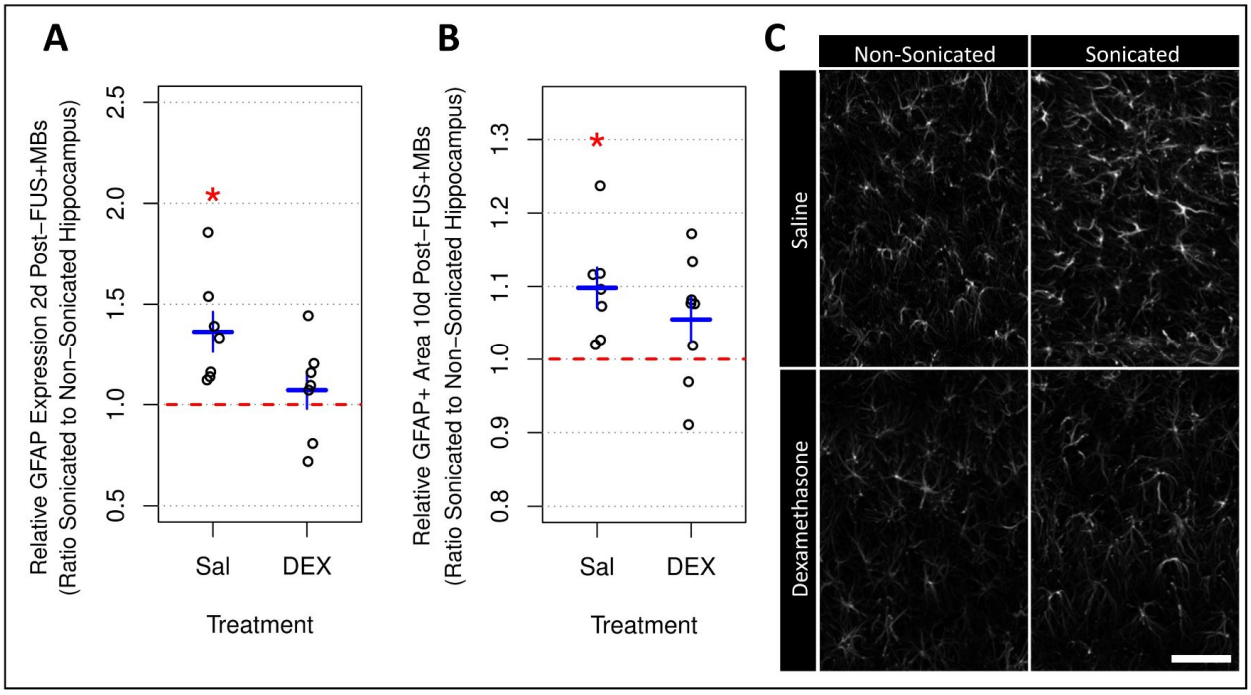

Figure 5.5. Relative GFAP Expression and Immunoreactive Density Following FUS+MB Exposure. (A) Two days following sonication, the mean ratio of GFAP expression in the sonicated to non-sonicated dorsal hippocampi for saline-treated animals was 1.36 ± 0.26 (p = 0.005). Animals receiving DEX displayed no significant differences (p = 0.56). (B) Ten days post-FUS+MBs, the mean ratio of GFAP immunoreactive density in the sonicated to non-sonicated dorsal hippocampi for saline-treated animals was 1.10 ± 0.07 (p = 0.01). Animals receiving DEX did not display a significant difference in dorsal hippocampal GFAP immunoreactive density between hemispheres (mean ratio of 1.06 ± 0.09 for GFAP immunoreactive density in the sonicated to the non-sonicated dorsal hippocampi; p = 0.11). (C) Representative images of GFAP immunoreactivity 10 days following FUS+MB exposure demonstrating reactive astrocytes in the sonicated hippocampus of saline-treated animals (scale bar = 100 µm). * indicates $p < 0.05$, paired Student's t-test. Red, horizontal, dashed line indicates no difference between sonicated and non-sonicated dorsal hippocampi. Error bars represent standard error of the mean. n = 7 saline-treated and 7 DEX-treated animals for analysis 2 days post-FUS+MB exposure. n = 7 saline-treated and 8 DEX-treated animals for analysis 10 days post-FUS+MB exposure.

GFAP immunoreactive density was assessed 10 days post-FUS+MB exposure in tissue sections using confocal imaging and an automated image analysis pipeline (**Figure 5.5B**). The mean ratio of GFAP

immunoreactive density in the sonicated to non-sonicated dorsal hippocampi for saline-treated animals (n = 7) was 1.10 ± 0.07 (p = 0.01). Animals receiving DEX (n = 8) did not display a significant difference in dorsal hippocampal GFAP immunoreactive density between hemispheres, with a mean ratio of 1.06 ± 0.09 (p = 0.11) for the sonicated to the non-sonicated hemispheres; however, the current study may be underpowered to detect significant differences in GFAP immunoreactive density, given the larger variance and smaller effect size in DEX-treated animals compared to saline-controls.

5.3.6. Vascular Changes

VEGF has well-established roles in vascular growth and remodeling. Previous work has demonstrated changes in VEGF expression following FUS+MB exposure [208,366]. In the current study, 2 days post-FUS+MB exposure, the mean ratio of VEGF expression in the sonicated to non-sonicated dorsal hippocampi (**Figure 5.6A**) for saline-treated animals was 1.35 ± 0.33 (p = 0.025). However, as with GFAP, ICAM1, and MCP1 expression, animals receiving DEX (n = 7) displayed no significant differences between hemispheres; the mean ratio of VEGF expression in the sonicated to non-sonicated dorsal hippocampi for DEX-treated animals was 1.06 ± 0.22 (p = 0.83).

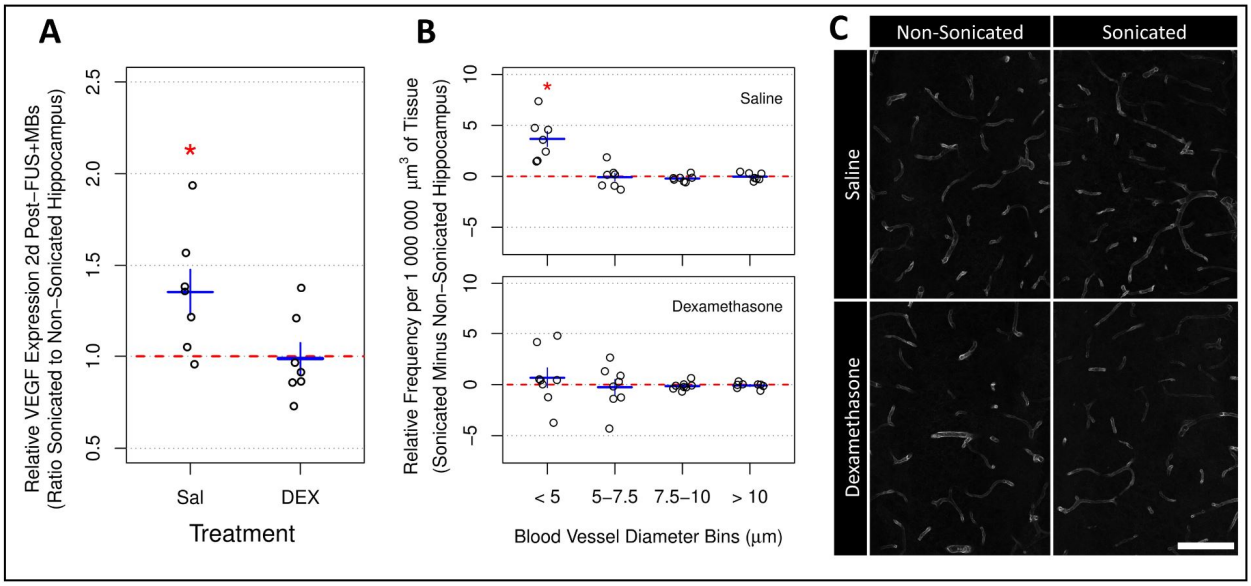

Figure 5.6. Relative VEGF Expression and Vascular Density Following FUS+MB Exposure. (A) Two days post-FUS+MBs, the mean ratio of VEGF expression in the sonicated to non-sonicated dorsal hippocampi for saline-treated animals was 1.35 ± 0.33 (p = 0.025). This effect was not present in animals receiving DEX following FUS+MBs (p = 0.83). (B) The density of small blood vessel segments (diameter < 5 µm) was

significantly greater in the sonicated hippocampus of saline-treated animals compared to the non-sonicated hippocampus (3.67 ± 2.11 more small blood vessel segments per 1 000 000 μm^3 than non-sonicated hippocampus; $p = 0.015$). No significant differences were observed for other sizes of blood vessels. Animals treated with DEX displayed no significant differences in blood vessel frequency between hemispheres for any size of vasculature. (C) Representative images of hippocampal vasculature 10 days following FUS+MB exposure demonstrating a small increase the density of small blood vessels in the sonicated hippocampus of saline-treated animals (scale bar = 100 µm). * indicates $p < 0.05$, paired Student's t-test. Red, horizontal, dashed line indicates no difference between sonicated and non-sonicated dorsal hippocampi. Error bars represent standard error of the mean. n = 7 saline-treated and 7 DEX-treated animals for analysis 2 days post-FUS+MB exposure. n = 7 saline-treated and 8 DEX-treated animals for analysis 10 days post-FUS+MB exposure.

To assess blood vessel growth, the frequency of blood vessel segments per unit volume of brain tissue was compared across the dorsal hippocampi between sonicated and non-sonicated hemispheres 10 days post-FUS+MBs (**Figure 5.6B**). For this analysis, the diameters of blood vessel segments were measured and binned by size. Consistent with a previous report [366], the volume-adjusted frequency of small blood vessel segments (diameter < 5 µm) was significantly greater in the sonicated hippocampus of saline-treated animals (n = 7) compared to the non-sonicated hippocampus (3.67 ± 2.11 more small blood vessel segments per 1 000 000 μm^3 than non-sonicated hippocampus; $p = 0.015$). No significant differences were observed for other sizes of blood vessels. Animals treated with DEX (n = 8) displayed no significant differences in blood vessel frequency between hemispheres for any size of vasculature.

5.4. Discussion

The results presented here explore the effects of post-sonication DEX administration on vascular permeability, inflammation, blood vessel growth, and astrocyte activation. While previous work has demonstrated that overt tissue damage can be avoided through the use of acoustic feedback control [134,232], transient effects on tissue health have been noted under experimental conditions that utilize methods of calibrating PNP based on MB activity. Given their magnitude and duration, the long-term impacts of these changes are unlikely to represent a prohibitive risk; however, multiple FUS+MB exposures with a high repetition frequency may allow for the accumulation of detrimental effects. Additionally, as with any medical intervention, there is a non-zero risk of adverse events (E.g. microhemorrhages). DEX administration may help to address these safety concerns by providing a means to expedite the restoration of BBB integrity and to reduce inflammation following FUS+MB exposure.

In the present study, post-sonication DEX administration was found to decrease vascular permeability at 2 hrs following FUS+MB exposure. Elevations in the expression of proteins related to inflammation were prevented at 2 days, and both measures of astrocyte activation and vascular growth were improved at 10 days following sonication in DEX-treated animals, compared with saline-treated controls.

Post-sonication DEX administration was found to alter the dynamics of vascular permeability in healthy brain tissue, leading to a significantly greater reduction in K^{trans} than in saline-controls at 2 hrs following FUS+MB exposure. This rapid effect on BBB permeability has previously been characterized in the context of C_6 glioma, with Shapiro *et al.* noting a 37% reduction in the K^{trans} of ^{14}C-alpha aminoisobutyric acid 1 hr following injection of DEX (10 mg/kg; ip), relative to baseline measurements [371]. Similarly, significant reductions in the K^{trans} of gadopentetate dimeglumine in glioblastoma vasculature have been reported 48-72 hrs following DEX administration (16 mg/day) in human patients [383].

Mechanisms through which DEX may act to alter BBB permeability include: increasing the expression of occludin [384,385] and zonula occludens-1 [385], preventing TNFα-dependent trafficking of tight junction proteins [386], altering vascular tone [387] and mean arterial pressure [388], and reducing cytokine-induced expression of matrix metalloproteinase-9 [389]. Given the rapidity of the effects observed in this study, it could be hypothesized that non-transcriptional actions of DEX on mean arterial pressure and/or TJ protein trafficking play a role in reducing BBB permeability following FUS+MB exposure. Regardless of the mechanisms, expediting the restoration of BBB integrity would be expected to reduce the accumulation of extravasated plasma proteins and to lessen the duration for which the brain is vulnerable to circulating pathogens.

Two days following FUS+MB exposure, saline-control animals displayed significantly elevated expression of MCP1 and ICAM1 in sonicated, relative to non-sonicated, dorsal hippocampi. Notably, animals that received DEX administration following exposure did not display these lateralized differences. Previous work has demonstrated the inhibitory effects of DEX on both MCP1 [390] and ICAM1 [369] expression. Given the role of these proteins in vascular inflammation and leukocyte endothelial transmigration [391,392], preventing prolonged elevations in their expression may be important for reducing the risk of tissue damage, specifically in the context of repeated FUS+MB exposures in close succession.

While saline-control animals displayed significantly elevated levels of MCP1 and ICAM1 two days following sonication (2.06- and 1.84-fold increase, respectively, relative to non-sonicated dorsal hippocampi), it is important to consider the magnitude of this change in relation to experimental conditions that result in significant, long lasting, tissue damage. Previous work has reported increases in MCP1 and ICAM1 expression of approximately 19- and 5-fold, respectively, relative to contralateral hemisphere, 24 hrs following FUS+MB exposure [208]. The expression of ICAM1 was found to be trending upwards at every time point (5 time points) from 0.5 to 24 hrs post-treatment. Of note, the parameters used in that work [208] have been shown to result in hemorrhage and persistent tissue damage [197], as well as to produce a significantly greater degree of inflammation than parameters similar to that used in the current study [198]. This suggests that while significant increases in the expression of inflammatory markers were detected, the magnitude of this increase did not reach levels previously shown to result in long-term, overt tissue damage.

In addition to the direct measurement of inflammatory markers, GFAP expression was assessed as an indicator of astrocyte activation [393]. At 2 and 10 days following FUS+MB exposure, protein expression and immunoreactive density of GFAP, respectively, were significantly elevated in the sonicated dorsal hippocampi of saline-control rats, a result that is consistent with previous reports [172,326]. The effect of DEX administration to prevent these changes may be due to its immunosuppressive actions and/or a more rapid restoration of BBB integrity following sonication, leading to reduced accumulation of plasma proteins known to correlate to astrocyte activation [394]. Given the enhanced phagocytic role astrocytes play when BBB permeability is increased [395], some degree of activation may be necessary to restore homeostatic conditions. The non-significant trend of increased GFAP immunoreactive density in the sonicated dorsal hippocampus of DEX-treated animals may reflect this process.

Within the CNS, acute inflammation can have a number of downstream effects, some of which have been observed following FUS+MB-mediated BBB permeability enhancement. It may be hypothesized that increases in the expression of VEGF [208,366], along with the vascular growth that has been observed post-sonication (described in *Chapter 4*) [366], may be influenced by inflammatory processes. In the current study, DEX administration was shown to prevent an increase in both VEGF expression at 2 days, and the density of small capillaries at 10 days post-FUS+MB exposure. The differential response observed in saline- and DEX-treated animals may be due to the anti-inflammatory effects of DEX, preventing a feedback response that reciprocally links inflammation and VEGF production [396]. By preventing an initial spike in the

production of inflammatory mediators, the concurrent and subsequent production of VEGF and vascular growth may be reduced.

Additionally, expediting the restoration of BBB integrity, which may act to reduce plasma protein extravasation and astrocyte activation, as well as suppressing the initiation of inflammatory processes, may contribute to a reduction in local metabolic demands in DEX-treated animals. Support for this notion comes from work demonstrating altered metabolism and increased energy demands in activated astrocytes [397]. It has also been hypothesized that the elevated capillary density in regions of increased metabolic demand [398] is mediated by the release of angiogenesis-stimulating factors from astrocytes [399]. Therefore, a hypothetical reduction in metabolic demand in the targeted hippocampus of DEX-treated animals, relative to saline-control animals, may eliminate this as a mechanism driving vascular growth; however, further work is required to interrogate this line of inquiry.

Surprisingly, no significant correlations were found between K^{trans}, measured at 15 min or 2 hrs post-sonication, and the expression of inflammatory markers or morphological changes, measured at 2 and 10 days post-sonication. This may be explained by a non-linear progression of these processes. For example, collecting samples at a single time point following FUS+MB exposure may capture peaks or valleys in the biphasic expression of specific proteins depending on the initial impact on BBB permeability. This lack of correlation has previously been observed in relation to vascular growth following sonication [366]. Conversely, strong correlations between changes in vascular permeability and the transcription of several inflammatory markers have been observed at 6 hrs following post-FUS+MBs [198]. This suggests that the time points of tissue collection in the current study may not have been conducive to the detection of correlations between K^{trans} and the expression of inflammatory markers or morphological changes.

Beyond the effects of DEX, this work also explored the relationship between acoustic emissions and changes in BBB permeability measured by DCE-MRI. This imaging technique allows for a more quantitative measure of vascular permeability than signal intensity changes in contrast-enhanced T1w imaging, a common approach in the field. Others have demonstrated the utility of DCE-MRI in assessing the half-life of increased vascular permeability [196,382], and extravasated concentration of doxorubicin [142,196] and Evans blue [121] following FUS+MB exposure. In the present study, a strong correlation was found between the exposure-average magnitude of $2f$ emissions and dorsal hippocampal $K^{trans,\ 15\ min}$; no strong correlations were detected with exposure-average or peak magnitude of $0.5f$, f, $1.5f$, or wideband emissions.

McDannold *et al.* previously demonstrated that second and third harmonic emissions strongly correlate to signal intensity changes in CE-T1w MRI when employing fixed PNP [111].

The data presented here suggest that the magnitude of $1.5f$ emissions during bursts that initiate a software-triggered drop in PNP are not significantly predictive of subsequent BBB permeability enhancement. Additionally, these results suggest that inertial cavitation, as assessed by the presence of wideband emissions, did not contribute substantially to the effects of sonication on vascular permeability. The strong correlation to $2f$ emissions emphasizes the notion that while inertial cavitation should be avoided, the modulation of stable cavitation may produce more predictable changes in BBB permeability. This concept has been integrated into closed-loop acoustic feedback control strategies, with promising results [134]. There are, however, considerable obstacles to address in making this approach universally applicable, such as the necessity of establishing a relationship between harmonic setpoint and changes in BBB permeability across species, MB types, transducer sensitivities, and driving frequencies. Future development of acoustic feedback control strategies may benefit from the combination of calibrating PNP based on a threshold event (I.e. sub- or ultraharmonics emissions) and modulating the magnitude of harmonic emissions.

5.4.1. Limitations

One potential limitation of this study is in the use of single-slice DCE-MRI. This approach assumes that changes in vascular permeability measured at the imaging plane are consistent throughout the dorsal hippocampus, as subsequent analyses were performed across this entire brain region. While the geometry of the ultrasound focus is ellipsoidal in the direction of propagation (**Figure 1.2A**), there may be small variations in BBB permeability above and below the imaging plane. Given that the length of the focus (I.e. axial full-width half-maximum pressure is 37.1 mm) is much larger than the slice thickness of imaging (1.0 mm) or the width of the dorsal hippocampus in the coronal plane (approximately 2 mm), this is not expected to substantially alter results. The imaging protocol was designed to achieve adequate contrast-to-noise ratio (1.35 for lowest K^{trans} measured) with high temporal (6.0 sec per image) and spatial resolution (voxel size of 0.24 x 0.24 x 1.0 mm), but at the expense of imaging volume (576 mm^3).

Another limitation of this work is the small number of inflammatory markers assessed. Inflammation involves the initiation of a wide range of pathways and changes in the expression, localization, and

function of a large number of proteins. Evaluating changes in the expression or immunoreactivity of a limited number of markers at two time points does not capture the complexity of the processes that follow FUS+MB exposure. The proteins evaluated in the current study were chosen based on results from previous array-based analyses, implicating their involvement in inflammatory processes following sonication [198,208,326]. Further work, however, is required to obtain a more complete picture of the effects of DEX on inflammation following FUS+MB exposure.

5.4.2. Conclusion

DEX administration following FUS+MB exposure was found to expedite the restoration of BBB integrity in the targeted dorsal hippocampi and prevent a subsequent elevation in the production of inflammatory markers. These results suggest that DEX may provide a means to modulate the degree to which BBB permeability is increased and enable repeated FUS+MB exposures with a reduced risk for tissue damage, induced by the accumulation of detrimental effects. Given its widespread clinical use and well documented mechanisms of action, the results presented here suggest that DEX administration following FUS+MB exposure may be warranted in clinical cases in which vascular damage is suspected and the goal of treatment is to restore or preserve neural function. Conversely, delivery of chemotherapeutics to glioblastomas may represent a scenario in which there would be no added benefit for the inclusion of DEX. This may also be the case for FUS+MB exposures where inflammatory processes may be involved mechanistically in the desired outcome, such as Aβ plaque clearance in patients with AD.

Chapter 6

Conclusions

A scarcity of brain-drug delivery strategies has curtailed the development of efficacious treatment options for a number of neuropathologies. The flexible, targeted, and non-invasive nature of FUS+MB exposure has motivated investigative attention and holds substantial potential to improve long-term prognoses for many individuals. A great need and promising preclinical results have led to early clinical testing; however, the study of sonication-induced bioeffects, free of therapeutic agent delivery, remains an area open for more detailed investigation. The importance of comprehensive characterization lays in providing adequate data to inform clinical risk assessments, a step particularly critical for medical interventions that target brain tissue. This type of research also has the potential to motivate the design of novel therapies or basic science tools that take advantage of the FUS+MB-induced activation of signalling pathways or the upregulation of specific proteins. The work presented in this thesis focused largely on characterizing the response of brain vasculature to FUS+MB-mediated BBB permeability enhancement and on mitigating the risks associated with this technique. *Chapter 6* contains a brief summary of the principal findings of this research and discusses potential avenues of future study.

6.1. Principal Findings

The work presented in *Chapter 2* explored the impact of FUS+MB-mediated BBB permeability enhancement on rat microvascular gene expression in the hippocampus at 6 and 24 hrs following sonication. This study was the first in-depth analysis of FUS+MB-induced gene expression changes in the brain and was instrumental in guiding subsequent research. There were several important observations from this analysis, the first being an increase in the transcription of a host of genes with key roles in acute inflammation. While this was consistent with previous observations of glial cell activation and downstream effects of inflammation, new insights into the time course and mediators of this response

were revealed. The most upregulated genes at 6 hrs following sonication included *Il1b*, *Ccl2*, *Ptx3*, *Ccl7*, and *Sele*, potentially implicating these factors as drivers of FUS+MB-induced inflammation and immune cell infiltration. Of note for the time course of this response was the non-significant differential expression at 24 hrs of several key proinflammatory genes, including *Il1b*, *Tnf*, *Cxcl1*, and *Il6*. Ultimately, these data would suggest that hippocampal microvasculature exhibit gene expression changes indicative of acute inflammation in the hours following sonication, a response that is present, but diminished, by 24 hrs.

Also of interest were changes detected in the transcription of genes involved with transcellular transport and blood vessel formation. The downregulation of *Abc1a*, *Slc22a6*, *and Slc22a8* at 6 hrs post-FUS+MB exposure may have implications for therapeutic agent delivery, as these genes code for proteins implicated in drug efflux (MDR1, organic anion transport-1, and -3, respectively) [292,299–301]. Thus, the reduced transcription of these genes may contribute to enhanced drug accumulation following sonication. In addition to large-molecule transporters, genes coding for ion transporters also displayed significant downregulation at 24 hrs, which may have transient implications for neural function. Lastly, bioinformatic analysis indicated that angiogenic processes may be activated at the 24 hr time point. This is consistent with observations following FUS+MB exposure in skeletal muscle [310,338,339], as well as with other situations in which BBB integrity is acutely compromised [236,247–251,272]. The results from this study informed much of the work detailed in subsequent chapters, as well as ongoing lines of inquiry.

Chapter 3 explored the effects of MB dose on both inflammation and BBB permeability enhancement. This study was chiefly motivated by a publication from *Kovacs et al.* [208] demonstrating severe inflammation following sonication, a result hypothesized to be largely attributable to the use of a high MB dose. To test this, NFκB signalling pathway-related differential gene expression was assessed at 6 hrs and 4 days following FUS+MB exposure for various sonication schemes. Using parameters comparable to those employed by Kovacs *et al.*, gene expression changes in whole brain tissue were closely replicated. These changes were accompanied by evidence of overt histological damage, including RBC extravasation and neuronal death. Conversely, a lower dose of MBs and the use of acoustic feedback control resulted in markedly dampened changes in the expression of genes related to the NFκB signalling pathway at either time point. This finding emphasizes the notion of a heterogeneous response to sonication across cell types, as differential expression of NFκB signalling pathway-related genes in microvascular samples displayed more substantial changes at 6 hrs following FUS+MB exposure (as described in *Chapter 2*). The work outlined in *Chapter 3* also suggests that the degree of BBB permeability enhancement following

sonication influences the extent of neuroinflammation, with the differential expression of several key regulators displaying positive linear correlations to signal intensity changes in CE-T1w images.

Motivated by bioinformatic analysis of FUS+MB-mediated differential gene expression in microvasculature (*Chapter 2*), *Chapter 4* described the study of blood vessel growth. At 7 and 14 days following FUS+MB exposure, hippocampal blood vessel density was found to be mildly elevated compared to the non-sonicated contralateral hemisphere. Relative newborn EC density, frequency of small blood vessel segments (I.e. less than 5 µm in diameter), and VEGFA immunoreactivity were also found to be increased in the sonicated hippocampus relative to the contralateral hemisphere. These effects on blood vessel density appear to be transient, displaying non-significant differences at 21 days following FUS+MB exposure. While the mechanisms driving angiogenic/angiolytic effects are unclear from this work, it is reasonable to hypothesize that inflammation and prolonged astrocyte activation may play a role. Additionally, it is unclear whether newly formed vasculature becomes perfused or contributes to recovery following FUS+MB exposure.

Finally, to address the risk associated FUS+MB-induced acute inflammation and to provide a means of controlling the degree and duration of enhanced BBB permeability, the work described in *Chapter 5* explored the effects of post-sonication DEX administration. Results demonstrated that DEX expedites the restoration of BBB integrity, as measured by DCE-MRI, and significantly limits the production of MCP1, ICAM1, GFAP, and VEGF, at 2 days following sonication. Additionally, indications of FUS+MB-induced astrocyte activation and vascular growth were diminished at 10 days in DEX-treated animals, relative to saline-treated controls. By reducing the impact of a single sonication on inflammatory processes and promoting recovery, DEX administration may allow for repeated sonications in closer succession with a reduced risk of accumulating detrimental effects. This would be especially beneficial in scenarios for which the goal of treatment is to restore or preserve neural function.

6.2. Future Directions

6.2.1. Enhanced Safety Assessments

There are a variety of questions pertinent to the assessment of FUS+MB exposure safety under different circumstances that remain unaddressed. One such question relates to understanding the relationship between exposure conditions and FUS+MB-induced inflammation. It is unclear whether inflammation is

purely driven by BBB permeability enhancement or if other factors contribute. Likewise, it is unclear whether subtle changes persist once inflammation has subsided. This is especially important in the context of repeated exposures. Thus far no study has systematically investigated the impact of exposure repetition frequency or number on the potential accumulation of detrimental tissue effects, nor has substantial attention been directed at evaluating the long-term impact of repeated FUS+MB exposures. In non-human primates, a maximum 13 sonications spread over up to 20 months in four animals is the longest study to date [321]. While no significant detrimental impacts on visual perception, decision making, or motor function were noted in this study, more thorough histological and behavioural analyses – with an emphasis on the use of sensitive measures – in a larger cohort of animals would provide a more detailed understanding of any potential latent effects.

Given the prevalence of chronic inflammation in a variety of neuropathologies for which FUS+MB-based treatment strategies may be employed, it is also important for work to be directed at exploring how sonication-induced acute inflammatory processes interact with existing inflammation. While behavioural improvements, increased microglial phagocytosis, and reduced plaque-load have been noted in mouse models of AD following repeated FUS+MB exposures [136,174], the impacts on chronic inflammatory processes have not been studied. It is possible that repeated exposures may slow disease progression in the short term but exacerbate pathology in the long-term. Further work is required in this regard for neuropathologies that are closely tied to chronic inflammation and that may conceivably require repeated exposures, with or without therapeutic agent delivery. Likewise, it will be important to analyse any toxicity associated with systemic delivery of therapeutic agents while BBB permeability is elevated above baseline; there is understandably very little detailed information regarding the response of brain tissue to drugs normally excluded by the BBB.

Extending from work presented in *Chapter 2* indicating a downregulation of sodium, potassium, and calcium ion channel gene expression, it is reasonable to hypothesize that neural function may be transiently altered following FUS+MB exposure. Indeed, Chu *et al.* have reported prolonged suppression of blood-oxygen level dependent responses and somatosensory evoked potentials with sonication parameters that induce significant RBC extravasations. This study also noted transient effects with parameters that did not produce overt tissue damage [191]; however, a detailed assessment of the populations of cells affected or the driving mechanisms are lacking. Determining the time course of potential changes for a range of exposure conditions and characterizing the ways in which neural function

is altered has importance for risk assessment. As iterated above, it may also be informative for such work to include an analysis of the effects of exposure repetition frequency and number.

6.2.2. Universal Metrics for Predicting Bioeffects Following FUS+MB Exposures

The reported impacts of FUS+MB-mediated BBB permeability enhancement on tissue health and morphology span an immense spectrum, from no discernible changes [175,211,400,401] to extensive hemorrhage and cell death [75,211,233]. This variance can, in part, be attributed to the difficulty of estimating *in situ* PNP. However, even with the implementation of methods to calibrate PNP based on *in vivo* MB response, substantial variation in BBB permeability enhancement and reported bioeffects persist. This creates perhaps the single greatest difficulty in characterizing the biological effects associated with FUS+MB exposures: developing universal metrics by which sonications can be compared between experimental setups and bioeffects can be predicted based on previous work. Without such metrics it is difficult to discern how exactly brain tissue will respond to a specific sonication. Rather than describing the bioeffects associated with FUS+MB-mediated BBB permeability enhancement, establishing bioeffects associated with a *particular classification* of exposure may have value for the interpretation of past and future work. While some efforts have been made in this regard, such as the inclusion of *cavitation dose* in some publications [110,121,402], thus far no robust means of comparison exist.

One common approach of comparing exposures *within* studies is to quantify the degree to which BBB permeability has been increased. Various strategies have been employed to this end, including the measurement of signal intensity changes in contrast enhanced MRI and the quantification of water-soluble dye extravasation. While these approaches have value in establishing correlations between BBB permeability enhancement and bioeffects within a given study, extending these measures to comparisons *between* studies is complex. For example, to accurately compare the K^{trans} of a specific MRI contrast agent at 15 minutes following sonication between studies with different experimental setups, it would be necessary to have consensus on many imaging and analysis parameters, including the dose of contrast agent, method of calculating the arterial input function, pharmacokinetic model employed, duration of imaging, T1 mapping approach, imaging parameters, etc.. In addition, the use of MRI scanners with equal field strengths and receiver coil sensitivities would be necessary for very accurate comparisons to be made, a requirement that is not feasible across institutes.

An emphasis on comparing metrics of BBB permeability enhancement across studies would also neglects FUS+MB-mediated bioeffects that are not related to vascular leakage. While MB behaviour drives BBB permeability enhancement, the stresses exerted on blood vessel walls may trigger signalling pathways that are independent of vascular leakage, nor track linearly with it. For example, volumetric oscillations of insonated MBs can induce both circumferential and shear stress within blood vessel walls, both of which are thought to contribute to BBB permeability changes [94]; however, these types of stresses are also known to trigger very different signalling pathways in ECs under physiological conditions [93,220]. While circumferential and shear stress may be pulling in the same direction with regards to BBB permeability enhancement, they may have opposing or separate influences on other bioeffects. Thus, being able to characterize *in vivo* MB response - a key contributor to the magnitude and types of stresses experienced by vascular walls - seems essential in comparing FUS+MB exposures between studies and predicting bioeffects; there are several factors that complicate this task.

The frequency spectra of acoustic emissions collected during sonication can provide some insight into the presence, absence, and relative magnitude of certain MB response characteristics; however, differences in the sensitivity and specificity of hydrophones used to collect these signals can preclude the direct comparison of data between studies. As an example, the absence of wideband emissions in work reporting elevated *Ccl2* expression may suggest that these factors are not causally linked or may simply indicate a lack of sufficient hydrophone sensitivity.

Likewise, hydrophone characteristics also have a bearing on the function acoustic feedback control algorithms. Sonications performed using identical algorithms, but with different hardware, may result in substantially different bioeffects. This is partly due to the polydispersed nature of commercially available MB formulations. Given that the resonance frequency of a MB is largely influenced by its size, as PNP is increased a growing fraction of MBs will begin oscillating in a manner that generates emissions at the frequency of interest. The PNP at which a sufficient number of MBs are producing signals that are detectable above baseline noise, and thus able to influence the function of the control algorithm, is dependent on hydrophone characteristics. These factors could contribute to disparity in observed bioeffects and BBB permeability enhancement between studies utilizing the same acoustic feedback control strategy but with different hydrophone characteristics.

An additional layer of complexity lies in the interpretation of magnitude measurements of acoustic emissions. For example, how would the outcomes of FUS+MB exposures compare between studies in which the magnitude of second harmonic emissions are equal, but MB dose differs by a factor of two? The behaviour of MBs in these studies necessarily differ in order to produce the same magnitude of emissions; however, any disparity in the biological outcomes of such exposures are not clear.

Further work is needed to establish metrics by which exposure conditions can be compared between studies and experimental setups. In the context of preclinical work, there may be value in establishing a series of standardized assessments for each FUS+MB protocol in order to determine the level of similarity between protocols and enable more accurate predictions of bioeffects. Given the difficulties in developing such metrics (discussed above), any assessment would necessarily be multifaceted and may include: (1) a measure of BBB permeability enhancement decay and return to baseline permeability, (2) a characterization of acoustic emissions, and (3) the quantification of specific biological responses.

For the first metric, establishing the decay rate of BBB permeability enhancement and return to baseline permeability using simple, widely available, and repeatable methods, such as quantification of Evans blue extravasation, may diminish the difficulty of comparing different methods of assessing BBB permeability between studies. To compare acoustic emissions, it may be important to first establish minimum requirements for detector characteristics. While comparisons of magnitude measurements may continue to pose challenges, signal analysis could include binary presence/absence descriptions (E.g. presence of wideband emissions) and coefficients of variation for frequencies of interest (to provide a unit-less indication of variance). Lastly, gene expression changes in whole brain tissue at specific time points following sonication would provide a simple metric by which exposure conditions could be compared. As an example, quantifying differential expression of *Ccl2*, *Il1b,* and *Icam1*, at 1, 2, and 6 hrs post-FUS+MB exposure may accomplish this goal.

These guidelines, or another combination of metrics, would not solve all the problems associated with comparing exposure conditions between experimental setups, but they may provide a pragmatic approach to better predict sonication-induced biological responses based on the findings of others. In establishing bioeffects associated with particular classifications of exposures, treatment strategies could be better tailored to particular pathologies.

6.3. Final Remarks

Since publication of the first experiments demonstrating BBB permeability enhancement using FUS and circulating MBs, the field has rapidly grown. Technological advances, biological characterization, and efficacious preclinical results have moved this drug delivery technique into clinical testing for a range of neuropathologies. While the safety profile of FUS+MB exposure appears adequate to aid in the treatment of severely diseased brain tissue, such as the delivery of chemotherapeutics to glioblastomas, further work is required to enable precise predictions of bioeffects based on exposure conditions, acoustic emissions, and post-sonication imaging. This knowledge will not only allow detailed risk assessment and strategic treatment planning but may also encourage the design of novel therapies that utilize the FUS+MB-induced activation of specific signalling pathways. While setbacks and sobering conclusions are unavoidable, with great momentum, investment, and careful research, the coming years are posed to be laden with substantial discovery and advancement.

Bibliography

1. Feigin, V. L. *et al.* Global, regional, and national burden of neurological disorders during 1990–2015: a systematic analysis for the Global Burden of Disease Study 2015. *Lancet Neurol.* **16**, 877–897 (2017).
2. Ali, G. C., Guerchet, M., Wu, Y. T., Prince, M. & Prina, M. The Global Prevalence of Dementia. in *World Alzheimer Report 2015* (Alzheimer's Disease International, 2015).
3. Fisher, A., Carney, G., Bassett, K. & Dormuth, C. R. Tolerability of Cholinesterase Inhibitors: A Population-Based Study of Persistence, Adherence, and Switching. *Drugs Aging* **34**, 221–231 (2017).
4. Delgado-López, P. D. & Corrales-García, E. M. Survival in glioblastoma: a review on the impact of treatment modalities. *Clin. Transl. Oncol.* **18**, 1062–1071 (2016).
5. Urbańska, K., Sokołowska, J., Szmidt, M. & Sysa, P. Glioblastoma multiforme - an overview. *Contemp. Oncol.* **18**, 307–312 (2014).
6. Nayak, L., Lee, E. Q. & Wen, P. Y. Epidemiology of brain metastases. *Curr. Oncol. Rep.* **14**, 48–54 (2012).
7. Pardridge, W. M. The blood-brain barrier: bottleneck in brain drug development. *NeuroRx* **2**, 3–14 (2005).
8. De Bock, M. *et al.* Endothelial calcium dynamics, connexin channels and blood–brain barrier function. *Prog. Neurobiol.* **108**, 1–20 (2013/9).
9. Xu, L., Nirwane, A. & Yao, Y. Basement membrane and blood–brain barrier. *Stroke Vasc Neurol* svn–2018–000198 (2018).
10. Hawkins, B. T. & Davis, T. P. The blood-brain barrier/neurovascular unit in health and disease. *Pharmacol. Rev.* **57**, 173–185 (2005).
11. Abbott, N. J., Patabendige, A. A. K., Dolman, D. E. M., Yusof, S. R. & Begley, D. J. Structure and function of the blood-brain barrier. *Neurobiol. Dis.* **37**, 13–25 (2010).
12. Joan Abbott, N., Rönnbäck, L. & Hansson, E. Astrocyte–endothelial interactions at the blood–brain barrier. *Nat. Rev. Neurosci.* **7**, 41–53 (2006).
13. Banerjee, S. & Bhat, M. A. Neuron-glial interactions in blood-brain barrier formation. *Annu. Rev. Neurosci.* **30**, 235–258 (2007).
14. Sweeney, M. D., Zhao, Z., Montagne, A., Nelson, A. R. & Zlokovic, B. V. Blood-Brain Barrier: From Physiology to Disease and Back. *Physiol. Rev.* **99**, 21–78 (2019).
15. Hladky, S. B. & Barrand, M. A. Fluid and ion transfer across the blood-brain and blood-cerebrospinal fluid barriers; a comparative account of mechanisms and roles. *Fluids Barriers CNS* **13**, 19 (2016).
16. Wong, A. D. *et al.* The blood-brain barrier: an engineering perspective. *Front. Neuroeng.* **6**, 7 (2013).
17. Pardridge, W. M. Drug transport across the blood–brain barrier. *J. Cereb. Blood Flow Metab.* **32**, 1959–1972 (2012).
18. Ghosh, C., Puvenna, V., Gonzalez-Martinez, J., Janigro, D. & Marchi, N. Blood-brain barrier P450 enzymes and multidrug transporters in drug resistance: a synergistic role in neurological diseases. *Curr. Drug Metab.* **12**, 742–749 (2011).
19. Engelhardt, B., Vajkoczy, P. & Weller, R. O. The movers and shapers in immune privilege of the CNS. *Nat. Immunol.* **18**, 123–131 (2017).
20. Frisella, W. A. *et al.* Intracranial injection of recombinant adeno-associated virus improves cognitive function in a murine model of mucopolysaccharidosis type VII. *Mol. Ther.* **3**, 351–358 (2001).
21. Lee, J. K. *et al.* Intracerebral transplantation of bone marrow-derived mesenchymal stem cells reduces amyloid-beta deposition and rescues memory deficits in Alzheimer's disease mice by modulation of immune

responses. *Stem Cells* **28**, 329–343 (2010).

22. Marks, W. J., Jr *et al.* Safety and tolerability of intraputaminal delivery of CERE-120 (adeno-associated virus serotype 2-neurturin) to patients with idiopathic Parkinson's disease: an open-label, phase I trial. *Lancet Neurol.* **7**, 400–408 (2008).
23. Muir, K. W., Sinden, J., Miljan, E. & Dunn, L. Intracranial delivery of stem cells. *Transl. Stroke Res.* **2**, 266–271 (2011).
24. Evans, B. K., Armstrong, S., Singer, G., Cook, R. D. & Burnstock, G. Intracranial injection of drugs: comparison of diffusion of 6-OHDA and guanethidine. *Pharmacol. Biochem. Behav.* **3**, 205–228 (1975).
25. Cserr, H. F. & Ostrach, L. H. Bulk flow of interstitial fluid after intracranial injection of blue dextran 2000. *Exp. Neurol.* **45**, 50–60 (1974).
26. Pedersen, C. A. & Prange, A. J., Jr. Induction of maternal behavior in virgin rats after intracerebroventricular administration of oxytocin. *Proc. Natl. Acad. Sci. U. S. A.* **76**, 6661–6665 (1979).
27. Lochhead, J. J. & Thorne, R. G. Intranasal delivery of biologics to the central nervous system. *Adv. Drug Deliv. Rev.* **64**, 614–628 (2012).
28. Dhuria, S. V., Hanson, L. R. & Frey, W. H., 2nd. Intranasal delivery to the central nervous system: mechanisms and experimental considerations. *J. Pharm. Sci.* **99**, 1654–1673 (2010).
29. Pardridge, W. M. Drug transport in brain via the cerebrospinal fluid. *Fluids Barriers CNS* **8**, 7 (2011).
30. Nagy, Z., Pappius, H. M., Mathieson, G. & Hüttner, I. Opening of tight junctions in cerebral endothelium. I. Effect of hyperosmolar mannitol infused through the internal carotid artery. *J. Comp. Neurol.* **185**, 569–578 (1979).
31. Dorovini-Zis, K., Bowman, P. D., Betz, A. L. & Goldstein, G. W. Hyperosmotic arabinose solutions open the tight junctions between brain capillary endothelial cells in tissue culture. *Brain Res.* **302**, 383–386 (1984).
32. Rapoport, S. I. Advances in osmotic opening of the blood-brain barrier to enhance CNS chemotherapy. *Expert Opin. Investig. Drugs* **10**, 1809–1818 (2001).
33. Neuwelt, E. A. *et al.* Therapeutic efficacy of multiagent chemotherapy with drug delivery enhancement by blood-brain barrier modification in glioblastoma. *Neurosurgery* **19**, 573–582 (1986).
34. Marchi, N. *et al.* Seizure-promoting effect of blood-brain barrier disruption. *Epilepsia* **48**, 732–742 (2007).
35. Doolittle, N. D. *et al.* Safety and efficacy of a multicenter study using intraarterial chemotherapy in conjunction with osmotic opening of the blood-brain barrier for the treatment of patients with malignant brain tumors. *Cancer* **88**, 637–647 (2000).
36. Hall, W. A. *et al.* Osmotic blood-brain barrier disruption chemotherapy for diffuse pontine gliomas. *J. Neurooncol.* **77**, 279–284 (2006).
37. McGregor, J. M., Bell, S. D., Doolittle, N. D., Murillo, T. P. & Neuwelt, E. A. Chapter 10 - Blood-Brain Barrier Disruption Chemotherapy. in *Handbook of Brain Tumor Chemotherapy, Molecular Therapeutics, and Immunotherapy (Second Edition)* (ed. Newton, H. B.) 145–153 (Academic Press, 2018).
38. Suzuki, M., Iwasaki, Y., Yamamoto, T., Konno, H. & Kudo, H. Sequelae of the osmotic blood-brain barrier opening in rats. *J. Neurosurg.* **69**, 421–428 (1988).
39. Killian, D. M., Hermeling, S. & Chikhale, P. J. Targeting the cerebrovascular large neutral amino acid transporter (LAT1) isoform using a novel disulfide-based brain drug delivery system. *Drug Deliv.* **14**, 25–31 (2007).
40. Foust, K. D. *et al.* Intravascular AAV9 preferentially targets neonatal neurons and adult astrocytes. *Nat. Biotechnol.* **27**, 59–65 (2009).
41. Afergan, E. *et al.* Delivery of serotonin to the brain by monocytes following phagocytosis of liposomes. *J. Control. Release* **132**, 84–90 (2008).
42. Kreuter, J., Alyautdin, R. N., Kharkevich, D. A. & Ivanov, A. A. Passage of peptides through the blood-brain barrier with colloidal polymer particles (nanoparticles). *Brain Res.* **674**, 171–174 (1995).
43. Dong, X. Current Strategies for Brain Drug Delivery. *Theranostics* **8**, 1481–1493 (2018).
44. Vykhodtseva, N. I., Hynynen, K. & Damianou, C. Histologic effects of high intensity pulsed ultrasound

exposure with subharmonic emission in rabbit brain in vivo. *Ultrasound Med. Biol.* **21**, 969–979 (1995).

45. Fyfe, M. C. & Chahl, L. A. Mast cell degranulation and increased vascular permeability induced by 'therapeutic' ultrasound in the rat ankle joint. *Br. J. Exp. Pathol.* **65**, 671–676 (1984).
46. McDannold, Hynynen, K., Wolf, D., Wolf, G. & Jolesz, F. MRI evaluation of thermal ablation of tumors with focused ultrasound. *J. Magn. Reson. Imaging* **8**, 91–100 (1998).
47. Lynn, J. G., Zwemer, R. L., Chick, A. J. & Miller, A. E. A new method for the generation and use of focused ultrasound in experimental biology. *J. Gen. Physiol.* **26**, 179–193 (1942).
48. Dewhirst, M. W., Viglianti, B. L., Lora-Michiels, M., Hanson, M. & Hoopes, P. J. Basic principles of thermal dosimetry and thermal thresholds for tissue damage from hyperthermia. *Int. J. Hyperthermia* **19**, 267–294 (2003).
49. Song, C. W. Effect of local hyperthermia on blood flow and microenvironment: a review. *Cancer Res.* **44**, 4721s–4730s (1984).
50. Frey, B. *et al.* Old and new facts about hyperthermia-induced modulations of the immune system. *Int. J. Hyperthermia* **28**, 528–542 (2012).
51. Takemoto, M. *et al.* The effect of various chemotherapeutic agents given with mild hyperthermia on different types of tumours. *Int. J. Hyperthermia* **19**, 193–203 (2003).
52. Overgaard, J. The current and potential role of hyperthermia in radiotherapy. *Int. J. Radiat. Oncol. Biol. Phys.* **16**, 535–549 (1989).
53. Song, C. W., Kang, M. S., Rhee, J. G. & Levitt, S. H. Effect of hyperthermia on vascular function in normal and neoplastic tissues. *Ann. N. Y. Acad. Sci.* **335**, 35–47 (1980).
54. Leith, J. T., Miller, R. C., Gerner, E. W. & Boone, M. L. Hyperthermic potentiation: biological aspects and applications to radiation therapy. *Cancer* **39**, 766–779 (1977).
55. Lepock, J. R. Cellular effects of hyperthermia: relevance to the minimum dose for thermal damage. *Int. J. Hyperthermia* **19**, 252–266 (2003).
56. Hand, J. W., Vernon, C. C. & Prior, M. V. Early experience of a commercial scanned focused ultrasound hyperthermia system. *Int. J. Hyperthermia* **8**, 587–607 (1992).
57. Shimm, D. S., Hynynen, K. H., Anhalt, D. P., Roemer, R. B. & Cassady, J. R. Scanned focussed ultrasound hyperthermia: initial clinical results. *Int. J. Radiat. Oncol. Biol. Phys.* **15**, 1203–1208 (1988).
58. Straube, W. L. *et al.* An ultrasound system for simultaneous ultrasound hyperthermia and photon beam irradiation. *Int. J. Radiat. Oncol. Biol. Phys.* **36**, 1189–1200 (1996).
59. Goldberg, S. N., Gazelle, G. S. & Mueller, P. R. Thermal ablation therapy for focal malignancy: a unified approach to underlying principles, techniques, and diagnostic imaging guidance. *AJR Am. J. Roentgenol.* **174**, 323–331 (2000).
60. Elias, W. J. *et al.* A pilot study of focused ultrasound thalamotomy for essential tremor. *N. Engl. J. Med.* **369**, 640–648 (2013).
61. Hynynen, K. *et al.* Pre-clinical testing of a phased array ultrasound system for MRI-guided noninvasive surgery of the brain--a primate study. *Eur. J. Radiol.* **59**, 149–156 (2006).
62. Rooney, J. A. & Nyborg, W. L. Acoustic Radiation Pressure in a Traveling Plane Wave. *Am. J. Phys.* **40**, 1825–1830 (1972).
63. Nyborg, W. L. Acoustic Streaming due to Attenuated Plane Waves. *J. Acoust. Soc. Am.* **25**, 68–75 (1953).
64. Konofagou, E. E. & Hynynen, K. Localized harmonic motion imaging: theory, simulations and experiments. *Ultrasound Med. Biol.* **29**, 1405–1413 (2003).
65. Ophir, J., Céspedes, I., Ponnekanti, H., Yazdi, Y. & Li, X. Elastography: a quantitative method for imaging the elasticity of biological tissues. *Ultrason. Imaging* **13**, 111–134 (1991).
66. Leighton, T. G. *The Acoustic Bubble*. **96**, (London: Academic Press, 1994).
67. Xu, Z., Hall, T. L., Fowlkes, J. B. & Cain, C. A. Optical and acoustic monitoring of bubble cloud dynamics at a tissue-fluid interface in ultrasound tissue erosion. *J. Acoust. Soc. Am.* **121**, 2421–2430 (2007).
68. Roberts, W. W. *et al.* Pulsed cavitational ultrasound: a noninvasive technology for controlled tissue ablation

(histotripsy) in the rabbit kidney. *J. Urol.* **175**, 734–738 (2006).
69. Gramiak, R. & Shah, P. M. Echocardiography of the aortic root. *Invest. Radiol.* **3**, 356–366 (1968).
70. Grayburn, P. A. Current and future contrast agents. *Echocardiography* **19**, 259–265 (2002).
71. Goertz, D. E., de Jong, N. & Van Der Steen, A. F. W. Attenuation and size distribution measurements of Definity and manipulated Definity populations. *Ultrasound Med. Biol.* **33**, 1376–1388 (2007).
72. Goertz, D. E. An overview of the influence of therapeutic ultrasound exposures on the vasculature: high intensity ultrasound and microbubble-mediated bioeffects. *Int. J. Hyperthermia* **31**, 134–144 (2015).
73. Lawrie, A. *et al.* Microbubble-enhanced ultrasound for vascular gene delivery. *Gene Ther.* **7**, 2023–2027 (2000).
74. Hynynen, K., McDannold, N., Vykhodtseva, N. & Jolesz, F. A. Noninvasive MR imaging-guided focal opening of the blood-brain barrier in rabbits. *Radiology* **220**, 640–646 (2001).
75. Jones, R. M. *et al.* Three-dimensional transcranial microbubble imaging for guiding volumetric ultrasound-mediated blood-brain barrier opening. *Theranostics* **8**, 2909–2926 (2018).
76. Huang, Y., Vykhodtseva, N. I. & Hynynen, K. Creating brain lesions with low-intensity focused ultrasound with microbubbles: a rat study at half a megahertz. *Ultrasound Med. Biol.* **39**, 1420–1428 (2013).
77. Huber, P. E. *et al.* Focused ultrasound (HIFU) induces localized enhancement of reporter gene expression in rabbit carotid artery. *Gene Ther.* **10**, 1600–1607 (2003).
78. Hynynen, K., Watmough, D. J. & Mallard, J. R. Design of ultrasonic transducers for local hyperthermia. *Ultrasound Med. Biol.* **7**, 397–402 (1981).
79. Cline, H. E. *et al.* MR temperature mapping of focused ultrasound surgery. *Magn. Reson. Med.* **31**, 628–636 (1994).
80. Lynn, J. G. & Putnam, T. J. Histology of Cerebral Lesions Produced by Focused Ultrasound. *Am. J. Pathol.* **20**, 637–649 (1944).
81. Fry, F. J. Transkull transmission of an intense focused ultrasonic beam. *Ultrasound Med. Biol.* **3**, 179–184 (1977).
82. Fry, F. J. & Goss, S. A. Further studies of the transkull transmission of an intense focused ultrasonic beam: lesion production at 500 kHz. *Ultrasound Med. Biol.* **6**, 33–38 (1980).
83. Thomas, J.-L. & Fink, M. A. Ultrasonic beam focusing through tissue inhomogeneities with a time reversal mirror: application to transskull therapy. *IEEE Trans. Ultrason. Ferroelectr. Freq. Control* **43**, 1122–1129 (1996).
84. Hynynen, K. & Jolesz, F. A. Demonstration of potential noninvasive ultrasound brain therapy through an intact skull. *Ultrasound Med. Biol.* **24**, 275–283 (1998).
85. Ebbini, E. S. & Cain, C. A. Experimental evaluation of a prototype cylindrical section ultrasound hyperthermia phased-array applicator. *IEEE Trans. Ultrason. Ferroelectr. Freq. Control* **38**, 510–520 (1991).
86. Lipsman, N. *et al.* MR-guided focused ultrasound thalamotomy for essential tremor: a proof-of-concept study. *Lancet Neurol.* **12**, 462–468 (2013).
87. Bakay, L., Ballantine, H. T., Jr, Hueter, T. F. & Sosa, D. Ultrasonically produced changes in the blood-brain barrier. *AMA Arch. Neurol. Psychiatry* **76**, 457–467 (1956).
88. Ballantine, H. T., Jr, Bell, E. & Manlapaz, J. Progress and problems in the neurological applications of focused ultrasound. *J. Neurosurg.* **17**, 858–876 (1960).
89. Shealy, C. N. & Crafts, D. Selective alteration of the blood-brain barrier. *J. Neurosurg.* **23**, 484–487 (1965).
90. Hynynen, K., McDannold, N., Vykhodtseva, N. & Jolesz, F. A. Noninvasive MR imaging-guided focal opening of the blood-brain barrier in rabbits. *Radiology* **220**, 640–646 (2001).
91. Lewin, P. A. & Bjørnø, L. Acoustically induced shear stresses in the vicinity of microbubbles in tissue. *J. Acoust. Soc. Am.* **71**, 728–734 (1982).
92. Wu, J. Theoretical study on shear stress generated by microstreaming surrounding contrast agents attached to living cells. *Ultrasound Med. Biol.* **28**, 125–129 (2002).
93. VanBavel, E. Effects of shear stress on endothelial cells: Possible relevance for ultrasound applications. *Prog.*

Biophys. Mol. Biol. **93**, 374–383 (2007/1).

94. Hosseinkhah, N. & Hynynen, K. A three-dimensional model of an ultrasound contrast agent gas bubble and its mechanical effects on microvessels. *Phys. Med. Biol.* **57**, 785–808 (2012).
95. Dayton, P., Klibanov, A., Brandenburger, G. & Ferrara, K. Acoustic radiation force in vivo: a mechanism to assist targeting of microbubbles. *Ultrasound Med. Biol.* **25**, 1195–1201 (1999).
96. Apfel, R. E. & Holland, C. K. Gauging the likelihood of cavitation from short-pulse, low-duty cycle diagnostic ultrasound. *Ultrasound Med. Biol.* **17**, 179–185 (1991).
97. Vykhodtseva, N., McDannold, N. & Hynynen, K. Induction of apoptosis in vivo in the rabbit brain with focused ultrasound and Optison®. *Ultrasound in Medicine and Biology* **32**, 1923–1929 (2006).
98. de Jong, N., Hoff, L., Skotland, T. & Bom, N. Absorption and scatter of encapsulated gas filled microspheres: theoretical considerations and some measurements. *Ultrasonics* **30**, 95–103 (1992).
99. Helfield, B., Chen, X., Qin, B. & Villanueva, F. S. Individual lipid encapsulated microbubble radial oscillations: Effects of fluid viscosity. *J. Acoust. Soc. Am.* **139**, 204–214 (2016).
100. Helfield, B. L. & Goertz, D. E. Nonlinear resonance behavior and linear shell estimates for Definity™ and MicroMarker™ assessed with acoustic microbubble spectroscopy. *J. Acoust. Soc. Am.* **133**, 1158–1168 (2013).
101. Liu, H.-L., Pan, C.-H., Ting, C.-Y. & Hsiao, M.-J. Opening of the blood-brain barrier by low-frequency (28-kHz) ultrasound: a novel pinhole-assisted mechanical scanning device. *Ultrasound Med. Biol.* **36**, 325–335 (2010).
102. Bing, K. F., Howles, G. P., Qi, Y., Palmeri, M. L. & Nightingale, K. R. Blood-brain barrier (BBB) disruption using a diagnostic ultrasound scanner and definity® in mice. *Ultrasound in Medicine and Biology* **35**, 1298–1308 (2009).
103. Schwartz, M. L. *et al.* Skull bone marrow injury caused by MR-guided focused ultrasound for cerebral functional procedures. *J. Neurosurg.* 1–5 (2018).
104. Pulkkinen, A., Werner, B., Martin, E. & Hynynen, K. Numerical simulations of clinical focused ultrasound functional neurosurgery. *Phys. Med. Biol.* **59**, 1679–1700 (2014).
105. Pichardo, S., Sin, V. W. & Hynynen, K. Multi-frequency characterization of the speed of sound and attenuation coefficient for longitudinal transmission of freshly excised human skulls. *Phys. Med. Biol.* **56**, 219–250 (2011).
106. Pajek, D. & Hynynen, K. The application of sparse arrays in high frequency transcranial focused ultrasound therapy: a simulation study. *Med. Phys.* **40**, 122901 (2013).
107. Sammartino, F. *et al.* Tractography-Based Ventral Intermediate Nucleus Targeting: Novel Methodology and Intraoperative Validation. *Mov. Disord.* **31**, 1217–1225 (2016).
108. Hosseinkhah, N., Goertz, D. E. & Hynynen, K. Microbubbles and blood-brain barrier opening: a numerical study on acoustic emissions and wall stress predictions. *IEEE Trans. Biomed. Eng.* **62**, 1293–1304 (2015).
109. Hynynen, K., McDannold, N., Martin, H., Jolesz, F. A. & Vykhodtseva, N. The threshold for brain damage in rabbits induced by bursts of ultrasound in the presence of an ultrasound contrast agent (Optison). *Ultrasound Med. Biol.* **29**, 473–481 (2003).
110. Tung, Y.-S., Vlachos, F., Choi, J. J. & Deffieux, T. In vivo transcranial cavitation threshold detection during ultrasound-induced blood–brain barrier opening in mice. *Phys. Med. Biol.* **55**, 6141–6155 (2010).
111. McDannold, N., Vykhodtseva, N. & Hynynen, K. Targeted disruption of the blood-brain barrier with focused ultrasound: association with cavitation activity. *Phys. Med. Biol.* **51**, 793–807 (2006).
112. McDannold, N., Vykhodtseva, N. & Hynynen, K. Blood-brain barrier disruption induced by focused ultrasound and circulating preformed microbubbles appears to be characterized by the mechanical index. *Ultrasound Med. Biol.* **34**, 834–840 (2008).
113. McDannold, N., Vykhodtseva, N. & Hynynen, K. Effects of acoustic parameters and ultrasound contrast agent dose on focused-ultrasound induced blood-brain barrier disruption. *Ultrasound Med. Biol.* **34**, 930–937 (2008).
114. O'Reilly, M. A., Waspe, A. C., Ganguly, M. & Hynynen, K. Focused-Ultrasound Disruption of the Blood-Brain

Barrier Using Closely-Timed Short Pulses: Influence of Sonication Parameters and Injection Rate. *Ultrasound Med. Biol.* **37**, 587–594 (2011/4).

115. Choi, J. J. *et al.* Noninvasive and localized blood-brain barrier disruption using focused ultrasound can be achieved at short pulse lengths and low pulse repetition frequencies. *J. Cereb. Blood Flow Metab.* **31**, 725–737 (2011).
116. Goertz, D. E., Wright, C. & Hynynen, K. Contrast agent kinetics in the rabbit brain during exposure to therapeutic ultrasound. *Ultrasound Med. Biol.* **36**, 916–924 (2010).
117. Chopra, R., Vykhodtseva, N. & Hynynen, K. Influence of exposure time and pressure amplitude on blood-brain-barrier opening using transcranial ultrasound exposures. *ACS Chem. Neurosci.* **1**, 391–398 (2010).
118. Song, K.-H. *et al.* Microbubble gas volume: A unifying dose parameter in blood-brain barrier opening by focused ultrasound. *Theranostics* **7**, 144–152 (2017).
119. Samiotaki, G., Vlachos, F., Tung, Y.-S. & Konofagou, E. E. A quantitative pressure and microbubble-size dependence study of focused ultrasound-induced blood-brain barrier opening reversibility in vivo using MRI. *Magn. Reson. Med.* **67**, 769–777 (2012).
120. McDannold, N., Vykhodtseva, N. & Hynynen, K. Use of ultrasound pulses combined with Definity for targeted blood-brain barrier disruption: a feasibility study. *Ultrasound Med. Biol.* **33**, 584–590 (2007).
121. Wu, S.-K. *et al.* Characterization of Different Microbubbles in Assisting Focused Ultrasound-Induced Blood-Brain Barrier Opening. *Sci. Rep.* **7**, 46689 (2017).
122. Treat, L. H. *et al.* Targeted delivery of doxorubicin to the rat brain at therapeutic levels using MRI-guided focused ultrasound. *International journal of cancer* **121**, 901–907 (2007).
123. Yang, F.-Y. *et al.* Quantitative evaluation of focused ultrasound with a contrast agent on blood-brain barrier disruption. *Ultrasound Med. Biol.* **33**, 1421–1427 (2007).
124. Itani, M. & Mattrey, R. F. The effect of inhaled gases on ultrasound contrast agent longevity in vivo. *Mol. Imaging Biol.* **14**, 40–46 (2012).
125. McDannold, N., Zhang, Y. & Vykhodtseva, N. The effects of oxygen on ultrasound-induced blood-brain barrier disruption in mice. *Ultrasound Med. Biol.* **43**, 469–475 (2017).
126. Samiotaki, G. *et al.* Pharmacokinetic analysis and drug delivery efficiency of the focused ultrasound-induced blood-brain barrier opening in non-human primates. *Magn. Reson. Imaging* **37**, 273–281 (2017).
127. Wu, S.-Y. *et al.* Characterizing Focused-Ultrasound Mediated Drug Delivery to the Heterogeneous Primate Brain In Vivo with Acoustic Monitoring. *Sci. Rep.* **6**, 37094 (2016).
128. McDannold, N., Arvanitis, C. D., Vykhodtseva, N. & Livingstone, M. S. Temporary disruption of the blood-brain barrier by use of ultrasound and microbubbles: safety and efficacy evaluation in rhesus macaques. *Cancer Res.* **72**, 3652–3663 (2012).
129. Faez, T. *et al.* Characterizing the subharmonic response of phospholipid-coated microbubbles for carotid imaging. *Ultrasound Med. Biol.* **37**, 958–970 (2011).
130. Sijl, J. *et al.* Combined optical and acoustical detection of single microbubble dynamics. *J. Acoust. Soc. Am.* **130**, 3271–3281 (2011).
131. Prosperetti, A. A general derivation of the subharmonic threshold for non-linear bubble oscillations. *J. Acoust. Soc. Am.* **133**, 3719–3726 (2013).
132. Chen, H., Kreider, W., Brayman, A. A., Bailey, M. R. & Matula, T. J. Blood vessel deformations on microsecond time scales by ultrasonic cavitation. *Phys. Rev. Lett.* **106**, 034301 (2011).
133. Arvanitis, C. D., Livingstone, M. S., Vykhodtseva, N. & McDannold, N. Controlled ultrasound-induced blood-brain barrier disruption using passive acoustic emissions monitoring. *PLoS One* **7**, e45783 (2012).
134. Sun, T. *et al.* Closed-loop control of targeted ultrasound drug delivery across the blood-brain/tumor barriers in a rat glioma model. *Proc. Natl. Acad. Sci. U. S. A.* **114**, E10281–E10290 (2017).
135. O'Reilly, M. A. & Hynynen, K. Blood-Brain Barrier: Real-time Feedback-controlled Focused Ultrasound Disruption by Using an Acoustic Emissions–based Controller. *Radiology* **263**, (2012).
136. Burgess, A. *et al.* Alzheimer disease in a mouse model: MR imaging-guided focused ultrasound targeted to

the hippocampus opens the blood-brain barrier and improves pathologic abnormalities and behavior. *Radiology* **273**, 736–745 (2014).

137. Lipsman, N. *et al.* Blood-brain barrier opening in Alzheimer's disease using MR-guided focused ultrasound. *Nat. Commun.* **9**, 2336 (2018).
138. McMahon, D., Poon, C. & Hynynen, K. Evaluating the safety profile of focused ultrasound and microbubble-mediated treatments to increase blood-brain barrier permeability. *Expert Opin. Drug Deliv.* (2019). doi:10.1080/17425247.2019.1567490
139. Doolittle, N. D. *et al.* Delivery of chemotherapy and antibodies across the blood-brain barrier and the role of chemoprotection, in primary and metastatic brain tumors: report of the Eleventh Annual Blood-Brain Barrier Consortium meeting. *J. Neurooncol.* **81**, 81–91 (2007).
140. Treat, L. H., McDannold, N., Zhang, Y., Vykhodtseva, N. & Hynynen, K. Improved anti-tumor effect of liposomal doxorubicin after targeted blood-brain barrier disruption by MRI-guided focused ultrasound in rat glioma. *Ultrasound Med. Biol.* **38**, 1716–1725 (2012).
141. Kovacs, Z. *et al.* Prolonged survival upon ultrasound-enhanced doxorubicin delivery in two syngenic glioblastoma mouse models. *J. Control. Release* **187**, 74–82 (2014).
142. Park, J., Aryal, M., Vykhodtseva, N., Zhang, Y.-Z. & McDannold, N. Evaluation of permeability, doxorubicin delivery, and drug retention in a rat brain tumor model after ultrasound-induced blood-tumor barrier disruption. *J. Control. Release* **250**, 77–85 (2017).
143. Fan, C.-H. *et al.* SPIO-conjugated, doxorubicin-loaded microbubbles for concurrent MRI and focused-ultrasound enhanced brain-tumor drug delivery. *Biomaterials* **34**, 3706–3715 (2013).
144. Alli, S. *et al.* Brainstem blood brain barrier disruption using focused ultrasound: A demonstration of feasibility and enhanced doxorubicin delivery. *J. Control. Release* **281**, 29–41 (2018).
145. Aryal, M., Vykhodtseva, N., Zhang, Y.-Z., Park, J. & McDannold, N. Multiple treatments with liposomal doxorubicin and ultrasound-induced disruption of blood-tumor and blood-brain barriers improve outcomes in a rat glioma model. *J. Control. Release* **169**, 103–111 (2013).
146. Arvanitis, C. D. *et al.* Mechanisms of enhanced drug delivery in brain metastases with focused ultrasound-induced blood-tumor barrier disruption. *Proc. Natl. Acad. Sci. U. S. A.* (2018). doi:10.1073/pnas.1807105115
147. Yang, F.-Y. *et al.* Pharmacokinetic Analysis of 111In-Labeled Liposomal Doxorubicin in Murine Glioblastoma after Blood-Brain Barrier Disruption by Focused Ultrasound. *PLoS One* **7**, e45468 (2012).
148. Mei, J., Cheng, Y., Song, Y. & Yang, Y. Experimental study on targeted methotrexate delivery to the rabbit brain via magnetic resonance imaging–guided focused ultrasound. *of Ultrasound in …* **28**, 871–880 (2009).
149. Liu, H.-L. *et al.* Blood-brain barrier disruption with focused ultrasound enhances delivery of chemotherapeutic drugs for glioblastoma treatment. *Radiology* **255**, 415–425 (2010).
150. Fan, C.-H. *et al.* Antiangiogenic-targeting drug-loaded microbubbles combined with focused ultrasound for glioma treatment. *Biomaterials* **34**, 2142–2155 (2013).
151. Wei, K.-C. *et al.* Focused Ultrasound-Induced Blood–Brain Barrier Opening to Enhance Temozolomide Delivery for Glioblastoma Treatment: A Preclinical Study. *PLoS One* **8**, e58995 (2013).
152. Dong, Q., He, L., Chen, L. & Deng, Q. Opening the Blood-Brain Barrier and Improving the Efficacy of Temozolomide Treatments of Glioblastoma Using Pulsed, Focused Ultrasound with a Microbubble Contrast Agent. *Biomed Res. Int.* **2018**, 6501508 (2018).
153. Lotfinia, M., Abdollahpour-Alitappeh, M., Hatami, B., Zali, M. R. & Karimipoor, M. Adeno-associated virus as a gene therapy vector: strategies to neutralize the neutralizing antibodies. *Clin. Exp. Med.* (2019). doi:10.1007/s10238-019-00557-8
154. Büning, H. & Mingozzi, F. Chapter 4 - Immune System Obstacles to In vivo Gene Transfer with Adeno-Associated Virus Vectors. in *Translating Gene Therapy to the Clinic* (eds. Laurence, J. & Franklin, M.) 45–64 (Academic Press, 2015).
155. Clément, N. Large-Scale Clinical Manufacturing of AAV Vectors for Systemic Muscle Gene Therapy. in *Muscle Gene Therapy* (eds. Duan, D. & Mendell, J. R.) 253–273 (Springer International Publishing, 2019).

156. Thévenot, E. *et al.* Targeted delivery of self-complementary adeno-associated virus serotype 9 to the brain, using magnetic resonance imaging-guided focused ultrasound. *Hum. Gene Ther.* **23**, 1144–1155 (2012).
157. Hsu, P.-H. *et al.* Noninvasive and targeted gene delivery into the brain using microbubble-facilitated focused ultrasound. *PLoS One* **8**, e57682 (2013).
158. Stavarache, M. A. *et al.* Safe and stable noninvasive focal gene delivery to the mammalian brain following focused ultrasound. *J. Neurosurg.* 1–10 (2018).
159. Wang, S., Olumolade, O. O., Sun, T., Samiotaki, G. & Konofagou, E. E. Noninvasive, neuron-specific gene therapy can be facilitated by focused ultrasound and recombinant adeno-associated virus. *Gene Ther.* **22**, 104–110 (2015).
160. Xhima, K., Nabbouh, F., Hynynen, K., Aubert, I. & Tandon, A. Noninvasive delivery of an α-synuclein gene silencing vector with magnetic resonance-guided focused ultrasound: Noninvasive Knockdown of Brain α-Syn. *Mov. Disord.* **14**, 467 (2018).
161. Burgess, A., Huang, Y., Querbes, W., Sah, D. W. & Hynynen, K. Focused ultrasound for targeted delivery of siRNA and efficient knockdown of Htt expression. *J. Control. Release* **163**, 125–129 (2012).
162. Huang, Q. *et al.* Targeted gene delivery to the mouse brain by MRI-guided focused ultrasound-induced blood-brain barrier disruption. *Exp. Neurol.* **233**, 350–356 (2012).
163. Lin, C.-Y. *et al.* Focused ultrasound-induced blood-brain barrier opening for non-viral, non-invasive, and targeted gene delivery. *J. Control. Release* **212**, 1–9 (2015).
164. Wang, H.-B. *et al.* Reduced ischemic injury after stroke in mice by angiogenic gene delivery via ultrasound-targeted microbubble destruction. *J. Neuropathol. Exp. Neurol.* **73**, 548–558 (2014).
165. Mead, B. P. *et al.* Targeted gene transfer to the brain via the delivery of brain-penetrating DNA nanoparticles with focused ultrasound. *J. Control. Release* **223**, 109–117 (2016).
166. Burgess, A. *et al.* Targeted delivery of neural stem cells to the brain using MRI-guided focused ultrasound to disrupt the blood-brain barrier. *PLoS One* **6**, e27877 (2011).
167. Alkins, R. *et al.* Focused ultrasound delivers targeted immune cells to metastatic brain tumors. *Cancer Res.* **73**, 1892–1899 (2013).
168. Jordão, J. F. *et al.* Antibodies targeted to the brain with image-guided focused ultrasound reduces amyloid-beta plaque load in the TgCRND8 mouse model of Alzheimer's disease. *PLoS One* **5**, e10549 (2010).
169. Kinoshita, M., McDannold, N., Jolesz, F. A. & Hynynen, K. Targeted delivery of antibodies through the blood–brain barrier by MRI-guided focused ultrasound. *Biochem. Biophys. Res. Commun.* **340**, 1085–1090 (2006).
170. Kinoshita, M., McDannold, N., Jolesz, F. A. & Hynynen, K. Noninvasive localized delivery of Herceptin to the mouse brain by MRI-guided focused ultrasound-induced blood-brain barrier disruption. *PNAS* **103**, 11719–11723 (2006).
171. Baseri, B. *et al.* Activation of signaling pathways following localized delivery of systemically administered neurotrophic factors across the blood-brain barrier using focused ultrasound and microbubbles. *Phys. Med. Biol.* **57**, N65–81 (2012).
172. Jordão, J. F. *et al.* Amyloid-β plaque reduction, endogenous antibody delivery and glial activation by brain-targeted, transcranial focused ultrasound. *Exp. Neurol.* **248**, 16–29 (2013).
173. Poon, C. T. *et al.* Time course of focused ultrasound effects on β-amyloid plaque pathology in the TgCRND8 mouse model of Alzheimer's disease. *Sci. Rep.* **8**, 14061 (2018).
174. Leinenga, G. & Götz, J. Scanning ultrasound removes amyloid-β and restores memory in an Alzheimer's disease mouse model. *Sci. Transl. Med.* **7**, 278ra33 (2015).
175. Leinenga, G. & Götz, J. Safety and efficacy of scanning ultrasound treatment of aged APP23 mice. *Front. Neurosci.* **12**, 55 (2018).
176. Nisbet, R. M. *et al.* Combined effects of scanning ultrasound and a tau-specific single chain antibody in a tau transgenic mouse model. *Brain* **140**, 1220–1230 (2017).
177. Bystritsky, A. *et al.* A review of low-intensity focused ultrasound pulsation. *Brain Stimul.* **4**, 125–136 (2011).
178. Fry, W. J. Use of intense ultrasound in neurological research. *Am. J. Phys. Med.* **37**, 143–147 (1958).

179. Tyler, W. J. *et al.* Remote excitation of neuronal circuits using low-intensity, low-frequency ultrasound. *PLoS One* **3**, e3511 (2008).
180. Rinaldi, P. C., Jones, J. P., Reines, F. & Price, L. R. Modification by focused ultrasound pulses of electrically evoked responses from an in vitro hippocampal preparation. *Brain Res.* **558**, 36–42 (1991).
181. Tufail, Y. *et al.* Transcranial pulsed ultrasound stimulates intact brain circuits. *Neuron* **66**, 681–694 (2010).
182. Min, B.-K. *et al.* Focused ultrasound modulates the level of cortical neurotransmitters: Potential as a new functional brain mapping technique. *Int. J. Imaging Syst. Technol.* **21**, 232–240 (2011).
183. Deffieux, T. *et al.* Low-intensity focused ultrasound modulates monkey visuomotor behavior. *Curr. Biol.* **23**, 2430–2433 (2013).
184. Blackmore, J., Shrivastava, S., Sallet, J., Butler, C. R. & Cleveland, R. O. Ultrasound Neuromodulation: A Review of Results, Mechanisms and Safety. *Ultrasound Med. Biol.* **45**, 1509–1536 (2019).
185. Kubanek, J. *et al.* Ultrasound modulates ion channel currents. *Sci. Rep.* **6**, 24170 (2016).
186. Chapman, R. A. Dependence on temperature of the conduction velocity of the action potential of the squid giant axon. *Nature* **213**, 1143–1144 (1967).
187. Lee, J. C. F., Callaway, J. C. & Foehring, R. C. Effects of temperature on calcium transients and Ca2+-dependent afterhyperpolarizations in neocortical pyramidal neurons. *J. Neurophysiol.* **93**, 2012–2020 (2005).
188. Prieto, M. L., Ömer, O., Khuri-Yakub, B. T. & Maduke, M. C. Dynamic response of model lipid membranes to ultrasonic radiation force. *PLoS One* **8**, e77115 (2013).
189. Guo, H. *et al.* Ultrasound Produces Extensive Brain Activation via a Cochlear Pathway. *Neuron* **98**, 1020–1030.e4 (2018).
190. Sato, T., Shapiro, M. G. & Tsao, D. Y. Ultrasonic Neuromodulation Causes Widespread Cortical Activation via an Indirect Auditory Mechanism. *Neuron* **98**, 1031–1041.e5 (2018).
191. Chu, P.-C. *et al.* Neuromodulation accompanying focused ultrasound-induced blood-brain barrier opening. *Sci. Rep.* **5**, 15477 (2015).
192. Carpentier, A. *et al.* Clinical trial of blood-brain barrier disruption by pulsed ultrasound. *Sci. Transl. Med.* **8**, 343re2–343re2 (2016).
193. Lipsman, N. *et al.* Initial experience of blood-brain barrier opening for chemotherapeutic-drug delivery to brain tumours by MR-guided focused ultrasound. *Neuro. Oncol.* **19**, vi9–vi9 (2017).
194. Fazekas, F. *et al.* Histopathologic analysis of foci of signal loss on gradient-echo T2*-weighted MR images in patients with spontaneous intracerebral hemorrhage: evidence of microangiopathy-related microbleeds. *AJNR Am. J. Neuroradiol.* **20**, 637–642 (1999).
195. Marty, B. *et al.* Dynamic study of blood-brain barrier closure after its disruption using ultrasound: a quantitative analysis. *J. Cereb. Blood Flow Metab.* **32**, 1948–1958 (2012).
196. Park, J., Zhang, Y., Vykhodtseva, N., Jolesz, F. A. & McDannold, N. J. The kinetics of blood brain barrier permeability and targeted doxorubicin delivery into brain induced by focused ultrasound. *J. Control. Release* **162**, 134–142 (2012).
197. Kovacs, Z. I. *et al.* MRI and histological evaluation of pulsed focused ultrasound and microbubbles treatment effects in the brain. *Theranostics* **8**, 4837–4855 (2018).
198. McMahon, D. & Hynynen, K. Acute inflammatory response following increased blood-brain barrier permeability induced by focused ultrasound is dependent on microbubble dose. *Theranostics* **7**, 3989–4000 (2017).
199. O'Reilly, M. A. *et al.* Investigation of the safety of focused ultrasound-induced blood-brain barrier opening in a natural canine model of aging. *Theranostics* **7**, 3573–3584 (2017).
200. Nandigam, R. N. K. *et al.* MR imaging detection of cerebral microbleeds: effect of susceptibility-weighted imaging, section thickness, and field strength. *AJNR Am. J. Neuroradiol.* **30**, 338–343 (2009).
201. Schwartz, R. B. *et al.* Hypertensive encephalopathy: findings on CT, MR imaging, and SPECT imaging in 14 cases. *AJR Am. J. Roentgenol.* **159**, 379–383 (1992).

202. Downs, M. E. *et al.* Long-term safety of repeated blood-brain barrier opening via focused ultrasound with microbubbles in non-human primates performing a cognitive task. *PLoS One* **10**, e0125911 (2015).
203. Downs, M. E., Buch, A., Karakatsani, M. E., Konofagou, E. E. & Ferrera, V. P. Blood-Brain Barrier Opening in Behaving Non-Human Primates via Focused Ultrasound with Systemically Administered Microbubbles. *Sci. Rep.* **5**, 15076 (2015).
204. Sheikov, N., McDannold, N., Vykhodtseva, N., Jolesz, F. & Hynynen, K. Cellular mechanisms of the blood-brain barrier opening induced by ultrasound in presence of microbubbles. *Ultrasound Med. Biol.* **30**, 979–989 (2004).
205. Sheikov, N. *et al.* Brain arterioles show more active vesicular transport of blood-borne tracer molecules than capillaries and venules after focused ultrasound-evoked opening of the blood-brain barrier. *Ultrasound Med. Biol.* **32**, 1399–1409 (2006).
206. Sheikov, N., McDannold, N., Sharma, S. & Hynynen, K. Effect of focused ultrasound applied with an ultrasound contrast agent on the tight junctional integrity of the brain microvascular endothelium. *Ultrasound Med. Biol.* **34**, 1093–1104 (2008).
207. Deng, J. *et al.* The role of caveolin-1 in blood-brain barrier disruption induced by focused ultrasound combined with microbubbles. *J. Mol. Neurosci.* **46**, 677–687 (2012).
208. Kovacs, Z. I. *et al.* Disrupting the blood-brain barrier by focused ultrasound induces sterile inflammation. *Proc. Natl. Acad. Sci. U. S. A.* **114**, E75–E84 (2017).
209. Alonso, A., Reinz, E., Fatar, M., Hennerici, M. G. & Meairs, S. Clearance of albumin following ultrasound-induced blood–brain barrier opening is mediated by glial but not neuronal cells. *Brain Res.* **1411**, 9–16 (2011).
210. Raymond, S. B. *et al.* Ultrasound enhanced delivery of molecular imaging and therapeutic agents in Alzheimer's disease mouse models. *PLoS One* **3**, e2175 (2008).
211. Kobus, T., Vykhodtseva, N., Pilatou, M., Zhang, Y. & McDannold, N. Safety Validation of Repeated Blood-Brain Barrier Disruption Using Focused Ultrasound. *Ultrasound Med. Biol.* **42**, 481–492 (2016).
212. McDannold, N., Vykhodtseva, N., Raymond, S., Jolesz, F. A. & Hynynen, K. MRI-guided targeted blood-brain barrier disruption with focused ultrasound: Histological findings in rabbits. *Ultrasound Med. Biol.* **31**, 1527–1537 (2005).
213. Hynynen, K. *et al.* Focal disruption of the blood-brain barrier due to 260-kHz ultrasound bursts: a method for molecular imaging and targeted drug delivery. *J. Neurosurg.* **105**, 445–454 (2006).
214. Liu, H.-L. *et al.* In vivo assessment of macrophage CNS infiltration during disruption of the blood-brain barrier with focused ultrasound: a magnetic resonance imaging study. *J. Cereb. Blood Flow Metab.* **30**, 177–186 (2010).
215. McMahon, D., Poon, C. & Hynynen, K. Increasing BBB Permeability via Focused Ultrasound: Current Methods in Preclinical Research. in *Blood-Brain Barrier* (ed. Barichello, T.) 267–297 (Springer New York, 2019).
216. Raymond, S. B., Skoch, J., Hynynen, K. & Bacskai, B. J. Multiphoton imaging of ultrasound/Optison mediated cerebrovascular effects in vivo. *J. Cereb. Blood Flow Metab.* **27**, 393–403 (2007).
217. Takahashi, M. *et al.* Guide wire-induced coronary artery spasm during percutaneous transluminal coronary angioplasty. A case report. *Angiology* **47**, 305–309 (1996).
218. Cho, E. E., Drazic, J., Ganguly, M., Stefanovic, B. & Hynynen, K. Two-Photon Fluorescence Microscopy Study of Cerebrovascular Dynamics in Ultrasound-Induced Blood—Brain Barrier Opening. *J. Cereb. Blood Flow Metab.* **31**, 1852–1862 (2011).
219. Burgess, A., Nhan, T., Moffatt, C., Klibanov, A. L. & Hynynen, K. Analysis of focused ultrasound-induced blood–brain barrier permeability in a mouse model of Alzheimer's disease using two-photon microscopy. *J. Control. Release* **192**, 243–248 (2014).
220. Lu, D. & Kassab, G. S. Role of shear stress and stretch in vascular mechanobiology. *J. R. Soc. Interface* **8**, 1379–1385 (2011).

221. Nhan, T. *et al.* Drug delivery to the brain by focused ultrasound induced blood-brain barrier disruption: quantitative evaluation of enhanced permeability of cerebral vasculature using two-photon microscopy. *J. Control. Release* **172**, 274–280 (2013).
222. Fan, Z., Liu, H., Mayer, M. & Deng, C. X. Spatiotemporally controlled single cell sonoporation. *Proc. Natl. Acad. Sci. U. S. A.* **109**, 16486–16491 (2012).
223. Deng, C. X., Sieling, F., Pan, H. & Cui, J. Ultrasound-induced cell membrane porosity. *Ultrasound Med. Biol.* **30**, 519–526 (2004).
224. Park, J., Fan, Z., Kumon, R. E., El-Sayed, M. E. H. & Deng, C. X. Modulation of intracellular Ca2+ concentration in brain microvascular endothelial cells in vitro by acoustic cavitation. *Ultrasound Med. Biol.* **36**, 1176–1187 (2010).
225. Park, J., Fan, Z. & Deng, C. X. Effects of shear stress cultivation on cell membrane disruption and intracellular calcium concentration in sonoporation of endothelial cells. *J. Biomech.* **44**, 164–169 (2011).
226. Zhou, Y., Kumon, R. E., Cui, J. & Deng, C. X. The size of sonoporation pores on the cell membrane. *Ultrasound Med. Biol.* **35**, 1756–1760 (2009).
227. Tachibana, K., Uchida, T., Ogawa, K., Yamashita, N. & Tamura, K. Induction of cell-membrane porosity by ultrasound. *Lancet* **353**, 1409 (1999).
228. Mehier-Humbert, S., Bettinger, T., Yan, F. & Guy, R. H. Plasma membrane poration induced by ultrasound exposure: implication for drug delivery. *J. Control. Release* **104**, 213–222 (2005).
229. Kudo, N., Okada, K. & Yamamoto, K. Sonoporation by single-shot pulsed ultrasound with microbubbles adjacent to cells. *Biophys. J.* **96**, 4866–4876 (2009).
230. Scarcelli, T. *et al.* Stimulation of hippocampal neurogenesis by transcranial focused ultrasound and microbubbles in adult mice. *Brain Stimul.* **7**, 304–307 (2014).
231. Mooney, S. J. *et al.* Focused Ultrasound-Induced Neurogenesis Requires an Increase in Blood-Brain Barrier Permeability. *PLoS One* **11**, e0159892 (2016).
232. O'Reilly, M. A. & Hynynen, K. Blood-brain barrier: real-time feedback-controlled focused ultrasound disruption by using an acoustic emissions-based controller. *Radiology* **263**, 96–106 (2012).
233. Baseri, B., Choi, J. J., Tung, Y.-S. & Konofagou, E. E. Multi-modality safety assessment of blood-brain barrier opening using focused ultrasound and definity microbubbles: a short-term study. *Ultrasound Med. Biol.* **36**, 1445–1459 (2010).
234. Hynynen, K., McDannold, N., Sheikov, N. A., Jolesz, F. A. & Vykhodtseva, N. Local and reversible blood-brain barrier disruption by noninvasive focused ultrasound at frequencies suitable for trans-skull sonications. *Neuroimage* **24**, 12–20 (2005).
235. Algattas, H. & Huang, J. H. Traumatic Brain Injury pathophysiology and treatments: early, intermediate, and late phases post-injury. *Int. J. Mol. Sci.* **15**, 309–341 (2013).
236. Prakash, R. & Carmichael, S. T. Blood-brain barrier breakdown and neovascularization processes after stroke and traumatic brain injury. *Curr. Opin. Neurol.* **28**, 556–564 (2015).
237. Dardiotis, E., Karanikas, V., Paterakis, K., Fountas, K. & M., G. Traumatic Brain Injury and Inflammation: Emerging Role of Innate and Adaptive Immunity. in *Brain Injury - Pathogenesis, Monitoring, Recovery and Management* (ed. Agrawal, A.) (InTech, 2012).
238. Jassam, Y. N., Izzy, S., Whalen, M., McGavern, D. B. & El Khoury, J. Neuroimmunology of Traumatic Brain Injury: Time for a Paradigm Shift. *Neuron* **95**, 1246–1265 (2017).
239. Ranaivo, H. R., Zunich, S. M., Choi, N., Hodge, J. N. & Wainwright, M. S. Mild Stretch-Induced Injury Increases Susceptibility to Interleukin-1β-Induced Release of Matrix Metalloproteinase-9 from Astrocytes. *J. Neurotrauma* **28**, 1757–1766 (2011).
240. Ding, Z., Zhang, J., Xu, J., Sheng, G. & Huang, G. Propofol administration modulates AQP-4 expression and brain edema after traumatic brain injury. *Cell Biochem. Biophys.* **67**, 615–622 (2013).
241. Goede, V., Brogelli, L., Ziche, M. & Augustin, H. G. Induction of inflammatory angiogenesis by monocyte chemoattractant protein-1. *Int. J. Cancer* **82**, 765–770 (1999).

242. Maloney, J. P. & Gao, L. Proinflammatory Cytokines Increase Vascular Endothelial Growth Factor Expression in Alveolar Epithelial Cells. *Mediators Inflamm.* **2015**, 387842 (2015).
243. Suidan, G. L. *et al.* CD8 T cell-initiated vascular endothelial growth factor expression promotes central nervous system vascular permeability under neuroinflammatory conditions. *J. Immunol.* **184**, 1031–1040 (2010).
244. Cho, J. & Gruol, D. L. The chemokine CCL2 activates p38 mitogen-activated protein kinase pathway in cultured rat hippocampal cells. *J. Neuroimmunol.* **199**, 94–103 (2008).
245. Perígolo-Vicente, R. *et al.* IL-6, A1 and A2aR: a crosstalk that modulates BDNF and induces neuroprotection. *Biochem. Biophys. Res. Commun.* **449**, 477–482 (2014).
246. Saha, R. N., Liu, X. & Pahan, K. Up-regulation of BDNF in astrocytes by TNF-alpha: a case for the neuroprotective role of cytokine. *J. Neuroimmune Pharmacol.* **1**, 212–222 (2006).
247. Kreipke, C. W., Morgan, R., Kallakuri, S. & Rafols, J. A. Behavioral pre-conditioning enhances angiogenesis and cognitive outcome after brain trauma. *Neurol. Res.* **29**, 388–394 (2007).
248. Wu, H. *et al.* Induction of angiogenesis and modulation of vascular endothelial growth factor receptor-2 by simvastatin after traumatic brain injury. *Neurosurgery* **68**, 1363–71; discussion 1371 (2011).
249. Sköld, M. K., von Gertten, C., Sandberg-Nordqvist, A.-C., Mathiesen, T. & Holmin, S. VEGF and VEGF receptor expression after experimental brain contusion in rat. *J. Neurotrauma* **22**, 353–367 (2005).
250. Dore-Duffy, P., Wang, X., Mehedi, A., Kreipke, C. W. & Rafols, J. A. Differential expression of capillary VEGF isoforms following traumatic brain injury. *Neurol. Res.* **29**, 395–403 (2007).
251. Morgan, R., Kreipke, C. W., Roberts, G., Bagchi, M. & Rafols, J. A. Neovascularization following traumatic brain injury: possible evidence for both angiogenesis and vasculogenesis. *Neurol. Res.* **29**, 375–381 (2007).
252. Bye, N. *et al.* Neurogenesis and glial proliferation are stimulated following diffuse traumatic brain injury in adult rats. *J. Neurosci. Res.* **89**, 986–1000 (2011).
253. Kernie, S. G., Erwin, T. M. & Parada, L. F. Brain remodeling due to neuronal and astrocytic proliferation after controlled cortical injury in mice. *J. Neurosci. Res.* **66**, 317–326 (2001).
254. Hayward, N. M. E. A. *et al.* Association of chronic vascular changes with functional outcome after traumatic brain injury in rats. *J. Neurotrauma* **27**, 2203–2219 (2010).
255. Kotas, M. E. & Medzhitov, R. Homeostasis, inflammation, and disease susceptibility. *Cell* **160**, 816–827 (2015).
256. Nathan, C. & Ding, A. Nonresolving inflammation. *Cell* **140**, 871–882 (2010).
257. Pekny, M. & Pekna, M. Astrocyte reactivity and reactive astrogliosis: costs and benefits. *Physiol. Rev.* **94**, 1077–1098 (2014).
258. Pekny, M., Wilhelmsson, U. & Pekna, M. The dual role of astrocyte activation and reactive gliosis. *Neurosci. Lett.* **565**, 30–38 (2014).
259. Hu, X. *et al.* Microglial and macrophage polarization—new prospects for brain repair. *Nat. Rev. Neurol.* **11**, 56–64 (2015).
260. Lucas, S.-M., Rothwell, N. J. & Gibson, R. M. The role of inflammation in CNS injury and disease. *Br. J. Pharmacol.* **147 Suppl 1**, S232–40 (2006).
261. Broman, T. & Lindberg-Broman, A. M. An Experimental Study of Disorders in the Permeability of the Cerebral Vessels ('the Blood-Brain-Barrier') Produced by Chemical and Physico-chemical Agents. *Acta Physiol. Scand.* **10**, 102–125 (1945).
262. Lossinsky, A. S., Vorbrodt, A. W. & Wisniewski, H. M. Scanning and transmission electron microscopic studies of microvascular pathology in the osmotically impaired blood-brain barrier. *J. Neurocytol.* **24**, 795–806 (1995).
263. Armstrong, B. K., Smith, Q. & Rapoport, S. I. OSMOTIC OPENING OF THE BLOOD-BRAIN BARRIER PERMEABILITY TO N-(2- HYDROXYPROPYL)METHACRYLAMIDE COPOLYMERS. EFFECT OF POLYMER aw, CHARGE AND HYDROPHOBICITY. *J. Control. Release* **10**, 27–35 (1989).
264. Siegal, T. *et al.* In vivo assessment of the window of barrier opening after osmotic blood–brain barrier

disruption in humans. *J. Neurosurg.* **92**, 599–605 (2000).

265. Tomiwa, K., Hazama, F. & Mikawa, H. Prevention of Tissue Damage with Filtration of the Perfusate. *Acta Pathol. Jpn.* **32**, 427435 (1982).
266. Thelin, E. P., Nelson, D. W. & Bellander, B.-M. A review of the clinical utility of serum S100B protein levels in the assessment of traumatic brain injury. *Acta Neurochir.* **159**, 209–225 (2017).
267. Bullard, D. E. & Bigner, D. D. Blood-brain barrier disruption in immature Fischer 344 rats. *J. Neurosurg.* **60**, 743–750 (1984).
268. Mainprize, T. *et al.* Blood-Brain Barrier Opening in Primary Brain Tumors with Non-invasive MR-Guided Focused Ultrasound: A Clinical Safety and Feasibility Study. *Sci. Rep.* **9**, 321 (2019).
269. Shi, Y. *et al.* Rapid endothelial cytoskeletal reorganization enables early blood-brain barrier disruption and long-term ischaemic reperfusion brain injury. *Nat. Commun.* **7**, 10523 (2016).
270. Knowland, D. *et al.* Stepwise recruitment of transcellular and paracellular pathways underlies blood-brain barrier breakdown in stroke. *Neuron* **82**, 603–617 (2014).
271. Merali, Z., Huang, K., Mikulis, D., Silver, F. & Kassner, A. Evolution of blood-brain-barrier permeability after acute ischemic stroke. *PLoS One* **12**, e0171558 (2017).
272. Rigau, V. *et al.* Angiogenesis is associated with blood-brain barrier permeability in temporal lobe epilepsy. *Brain* **130**, 1942–1956 (2007).
273. Vazana, U. *et al.* Glutamate-Mediated Blood-Brain Barrier Opening: Implications for Neuroprotection and Drug Delivery. *J. Neurosci.* **36**, 7727–7739 (2016).
274. Dey, A., Kang, X., Qiu, J., Du, Y. & Jiang, J. Anti-Inflammatory Small Molecules To Treat Seizures and Epilepsy: From Bench to Bedside. *Trends Pharmacol. Sci.* **37**, 463–484 (2016).
275. Marchi, N. *et al.* Efficacy of anti-inflammatory therapy in a model of acute seizures and in a population of pediatric drug resistant epileptics. *PLoS One* **6**, e18200 (2011).
276. Guo, S. *et al.* Effects of Controlled Cortical Impact on the Mouse Brain Vasculome. *J. Neurotrauma* **33**, 1303–1316 (2016).
277. Rossi, B., Angiari, S., Zenaro, E., Budui, S. L. & Constantin, G. Vascular inflammation in central nervous system diseases: adhesion receptors controlling leukocyte–endothelial interactions. *J. Leukoc. Biol.* **89**, 539–556 (2011).
278. Todd, M. M., Weeks, J. B. & Warner, D. S. Cerebral blood flow, blood volume, and brain tissue hematocrit during isovolemic hemodilution with hetastarch in rats. *Am. J. Physiol.* **263**, H75–82 (1992).
279. Yousif, S. *et al.* Expression of drug transporters at the blood–brain barrier using an optimized isolated rat brain microvessel strategy. *Brain Res.* **1134**, 1–11 (2007).
280. Mojsilovic-Petrovic, J., Nesic, M., Pen, A., Zhang, W. & Stanimirovic, D. Development of rapid staining protocols for laser-capture microdissection of brain vessels from human and rat coupled to gene expression analyses. *J. Neurosci. Methods* **133**, 39–48 (2004).
281. Liberto, C. M., Albrecht, P. J., Herx, L. M., Yong, V. W. & Levison, S. W. Pro-regenerative properties of cytokine-activated astrocytes. *J. Neurochem.* **89**, 1092–1100 (2004).
282. Tovar-y-Romo, L. B., Penagos-Puig, A. & Ramírez-Jarquín, J. O. Endogenous recovery after brain damage: molecular mechanisms that balance neuronal life/death fate. *J. Neurochem.* **136**, 13–27 (2016).
283. Whitney, N. P., Eidem, T. M., Peng, H., Huang, Y. & Zheng, J. C. Inflammation mediates varying effects in neurogenesis: relevance to the pathogenesis of brain injury and neurodegenerative disorders. *J. Neurochem.* **108**, 1343–1359 (2009).
284. Goldstein, E. Z., Church, J. S., Hesp, Z. C., Popovich, P. G. & McTigue, D. M. A silver lining of neuroinflammation: Beneficial effects on myelination. *Exp. Neurol.* **283**, 550–559 (2016).
285. Croll, S. D. *et al.* VEGF-mediated inflammation precedes angiogenesis in adult brain. *Exp. Neurol.* **187**, 388–402 (2004).
286. Rogers, J., Strohmeyer, R., Kovelowski, C. J. & Li, R. Microglia and inflammatory mechanisms in the clearance of amyloid beta peptide. *Glia* **40**, 260–269 (2002).

287. Sansbury, B. E. & Spite, M. Resolution of Acute Inflammation and the Role of Resolvins in Immunity, Thrombosis, and Vascular Biology. *Circ. Res.* **119**, 113–130 (2016).
288. Zanotti, L. *et al.* Mouse mesenchymal stem cells inhibit high endothelial cell activation and lymphocyte homing to lymph nodes by releasing TIMP-1. *Leukemia* **30**, 1143–1154 (2016).
289. Lee, W., Ku, S.-K., Na, D. H. & Bae, J.-S. Anti-Inflammatory Effects of Lysozyme Against HMGB1 in Human Endothelial Cells and in Mice. *Inflammation* **38**, 1911–1924 (2015).
290. Kim, J. R., Horton, N. C., Mathew, S. O. & Mathew, P. A. CS1 (SLAMF7) inhibits production of proinflammatory cytokines by activated monocytes. *Inflamm. Res.* **62**, 765–772 (2013).
291. Cho, H. *et al.* Localized Down-regulation of P-glycoprotein by Focused Ultrasound and Microbubbles induced Blood-Brain Barrier Disruption in Rat Brain. *Sci. Rep.* **6**, 31201 (2016).
292. Löscher, W. & Potschka, H. Blood-brain barrier active efflux transporters: ATP-binding cassette gene family. *NeuroRx* **2**, 86–98 (2005).
293. Jung, N. *et al.* Relevance of the organic cation transporters 1 and 2 for antiretroviral drug therapy in human immunodeficiency virus infection. *Drug Metab. Dispos.* **36**, 1616–1623 (2008).
294. VanWert, A. L. & Sweet, D. H. Impaired clearance of methotrexate in organic anion transporter 3 (Slc22a8) knockout mice: a gender specific impact of reduced folates. *Pharm. Res.* **25**, 453–462 (2008).
295. Cha, S. H. *et al.* Identification and characterization of human organic anion transporter 3 expressing predominantly in the kidney. *Mol. Pharmacol.* **59**, 1277–1286 (2001).
296. Li, L., Agarwal, S. & Elmquist, W. F. Brain efflux index to investigate the influence of active efflux on brain distribution of pemetrexed and methotrexate. *Drug Metab. Dispos.* **41**, 659–667 (2013).
297. Apiwattanakul, N. *et al.* Transport properties of nonsteroidal anti-inflammatory drugs by organic anion transporter 1 expressed in Xenopus laevis oocytes. *Mol. Pharmacol.* **55**, 847–854 (1999).
298. Tahara, H. *et al.* A species difference in the transport activities of H2 receptor antagonists by rat and human renal organic anion and cation transporters. *J. Pharmacol. Exp. Ther.* **315**, 337–345 (2005).
299. Urquhart, B. L. & Kim, R. B. Blood-brain barrier transporters and response to CNS-active drugs. *Eur. J. Clin. Pharmacol.* **65**, 1063–1070 (2009).
300. Licinio, J. & Wong, M.-L. *Pharmacogenomics: The Search for Individualized Therapies*. (John Wiley & Sons, 2009).
301. Nigam, S. K. *et al.* The organic anion transporter (OAT) family: a systems biology perspective. *Physiol. Rev.* **95**, 83–123 (2015).
302. Goralski, K. B., Hartmann, G., Piquette-Miller, M. & Renton, K. W. Downregulation of mdr1a expression in the brain and liver during CNS inflammation alters the in vivo disposition of digoxin. *Br. J. Pharmacol.* **139**, 35–48 (2003).
303. Ronaldson, P. T. & Bendayan, R. HIV-1 viral envelope glycoprotein gp120 triggers an inflammatory response in cultured rat astrocytes and regulates the functional expression of P-glycoprotein. *Mol. Pharmacol.* **70**, 1087–1098 (2006).
304. Ashraf, T. *et al.* Role of anti-inflammatory compounds in human immunodeficiency virus-1 glycoprotein120-mediated brain inflammation. *J. Neuroinflammation* **11**, 91 (2014).
305. Fernandez, C., Buyse, M., German-Fattal, M. & Gimenez, F. Influence of the pro-inflammatory cytokines on P-glycoprotein expression and functionality. *J. Pharm. Pharm. Sci.* **7**, 359–371 (2004).
306. Cherrington, N. J., Slitt, A. L., Li, N. & Klaassen, C. D. Lipopolysaccharide-mediated regulation of hepatic transporter mRNA levels in rats. *Drug Metab. Dispos.* **32**, 734–741 (2004).
307. Ashraf, T., Ronaldson, P. T., Persidsky, Y. & Bendayan, R. Regulation of P-glycoprotein by human immunodeficiency virus-1 in primary cultures of human fetal astrocytes. *J. Neurosci. Res.* **89**, 1773–1782 (2011).
308. Seegers, U., Potschka, H. & Löscher, W. Transient increase of P-glycoprotein expression in endothelium and parenchyma of limbic brain regions in the kainate model of temporal lobe epilepsy. *Epilepsy Res.* **51**, 257–268 (2002).

309. Zhang, L., Ong, W. Y. & Lee, T. Induction of P-glycoprotein expression in astrocytes following intracerebroventricular kainate injections. *Exp. Brain Res.* **126**, 509–516 (1999).
310. Song, J., Qi, M., Kaul, S. & Price, R. J. Stimulation of arteriogenesis in skeletal muscle by microbubble destruction with ultrasound. *Circulation* **106**, 1550–1555 (2002).
311. Chen, B. P. *et al.* DNA microarray analysis of gene expression in endothelial cells in response to 24-h shear stress. *Physiol. Genomics* **7**, 55–63 (2001).
312. Naldini, A. & Carraro, F. Role of inflammatory mediators in angiogenesis. *Curr. Drug Targets Inflamm. Allergy* **4**, 3–8 (2005).
313. Xiong, Y., Mahmood, A. & Chopp, M. Angiogenesis, neurogenesis and brain recovery of function following injury. *Curr. Opin. Investig. Drugs* **11**, 298–308 (2010).
314. Miller, F. *et al.* The MAP kinase pathway mediates transcytosis induced by TNF-α in an in vitro blood–brain barrier model. *Eur. J. Neurosci.* **22**, 835–844 (2005).
315. Stamatovic, S. M., Keep, R. F., Wang, M. M., Jankovic, I. & Andjelkovic, A. V. Caveolae-mediated internalization of occludin and claudin-5 during CCL2-induced tight junction remodeling in brain endothelial cells. *J. Biol. Chem.* **284**, 19053–19066 (2009).
316. Schott, J. M. & Revesz, T. Inflammation in Alzheimer's disease: insights from immunotherapy. *Brain* **136**, 2654–2656 (2013).
317. El Khoury, J. *et al.* Ccr2 deficiency impairs microglial accumulation and accelerates progression of Alzheimer-like disease. *Nat. Med.* **13**, 432–438 (2007).
318. Michaud, J.-P., Bellavance, M.-A., Préfontaine, P. & Rivest, S. Real-time in vivo imaging reveals the ability of monocytes to clear vascular amyloid beta. *Cell Rep.* **5**, 646–653 (2013).
319. Guillot-Sestier, M.-V., Doty, K. R. & Town, T. Innate Immunity Fights Alzheimer's Disease. *Trends Neurosci.* **38**, 674–681 (2015).
320. Subramanian, A. *et al.* Gene set enrichment analysis: a knowledge-based approach for interpreting genome-wide expression profiles. *Proc. Natl. Acad. Sci. U. S. A.* **102**, 15545–15550 (2005).
321. Downs, M. E. *et al.* Long-Term Safety of Repeated Blood-Brain Barrier Opening via Focused Ultrasound with Microbubbles in Non-Human Primates Performing a Cognitive Task. *PLoS One* **10**, e0125911 (2015).
322. Mullin, L. *et al.* Effect of anesthesia carrier gas on in vivo circulation times of ultrasound microbubble contrast agents in rats. *Contrast Media Mol. Imaging* **6**, 126–131 (2011).
323. Wu, H. *et al.* Acoustic characterization and pharmacokinetic analyses of new nanobubble ultrasound contrast agents. *Ultrasound Med. Biol.* **39**, 2137–2146 (2013).
324. Zheng, Z. & Yenari, M. A. Post-ischemic inflammation: molecular mechanisms and therapeutic implications. *Neurol. Res.* **26**, 884–892 (2004).
325. Shen, W., Zhang, C. & Zhang, G. Nuclear factor kappaB activation is mediated by NMDA and non-NMDA receptor and L-type voltage-gated Ca(2+) channel following severe global ischemia in rat hippocampus. *Brain Res.* **933**, 23–30 (2002).
326. McMahon, D., Bendayan, R. & Hynynen, K. Acute effects of focused ultrasound-induced increases in blood-brain barrier permeability on rat microvascular transcriptome. *Sci. Rep.* **7**, 45657 (2017).
327. Berti, R. *et al.* Quantitative real-time RT-PCR analysis of inflammatory gene expression associated with ischemia-reperfusion brain injury. *J. Cereb. Blood Flow Metab.* **22**, 1068–1079 (2002).
328. Williams, A. J., Dave, J. R. & Tortella, F. C. Neuroprotection with the proteasome inhibitor MLN519 in focal ischemic brain injury: relation to nuclear factor kappaB (NF-kappaB), inflammatory gene expression, and leukocyte infiltration. *Neurochem. Int.* **49**, 106–112 (2006).
329. Downs, M. E. *et al.* Correction: Long-Term Safety of Repeated Blood-Brain Barrier Opening via Focused Ultrasound with Microbubbles in Non-Human Primates Performing a Cognitive Task. *PLoS One* **10**, e0130860 (2015).
330. Horodyckid, C. *et al.* Safe long-term repeated disruption of the blood-brain barrier using an implantable ultrasound device: a multiparametric study in a primate model. *J. Neurosurg.* 1–11 (2016).

331. Dénes, A., Humphreys, N., Lane, T. E., Grencis, R. & Rothwell, N. Chronic systemic infection exacerbates ischemic brain damage via a CCL5 (regulated on activation, normal T-cell expressed and secreted)-mediated proinflammatory response in mice. *J. Neurosci.* **30**, 10086–10095 (2010).
332. Pleines, U. E., Stover, J. F., Kossmann, T., Trentz, O. & Morganti-Kossmann, M. C. Soluble ICAM-1 in CSF coincides with the extent of cerebral damage in patients with severe traumatic brain injury. *J. Neurotrauma* **15**, 399–409 (1998).
333. Signoretti, S., Vagnozzi, R., Tavazzi, B. & Lazzarino, G. Biochemical and neurochemical sequelae following mild traumatic brain injury: summary of experimental data and clinical implications. *Neurosurg. Focus* **29**, E1 (2010).
334. Redell, J. B., Zhao, J. & Dash, P. K. Altered expression of miRNA-21 and its targets in the hippocampus after traumatic brain injury. *J. Neurosci. Res.* **89**, 212–221 (2011).
335. Doyle, K. P., Simon, R. P. & Stenzel-Poore, M. P. Mechanisms of ischemic brain damage. *Neuropharmacology* **55**, 310–318 (2008).
336. Helmy, A., De Simoni, M.-G., Guilfoyle, M. R., Carpenter, K. L. H. & Hutchinson, P. J. Cytokines and innate inflammation in the pathogenesis of human traumatic brain injury. *Prog. Neurobiol.* **95**, 352–372 (2011).
337. Burgess, A. *et al.* Alzheimer disease in a mouse model: MR imaging-guided focused ultrasound targeted to the hippocampus opens the blood-brain barrier and improves pathologic abnormalities and behavior. *Radiology* **273**, 736–745 (2014).
338. Chappell, J. C., Klibanov, A. L. & Price, R. J. Ultrasound-microbubble-induced neovascularization in mouse skeletal muscle. *Ultrasound Med. Biol.* **31**, 1411–1422 (2005).
339. Johnson, C. A. & O'Brien, W. D., Jr. The angiogenic response is dependent on ultrasound contrast agent concentration. *Vasc. Cell* **4**, 10 (2012).
340. Patel, A., Schoen, S. J. & Arvanitis, C. Closed Loop Spatial and Temporal Control of Cavitation Activity with Passive Acoustic Mapping. *IEEE Trans. Biomed. Eng.* (2018). doi:10.1109/TBME.2018.2882337
341. Bergers, G. *et al.* Matrix metalloproteinase-9 triggers the angiogenic switch during carcinogenesis. *Nat. Cell Biol.* **2**, 737–744 (2000).
342. Im, E., Venkatakrishnan, A. & Kazlauskas, A. Cathepsin B regulates the intrinsic angiogenic threshold of endothelial cells. *Mol. Biol. Cell* **16**, 3488–3500 (2005).
343. Nangia-Makker, P. *et al.* Galectin-3 induces endothelial cell morphogenesis and angiogenesis. *Am. J. Pathol.* **156**, 899–909 (2000).
344. Liu, D., Evans, I., Britton, G. & Zachary, I. The zinc-finger transcription factor, early growth response 3, mediates VEGF-induced angiogenesis. *Oncogene* **27**, 2989–2998 (2008).
345. Garmy-Susini, B. & Varner, J. A. Circulating endothelial progenitor cells. *Br. J. Cancer* **93**, 855–858 (2005).
346. Asahara, T. *et al.* Isolation of putative progenitor endothelial cells for angiogenesis. *Science* **275**, 964–967 (1997).
347. Bautch, V. L. VEGF-directed blood vessel patterning: from cells to organism. *Cold Spring Harb. Perspect. Med.* **2**, a006452 (2012).
348. McMahon, D. & Hynynen, K. Reply to Kovacs et al.: Concerning acute inflammatory response following focused ultrasound and microbubbles in the brain. *Theranostics* **8**, 2249–2250 (2018).
349. Kovacs, Z. I., Burks, S. R. & Frank, J. A. Focused ultrasound with microbubbles induces sterile inflammatory response proportional to the blood brain barrier opening: Attention to experimental conditions. *Theranostics* **8**, 2245–2248 (2018).
350. Jalali, S., Huang, Y., Dumont, D. J. & Hynynen, K. Focused ultrasound-mediated bbb disruption is associated with an increase in activation of AKT: experimental study in rats. *BMC Neurol.* **10**, 114 (2010).
351. Stamatovic, S. M., Keep, R. F., Mostarica-Stojkovic, M. & Andjelkovic, A. V. CCL2 Regulates Angiogenesis via Activation of Ets-1 Transcription Factor1. *J. Immunol.* **177**, 2651–2661 (2006).
352. Low-Marchelli, J. M. *et al.* Twist1 induces CCL2 and recruits macrophages to promote angiogenesis. *Cancer Res.* **73**, 662–671 (2013).

353. Ehling, J. *et al.* CCL2-dependent infiltrating macrophages promote angiogenesis in progressive liver fibrosis. *Gut* **63**, 1960–1971 (2014).
354. Voronov, E., Carmi, Y. & Apte, R. N. The role IL-1 in tumor-mediated angiogenesis. *Front. Physiol.* **5**, 114 (2014).
355. Liao, Y.-Y. *et al.* CCL3 promotes angiogenesis by dysregulation of miR-374b/ VEGF-A axis in human osteosarcoma cells. *Oncotarget* **7**, 4310–4325 (2016).
356. Scapini, P. *et al.* CXCL1/macrophage inflammatory protein-2-induced angiogenesis in vivo is mediated by neutrophil-derived vascular endothelial growth factor-A. *J. Immunol.* **172**, 5034–5040 (2004).
357. Wang, D. *et al.* CXCL1 induced by prostaglandin E2 promotes angiogenesis in colorectal cancer. *J. Exp. Med.* **203**, 941–951 (2006).
358. Borsini, A., Zunszain, P. A., Thuret, S. & Pariante, C. M. The role of inflammatory cytokines as key modulators of neurogenesis. *Trends Neurosci.* **38**, 145–157 (2015).
359. Ekdahl, C. T., Kokaia, Z. & Lindvall, O. Brain inflammation and adult neurogenesis: the dual role of microglia. *Neuroscience* **158**, 1021–1029 (2009).
360. Schwartz, M. & Deczkowska, A. Neurological Disease as a Failure of Brain-Immune Crosstalk: The Multiple Faces of Neuroinflammation. *Trends Immunol.* **37**, 668–679 (2016).
361. Ronaldson, P. T. & Bendayan, R. HIV-1 viral envelope glycoprotein gp120 triggers an inflammatory response in cultured rat astrocytes and regulates the functional expression of P-glycoprotein. *Mol. Pharmacol.* **70**, 1087–1098 (2006).
362. Silburt, J., Lipsman, N. & Aubert, I. Disrupting the blood-brain barrier with focused ultrasound: Perspectives on inflammation and regeneration. *Proc. Natl. Acad. Sci. U. S. A.* (2017). doi:10.1073/pnas.1710761114
363. Kovacs, Z. I., Burks, S. R. & Frank, J. A. Reply to Silburt et al.: Concerning sterile inflammation following focused ultrasound and microbubbles in the brain. *Proc. Natl. Acad. Sci. U. S. A.* (2017). doi:10.1073/pnas.1711544114
364. Mooney, S. J., Nobrega, J. N., Levitt, A. J. & Hynynen, K. Antidepressant effects of focused ultrasound induced blood-brain-barrier opening. *Behav. Brain Res.* **342**, 57–61 (2018).
365. Fan, C.-H. *et al.* Noninvasive, Targeted, and Non-Viral Ultrasound-Mediated GDNF-Plasmid Delivery for Treatment of Parkinson's Disease. *Sci. Rep.* **6**, 19579 (2016).
366. McMahon, D., Mah, E. & Hynynen, K. Angiogenic response of rat hippocampal vasculature to focused ultrasound-mediated increases in blood-brain barrier permeability. *Sci. Rep.* **8**, 12178 (2018).
367. Shaikh, S., Verma, H., Yadav, N., Jauhari, M. & Bullangowda, J. Applications of Steroid in Clinical Practice: A Review. *International Scholarly Research Notices* **2012**, (2012).
368. Limbourg, F. P. & Liao, J. K. Nontranscriptional actions of the glucocorticoid receptor. *J. Mol. Med.* **81**, 168–174 (2003).
369. Yang, J.-T. *et al.* Dexamethasone inhibits ICAM-1 and MMP-9 expression and reduces brain edema in intracerebral hemorrhagic rats. *Acta Neurochir.* **153**, 2197–2203 (2011).
370. Gu, Y.-T., Zhang, H. & Xue, Y.-X. Dexamethasone treatment modulates aquaporin-4 expression after intracerebral hemorrhage in rats. *Neurosci. Lett.* **413**, 126–131 (2007).
371. Shapiro, W. R. *et al.* Temporal effects of dexamethasone on blood-to-brain and blood-to-tumor transport of 14C-alpha-aminoisobutyric acid in rat C6 glioma. *J. Neurooncol.* **8**, 197–204 (1990).
372. Stegmayr, C. *et al.* Influence of blood-brain barrier permeability on O-(2-18F-fluoroethyl)-L-tyrosine uptake in rat gliomas. *Eur. J. Nucl. Med. Mol. Imaging* **44**, 408–416 (2017).
373. Neuwelt, E. A., Barnett, P. A., Bigner, D. D. & Frenkel, E. P. Effects of adrenal cortical steroids and osmotic blood-brain barrier opening on methotrexate delivery to gliomas in the rodent: the factor of the blood-brain barrier. *Proc. Natl. Acad. Sci. U. S. A.* **79**, 4420–4423 (1982).
374. Doolittle, N. D. *et al.* Safety and efficacy of a multicenter study using intraarterial chemotherapy in conjunction with osmotic opening of the blood-brain barrier for the treatment of patients with malignant brain tumors. *Cancer* **88**, 637–647 (2000).

375. Shen, Y. *et al.* T1 relaxivities of gadolinium-based magnetic resonance contrast agents in human whole blood at 1.5, 3, and 7 T. *Invest. Radiol.* **50**, 330–338 (2015).
376. Tofts, P. S. & Kermode, A. G. Measurement of the blood-brain barrier permeability and leakage space using dynamic MR imaging. 1. Fundamental concepts. *Magn. Reson. Med.* **17**, 357–367 (1991).
377. Kovar, D. A., Lewis, M. & Karczmar, G. S. A new method for imaging perfusion and contrast extraction fraction: Input functions derived from reference tissues. *J. Magn. Reson. Imaging* **8**, 1126–1134 (1998).
378. Heisen, M. *et al.* The use of a reference tissue arterial input function with low-temporal-resolution DCE-MRI data. *Phys. Med. Biol.* **55**, 4871–4883 (2010).
379. Wang, S. *et al.* Arterial input functions (AIFs) measured directly from arteries with low and standard doses of contrast agent, and AIFs derived from reference tissues. *Magn. Reson. Imaging* **34**, 197–203 (2016).
380. Yankeelov, T. E. *et al.* Comparison of a reference region model with direct measurement of an AIF in the analysis of DCE-MRI data. *Magn. Reson. Med.* **57**, 353–361 (2007).
381. Sato, Y. *et al.* Three-dimensional multi-scale line filter for segmentation and visualization of curvilinear structures in medical images. *Med. Image Anal.* **2**, 143–168 (1998).
382. Chai, W.-Y. *et al.* Magnetic-resonance imaging for kinetic analysis of permeability changes during focused ultrasound-induced blood-brain barrier opening and brain drug delivery. *J. Control. Release* **192**, 1–9 (2014).
383. Armitage, P. A., Schwindack, C., Bastin, M. E. & Whittle, I. R. Quantitative assessment of intracranial tumor response to dexamethasone using diffusion, perfusion and permeability magnetic resonance imaging. *Magn. Reson. Imaging* **25**, 303–310 (2007).
384. Gu, Y.-T., Qin, L.-J., Qin, X. & Xu, F. The molecular mechanism of dexamethasone-mediated effect on the blood–brain tumor barrier permeability in a rat brain tumor model. *Neurosci. Lett.* **452**, 114–118 (2009).
385. Romero, I. A. *et al.* Changes in cytoskeletal and tight junctional proteins correlate with decreased permeability induced by dexamethasone in cultured rat brain endothelial cells. *Neurosci. Lett.* **344**, 112–116 (2003).
386. Aveleira, C. A., Lin, C.-M., Abcouwer, S. F., Ambrósio, A. F. & Antonetti, D. A. TNF-α signals through PKCζ/NF-κB to alter the tight junction complex and increase retinal endothelial cell permeability. *Diabetes* **59**, 2872–2882 (2010).
387. Hafezi-Moghadam, A. *et al.* Acute cardiovascular protective effects of corticosteroids are mediated by non-transcriptional activation of endothelial nitric oxide synthase. *Nat. Med.* **8**, 473–479 (2002).
388. Ekerbiçer, N. *et al.* Effects of acute treatment with dexamethasone on hemodynamic and histopathological changes in rats. *Biotech. Histochem.* **87**, 385–396 (2012).
389. Harkness, K. A. *et al.* Dexamethasone regulation of matrix metalloproteinase expression in CNS vascular endothelium. *Brain* **123 (Pt 4)**, 698–709 (2000).
390. Harkness, K. A., Sussman, J. D., Davies-Jones, G. A. B., Greenwood, J. & Woodroofe, M. N. Cytokine regulation of MCP-1 expression in brain and retinal microvascular endothelial cells. *J. Neuroimmunol.* **142**, 1–9 (2003).
391. Stanimirovic, D. & Satoh, K. Inflammatory mediators of cerebral endothelium: a role in ischemic brain inflammation. *Brain Pathol.* **10**, 113–126 (2000).
392. Steffen, B. J., Butcher, E. C. & Engelhardt, B. Evidence for involvement of ICAM-1 and VCAM-1 in lymphocyte interaction with endothelium in experimental autoimmune encephalomyelitis in the central nervous system in the SJL/J mouse. *Am. J. Pathol.* **145**, 189–201 (1994).
393. Eng, L. F. & Ghirnikar, R. S. GFAP and Astrogliosis. *Brain Pathol.* **4**, 229–237 (1994).
394. Okimura, Y. *et al.* Reactive astrocytes in acute stage after experimental brain injury: relationship to extravasated plasma protein and expression of heat shock protein. *J. Neurotrauma* **13**, 385–393 (1996).
395. Jung, Y.-J. & Chung, W.-S. Phagocytic Roles of Glial Cells in Healthy and Diseased Brains. *Biomol. Ther.* **26**, 350–357 (2018).
396. Kasselman, L. J. *et al.* Dexamethasone treatment and ICAM-1 deficiency impair VEGF-induced angiogenesis in adult brain. *J. Vasc. Res.* **44**, 283–291 (2007).

397. Dienel, G. A. & Cruz, N. F. Astrocyte activation in working brain: energy supplied by minor substrates. *Neurochem. Int.* **48**, 586–595 (2006).

398. Tuor, U. I., Kurpita, G. & Simone, C. Correlation of local changes in cerebral blood flow, capillary density, and cytochrome oxidase during development. *J. Comp. Neurol.* **342**, 439–448 (1994).

399. Harder, D. R., Zhang, C. & Gebremedhin, D. Astrocytes function in matching blood flow to metabolic activity. *News Physiol. Sci.* **17**, 27–31 (2002).

400. Tsai, H.-C. *et al.* Safety evaluation of frequent application of microbubble-enhanced focused ultrasound blood-brain-barrier opening. *Sci. Rep.* **8**, 17720 (2018).

401. Blackmore, D. G. *et al.* Multimodal analysis of aged wild-type mice exposed to repeated scanning ultrasound treatments demonstrates long-term safety. *Theranostics* **8**, 6233–6247 (2018).

402. Yang, Y. *et al.* Cavitation dose painting for focused ultrasound-induced blood-brain barrier disruption. *Sci. Rep.* **9**, 2840 (2019).

Appendix

Appendix Table 2.1: Upregulated genes in hippocampal microvessels at either 6 or 24 hrs following sonication (versus contralateral hemisphere)

		6 hrs Post-FUS+MBs		24 hrs Post-FUS+MBs	
Entrez ID	**Gene Symbol**	**Log2 FC**	**Adjusted P-Value**	**Log2 FC**	**Adjusted P-Value**
24153	*A2m*	0.37	0.585	1.73	0.019
300475	*Adamts8*	1.60	0.025	0.41	0.619
29624	*Alox5ap*	-0.21	0.705	1.13	0.032
54323	*Arc*	1.39	0.002	-0.42	0.273
498282	*Arhgap30*	0.30	0.546	1.01	0.043
497990	*Arl5c*	1.12	0.012	0.16	0.778
304648	*Asf1b*	-0.11	0.816	1.38	0.004
78971	*Birc3*	2.30	0.005	1.29	0.085
367901	*Btk*	-0.07	0.905	1.02	0.037
312705	*C1r*	-0.27	0.558	1.41	0.007
192262	*C1s*	0.10	0.874	1.69	0.004
24232	*C3*	1.26	0.031	1.55	0.023
84007	*C3ar1*	0.60	0.116	1.01	0.026
297339	*Capg*	-0.35	0.579	1.40	0.033
311327	*Casc5*	-0.09	0.897	1.17	0.034
24770	*Ccl2*	4.73	<0.001	1.70	0.083
25542	*Ccl3*	1.83	0.005	0.44	0.495
287910	*Ccl6*	0.68	0.454	1.94	0.045
287561	*Ccl7*	3.57	0.005	1.56	0.170
114494	*Ccna2*	-0.17	0.760	1.00	0.043
60463	*Ccr2*	2.42	0.106	4.11	0.023
117029	*Ccr5*	0.62	0.191	1.15	0.036
60350	*Cd14*	1.20	0.030	1.17	0.048
29185	*Cd37*	0.31	0.496	1.10	0.026
25406	*Cd44*	0.75	0.102	1.11	0.036
287435	*Cd68*	-0.03	0.971	1.52	0.006
303747	*Cd7*	0.07	0.939	1.54	0.031
25599	*Cd74*	0.34	0.732	2.64	0.009
366065	*Cers6*	1.12	0.006	-0.34	0.400
680338	*Clec12a*	-0.61	0.505	2.25	0.024
474143	*Clec4a*	-0.45	0.284	1.15	0.023
297584	*Clec4a2*	0.10	0.945	2.12	0.046
362431	*Clec4a3*	-0.68	0.272	1.87	0.012
502902	*Clec7a*	0.93	0.491	3.01	0.036
406864	*Clic1*	0.59	0.233	1.59	0.011
155151	*Coro1a*	1.00	0.040	0.63	0.205
24268	*Cp*	-0.01	0.990	1.86	0.002
24273	*Cryaa*	1.12	0.053	1.28	0.045
171081	*Csf2rb*	2.38	0.025	1.55	0.140
252929	*Ctsz*	0.25	0.609	1.37	0.012
89808	*Cx3cl1*	1.07	0.002	-0.51	0.089
81503	*Cxcl1*	2.74	0.003	0.47	0.621
305236	*Cxcl11*	2.25	0.003	1.07	0.097

497942	*Cxcl16*	0.70	0.201	1.31	0.039
66021	*Cybb*	-0.26	0.720	1.40	0.040
170901	*Efna3*	1.13	0.018	-0.40	0.421
25148	*Egr3*	1.23	0.005	-0.42	0.294
81505	*Emp3*	-0.15	0.818	1.24	0.031
295279	*Fcgr1a*	0.01	0.988	1.16	0.026
304966	*Fcgr3a*	0.08	0.936	1.44	0.048
114091	*Fcnb*	2.81	0.008	0.84	0.440
362332	*Flnc*	-0.17	0.761	1.08	0.039
314322	*Fos*	1.31	0.046	0.62	0.376
25445	*Fosl1*	2.06	0.006	0.51	0.517
499537	*Fyb*	0.52	0.257	1.09	0.036
171164	*Gbp2*	1.15	0.032	0.32	0.611
24387	*Gfap*	0.29	0.468	1.54	0.002
499914	*Gins1*	-0.28	0.739	2.04	0.012
299783	*Glipr1*	1.66	0.194	2.90	0.045
679819	*Glipr2*	0.64	0.161	1.40	0.012
113940	*Gmfg*	0.17	0.770	1.12	0.033
690825	*Gngt2*	0.28	0.775	1.78	0.041
113955	*Gpnmb*	-0.28	0.571	1.69	0.003
24409	*Grin2a*	1.03	0.026	-0.77	0.092
311984	*Gsap*	0.70	0.159	1.16	0.041
502125	*Hist1h2ah*	0.00	0.996	1.00	0.042
24471	*Hspb1*	0.17	0.785	1.56	0.012
306564	*Htra4*	1.47	0.005	0.14	0.823
293618	*Ifitm1*	-0.13	0.838	1.50	0.011
287813	*Igsf7*	0.78	0.424	2.18	0.039
24494	*Il1b*	3.18	0.003	0.35	0.762
24498	*Il6*	2.85	0.016	1.78	0.119
368066	*Inmt*	0.40	0.596	1.65	0.032
292060	*Irf8*	0.61	0.185	1.07	0.043
290651	*Isyna1*	-0.62	0.054	1.07	0.007
25021	*Itgam*	0.66	0.121	1.55	0.005
309684	*Itgb2*	0.47	0.427	1.38	0.034
24517	*Junb*	1.17	0.027	0.81	0.118
297666	*Klra5*	-0.25	0.657	1.85	0.003
317676	*Lat2*	0.08	0.885	1.22	0.011
170496	*Lcn2*	2.02	0.008	2.91	0.002
306071	*Lcp1*	0.36	0.558	1.37	0.034
83781	*Lgals3*	0.42	0.527	2.29	0.004
60584	*Lif*	1.13	0.018	-0.02	0.984
292594	*Lilrb4*	1.76	0.088	3.23	0.011
315691	*Lingo1*	1.37	0.013	-0.86	0.104
361680	*Lsp1*	1.05	0.183	2.08	0.026
291359	*Ly86*	-0.12	0.836	1.40	0.012
25211	*Lyz2*	0.79	0.321	1.77	0.044
291885	*Mcm5*	0.20	0.633	1.10	0.012
29685	*Mcm6*	0.17	0.682	1.01	0.019
291234	*Mki67*	-0.35	0.584	1.83	0.011
81687	*Mmp9*	2.53	0.006	1.55	0.083
304988	*Mnda*	0.55	0.521	1.75	0.045
361735	*Ms4a6a*	0.20	0.801	1.46	0.036
293749	*Ms4a6bl*	-0.86	0.091	1.43	0.020
314654	*Myo1f*	0.00	0.997	1.14	0.036
58982	*Ncan*	0.19	0.656	1.51	0.002
309452	*Nfkb2*	1.21	0.046	0.40	0.571
266777	*Nptx1*	1.32	0.028	-0.89	0.136
288475	*Nptx2*	1.55	<0.001	-0.40	0.234

83834	*Nrn1*	1.23	0.026	-0.99	0.078
24609	*Odc1*	1.03	0.023	0.70	0.112
289247	*Olr1584*	0.37	0.508	1.11	0.050
310132	*Osmr*	1.33	0.048	1.06	0.123
363041	*Pate4*	1.61	0.008	1.08	0.071
54320	*Pdpn*	0.40	0.429	1.23	0.031
85311	*Pla1a*	1.17	0.038	1.56	0.019
297694	*Plbd1*	-0.44	0.379	1.19	0.034
298199	*Plin2*	0.26	0.561	1.13	0.018
302562	*Plp2*	-0.06	0.938	1.29	0.032
59103	*Ptges*	2.03	0.005	0.82	0.216
362524	*Ptpn3*	1.02	0.045	-0.55	0.298
116689	*Ptpn6*	-0.05	0.939	1.11	0.034
689388	*Ptx3*	3.12	0.005	1.24	0.235
282817	*Pycard*	-0.06	0.943	1.36	0.025
365042	*Rab32*	0.92	0.150	1.42	0.050
366957	*Rac2*	0.82	0.158	1.65	0.020
364190	*Rasl10a*	1.11	0.026	-0.37	0.492
100360982	*Relb*	1.30	0.034	0.55	0.403
360857	*Rgs16*	1.43	0.050	0.90	0.229
289076	*Rgs18*	0.01	0.991	1.57	0.026
362993	*Rnd1*	1.65	0.013	-0.57	0.410
309621	*RT1-Ba*	0.44	0.629	2.41	0.012
309622	*RT1-Bb*	0.21	0.852	2.53	0.014
294269	*RT1-Da*	0.47	0.683	2.91	0.014
294273	*RT1-DMb*	0.01	0.986	1.05	0.025
81778	*S100a10*	0.31	0.647	1.28	0.046
445415	*S100a11*	-0.35	0.626	1.45	0.038
24615	*S100a4*	-0.24	0.732	1.62	0.020
25544	*Sele*	3.82	<0.001	0.40	0.650
313057	*Serinc2*	1.66	0.004	-0.34	0.560
24795	*Serpina3n*	0.98	0.212	1.86	0.039
24617	*Serpine1*	2.37	0.036	1.97	0.089
155183	*Skap2*	-0.07	0.896	1.01	0.023
364049	*Slamf7*	-0.20	0.708	1.08	0.035
289235	*Slamf9*	-0.58	0.238	1.11	0.047
246239	*Slc15a3*	1.24	0.018	0.82	0.107
366568	*Slc30a3*	1.23	0.049	-1.03	0.106
499587	*Slc7a14*	1.19	0.046	-1.05	0.088
303378	*Slfn13*	-0.18	0.756	1.23	0.025
24787	*Sod2*	1.31	0.009	0.28	0.623
294043	*Sorcs3*	1.07	0.025	-0.31	0.568
308341	*Ssc5d*	-0.35	0.310	1.02	0.014
292483	*Stx11*	1.17	0.035	-0.06	0.950
24886	*Tbxas1*	-0.08	0.912	1.10	0.049
116510	*Timp1*	1.27	0.059	2.59	0.003
24834	*Tk1*	-0.30	0.312	1.02	0.006
684440	*Tlr8*	-0.64	0.307	1.51	0.034
316516	*Tmbim1*	0.41	0.395	1.37	0.014
299339	*Tnfaip2*	2.14	0.005	0.52	0.495
683206	*Tnfaip3*	1.03	0.034	0.07	0.923
686008	*Tnfrsf22*	1.09	0.042	0.23	0.738
500590	*Tnfrsf9*	1.06	0.007	0.24	0.579
301229	*Trem1*	2.10	0.037	1.50	0.140
78969	*Trib1*	1.06	0.005	0.46	0.176
307351	*Tubb6*	0.65	0.232	1.53	0.021
361537	*Tyrobp*	0.36	0.393	1.17	0.018

Log2FC = log2 fold change

Appendix Table 2.2: Downregulated genes in hippocampal microvessels at either 6 or 24 hrs following sonication (versus contralateral hemisphere)

		6 hrs Post-FUS+MBs		24 hrs Post-FUS+MBs	
Entrez ID	**Gene Symbol**	**Log2 FC**	**Adjusted P-Value**	**Log2 FC**	**Adjusted P-Value**
287788	*Abca9*	-1.38	0.002	0.26	0.548
170913	*Abcb1a*	-1.14	0.042	0.08	0.927
314800	*Acss3*	-1.07	0.028	0.23	0.700
100363275	*Adgra2*	-1.07	0.025	0.38	0.443
24172	*Adh1*	-1.30	0.029	0.60	0.335
116676	*Aldh1a2*	-1.20	0.006	0.76	0.070
171100	*Angptl2*	-1.22	0.034	0.90	0.119
81641	*Anpep*	-1.03	0.007	0.52	0.151
29473	*Aoc3*	-1.31	0.021	0.32	0.616
306805	*Aspn*	-1.83	0.012	0.18	0.854
59302	*Bmp15*	-1.04	0.013	-0.30	0.497
85272	*Bmp7*	-1.33	0.004	0.69	0.092
140724	*Cacng3*	1.07	0.109	-1.55	0.040
24932	*Cd4*	-1.04	0.024	0.58	0.195
503009	*Cdkl4*	0.18	0.790	-1.34	0.034
365871	*Ciart*	-1.01	0.048	0.29	0.634
245978	*Cklf*	-1.32	0.021	0.66	0.240
294141	*Clic2*	-1.35	0.034	0.29	0.717
310201	*Cmbl*	-1.16	0.026	-0.06	0.946
114020	*Cml5*	-1.56	0.014	-0.19	0.819
84352	*Col1a2*	-1.01	0.006	0.48	0.164
361289	*Colec12*	-1.01	0.006	0.30	0.419
360611	*Copz2*	-1.06	0.003	0.71	0.039
500046	*Cped1*	-1.46	0.009	0.16	0.818
83575	*Cpz*	-1.23	0.002	0.26	0.475
498392	*Cytl1*	-1.09	0.032	-0.06	0.937
366270	*Edn3*	-1.32	0.009	-0.09	0.905
365691	*Egflam*	-1.12	0.025	0.16	0.806
25043	*Eln*	-1.11	0.031	0.31	0.610
85496	*Enpp1*	-1.09	0.013	0.35	0.437
25315	*Ephx1*	-1.30	0.003	0.15	0.762
156826	*Eya2*	-1.02	0.013	0.88	0.040
362336	*Fam180a*	-2.20	0.001	0.53	0.352
691221	*Faxdc2*	-1.02	0.039	0.22	0.726
29558	*Fcgrt*	-1.26	0.006	0.39	0.381
499856	*Fibin*	-1.07	0.015	0.27	0.590
362366	*Fkbp14*	-1.14	0.009	0.36	0.407
297123	*Fkbp9*	-1.15	0.013	0.49	0.276
25256	*Fmo1*	-1.46	0.006	0.27	0.645
84493	*Fmo3*	-1.38	0.033	0.46	0.522
64507	*Fmod*	-1.26	0.007	0.44	0.335
79209	*Frk*	-1.93	0.009	0.16	0.872
24947	*Gabra3*	0.75	0.211	-1.34	0.048
394266	*Gjb2*	-1.58	0.004	0.13	0.853
84403	*Gjb6*	-1.04	0.048	-0.48	0.395
25236	*Gpc3*	-1.28	0.011	0.45	0.376
60667	*Gpr20*	-1.06	0.042	-0.06	0.942
300850	*Gsta4*	-1.20	0.014	0.04	0.958
24424	*Gstm2*	-1.70	0.006	0.21	0.776
362540	*Hacd4*	-1.03	0.049	0.46	0.426
24450	*Hmgcs2*	-1.08	0.028	-0.31	0.578
100359865	*Hrct1*	-1.08	0.049	0.16	0.834
161476	*Hspb2*	-1.09	0.007	0.48	0.212

686539	*Islr*	-1.31	0.009	0.80	0.099
25118	*Itga1*	-1.02	0.042	0.23	0.723
364786	*Itga8*	-1.09	0.038	0.13	0.866
100361376	*Kank2*	-1.04	0.012	0.15	0.769
316758	*Lama1*	-1.11	0.016	0.44	0.334
361303	*Lims2*	-1.06	0.032	0.13	0.853
100361383	*LOC100361383*	-1.07	0.040	-0.02	0.978
685513	*LOC685513*	-1.04	0.038	0.80	0.113
688126	*LOC688126*	-1.15	0.030	0.06	0.938
315714	*Loxl1*	-1.04	0.006	0.49	0.160
81682	*Lum*	-1.18	0.027	0.64	0.234
304131	*Map3k7cl*	-1.28	0.030	0.31	0.666
292671	*Mill1*	-1.67	0.006	0.19	0.796
300679	*Mpzl2*	-1.48	0.026	0.28	0.737
498011	*Mrc2*	-1.02	0.009	0.37	0.336
404641	*Mrgprh*	-1.49	0.028	0.06	0.959
361734	*Ms4a4a*	-1.36	0.039	0.88	0.188
313770	*Mxra8*	-1.19	0.006	0.40	0.333
24582	*Myh11*	-1.11	0.042	0.36	0.579
64570	*Nat8*	-1.47	0.009	0.16	0.829
312401	*Ndnf*	-1.63	0.003	0.18	0.764
246172	*Nexn*	-1.01	0.029	0.16	0.792
100912108	*Nupr1*	-1.15	0.028	0.80	0.120
500992	*Nxpe1*	-1.51	0.026	0.03	0.981
304507	*Oas1i*	-1.20	0.042	0.53	0.410
291015	*Ogn*	-1.04	0.004	0.11	0.803
83717	*Omd*	-1.75	0.002	-0.01	0.984
29569	*Pcolce*	-1.05	0.007	0.45	0.227
89813	*Pdk4*	-1.48	0.005	0.03	0.974
685611	*Phldb2*	-1.07	0.023	0.12	0.853
64672	*Pln*	-1.59	0.005	0.52	0.337
84400	*Prelp*	-1.07	0.009	0.34	0.403
60357	*Prom1*	-1.26	0.042	-0.06	0.949
171452	*Rab3il1*	-1.04	0.005	0.56	0.098
294789	*Ranbp3l*	-1.39	0.013	0.78	0.145
361819	*RGD1566085*	-1.08	0.049	-0.13	0.870
297757	*Sbspon*	-1.01	0.050	0.34	0.578
140927	*Selenbp1*	-1.22	0.006	0.01	0.984
84402	*Sfrp1*	-1.34	0.013	0.12	0.879
64846	*Slc13a3*	-1.31	0.043	0.48	0.518
503568	*Slc13a4*	-1.72	0.002	0.07	0.914
287450	*Slc16a11*	-1.14	0.020	-0.13	0.847
295356	*Slc16a4*	-1.11	0.015	0.27	0.602
29509	*Slc22a6*	-1.83	0.003	0.18	0.794
83500	*Slc22a8*	-1.19	0.028	0.00	0.997
170840	*Slc40a1*	-1.42	0.028	0.10	0.913
171163	*Slc6a13*	-1.85	0.001	0.24	0.671
170698	*Slco1a2*	-1.13	0.037	0.29	0.659
306147	*Slitrk1*	0.62	0.332	-1.41	0.045
25554	*Snai2*	-1.03	0.018	0.47	0.267
498159	*Spry3*	0.61	0.260	-1.19	0.048
83783	*Sult1a1*	-1.56	0.008	-0.09	0.910
192189	*Syt17*	0.28	0.620	-1.16	0.037
292406	*Thbs2*	-1.04	0.003	0.38	0.231
245953	*Tmem37*	-1.26	0.007	0.59	0.182
293874	*Trpm6*	-1.27	0.025	0.62	0.275
117514	*Txnip*	-1.02	0.009	0.44	0.241
89818	*Vamp5*	-1.07	0.013	0.62	0.140

361954	*Veph1*	-1.01	0.005	0.37	0.267
24877	*Vsnl1*	0.54	0.240	-1.02	0.048
64566	*Wnt5a*	-1.08	0.013	0.05	0.934
361552	*Wtip*	-1.50	0.014	0.16	0.848

Log2FC = log2 fold change

Appendix Table 2.3: Differential expression of selected genes at 6 and 24 hrs post-FUS+MB exposure as measured by microarray analysis and qRT-PCR

	Log2 Fold Change Compared to Contralateral Hemisphere (adjusted p-value)			
	6 hrs Post-FUS+MBs		24 hrs Post-FUS+MBs	
Gene Symbol	**Microarray**	**qRT-PCR**	**Microarray**	**qRT-PCR**
Abcb1a	**-1.14 (0.044)**	**-3.14 (0.049)**	0.08 (0.928)	0.68 (0.394)
Ccl2	**4.73 (<0.001)**	**6.16 (0.021)**	1.70 (0.086)	2.79 (0.255)
Cd74	0.34 (0.741)	0.23 (0.835)	**2.64 (0.010)**	**3.99 (0.001)**
Gfap	0.29 (0.479)	-0.17 (0.762)	**1.54 (0.003)**	**2.05 (<0.001)**
Itgb2	0.47 (0.479)	0.36 (0.613)	**1.38 (0.035)**	**1.77 (0.011)**
Lcn2	**2.02 (0.008)**	**2.16 (0.036)**	**2.91 (0.003)**	**4.41 (<0.001)**
Serpine1	**2.37 (0.037)**	**3.42 (0.013)**	1.97 (0.092)	**3.07 (0.043)**
Slc22a6	**-1.83 (0.003)**	**-2.98 (0.001)**	0.18 (0.801)	0.51 (0.386)

Linear correlation of log2FC assessed by qRT-PCR vs microarray: $r^2 = 0.96$, slope = 0.66

Appendix Table 3.1: Differential expression relative to control regions at 6 hrs post-FUS+MB exposure

Gene Names	Log2FC: Scheme 1	P-Value: Scheme 1	Log2FC: Scheme 2	P-Value: Scheme 2	Log2FC: Scheme 3	P-Value: Scheme 3
Agt	-0.8	0.407	0.48	0.729	-0.16	0.861
Akt1	-0.14	0.178	0.32	0.624	-0.09	0.685
Atf1	0.08	0.503	1.01	0.291	0.62	0.287
Atf2	0.49	0.205	1.32	0.367	1.15	0.244
Bcl10	0.62	0.443	0.87	0.327	0.6	0.189
Bcl2a1	0.35	0.599	2.43	0.144	1.4	0.175
Bcl2l1	0.56	0.262	0.63	0.449	0.3	0.433
Bcl3	0.25	0.503	1.77	0.074	1.78	0.053
Birc3	0.6	0.45	3.82	0.014	3.66	0.004
Card10	-0.33	0.308	0.29	0.404	-0.8	0.085
Card11	-0.79	0.152	0.33	0.648	-0.23	0.287
Casp1	-0.31	0.611	1.21	0.454	0.75	0.448
Casp8	0.34	0.554	0.81	0.535	0.42	0.425
Ccl2	1.94	0.219	5.73	0.024	5.44	0.014
Ccl5	-0.27	0.699	1.99	0.092	1.77	0.174
Cd40	-0.04	0.881	1.87	0.119	1.72	0.143
Cflar	0.47	0.144	0.91	0.234	0.64	0.209
Chuk	0.12	0.509	0.66	0.362	0.34	0.322
Crebbp	0.22	0.383	0.31	0.658	0.33	0.331
Csf1	-0.04	0.791	1.3	0.109	0.77	0.445
Csf2	-0.21	0.139	0.54	0.392	-0.49	0.28
Csf3	-0.46	0.087	1.29	0.388	-0.49	0.28
Egfr	-0.63	0.094	0.51	0.558	0.02	0.946
Egr1	0.9	0.429	1.33	0.093	0.81	0.04
Eif2ak2	0.35	0.486	0.47	0.537	0.3	0.591
F2r	0.28	0.377	0.61	0.273	0.08	0.82
Fadd	0.17	0.41	0.64	0.39	0.27	0.179
Faslg	0.18	0.841	0.75	0.356	0.37	0.002
Fos	0.53	0.457	2.36	0.025	2.16	0.025
Hmox1	-0.12	0.752	2.51	0.145	1.54	0.304
Icam1	0.69	0.237	2.63	0.065	2.14	0.071

Ifna1	0.02	0.948	0.09	0.63	-0.46	0.32
Ifng	-0.46	0.087	0.09	0.63	-0.49	0.28
Ikbkb	-0.17	0.576	0.62	0.394	0.21	0.419
Ikbke	0.05	0.922	0.12	0.78	-0.12	0.606
Ikbkg	0.01	0.976	0.6	0.411	0.19	0.539
Il10	-0.16	0.352	0.37	0.403	-0.49	0.28
Il1a	-0.42	0.162	1.98	0.294	0.77	0.399
Il1b	0.6	0.366	4.36	0.058	3.53	0.053
Il1r1	-0.72	0.069	0.69	0.568	0.04	0.948
Irak1	-0.05	0.697	0.37	0.617	0.06	0.833
Irak2	0.19	0.58	1.17	0.093	0.66	0.2
Irak4	-0.06	0.862	0.34	0.71	-0.09	0.843
Irf1	0.06	0.822	1.79	0.134	1.61	0.182
Jun	0.16	0.77	0.74	0.375	0.71	0.337
LOC687813	-1.12	0.13	0.21	0.849	-0.84	0.076
Lta	0.06	0.859	0.34	0.333	-0.48	0.293
Ltbr	-0.09	0.767	1.11	0.341	0.87	0.267
Map2k3	0.29	0.378	2.13	0.214	1.76	0.273
Map3k1	0.64	0.541	0.99	0.335	0.5	0.34
Mapk3	-0.03	0.928	0.33	0.661	0.26	0.438
Myd88	-0.13	0.619	0.79	0.265	0.41	0.541
Nfkb1	0.35	0.227	1.01	0.151	0.74	0.121
Nfkb2	0.11	0.575	2.04	0.056	1.49	0.184
Nfkbia	0.02	0.95	1.91	0.129	1.17	0.25
Kat2b	0.17	0.579	0.76	0.408	0.32	0.524
Psip1	0.35	0.329	0.4	0.593	0.24	0.45
Raf1	0.25	0.225	0.55	0.413	0.43	0.221
Rel	0.44	0.349	1.29	0.049	0.96	0.019
Rela	0.21	0.45	1	0.202	0.62	0.238
Ripk1	0.06	0.815	0.58	0.442	-0.84	0.397
Ripk2	0.22	0.34	0.93	0.201	-0.25	0.411
Smad4	0.04	0.759	0.57	0.434	0.25	0.423
Stat1	0.01	0.949	0.44	0.604	0.14	0.669
Tbk1	0.33	0.252	0.74	0.371	0.53	0.165
Timp1	0.21	0.695	3.3	0.079	2.78	0.151
Tlr1	0.28	0.732	2.22	0.046	1.91	0.051
Tlr2	0.07	0.877	1.61	0.231	1.32	0.223
Tlr3	-0.17	0.79	0.6	0.651	0.01	0.965
Tlr4	-0.65	0.081	-0.74	0.048	-0.77	0.308
Tlr6	-0.26	0.601	0.97	0.401	0.62	0.511
Tlr9	0.07	0.671	0.46	0.274	-0.45	0.344
Tnf	0.84	0.302	4.02	0.023	3.18	0.012
Tnfrsf10b	-0.84	0.127	0.69	0.337	-0.07	0.914
Tnfrsf1a	-0.19	0.665	2.19	0.279	1.54	0.32
Tnfrsf1b	0.47	0.703	1.47	0.26	0.43	0.68
Tnfsf10	-0.36	0.374	0.07	0.953	-0.39	0.227
Tnfsf14	-0.21	0.14	0.09	0.63	-0.22	0.695
Tollip	-0.1	0.826	1.27	0.411	1.53	0.249
Tradd	0.79	0.488	0.51	0.527	-0.27	0.529
Traf2	0.05	0.644	0.65	0.462	0.27	0.585
Traf3	0.16	0.64	-0.01	0.988	-0.04	0.766
Traf6	-0.06	0.297	0.55	0.477	0.33	0.405
Zap70	0	0.993	0.09	0.63	-0.49	0.28

Log2FC = log2 fold change

Appendix Table 3.2: Differential expression relative to control regions at 4 days post-FUS+MB exposure

Gene Names	Log2FC: Scheme 1	P-Value: Scheme 1	Log2FC: Scheme 2	P-Value: Scheme 2	Log2FC: Scheme 3	P-Value: Scheme 3
Agt	-0.62	0.543	-0.33	0.809	-0.27	0.655
Akt1	0.1	0.781	0.11	0.894	0.31	0.646
Atf1	0.35	0.024	0.11	0.513	0.28	0.035
Atf2	0.35	0.286	0.05	0.927	0.16	0.326
Bcl10	0.16	0.167	0.58	0.226	0.24	0.095
Bcl2a1	0.95	0.601	1.73	0.123	1.95	0.476
Bcl2l1	-0.36	0.481	0.38	0.404	0.54	0.172
Bcl3	0.39	0.695	0.41	0.574	1.13	0.461
Birc3	1.3	0.431	0.58	0.361	1.91	0.346
Card10	-0.6	0.103	0.26	0.765	-0.37	0.011
Card11	0.24	0.72	1.01	0.374	0.18	0.553
Casp1	-0.04	0.945	0.85	0.372	0	0.996
Casp8	1.54	0.368	1.66	0.123	1.89	0.378
Ccl2	-0.51	0.032	1.27	0.276	-0.12	0.732
Ccl5	-0.67	0.406	0.02	0.967	-0.23	0.792
Cd40	-0.13	0.579	0.91	0.297	-0.17	0.529
Cflar	0.16	0.432	-0.14	0.128	0	0.98
Chuk	0.22	0.298	0.13	0.494	0.87	0.287
Crebbp	1.5	0.31	-0.11	0.303	1.4	0.38
Csf1	0.46	0.139	0.87	0.118	0.71	0.06
Csf2	-1.31	0.249	0.28	0.714	-0.5	0.233
Csf3	-0.25	0.57	-0.27	0.404	0.12	0.753
Egfr	0.17	0.602	-0.31	0.34	0.46	0.488
Egr1	1.75	0.219	0.87	0.304	2.12	0.211
Eif2ak2	-0.12	0.399	0.28	0.579	-0.13	0.539
F2r	-0.18	0.455	1.15	0.423	0.28	0.719
Fadd	0.15	0.726	0.55	0.402	1.06	0.133
Faslg	-0.43	0.606	-0.43	0.398	-0.31	0.347
Fos	0.36	0.57	0.51	0.577	0.52	0.313
Hmox1	0.59	0.509	1.51	0.275	0.91	0.117
Icam1	-0.63	0.453	1.15	0.059	-0.07	0.897
Ifna1	0.63	0.616	0.26	0.726	0.93	0.475
Ifng	0.03	0.967	0.06	0.91	0.41	0.563
Ikbkb	-0.25	0.526	0.5	0.495	0.05	0.711
Ikbke	-1.03	0.17	0.65	0.272	-0.44	0.607
Ikbkg	1.33	0.419	0.01	0.95	1.4	0.387
Il10	1.21	0.526	-0.27	0.404	1.87	0.434
Il1a	-0.68	0.343	0.1	0.868	-0.15	0.695
Il1b	-0.37	0.622	0.61	0.38	0.64	0.467
Il1r1	-0.43	0.262	0.56	0.423	0.11	0.851
Irak1	0.05	0.65	-0.04	0.907	0.15	0.583
Irak2	-0.04	0.928	-0.11	0.496	-0.52	0.255
Irak4	-0.13	0.617	0.41	0.205	-0.51	0.091
Irf1	0.93	0.461	0.21	0.647	1.22	0.432
Jun	-0.59	0.453	0.52	0.188	0.02	0.957
LOC687813	-0.17	0.593	0.57	0.386	0.65	0.527
Lta	0.08	0.904	0.2	0.772	1.14	0.46
Ltbr	1.42	0.329	0.89	0.305	1.57	0.321
Map2k3	0.46	0.442	0.26	0.469	1.14	0.23
Map3k1	-0.05	0.808	0.59	0.453	0.16	0.557
Mapk3	-0.04	0.729	0.39	0.294	0.58	0.166
Myd88	-0.06	0.858	0.03	0.968	-0.15	0.453
Nfkb1	-0.1	0.353	0.07	0.792	0.21	0.24
Nfkb2	-1.65	0.29	0.23	0.697	-1.15	0.319
Nfkbia	-1.02	0.285	0.16	0.761	-0.8	0.304

Kat2b	0.79	0.398	0.39	0.307	0.95	0.263
Psip1	0.24	0.47	0.29	0.434	0.36	0.106
Raf1	1.45	0.348	0.17	0.675	1.26	0.387
Rel	-0.49	0.709	0.7	0.13	-0.19	0.834
Rela	0.65	0.33	0.81	0.319	0.81	0.387
Ripk1	0.59	0.38	0.31	0.221	1.27	0.244
Ripk2	-0.13	0.713	0.94	0.347	0.19	0.339
Smad4	0.12	0.551	0.48	0.58	0.56	0.385
Stat1	-0.25	0.21	0.62	0.46	0.38	0.545
Tbk1	0.25	0.52	0.44	0.33	0.37	0.036
Timp1	0.53	0.413	2.41	0.077	1.2	0.098
Tlr1	0.24	0.563	1.55	0.009	0.76	0.398
Tlr2	0.32	0.508	1.38	0.184	0.52	0.646
Tlr3	1.08	0.464	1.33	0.14	1.17	0.487
Tlr4	0.92	0.296	0.75	0.282	0.58	0.568
Tlr6	-0.32	0.519	0.51	0.506	-0.4	0.529
Tlr9	0.12	0.737	1.32	0.183	0.32	0.276
Tnf	-0.2	0.843	0.03	0.976	0.81	0.553
Tnfrsf10b	-0.65	0.17	-0.04	0.821	-0.25	0.638
Tnfrsf1a	-0.42	0.372	0.18	0.807	0.02	0.966
Tnfrsf1b	0.14	0.852	1.1	0.388	0.51	0.5
Tnfsf10	-0.8	0.153	-0.13	0.844	0.08	0.882
Tnfsf14	-1.83	0.287	0.01	0.983	-1.18	0.319
Tollip	0.29	0.419	0.25	0.732	0.2	0.485
Tradd	-1.56	0.315	-0.05	0.897	-1.51	0.369
Traf2	0.06	0.818	-0.32	0.156	0.78	0.418
Traf3	1.1	0.457	-0.03	0.962	1.59	0.385
Traf6	-0.37	0.533	0.34	0.49	0.08	0.415
Zap70	0.04	0.953	0.23	0.747	0.76	0.492

Log2FC = log2 fold change

Appendix Table 4.1: Justifications and explanations for methods detailed in Chapter 4

Method Details	**Explanations/Justifications**
Rats were transcardially perfused with ice-cold phosphate buffer (0.1 M, pH 7.4), followed by 4% paraformaldehyde	• Removal of blood from circulation allows for a clearer visualization of cerebral vasculature by reducing autofluorescence from red blood cells and nonspecific antibody binding • Proper osmolarity and pH of perfusing solution acts to maintain the structure of tissue for subsequent analysis (E.g. preventing substantial shrinkage or swelling of cells prior to fixation) • Paraformaldehyde cross-links proteins to maintain tissue structure for subsequent analysis
Brains were transferred to 30% sucrose solution and stored at 4^{o} C until fully saturated	• Sucrose acts as a cryoprotectant by helping prevent ice crystal formation in tissue when water freezes. The expansion of water during freezing can disrupt cell membranes and create a loose extracellular matrix that can confound structural analyses
Tissue was sectioned at 40 µm thickness	• Cutting thickness was meant to balance antibody penetration, section integrity during immunohistochemistry procedure, and the volume of tissue within a single section available for analysis • Thin sections allow more thorough antibody penetration • Thick sections are resistant to tearing and provide a greater volume of tissue for analysis per section

Tissue sections were co-stained for BrdU and glucose transporter-1 (GLUT1)	• BrdU is an exogenous molecule that is incorporated into replicating DNA. The presence of BrdU within the nucleus of a cell indicates that the cell has either divided or has performed extensive DNA repair while intracellular BrdU concentrations are high • GLUT1 is a glucose transporter that is found in cerebrovascular endothelial cells • The colocalization of BrdU and GLUT1 is indicative of cerebrovascular endothelial cell division, a necessary step for angiogenesis in the brain
Antigen retrieval consisted of 90 min in 2 M HCl, followed by 10 min in 0.1 M borate buffer (pH 8.5)	• Antigen retrieval is meant to reverse the masking of epitopes that can occur during fixation. Unmasking epitopes allows for antibodies to interact with and bind to their intended cites within a target protein • Acid-based antigen retrieval methods are commonplace for a variety of antigens, including BrdU
Sections were blocked for 1 hr at room temperature prior to primary antibody incubation (0.1% Triton X-100, 1% bovine serum albumin, 2% goat serum, 1x PBS)	• Blocking reduces the amount of nonspecific staining by physically hindering the binding of antibodies to nonspecific sites • Serum from the source species for the secondary antibody can be used for this because it contains IgGs that will bind to nonspecific sites throughout the tissue section but will not bind with high efficiency to the secondary antibody. This acts to reduce background staining intensity, increasing SNR
Sections were mounted with an aqueous mounting media containing DAPI	• DAPI is incorporated into all cell nuclei and allows anatomical landmarks to be located within the brain • Co-localization of DAPI and BrdU allows confirmation of the nuclear localization of BrdU, reducing the false positive rate
Confocal image-stacks were collected with 2 µm spacing at resolution of 1.24 µm/pixel (xy pixel dimension)	• The pixels resolution in the z-direction for the objective lens used in this study was approximately 3 microns • Spacing in the z-direction was meant to ensure a complete capture of all signal within the imaging volume by overlapping imaging volume between sequential optical sections • The pixel resolution in the xy-direction was chosen to ensure the ability to resolve small capillaries (I.e. less than 3 microns in diameter)
Images were collected in the three major subfields of the hippocampus: cornus amonis 1 (CA1), CA3, and dentate gyrus (DG)	• Imaging of the three major subfields was designed to obtain a general picture of how the hippocampus responds to intervention, as well as to possibility discern region-specific changes
Image stacks were cropped in the z-direction, keeping 5 images starting at the first complete optical section	• Tissue shrinkage and non-uniform adherence to glass slides restricted the number of complete optical sections that could be consistently captured in all tissue sections • Keeping 5 optical sections per imaging volume was designed to maintain consistency throughout the analysis
GLUT1 Segmentation pipeline: 1. Background signal intensity in the GLUT1 channel was reduced with subtraction of the BrdU channel with high intensity pixels removed	• The use of a secondary antibody for BrdU staining that was raised in rat produced a large amount of background staining in that channel. This background staining was substantially lower in vascular and perivascular regions of the tissue and thus provided a means of reducing background fluorescence in the GLUT1 channel • The removal of high intensity pixels (BrdU positive cells) from the BrdU channel prior to background subtraction was necessary to prevent these regions of the GLUT1 channel from being removed, as they could be part of the blood vessel
2. Blood vessels were emphasized in maximum intensity projections with the *Tubeness* plugin (ImageJ)	• The Tubeness plugin (ImageJ) can be used to detect tube-like structures within each image. This plugin uses eigenvalues of the Hessian matrix to calculate a measure of tubeness for each pixel within an image. Emphasizing 'tube-like structures' within each image acts to reduce the influence of signal intensity on the area of tissue segmented as GLUT1-positive • The GLUT1 pipeline removed the relationship between CNR and segmented area

3. log2 transformed and averaged within animals to obtain hippocampal means.	• Log2 transformation of ratios allows averaging these ratios across subfield and animals without a skew towards positive fold changes
Diameters of blood vessel segments were manually measured	• Blood vessel segments were defined as any distinct length of vasculature • When vessels branched, each of the branches were counted as a blood vessel segment
Blood vessel diameters were, binned to <5 µm, 5-7.5 µm, 7.5-10 µm, and >10 µm	• Bin sizes were based on both the pixel size of the images (integer multiples of the spatial resolution of images) and the size distribution of typical rat cerebrovascular capillaries, which tend to centre around 5 microns in diameter

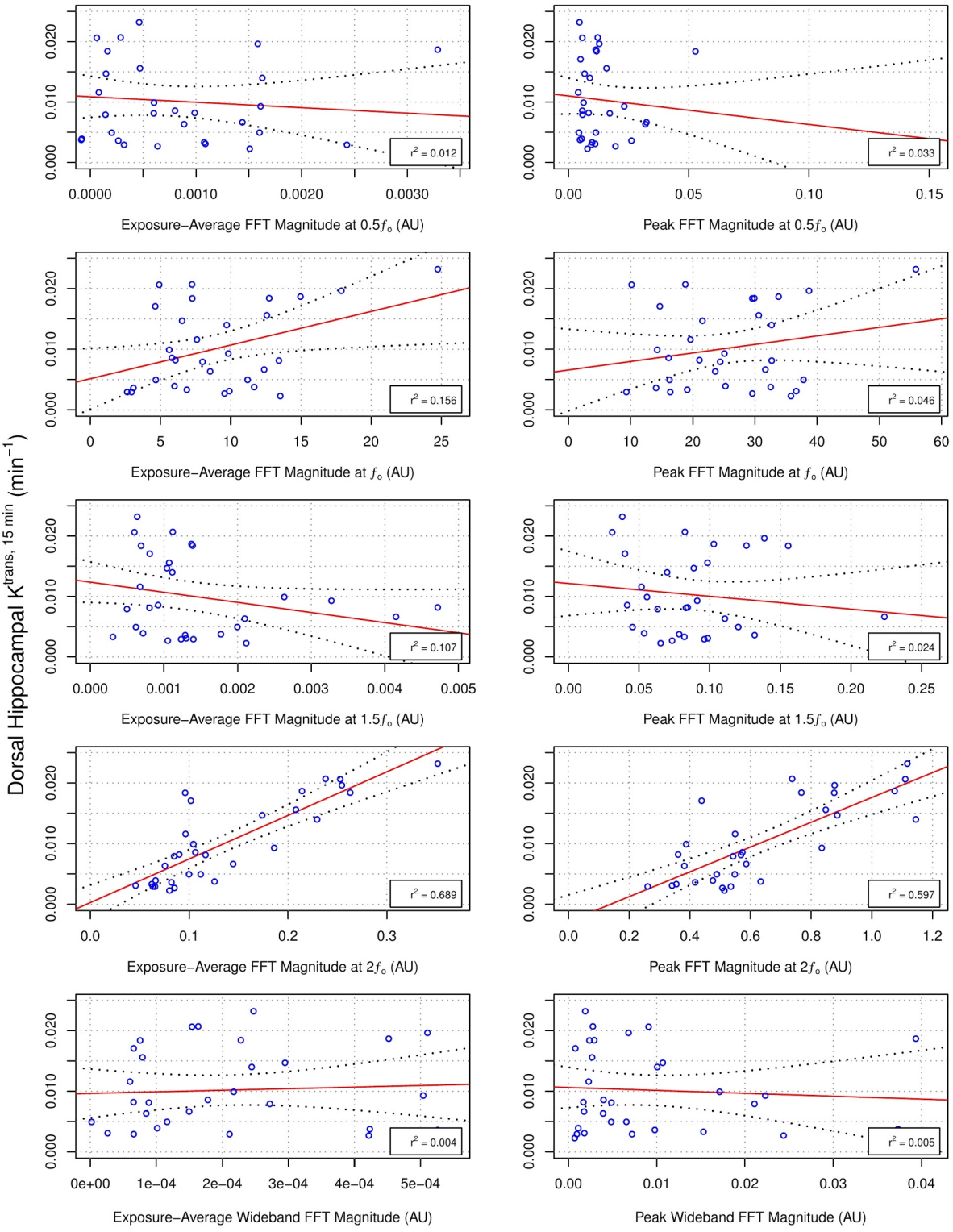

Appendix Figure 5.1: Correlation between acoustic emissions and post-FUS+MBs dorsal hippocampal $K^{trans,\ 15\ min}$. Hydrophone signals captured during FUS+MB exposures were analysed retrospectively to explore potential relationships between $K^{trans,\ 15\ min}$ measurements and spectral characteristics of the acquired acoustic emissions. The treatment-average and peak magnitude of $0.5f$, f, $1.5f$, $2f$, and wideband emissions displayed in relation to $K^{trans,\ 15\ min}$ in the sonicated dorsal hippocampus. Black dotted lines indicate 95% confidence intervals. AU = arbitrary units.